FAST MARCHING METHOD WITH MULTIPHASE FLOW AND COMPOSITIONAL EFFECTS

A Thesis

by

YUSUKE FUJITA

Submitted to the Office of Graduate and Professional Studies of
Texas A&M University
in partial fulfillment of the requirements for the degree of

MASTER OF SCIENCE

Chair of Committee,	Akhil Datta-Gupta
Committee Members,	Michael J. King
	Debjyoti Banerjee
Head of Department,	A. Daniel Hill

August 2014

Major Subject: Petroleum Engineering

ABSTRACT

In current petroleum industry, there is a lack of effective reservoir simulators for modeling shale and tight sand reservoirs. An unconventional resource modeling requires an accurate flow characterization of complex transport mechanisms caused by the interactions among fractures, inorganic matrices, and organic rocks. Pore size in shale and tight sand reservoirs typically ranges in nanometers, which results in ultralow permeability (nanodarcies) and a high capillary pressure in the confined space. In such extremely low permeability reservoirs, adsorption/desorption and diffusive flow processes play important roles for a fluid flow behavior in addition to heterogeneity-driven convective flow.

In this study, the concept of "Diffusive Time of Flight" (DTOF) is generalized for multiphase and multicomponent flow problems on the basis of the asymptotic theory. The proposed approach consists of two decoupled steps – (1) calculation of well drainage volumes along a propagating 'peak' pressure front, and (2) numerical simulation based on the transformed 1-D coordinates. Geological heterogeneities distributed in 3-D space are integrated by tracking the propagation of 'peak' pressure front using a "Fast Marching Method" (FMM), and subsequently, the drainage volumes are evaluated along the outwardly propagation contours. A DTOF-based numerical simulation is performed by treating a series of the DTOF as a spatial coordinate. This approach is analogous to streamline simulation, whereby a multidimensional simulation is transformed into 1-D coordinates resulting in substantial savings in computational

time, thus allowing for high resolution simulation. However, instead of using a convective time of flight (CTOF), a diffusive time of flight is introduced in the modeling of a pressure front propagation.

The overall workflow, which consist of the FMM and numerical simulation, is described in detail for single-phase, two-phase, blackoil, and compositional cases. The model validation is firstly performed on single-porosity systems with and without geological heterogeneity, then extended to multi-continuum domains including dual-porosity fractured reservoir and triple-continuum system. The large-scale unconventional models are finally demonstrated in consideration of the permeability correction for shale gas system and capillarity incorporation for confined phase behavior in multiphase shale oil system.

DEDICATION

To my family: Saori and Mikino

ACKNOWLEDGEMENTS

I would like to thank my committee chair, Dr. Datta-Gupta, and my committee members, Dr. King and Dr. Banerjee for their guidance and support throughout the course of this research. I would also like to express my sincere gratitude to Dr. Arihara for his encouragement and support during my undergraduate studies at Waseda University and his recommendation for the graduate study at Texas A&M University.

I would also like to extend my appreciation to JX Nippon Oil & Gas Exploration Corporation for their support.

Thanks go to my friends and colleagues and the department faculty and staff for making my time at Texas A&M University a great experience.

I also want to thank my mother and father for their encouragement and my wife for her patience and love. Also, special thanks to my beloved daughter. I hope that someday I will be able to help you achieve your dream as the people acknowledged here have helped me.

NOMENCLATURE

A	Surface area
A_k	k th order pressure amplitude in Fourier domain
b	Slippage factor
B_α	Formation volume factor of phase α
C_k	Dissolved gas concentration in Kerogen
C_m	Adsorbed gas concentration on nanopore surface
c_r	Rock compressibility
c_t	Total compressibility
c_α	Fluid compressibility of phase α
D_c	Gas diffusion coefficient
D_m	Effective Knudsen diffusion coefficient
D_k	Knudsen diffusion coefficient
F	Dimensionless slippage factor
J	Flux
K_n	Knudsen number
K_j	K-value of component j
k	Absolute permeability
k_{app}	Apparent permeability
$k_{r\alpha}$	Relative permeability of phase α
k_∞	Darcy permeability

M_k	Permeability multiplier
M_w	Molecular weight
M_ϕ	Exponential rock compressibility function
n	Time-step level
P	Pressure
P_L	Langmuir pressure
q_α	Unit volume production rate of phase α at wellbore condition
$q_{\alpha s}$	Surface volume production rate of phase α
$\tilde{q}_j$	Unit molar production rate of component j
$\tilde{q}_{wj}$	Well molar production rate of component j
R	Universal gas constant
r	Pore radius
S_α	Saturation of phase α
T	Temperature
T_i	Transmissibility at grid i
t	Time
$\mathbf{u}_\alpha$	Fluid velocity of phase α
V_L	Langmuir volume
V_p	Drainage volume
v_i	Derivative of drainage 'bulk' volume at grid i
w_i	Derivative of drainage 'pore' volume at grid i
$\mathbf{x}$	Spatial location

x_j	Oil mole fraction of component j
y_j	Gas mole fraction of component j
z	Compressibility factor
α	Phase (oil, gas, or water)
α_{diff}	Diffusivity
λ_α	Fluid mobility of phase α
λ_t	Total mobility
μ_α	Fluid viscosity of phase α
ω	Frequency in Fourier domain
ϕ	Porosity
ϕ_j	Fugacity coefficient of component j
τ	Diffusive time of flight
Γ	Transfer function
ξ_α	Molar density of phase α

TABLE OF CONTENTS

Page

LIST OF FIGURES

Page

LIST OF TABLES

Page

CHAPTER I

INTRODUCTION AND STUDY OBJECTIVES

1.1 Asymptotic Approach

Predicting oil and gas production from subsurface permeable media is a very important task in the reservoir engineering field. In general, subsurface dynamic model involves many mathematical and physical assumptions in order to simplify the description of Earth's internal structure and to reduce the demand of computation time. Analytical solutions (i.e. material balance method, pressure transient analysis, rate transient analysis) are the most restricted or simplified models that require the reservoir to be isotropic and homogeneous in most cases. Numerical simulation removes such approximations and limitations by decomposing a continuous domain into a finite set of discrete counterparts. In the petroleum industry, reservoir simulation model is traditionally used for constructing a subsurface system associated with spatial heterogeneities (i.e. porosity, permeability, water saturation). The simulation outcomes are utilized for the purpose of improving estimation of hydrocarbon reserves, identifying fluid flow and geological characteristics, and more importantly, optimizing the strategies regarding the field developments.

For a long time, streamline-based flow simulation has been widely recognized as an efficient approach for modeling fluid dynamics in porous media. The principle underlying the streamline simulation is to decompose the multidimensional transport equations into a series of 1-D equations along streamlines (Datta-Gupta and King 2007).

The evolution of flood fronts and the interactions between production and injection wells can be easily identified using the concept of convective time of flight (CTOF).

Another important concept related to the theory of pressure propagation in porous media has been proposed by Lee (1982) who defined a 'radius of investigation' as the propagation distance of a 'peak' pressure disturbance for an impulse source or sink. The radius of investigation can be analytically calculated under limitations of homogeneous and isotropic reservoirs; however, such analytical solution is not applicable for complex geometries and heterogeneous media. Datta-Gupta et al. (2011) generalized the concept of radius of investigation to heterogeneous field by introducing a diffusive time of flight (DTOF) which corresponds to the arrival time of a 'peak' pressure front. High frequency asymptotic solution of the diffusivity equation leads to the Eikonal equation for a pressure 'front' propagation in the presence of spatial heterogeneities (Vasco and Datta-Gupta 1999, Vasco et al. 2000, Datta-Gupta and King 2007). This asymptotic solution can be solved very efficiently by using the Fast Marching Method (FMM) (Sethian 1996, Sethian 1999) as shown by Datta-Gupta et al. (2001) for reservoir engineering purpose. The FMM is a class of front tracking algorithm for solving the Eikonal equation and similar to the Dijkstra algorithm (Dijkstra 1959) that finds shortest path on graphs. The DTOF can be obtained along its trajectory using the FMM calculation. Well drainage volume is successively calculated by contouring a specific DTOF and by summing up the pore volumes inside the contour. Zhang et al (2014) proposed a DTOF-based numerical simulation associated with the transformation of a fluid transport coordinate from the physical 3-D space to the 1-D DTOF space. As

in the CTOF applied to the streamline simulation, the DTOF embodies geological heterogeneities and reduces 3-D heterogeneity to a 1-D homogeneous problem along its coordinate. This dimension reduction results in substantial savings in computational time and allows for high resolution reservoir simulation.

1.2 Characteristics of Unconventional Reservoirs

The U.S. Energy Information Administration (EIA) defines the term 'unconventional' as a complex interactive function of resources characteristics, the available exploration and production technologies, the current economic environment, and the scale, frequency, and duration of production from the resources. Shale oil and gas reservoirs are the typical unconventional resources which contain a huge amount of hydrocarbons in the fine-grained sedimentary rock composed of mud from flakes of clay minerals and tiny fragments of other minerals. The EIA (2013) estimates that technically recoverable shale oil and gas resources in the U.S. comprise 58 billion barrels of crude oil and 665 trillion cubic feet of natural gas as of 2013, which are approximately 26% of the total domestic oil reserves and 27% of the total domestic natural gas reserves. They also suggest that, because shale oil and gas have proven to be quickly producible in large volume at a relatively low cost, shale oil and gas resources have revolutionized the U.S. oil and natural gas production, providing 29% of the total U.S. crude oil production and 40% of the total natural gas production in 2012. Based on the success of the U.S. shale plays, several countries have begun to evaluate and test the production and potential of shale formations located in their countries.

The first shale play in the U.S. was started in the Barnett shale formation located in North-Central Texas. More than 16,000 vertical, directional, and horizontal wells have been drilled in the formation since the early 1990s, and by the end of 2012, approximately 13 trillion cubic feet of natural gas has been produced (Browning et al. 2013). The development of the Barnett shale has changed the U.S. natural gas play map significantly. Browning et al. (2013) summarized the number of wells spud in the Barnett and the change of the well types. In the early 2000s, the drilling in the Barnett switched from vertical wells to horizontal wells. In the first 7 month of 2011, more than 98% of wells (1,007 wells) drilled in the Barnett were horizontal, whereas the other 2% (18 wells) were vertical and directional wells. Successes of shale plays in the U.S. owe to the dramatic improvement in drilling efficiency and well completion technologies over the past several years. In the recent U.S. shale plays, the formations are drilled horizontally and then completed with multistage hydraulic fractures, such as the Bakken, Barnett, Montney, Haynesville, Marcellus, and the most recently the Eagle Ford, Niobrara, and Utica shales.

Over the past decade, the transport mechanisms in unconventional reservoirs have been widely studied in order to better understand their characteristics (Kuila et al 2011, Javadpour et al. 2007, Javadpour 2009, Sakhaee-Pour et al. 2012). It has been found that the techniques and mathematical flow models used in conventional reservoirs may not be adequate for unconventional reservoirs (Aguilera 2010, Michel et al. 2011, Swami et al. 2012, Arogundade et al. 2012). The fluid flow mechanisms in hydraulically-fractured shale and tight sand reservoirs are farther complicated by many

co-existing physical factors, such as (1) severe geological heterogeneities of the permeable media due to the variation among fractures, inorganic rock matrix, and organic matters, (2) Knudsen diffusion and slippage effects in nano-scale pores, (3) high-velocity turbulent flow in the perforations or hydraulic fractures, (4) adsorption/desorption on the surface of organic rocks, (5) geomechanics effects in fractured space, and (6) high capillarity in the confined system. Currently, there is no consensus or standardized approach on the theory and frameworks for modeling the transport behaviors in such complex reservoirs, although there is a growing demand in the area of unconventional resource evaluation and predictions.

In shale gas reservoirs, the contained hydrocarbon usually exists in several states in fracture, matrix, and organic matter. Aguilera et al. (2010) suggest that gas molecules trapped and stored in shale can be divided into five different types: (1) gas adsorbed into the Kerogen material, (2) free gas trapped in inorganic matrix porosity, (3) free gas trapped in natural fractures, (4) free gas stored in hydraulic fractures created during the stimulation of the shale reservoir, and (5) free gas trapped in a pore network developed within the organic matter or Kerogen material. Biswas (2011) pointed out that the flow of gas through the fracture network in shale is the consequence of gas desorption and diffusion which transport it within the matrix-fracture interface.

Nelson (2009) investigated the pore-throat distributions in sandstones, tight sandstones, and shales using a scanning electron microscopy (SEM) and mercury injection as illustrated in **Fig. 1.1**. The pore-throat size (diameter) of conventional sandstones ranges from 2 to 20 μm, whereas the pore-throat size of tight sandstones

ranges from 20 nm to 1 μm. The pore-throat size of shales ranges from 5 to 100 nm, which is approximately 100 times smaller than that of conventional sandstones.

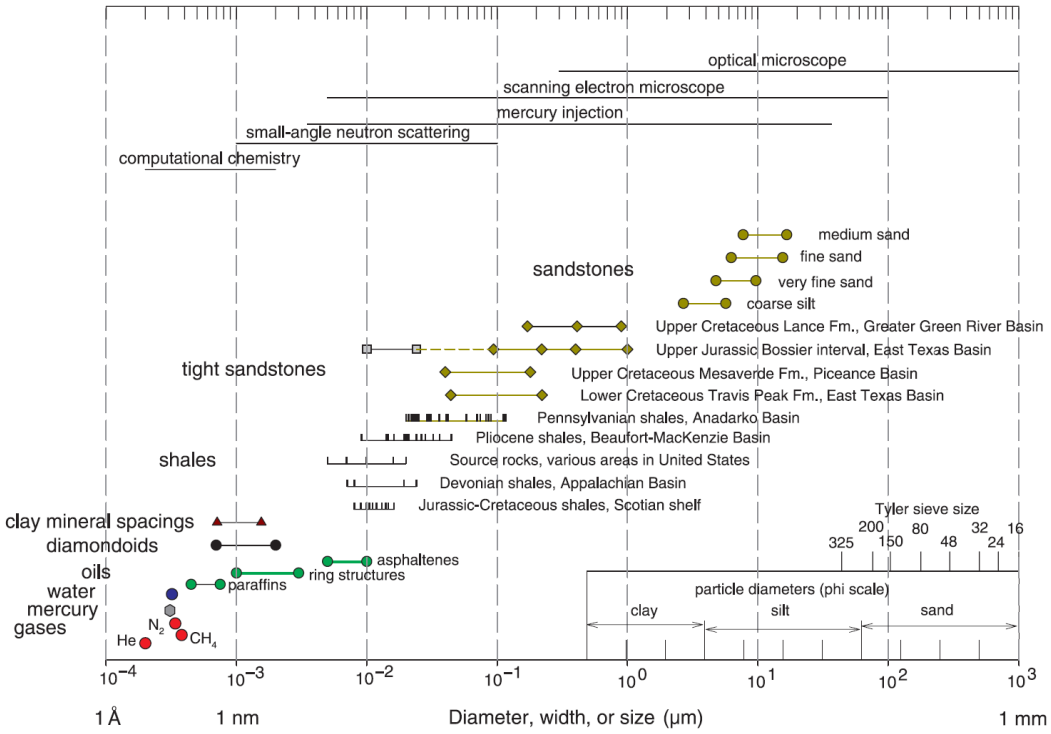

Fig. 1.1 – Pore throat sizes in sandstone, tight sandstone, and shales (Nelson 2009).

A similar petrophysical investigation was conducted by Curtis et al. (2012) who identified the pore spaces in actual shale gas formations using SEM as shown in **Fig. 1.2**. In the figure, the dark gray material represents the organic matter, which is indicated by black arrows, and the white material represents the inorganic material. Pores within the organic matter ('Kerogen porosity') can be seen in the core sample of the Woodford and Horn River shale samples. In contrast, slit-like pores in the inorganic matrix (matrix

porosity) are dominant in the core sample of the Haynesville shale. The authors concluded that the Kerogen pore structure was found in nanometer size and occupied 40 – 50 % of the Kerogen body.

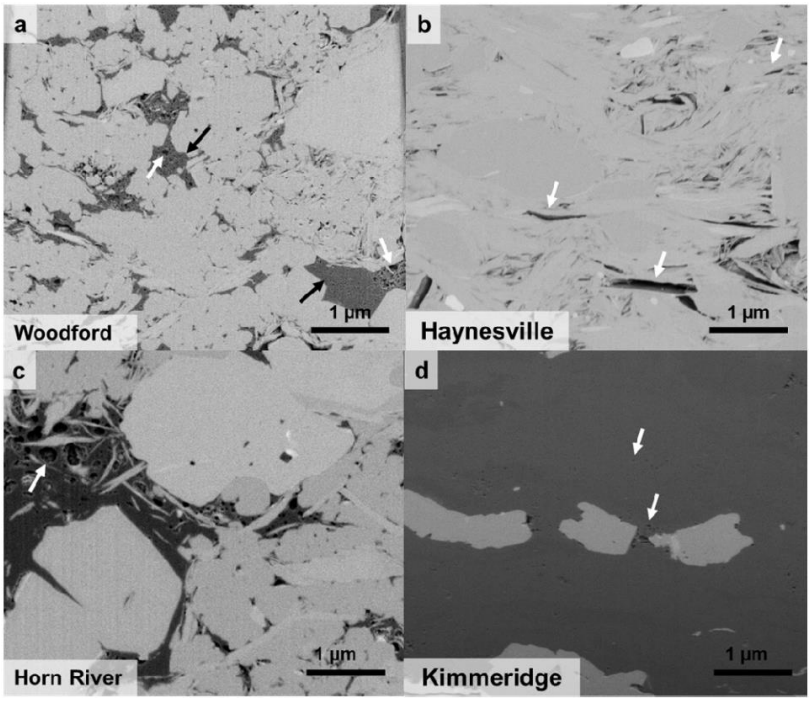

Fig. 1.2 – Pores in shale formation. The shale samples were taken from the (a) Woodford shale, (b) Haynesville shale. (C) Horn River shale, and (D) Kimmeridge shale. The pore examples are indicated by white arrow. (Curtis et al. 2012).

In such confined situations, nano-scale pores ("nanopores") play two important roles for gas flow behavior (Javadpour et al. 2007). First, for same pore volume, the exposed surface area in nanopores is much larger than that in micro-scale pores ("micropores"). The increase of the exposed surface area results in an increase of the volume of adsorbed gases. Suppose that there is a spherical pore covered by organic

material. Within this pore, gas molecules are contained in two states which are free gas and adsorbed gas. The volume of free gas compressed in a spherical pore is simply defined by the pore volume, which is $4\pi r^3/3$, where r is the radius of a sphere. In contrast, adsorbed gases are stocked to the surface area of the pore, which is $4\pi r^2$. Consequently, the relative importance of the adsorbed gases to free gas is defined by the ratio of the exposed surface area to the volume of free gas, that is $3/r$. This implies that the relative importance of adsorbed gas is inversely proportional to the size of the pore. Secondly, nano-scale pore structures can cause the violation of the basic assumption behind the usage of the standard Darcy's law due to Knudsen diffusion and slippage effects on the pore surface. As described above, the relative importance of pore surface area to pore volume is inversely proportional to the pore size. This means that the frequency of slippage and collision on the pore surface will increase as the pore size becomes smaller. The gas molecules tend to collide on the pore walls and slip at the wall surface instead of having the zero-velocity Hagen-Poiseuille flow.

Traditionally, the Darcy's law has been widely used in the petroleum engineering field to approximate a fluid velocity profile based on the following assumptions.

(1) Flow direction aligns with the direction of pressure gradient.

(2) There is no slippage and diffusion (collision) on pore wall.

(3) Fluid flows under laminar flow conditions.

Fig. 1.3 illustrates the relationship between the actual fluid velocity and the Darcy's approximation flow. The black line shows the actual gas velocity profile as a function of differential pressure. The red-dot line represents the Darcy's law based on the linear

approximation. In a high pressure region, the deviations of the actual flow from the linear flow (black-dot line) are caused by non-laminar flow (turbulent flow, Forchheimer flow), which often occurs in the perforations or fractures close to the wellbore of gas wells. In contrast, the deviations in a low pressure region are due to the slippage and Knudsen diffusion, which occur at very low pressure condition (1,000 psia~) or often in nanodarcy-scale permeable media.

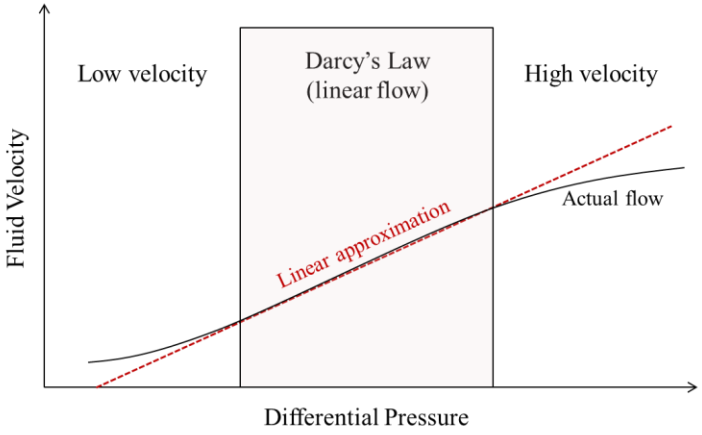

Fig. 1.3 – Fluid velocity profile as a function of differential pressure.

Klinkenberg (1941) recognized gas slippage in subsurface porous media and observed that at very low pressure, the actual flow rate significantly deviates from the one predicted by the conventional linear flow approximation (Darcy's law), a phenomena that is called Klinkenberg effect. He proposed the following correction to gas permeability accounting for its pressure dependency due to slippage on pore surface.

$$k_{app} = k_{\infty}\left(1 + \frac{b}{P}\right) \tag{1.1}$$

where k_{∞} denotes the permeability measured with non-slip boundary condition (Darcy's permeability) and b represents the correction factor for slippage (slippage factor). Over the decades, many authors have measured the apparent permeability and defined the Klinkenberg slippage factor based on the observations and theoretical works (Jones et al. 1980, Sampath et al. 1982, Ertekin et al. 1986, Florence et al. 2007, Javadpour et al. 2007, Civian 2010, Michel et al. 2011, Swami et al. 2012). Contrary to the conventional understanding that the Klinkenberg effect has an impact on the fluid flow at low pressure only, several authors observed that it affects the flow behavior for a smaller pore throat and for a low flowing bottom-hole pressure as well.

1.3 Research Objectives and Thesis Outline

The objective of this research is to extend the DTOF theory for multipurpose reservoir simulation including multi-continuum reservoir modeling and multiphase flow simulation. In addition to theoretical developments, an emphasis is placed on the application to unconventional reservoir modeling with the incorporation of nano-scale pore surface effects on gas permeability and the modification of the fluid phase behavior calculation in such confined reservoirs.

This research is comprised of two main components. First, in **Chapter II**, the DTOF-based flow simulation is applied in single-phase flow problems based on the Fast Marching Method (FMM). This simulation procedure consists of two decoupled steps – (1) calculation of well drainage volumes along a pressure propagation front using the FMM, and (2) successive numerical simulation based on the transformed 1-D

coordinate. The continuous DTOF contour is discretized into finite sets of the 1-D grids using a finite difference approach. On the basis of the 1-D transport equation, the DTOF formulation is extended to the dual-porosity reservoir modeling with the Warren and Root pseudo-steady state type method (Warren and Root 1963). The DTOF-based flow simulation is further applied to a triple-continuum modeling to satisfy the needs of the additional physical mechanisms in unconventional reservoirs. In this research, the discussion includes the Knudsen diffusion and slippage effects, adsorption/diffusion, rock compaction in fractures, and gas diffusion from the organic matter. The unconventional reservoir characteristics are comprehensively investigated by accounting for the Kerogen-matrix interaction as well as the matrix-fracture interaction with the correction of the gas permeability. The proposed DTOF-based formulation is validated through a numerical simulation for synthetic single-porosity, dual-porosity, and triple-continuum models, respectively.

Second, in **Chapter III**, the DTOF theory is generalized to the multiphase and multicomponent flow problems. The theoretical developments of the DTOF-based formulation begin from the derivation of the multiphase DTOF by introducing the asymptotic approach to the mass balance equation. The multiphase DTOF has a similar form to the single-phase DTOF and amenable to the coordinate transformation by the use of the same way as the single-phase flow equation. This transformation requires the assumption that the changes of the spatially-dependent variables (pressure and saturation) are aligned with the DTOF gradient. In the proposed method, the reservoir unknowns (i.e. pressure, saturation, mole fractions) are simultaneously solved using the

fully implicit method. The multiphase DTOF is applied in the multiphase (blackoil) and multicomponent (compositional) simulations as with the single-phase simulation. The three-phase blackoil simulation is then extended to the dual-porosity model. An extra effort is put on the modeling of the confined phase behavior in nano-scale porous reservoirs by incorporating the capillary pressure effects on the thermodynamic equilibrium calculation. At the end of this chapter, several simulation results are presented for the validations of the blackoil and compositional reservoir models.

In **Chapter IV**, the research is concluded with a summary of the key results of the theoretical developments and model validations. Recommendations and proposals for further research are also presented.

CHAPTER II

MULTI-CONTINUUM MODELING BASED ON FAST MARCHING METHOD

This chapter presents the DTOF-based numerical simulation for a single-phase fluid flow based on the Fast Marching Method (FMM). We first introduce the asymptotic theory for the propagation of pressure front in heterogeneous permeable media. The base concepts were proposed by Lee (1982) who defined the radius of investigation in the homogeneous field, and his theory was later generalized by Datta-Gupta et al. (2001) for the heterogeneous permeable media. The speed of the pressure propagation has a form of Eikonal equation and is efficiently solved using the FMM. Zhang et al. (2014) proposed a new simulation method associated with the transformation of the fluid flow coordinate from the physical 3-D space to 1-D DTOF space. In this numerical simulation, the spatial variables (i.e. pressure) are solved along the transformed 1-D coordinate using the finite difference scheme. In this chapter, we present the mathematical fundamentals and numerical details based on the convective fluid transport along the 1-D coordinate system.

In addition, we focus on the application of the FMM as a tool of the modeling for unconventional reservoirs. Shale and tight gas reservoirs are comprised of nanodarcy permeable media which give rise to non-Darcy effects on the fluid flow such as Knudsen diffusion and slippage effect. Furthermore, there are occasions when the conventional single-continuum approach is not suitable for modeling shale and tight gas reservoirs due to its geological and geophysical characteristics. The DTOF-based numerical

simulation is extended to the dual-porosity modeling and further triple-continuum approach including a modification on the traditional Darcy's law.

2.1 Introduction to Fluid Flow in Porous Media

Isothermal fluid flow through porous, permeable rock is governed by three fundamental equations – conservation of mass, momentum equation, and equation of state. The general fluid transport equation can be derived by making the assumptions that the mass fluxes due to the diffusion and dispersion (i.e. molecular diffusion) are small relative to the convective flux and that there is no chemical reaction (i.e. adsorption) between fluids and solids. The first equation, conservation of mass, states that the mass in a closed system must remain constant over time if it is not removed (produced) or added (injected). For single phase fluid flow, the conservation of mass is given by the following form.

$$\frac{\partial(\phi\rho)}{\partial t} = -\nabla \bullet (\rho \mathbf{u}) \tag{2.1}$$

where ϕ is porosity, ρ is fluid density, and $\mathbf{u}$ is the Darcy velocity. In this equation, two boundary conditions (inner and outer boundaries) and one initial condition are imposed to complete the formulation. The inner boundary is usually a sink or source (wellbore) from which the fluids are produced or injected, and the outer boundary is generally a no-flow condition (closed finite domain). The initial condition is defined as the reservoir to be at a uniform pressure at the initial time. In the Cartesian coordinate system, the divergence of the fluid velocity is equal to the scalar-valued function along x-, y-, and z-directions.

$$\nabla \bullet \mathbf{u} = \frac{\partial u_x}{\partial x} + \frac{\partial u_y}{\partial y} + \frac{\partial u_z}{\partial z} \tag{2.2}$$

The second equation, momentum equation is given by a linear flow approximation (Darcy's law). We neglect a gravity term for convenience.

$$\mathbf{u} = -\frac{\mathbf{k}}{\mu}\nabla P \tag{2.3}$$

In this equation, the fluid flows as a linear function of the differential pressure. Substituting **Eq. (2.3)** into **Eq. (2.1)** yields

$$\frac{\partial(\phi\rho)}{\partial t} = \nabla \bullet \left(\rho \frac{\mathbf{k}}{\mu}\nabla P\right) \tag{2.4}$$

The third equation, the equation of state describes the relation between the system condition (i.e. pressure, temperature) and the static fluid state (i.e. volume, density). For slightly-compressible fluids (liquid), the isothermal fluid density is given by linear approximation in terms of pressure, using a Taylor series expansion.

$$\rho = \rho^o e^{c_f(P-P^o)} \approx \rho^o \left(1 + c_f(P - P^o)\right) \tag{2.5}$$

where c_f denotes a fluid compressibility and ρ^o and P^o are the reference fluid density and pressure, respectively. The porosity is also expressed as the same form.

$$\phi = \phi e^{c_r(P-P^o)} \approx \phi^o\big(1 + c_r(P - P^o)\big) \tag{2.6}$$

where c_r denotes a rock compressibility. Substituting **Eqs. (2.5)** and **(2.6)** into **Eq. (2.4)** and carrying out the time differentiation in the left hand side of **Eq. (2.4)**, we obtain the well-known diffusivity equation for slightly-compressible fluids.

$$\phi(\mathbf{x})\mu c_t \frac{\partial P(\mathbf{x},t)}{\partial t} = \nabla \bullet \big(k(\mathbf{x})\nabla P(\mathbf{x},t)\big) \tag{2.7}$$

For compressible fluids (gas), the fluid compressibility is usually not assumed to be constant. In such case, the equation of state is given by the real gas law.

$$\rho = \frac{PM_w}{zRT} \tag{2.8}$$

where M_w denotes molecular weight, z represents the compressibility factor, and R is universal gas constant. Using **Eq. (2.8)** instead of **Eq. (2.5)**, the diffusivity equation for compressible fluids is written as

$$\phi(\mathbf{x})\mu c_t \frac{\partial m(\mathbf{x},t)}{\partial t} = \nabla \bullet \left(k(\mathbf{x})\nabla m(\mathbf{x},t)\right) \tag{2.9}$$

where $m(\mathbf{x},t)$ represents the pseudo-pressure function.

$$m(\mathbf{x},t) = 2\int_{Po}^{P} \frac{P}{z\mu} dP \tag{2.10}$$

For both slightly-compressible and compressible fluids, we have the same partial differential equation form which describes the fluid mass dynamics in subsurface porous media.

2.2 Methods: Asymptotic Approach

2.2.1 Asymptotic Pressure Solution

When a single phase, slightly compressible fluid flows in a heterogeneous permeable media, the fluid pressure behavior is governed by the diffusivity equation. Rearranging **Eq. (2.7)**, we obtain

$$\phi(\mathbf{x})\mu c_t \frac{\partial P(\mathbf{x},t)}{\partial t} = \nabla k(\mathbf{x}) \bullet \nabla P(\mathbf{x},t) + k(\mathbf{x}) \bullet \nabla^2 P(\mathbf{x},t) \tag{2.11}$$

where $P(\mathbf{x},t)$ is pressure on the location **x** at the time t. We consider the equation in the frequency domain by applying a Fourier transform.

$$\tilde{P}(\mathbf{x},\omega) = \int_{-\infty}^{\infty} P(\mathbf{x},t)e^{-i\omega t}dt \tag{2.12}$$

In the frequency domain, the diffusivity equation is written as

$$\phi(\mathbf{x})\mu c_t(-i\omega)\tilde{P}(\mathbf{x},\omega) = \nabla k(\mathbf{x}) \bullet \nabla\tilde{P}(\mathbf{x},\omega) + k(\mathbf{x}) \bullet \nabla^2\tilde{P}(\mathbf{x},\omega) \tag{2.13}$$

The asymptotic approach attempts to find a solution of the diffusivity equation that mimics the one found in wave propagation and is based on the asymptotic ray theory. The asymptotic ray theory forms the mathematical basis for geometrical ray theory and has been extensively used in both electromagnetic (Virieux et al. 1994) and seismic wave propagation (Cerveny et al. 1978). The method has also proved suitable in the analysis of a front propagation in general (Sethian 1996) and petroleum engineering in terms of streamlines and flood fronts (Datta-Gupta and King 2007).

Following the previous works in the diffusive electromagnetic imaging and hydrology (Virieux et al. 1994, Vasco et al. 2000, Datta-Gupta et al. 2001), the asymptotic pressure solution can be written as an infinite sum.

$$\tilde{P}(\mathbf{x},\omega) = e^{-\sqrt{-i\omega}\tau(\mathbf{x})}\sum_{k=0}^{\infty}\frac{A_k(\mathbf{x})}{\left(\sqrt{-i\omega}\right)^k} \tag{2.14}$$

where $\tau(\mathbf{x})$ represents the phase of a propagating wave and thus, describes the geometry of a propagation front. $A_k(\mathbf{x})$ are real functions that relate to the amplitude of the wave. A solution of **Eq. (2.14)** can be interpreted on physical grounds based on the scaling behavior of diffusive flow. The motivation for using a solution in inverse power of ω is that the initial terms of the series are the most important when ω is large (high-frequency limit) and represent the rapidly varying components of the solution or the propagation of

a sharp front (Vasco et al. 2000). The functions $\tau(\mathbf{x})$ and $A_k(\mathbf{x})$ are unknowns. The asymptotic solution **Eq. (2.14)** is the sum of infinite number of functions $A_k(\mathbf{x})$, but the important physical quantities are represented only in the first few terms. Therefore, a leading-order solution of **Eq. (2.14)** is obtained by

$$\tilde{P}(\mathbf{x},\omega) = e^{-\sqrt{-i\omega}\tau(\mathbf{x})}A_0(\mathbf{x}) \tag{2.15}$$

Notice that the first and second derivatives of **Eq. (2.15)** with respect to the location **x** is written as

$$\nabla\tilde{P}(\mathbf{x},\omega) = -\sqrt{-i\omega}\nabla\tau(\mathbf{x})e^{-\sqrt{-i\omega}\tau(\mathbf{x})}A_0(\mathbf{x}) + e^{-\sqrt{-i\omega}\tau(\mathbf{x})}\nabla A_0(\mathbf{x}) \tag{2.16}$$

$$\begin{aligned}\nabla^2\tilde{P}(\mathbf{x},\omega) = {} & (-i\omega)\big(\nabla\tau(\mathbf{x})\big)^2 e^{-\sqrt{-i\omega}\tau(\mathbf{x})}A_0(\mathbf{x}) \\ & - \sqrt{-i\omega}\nabla^2\tau(\mathbf{x})e^{-\sqrt{-i\omega}\tau(\mathbf{x})}A_0(\mathbf{x}) \\ & - 2\sqrt{-i\omega}\nabla\tau(\mathbf{x})e^{-\sqrt{-i\omega}\tau(\mathbf{x})}\nabla A_0(\mathbf{x}) + e^{-\sqrt{-i\omega}\tau(\mathbf{x})}\nabla^2 A_0(\mathbf{x})\end{aligned} \tag{2.17}$$

Inserting **Eqs. (2.15)** - **(2.17)** into **Eq. (2.13)** and arranging the equation in terms of powers of $\sqrt{-i\omega}$, we obtain the following quadratic equation.

$$\begin{aligned}&[\phi(\mathbf{x})\mu c_t - k(\mathbf{x})\nabla^2\tau(\mathbf{x})]A_0(\mathbf{x})\big(\sqrt{-i\omega}\big)^2 \\ &+[k(\mathbf{x})\nabla^2\tau(\mathbf{x})A_0(\mathbf{x}) + 2k(\mathbf{x})\nabla\tau(\mathbf{x})\nabla A_0(\mathbf{x}) + \nabla k(\mathbf{x})\nabla\tau(\mathbf{x})A_0(\mathbf{x})]\sqrt{-i\omega} \\ &-[\nabla k(\mathbf{x})\nabla A_0(\mathbf{x}) + k(\mathbf{x})\nabla^2 A_0(\mathbf{x})] = 0\end{aligned} \tag{2.18}$$

The first term in the left hand side of **Eq. (2.18)** is imaginary part, the second term is related to the square root of $(-i\omega)$, and the third term is real part. Since all these three terms equal to zero, the first term (highest power) leads the equation for the phase $\tau(x)$ of the propagation equation.

$$\nabla\tau(\mathbf{x}) \bullet k(\mathbf{x}) \bullet \nabla\tau(\mathbf{x}) = \phi(\mathbf{x})\mu c_t \tag{2.19}$$

Eq. (2.19) corresponds to the equation for propagation of pressure front. This equation is rewritten as

$$|\nabla\tau(\mathbf{x})|\sqrt{\alpha_{\text{diff}}(\mathbf{x})} = 1 \tag{2.20}$$

where $\alpha_{\text{diff}}(\mathbf{x})$ represents the propagation speed of the pressure front and is called 'diffusivity', given by

$$\alpha_{\text{diff}}(\mathbf{x}) = \frac{k(\mathbf{x})}{\phi(\mathbf{x})\mu c_t} \tag{2.21}$$

It is important to notice that **Eq. (2.20)** is a form of the well-known Eikonal equation which explains a variety of propagation behaviors. Integrating **Eq. (2.20)** over the propagation trajectory Σ, we obtain

$$\tau(\mathbf{x}) = \int_{\Sigma} \frac{1}{\sqrt{\alpha_{\text{diff}}(\mathbf{x})}} dr \tag{2.22}$$

By analogy of the convective time of flight (CTOF) applied in the streamline simulation, we can see the pressure wave front travels with a velocity of $\sqrt{\alpha_{\text{diff}}(\mathbf{x})}$. We define a 'diffusive' time of flight (DTOF) for a propagation of a pressure front (Datta-Gupta at al. 2001). Notice that the unit of DTOF is the square root of time which is consistent with scaling behavior of diffusive flow. Vasco and Finsterle (2004) pointed out that at transient flow conditions, these trajectories are not necessarily the streamlines and are strictly given by the ray equations in seismology.

2.2.2 Fast Marching Method

Eq. (2.20) implies that the gradient of arrival time of pressure propagation front is inversely proportional to the propagation speed (square root of the diffusivity). This is a form of the Eikonal equation, and this equation can be solved very efficiently using a class of front tracking methods called "Fast Marching Method" (Sethian 1996). The basic framework comprises the following steps (Sethian 1999).

(1) Label all grid nodes as *unknown*.

(2) Assign τ (usually zero) to the nodes corresponding to the initial position of the propagating front and label them as *accepted*.

(3) For each node that is *accepted*, locate its immediate neighboring nodes that are *unknown* and label them as *considered*.

(4) For each node labeled *considered*, update its τ based on its *accepted* neighbors using the minimum of local solutions of **Eq. (2.20)**.

(5) Once all nodes labeled *considered* have been locally updated, we pick the node which has the minimum τ among them and label it as *accepted*.

(6) Go to step (3) until all nodes are *accepted*.

In a 2-D 5-stencil Cartesian coordinate model, these steps are illustrated in **Fig. 2.1** and explained by Xie et al. (2012). In this example, we put an arbitrary single point as the initial position of the propagating front and label it as *accepted* (solid) as shown in **(a)**. Then its immediate neighbors A, B, C, and D are marked as *considered* (circle) as shown in **(b)**. After the τ for A, B, C, and D have been updated, we pick the smallest one (suppose it is A) and mark it as *accepted* as shown in **(c)**. Then its neighbors E, G, and F

are added into the *considered* as shown in **(d)**. These steps will repeat for the next *accepted* point (suppose it is D) as shown in **(e)** and **(f)**. The local solution of τ is updated with a standard finite difference notation (Sethian 1996).

$$\max\left(D_{ij}^{-x}\tau, -D_{ij}^{+x}\tau, 0\right)^2 + \max\left(D_{ij}^{-y}\tau, -D_{ij}^{+y}\tau, 0\right)^2 = \frac{1}{\alpha_{\text{diff}}} \tag{2.23}$$

where D is a gradient approximated with first-order forward finite difference scheme. In x-direction, $D_{ij}^{-x}\tau = \left(\tau_{i,j} - \tau_{i-1,j}\right)/\Delta x$ and $D_{ij}^{+x}\tau = \left(\tau_{i+1,j} - \tau_{i,j}\right)/\Delta x$. Same equations hold in y-direction, $D_{ij}^{-y}\tau = \left(\tau_{i,j} - \tau_{i,j-1}\right)/\Delta y$ and $D_{ij}^{+y}\tau = \left(\tau_{i,j+1} - \tau_{i,j}\right)/\Delta y$.

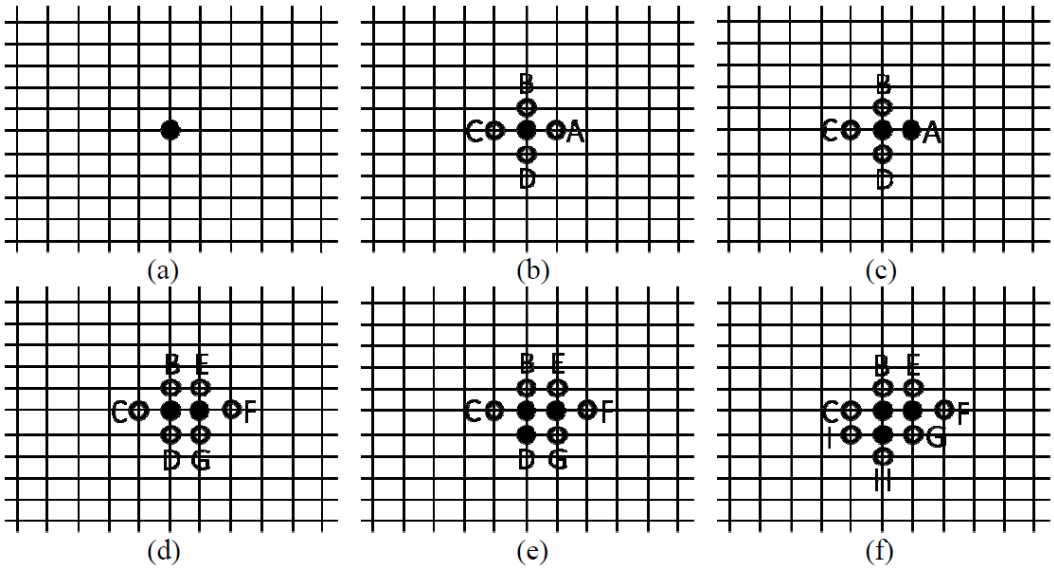

Fig. 2.1 – Illustration of Fast Marching M No table of figures entries found.**ethod (Xie et al. 2012). The circles represent 'considered' state and black solids denote 'accepted' state.**

Notice that the FMM is single-pass algorithm and the τ solutions are constructed sequentially from the small values to large value. After the FMM calculation, the

drainage ‘pore’ volumes are successively calculated by summing up all the pore volumes inside the specific τ contour.

2.2.3 Coordinate Transformation

The DTOF-based 1-D transport equation was first proposed by Zhang et al. (2014). The multidimensional fluid flow equations are decomposed into the series of 1-D τ-contours using the proposed coordinate transformation, and then the spatially dependent variables (pressure) are solved on each discretized τ-contour. The coordinate transformation from the physical space to 1-D τ-coordinate is achieved by assuming that pressure gradient aligns with τ gradient direction.

$$\nabla P = \frac{\partial P}{\partial \tau} \nabla \tau \tag{2.24}$$

This fundamental assumption implies that the contour surfaces of τ are identical to the contour surfaces of pressure. According to the propagation equation (**Eq. (2.19)**), the absolute permeability is written with relation to τ.

$$k = \frac{1}{(\nabla \tau)^2} (\phi \mu c_t)_{\text{init}} \tag{2.25}$$

Substituting **Eqs. (2.24)** and **(2.25)** into the Darcy’s law (**Eq. (2.3)**), we obtain the τ-based velocity equation.

$$u = -\frac{(\phi \mu c_t)_{\text{init}}}{\mu} \frac{1}{|\nabla \tau|} \frac{\partial P}{\partial \tau} \tag{2.26}$$

The basic concept behind the coordinate transformation is that we partition the Cartesian domain into a series of non-overlapping surface (τ-contour). The surface contour begins from the point of sink or source (inner boundary) and it evolves to the

entire domain, Ω. Consider a very thin layer of volume enclosed by two contours surfaces, $d\Omega(\tau)$ and $d\Omega(\tau + \Delta\tau)$. The volume element of this thin layer, dV is corresponding to the product of the surface area dA and the layer thickness $\Delta\tau/|\nabla\tau|$. Therefore, we have

$$dV = \frac{\nabla\tau}{|\nabla\tau|} dA \tag{2.27}$$

Zhang et al. (2014) showed the coordinate transformation of the diffusivity equation for both slightly-compressible (**Eq. (2.7)**) and compressible fluids (**Eq. (2.9)**), respectively. Here, we transform the general mass balance equation on the τ-coordinate instead of using the diffusivity equation for the purpose of general numerical simulation. We take a volumetric integral of the conventional mass balance equation, **Eq. (2.1)** over the domain, Ω.

$$\int_{\Omega} \frac{\partial(\phi\rho)}{\partial t} dV = -\int_{\Omega} \nabla \bullet (\rho \mathbf{u}) dV \tag{2.28}$$

The flux term (RHS) in **Eq. (2.28)** is transformed to the surface integral by applying a divergence theorem.

$$\int_{\Omega} \nabla \bullet (\rho \mathbf{u}) dV = \int_{d\Omega} (\rho \mathbf{u}) \bullet \vec{\mathbf{n}}\, dA = \int_{d\Omega(\tau)} (\rho \mathbf{u}) \bullet \frac{\nabla\tau}{|\nabla\tau|}\, dA \tag{2.29}$$

As discussed above, the volume element is identical to the integral of two adjacent surfaces. On the other hand, the accumulation term (LHS) in **Eq. (2.28)** is also transformed to surface integral by substituting **Eq. (2.27)**.

$$\int_{\Omega} \frac{\partial(\phi\rho)}{\partial t} dV = \nabla\tau \int_{d\Omega(\tau)} \frac{\partial(\phi\rho)}{\partial t} \frac{1}{|\nabla\tau|} dA \tag{2.30}$$

Inserting **Eqs. (2.29)** and **(2.30)** into **Eq. (2.28)**, we obtain the surface integral form of the mass balance equation.

$$\nabla\tau \int_{d\Omega(\tau)} \frac{\partial(\phi\rho)}{\partial t} \frac{1}{|\nabla\tau|} dA = -\int_{d\Omega(\tau)} (\rho \mathbf{u}) \bullet \frac{\nabla\tau}{|\nabla\tau|}\, dA \tag{2.31}$$

Substituting the DTOF-based velocity equation (**Eq. (2.26)**) into **Eq. (2.31)**, we have

$$\int_{d\Omega(\tau)} \frac{\partial(\phi\rho)}{\partial t} \frac{1}{|\nabla\tau|} dA = \frac{1}{\nabla\tau} \left(\int_{d\Omega(\tau)} \rho \frac{(\phi\mu c_t)_{\text{init}}}{\mu} \frac{\partial P}{\partial \tau} \bullet \frac{1}{|\nabla\tau|} dA \right) \tag{2.32}$$

Let $\Delta\tau \to 0$. **Eq. (2.32)** is rewritten as

$$\int_{d\Omega(\tau)} \frac{\partial\left(M_\phi \rho\right)}{\partial t} \frac{\phi_{\text{init}}}{|\nabla\tau|} dA = \frac{\partial}{\partial\tau} \left(\int_{d\Omega(\tau)} \rho \frac{(\mu c_t)_{\text{init}}}{\mu} \frac{\partial P}{\partial \tau} \bullet \frac{\phi_{\text{init}}}{|\nabla\tau|} dA \right) \tag{2.33}$$

where ϕ_{init} denotes the porosity at initial condition, and M_ϕ represents the exponential rock compressibility function.

$$M_\phi = e^{c_r (P - P_{\text{init}})} \tag{2.34}$$

Taking a surface integral of **Eq. (2.27)** over the τ-contour, we can define the w-function.

$$\int_{d\Omega(\tau)} \frac{\phi_{\text{init}}}{|\nabla\tau|} dA = \frac{dV_p}{d\tau} = w(\tau) \tag{2.35}$$

Notice that the w-function is the derivative of the drainage 'pore' volume V_p with respect to the diffusive time of flight τ. Substituting the w-function (**Eq. (2.35)**) into the both sides of **Eq. (2.33)**, we obtain the following fluid transport equation along 1-D τ-coordinate.

$$w(\tau) \int_{d\Omega(\tau)} \frac{\partial\left(M_\phi \rho\right)}{\partial t} dA = \frac{\partial}{\partial\tau} \left(w(\tau) \int_{d\Omega(\tau)} \rho \frac{(\mu c_t)_{\text{init}}}{\mu} \frac{\partial P}{\partial \tau} dA \right) \tag{2.36}$$

In **Eq. (2.36)**, the pressure P is the location- and time-dependent variables. Now, we assume that P is a function of τ and t (i.e. the pressure gradient align with the τ gradient). Therefore, we can take the terms outside the integral. Therefore, The DTOF-based mass balance equation can be written as follows.

$$w(\tau)\frac{\partial\left(M_\phi \rho\right)}{\partial t} = \frac{\partial}{\partial \tau}\left(w(\tau)\rho\frac{(\mu c_t)_{\text{init}}}{\mu}\frac{\partial P}{\partial \tau}\right) \tag{2.37}$$

Comparing the transformed mass balance equation (**Eq. (2.37)**) with the general mass balance form (**Eq. (2.1)**), the transformation of the flux term is defined as follows.

$$\nabla \bullet (\rho \mathbf{u}) \equiv -\frac{\phi_{\text{init}}}{w(\tau)}\frac{\partial}{\partial \tau}\left(w(\tau)\rho\frac{(\mu c_t)_{\text{init}}}{\mu}\frac{\partial P}{\partial \tau}\right) \tag{2.38}$$

Notice that **Eq. (2.37)** is a complete 1-D transport equation that fully embeds the geological heterogeneities (i.e. porosity, permeability) on the τ-coordinates and is numerically solved using a finite difference scheme. This simulation approach is quite similar to that of streamline approach and we solve the pressure equation along 1-D DTOF coordinate instead of solving the saturation equation along 1-D CTOF. The generalization to the anisotropic medium is written in **APPENDIX A**.

2.2.4 One-Dimensional Discrete Model

For the application of the DTOF formulation to the numerical simulation, we discretize the governing partial differential equation (**Eq. (2.37)**) in terms of space and time based on a finite difference method. **Fig. 2.2** shows the illustration of the 1-D simple coordinate system discretized into finite sets of grid blocks. In this illustration, the two boundary conditions are imposed on its left and right edges. The inner boundary

(left edge) is the wellbore constrained by the bottom-hole pressure or production rate, and the outer boundary (right edge) is the no-flow boundary.

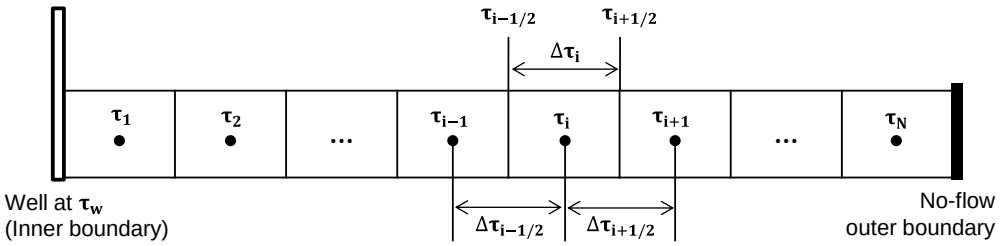

Fig. 2.2 – 1-D finite difference discretization.

Based on **Eq. (2.38)**, the single-phase mass balance equation is transformed into τ-coordinate system as follows.

$$\frac{\partial(\phi\rho)}{\partial t} = \frac{\phi_{\text{init}}}{w(\tau)}\frac{\partial}{\partial\tau}\left(w(\tau)\rho\frac{(\mu c_t)_{\text{init}}}{\mu}\frac{\partial P}{\partial\tau}\right) + \rho q \tag{2.39}$$

where q is the volumetric production rate per unit volume per unit time at wellbore. The source/sink (well) term is imposed on the inner boundary; hence it only appears in the equation at the first grid. Dividing **Eq. (2.39)** by the surface density ρ_{sc} and initial porosity ϕ_{init}, **Eq. (2.39)** can be written as the mass balance equation on the standard volume basis.

$$\frac{\partial}{\partial t}\left(\frac{M_\phi}{B}\right) = \frac{1}{w(\tau)}\frac{\partial}{\partial\tau}\left(w(\tau)\frac{(\mu c_t)_{\text{init}}}{B\mu}\frac{\partial P}{\partial\tau}\right) + \frac{1}{\phi_{\text{init}}}\frac{q}{B} \tag{2.40}$$

where $B\ (=\rho_{sc}/\rho)$ is the formation volume factor (FVF).

Suppose we discretize the flux term in **Eq. (2.40)** around the grid block i. The partial derivatives are approximated by the standard finite difference approximation involving the backward, forward, and central differences as follows.

$$\begin{aligned}\frac{\partial}{\partial\tau}\left(C\frac{\partial P}{\partial\tau}\right)\Big|_i &= \frac{1}{\tau_{i+1/2}-\tau_{i-1/2}}\left(C_{i+1/2}\frac{\partial P}{\partial\tau}\Big|_{i+1/2} - C_{i-\frac{1}{2}}\frac{\partial P}{\partial\tau}\Big|_{1-1/2}\right)\\ &= \frac{1}{\Delta\tau_i}\left[C_{i+1/2}\left(\frac{P_{i+1}-P_i}{\tau_{i+1}-\tau_i}\right) - C_{i-1/2}\left(\frac{P_i-P_{i-1}}{\tau_i-\tau_{i-1}}\right)\right]\\ &= \frac{1}{\Delta\tau_i}\left[\frac{C_{i+1/2}}{\Delta\tau_{i+1/2}}(P_{i+1}-P_i) - \frac{C_{i-1/2}}{\Delta\tau_{i-1/2}}(P_i-P_{i-1})\right]\end{aligned} \tag{2.41}$$

where C represents the grid-dependent parameter (i.e. grid volume, mobility), $\Delta\tau_i$is the grid length of the cell i, and $\Delta\tau_{i\pm1/2}$ is the length from the center of the grid i to the center of the grid $i\pm1$.Using **Eq. (2.41)**, the flux term is discretized into the 1-D coordinate.

$$\frac{\partial}{\partial\tau}\left(w(\tau)\frac{(\mu c_t)_{\text{init}}}{B\mu}\frac{\partial P}{\partial\tau}\right) = \frac{T_{i-1/2}P_{i-1/2} - \left(T_{i-1/2}-T_{i+1/2}\right)P_i + T_{i+1/2}P_{i+1}}{\Delta\tau_i} \tag{2.42}$$

where $T_{i\pm1/2}$ represents the transmissibility on the grid interface between i and $i\pm1$.

$$T_{i\pm1/2} = \frac{w_{i\pm1/2}}{\Delta\tau_{i\pm1/2}}(\mu c_t)_{\text{init},i\pm1/2}\left(\frac{1}{B\mu}\right)_{up} \tag{2.43}$$

where the subscript up denotes the upstream grid. The flow mobility is determined by the up-winding scheme. The discretized w-functions, w_i, $w_{i-1/2}$, and $w_{i+1/2}$ are obtained by central, backward, and forward differences, respectively.

$$w_i = \left(\frac{dV_p}{d\tau}\right)_i = \frac{V_{p,i+1/2}-V_{p,i-1/2}}{\tau_{i+1/2}-\tau_{i-1/2}} \tag{2.44}$$

$$w_{i-1/2} = \left(\frac{dV_p}{d\tau}\right)_{i-1/2} = \frac{V_{p,i} - V_{p,i-1}}{\tau_i - \tau_{i-1}} \tag{2.45}$$

$$w_{i+1/2} = \left(\frac{dV_p}{d\tau}\right)_{i+1/2} = \frac{V_{p,i+1} - V_{p,i}}{\tau_{i+1} - \tau_i} \tag{2.46}$$

Using **Eq. (2.42)** and carrying out the time differentiation, the finite difference equation of **Eq. (2.40)** is written as follows.

$$T_{i-1/2}^{n+1} P_{i-1}^{n+1} - \left(T_{i-1/2}^{n+1} + T_{i+1/2}^{n+1}\right) P_i^{n+1} + T_{i+1/2}^{n+1} P_{i+1}^{n+1} = \frac{w_i \Delta\tau_i}{\Delta t^{n+1}} \left[\left(\frac{M_{\phi,i}^{n+1}}{B_i^{n+1}}\right) - \left(\frac{M_{\phi,i}^{n}}{B_i^{n}}\right)\right] - \frac{w_i \Delta\tau_i}{\phi_{\text{init},i}} \frac{q^{n+1}}{B_i^{n+1}} \tag{2.47}$$

where $n+1$ denotes the time-step level and M_ϕ represents the exponential rock compressibility function (**Eq. (2.34)**). Notice that the well term is imposed only on the first grid ($i = 1$) neighboring the inner boundary.

On the 1-D grid system, $\Delta\tau_i$ is the length of the grid i and $w_i\Delta\tau_i$ corresponds to the 'pore' volume of the grid block i. Hence, $w_i\Delta\tau_i/\phi_{\text{init}}$ is equivalent to the 'bulk' volume of the grid i. As described in **Eq. (2.47)**, the standard volume production rate is given by

$$q_s^{n+1} = \frac{w_1 \Delta\tau_1}{\phi_{\text{init}}} \frac{q^{n+1}}{B_1^{n+1}} \tag{2.48}$$

where the subscript 1 denotes the first grid block and q_s^{n+1} represents the surface volume flow rate at the time $n+1$. **Eq. (2.48)** is rewritten by using the DTOF-based velocity equation (**Eq. (2.26)**).

$$q_s^{n+1} = \frac{w_1 \Delta\tau_1}{\phi_{\text{init}}} \left[\frac{1}{\Delta\tau_1} (\phi\mu c_t)_{\text{init},1} \left(\frac{1}{B\mu}\right)_1^{n+1} \left(\frac{P_1^{n+1} - P_{wf}^{n+1}}{\tau_1 - \tau_{\text{well}}}\right)\right] \tag{2.49}$$

Rearranging **Eq. (2.49)**, the surface production rate is calculated as follows.

$$q_s^{n+1} = w_1(\mu c_t)_{\text{init},1}\left(\frac{1}{B\mu}\right)_1^{n+1}\left(\frac{P_1^{n+1} - P_{wf}^{n+1}}{\tau_1 - \tau_{\text{well}}}\right) \tag{2.50}$$

For each grid, we assign **Eq. (2.47)** as a governing equation and solve the corresponding spatial unknown variable P_i^{n+1}. The inner boundary condition is imposed by **Eq. (2.50)**. The numerical simulation procedure and derivative calculations for constructing the Jacobian are described in **APPENDIX B**.

2.3 Approach: Multi-Continuum Modeling

2.3.1 Dual-Porosity Model

Fractured reservoirs are characterized by a presence of two distinct porous systems – fractured porous networks and fine grained matrix blocks. In naturally fractured reservoirs or hydraulically fractured wells, the mass exchange between matrix and fracture is an important component due to their geological characteristics. The fracture network is highly conductive, but can store very little fluid due to its very low porosity, while the matrix system has low conductivity and large storage capacity relative to the fracture. The concept of dual-porosity single-permeability (DPSP) model is that the two over-lapping continua, fracture system and matrix system, coexist and interact each other (Barenblatt et al. 1960, Warren and Root 1963, Kazemi 1979). The fluid transport equation in the fracture system is given by an ordinary porous medium with an additional connection to the matrix block, whereas the matrix blocks act only as a source to the fracture system. The advantage of the dual-porosity modeling is that this approach is computationally inexpensive compared with the Discrete Fracture Network

(DFN) method which incorporates all fractures in various locations with complex fracture geometries. **Fig. 2.3** shows the illustrations of the fracture geometries in actual reservoir and the simplified grid block geometries in the dual-porosity model. The dual-porosity modeling has been traditionally utilized to model the fluid flows on the various scale medium using two simple coordinate systems (Blair et al. 1964, Yamamoto et al. 1971, Kazemi et al. 1979, Dean et al. 1988).

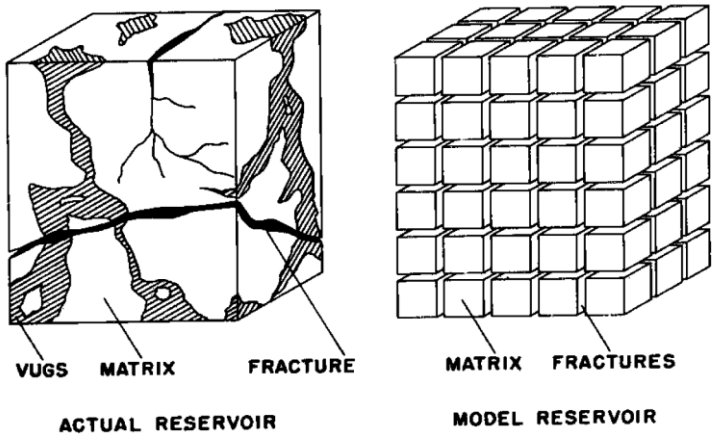

Fig. 2.3 – Discretization of the fractured porous medium (Warren and Root 1963).

In this research, the Warren and Root pseudo-steady state equation is used to complete the dual-porosity formulation (Warren and Root 1963). The mass balance equation in the fractured system is written by general mass balance equation (**Eq. (2.4)**) with the addition of a matrix-fracture mass exchange term.

$$\frac{\partial(\rho\phi_f)}{\partial t} = \nabla \bullet \left(\rho \frac{k_f}{\mu} \nabla P_f\right) - \rho\Gamma + \rho q_f \tag{2.51}$$

where ϕ_f represents the fracture porosity, k_f denotes the fracture permeability, and Γ represents the matrix-fracture volume transfer function. The sink or source term q_f is imposed on the inner boundary condition of the fracture flow equation. In **Eq. (2.51)**, the transfer function is given by the Darcy equation-like form (Kazemi et al. 1976).

$$\Gamma = \sigma \frac{k_m}{\mu_{up}} \left(P_f - P_m\right) \tag{2.52}$$

where σ denotes the shape factor (fracture density) that defines the connectivity between the matrix block and the surrounding fracture network. It is reasonable assumption that the mastic-fracture volume transfer is always governed by the matrix permeability (k_m) due to its low conductivity. The fluid viscosity is determined by the upstream weighting (i.e. if $P_f < P_m$, then $\mu = \mu(P_m)$). We ignore the gravitational forces in the transfer term and assume a pseudo-steady state behavior in the matrix block. Based on **Eqs. (2.51)** and **(2.52)**, we obtain the following fracture equation.

$$\frac{\partial\left(\rho\phi_f\right)}{\partial t} = \nabla \bullet \left(\rho \frac{k_f}{\mu} \nabla P_f\right) - \sigma\rho \frac{k_m}{\mu} \left(P_f - P_m\right) + \rho q_f \tag{2.53}$$

In contrast, the matrix flow equation is written as follows.

$$\frac{\partial(\rho\phi_m)}{\partial t} = \sigma\rho \frac{k_m}{\mu} \left(P_f - P_m\right) \tag{2.54}$$

where ϕ_m and k_m represent the matrix porosity and permeability, respectively. On the matrix coordinate system, the both inner and outer boundary conditions are imposed as no-flow boundary, thus the well term is absent in **Eq. (2.54)**. The matrix system only plays as an additional source to the fracture system driven by the differential pressure between fracture and matrix blocks.

For the application of the dual-porosity modeling in the DTOF-based flow simulation, we make the following assumptions.

- The FMM calculation only involves the fracture coordinate system. This means that the FMM calculates the front of the pressure propagation based on the fracture heterogeneities (k_f and ϕ_f). The drainage volume is obtained along the τ-coordinate without consideration for the matrix system.
- For simplifying assumption, the matrix properties (i.e. matrix porosity, permeability, shape factor) are assumed to be homogeneous and isotropic, because the geological heterogeneities of the matrix system are not accounted for the DTOF and successive drainage volume calculation.

These treatments will be valid when the fracture network is the system in which the pressure front primarily propagates through and when the matrix serves only as fluid source to the fracture system. The schematic of the DTOF-based dual-porosity model is illustrated in **Fig 2.4**.

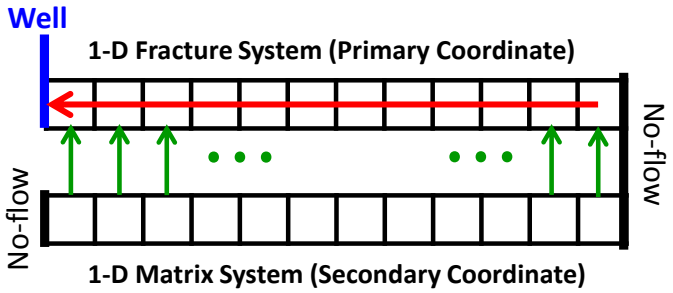

Fig. 2.4 – Dual-porosity model on the 1-D DTOF coordinate.

Applying the coordinate transformation on the fracture flow equation (**Eq. (2.38)**), we obtain the DTOF-based fracture transport equation.

$$\frac{\partial}{\partial t}\left(\frac{\phi_f}{B}\right) = \frac{\phi_{f,\text{init}}}{w(\tau)}\frac{\partial}{\partial \tau}\left(w(\tau)\frac{(\mu c_t)_{\text{init}}}{B\mu}\frac{\partial P_f}{\partial \tau}\right) - \sigma\frac{k_m}{B\mu}\left(P_f - P_m\right) + \frac{q_f}{B} \tag{2.55}$$

where $\phi_{f,\text{init}}$ is the initial fracture porosity. Rearranging **Eq. (2.55)** yields the following fracture equation.

$$w(\tau)\frac{\partial}{\partial t}\left(\frac{M_\phi}{B}\right) = \frac{\partial}{\partial \tau}\left(w(\tau)\frac{(\mu c_t)_{\text{init}}}{B\mu}\frac{\partial P_f}{\partial \tau}\right) - \frac{w(\tau)}{\phi_{f,\text{init}}}\sigma\frac{k_m}{B\mu}\left(P_f - P_m\right) + q_{sf} \tag{2.56}$$

where $w(\tau)/\phi_{f,\text{init}}$ represents the fracture drainage 'bulk' volume that is directly obtained from the FMM calculation. The surface volume production rate q_{sf} is corresponding to **Eq. (2.48)** and calculated using the same equation as the single-porosity case (**Eq. (2.50)**). As discussed, the matrix permeability k_m and shape factor σ is treated as a constant parameter over the domain. Thus, the spatial heterogeneities that explicitly appears in **Eq. (2.56)** are the fracture drainage 'pore' volumes and fracture drainage 'bulk' volumes. We define the fracture drainage 'bulk' volume as

$$v(\tau) = \frac{w(\tau)}{\phi_{f,\text{init}}} \tag{2.57}$$

The DTOF-based matrix equation is obtained by multiplying the fracture drainage 'bulk' volume on the both sides of **Eq. (2.54)**, while the equation form still remains same.

$$\frac{\partial}{\partial t}\left(\frac{\phi_m}{B}\right) = \sigma\frac{k_m}{B\mu}\left(P_f - P_m\right) \tag{2.58}$$

Notice that the overall dual-porosity equation is obtained by substituting the matrix equation (**Eq. (2.58)**) into the fracture flow equation (**Eq. (2.55)**) as follows.

$$\frac{\partial}{\partial t}\left(\frac{\phi_f}{B}\right)+\frac{\partial}{\partial t}\left(\frac{\phi_m}{B}\right)=\frac{\phi_{f,\mathrm{init}}}{w(\tau)}\frac{\partial}{\partial \tau}\left(w(\tau)\frac{(\mu c_t)_{\mathrm{init}}}{B\mu}\frac{\partial P_f}{\partial \tau}\right)+\frac{q_f}{B} \tag{2.59}$$

The above equation implies that the inter-cell fluid transport takes place only through the fracture networks and the fluids, which are accumulated in the 1-D matrix blocks, are linked only through the fracture system.

As with the single-porosity model, the DTOF-based dual-porosity governing equations are discretized using a finite difference approximation. The finite difference equation of the fracture system is written as

$$\begin{aligned} &T_{i-1/2}^{n+1}P_{f,i-1}^{n+1}-\left(T_{i-1/2}^{n+1}+T_{i+1/2}^{n+1}\right)P_{f,i}^{n+1}+T_{i+1/2}^{n+1}P_{f,i+1}^{n+1} \\ &\quad=\frac{w_i\Delta\tau_i}{\Delta t^{n+1}}\left[\left(\frac{M_{\phi,i}^{n+1}}{B_i^{n+1}}\right)-\left(\frac{M_{\phi,i}^{n}}{B_i^{n}}\right)\right]+v_i\Delta\tau_i T_{FM,i}^{n+1}\left(P_{f,i}^{n+1}-P_{m,i}^{n+1}\right)-q_{sf}^{n+1} \end{aligned} \tag{2.60}$$

where v_i is the drainage 'bulk' volume of the grid block i (**Eq. (2.57)**) and $T_{FM,i}^{n+1}$ is the matrix-fracture transfer function with an upstream weighting. The well term q_{sf}^{n+1} appeares only in the equation of the grid neighboring the wellbore.

$$T_{FM,i}^{n+1}=\sigma k_m\left(\frac{1}{B\mu}\right)_{up} \tag{2.61}$$

The finite difference equation of the matrix system is written as

$$\frac{1}{\Delta t^{n+1}}\left[\left(\frac{\phi_{m,i}^{n+1}}{B_i^{n+1}}\right)-\left(\frac{\phi_{m,i}^{n}}{B_i^{n}}\right)\right]-T_{FM,i}^{n+1}\left(P_{f,i}^{n+1}-P_{m,i}^{n+1}\right)=0 \tag{2.62}$$

We assign **Eqs. (2.60)** and **(2.62)** to each discretized fracture and matrix grids, respectively, and solve the corresponding unknown variables, $P_{f,i}^{n+1}$ and $P_{m,i}^{n+1}$. The numerical simulation procedure and derivative calculations for constructing the Jacobian are described in **APPENDIX B**.

2.3.2 Gas Permeability in Nanoporous Media

Knudsen number is a widely-recognized system identification parameter that determines a flow regime at given flow condition and fluid properties. This dimensionless parameter is defined by the ratio of a gas mean-free-path λ to a physical length (usually the pore radius r) (Civian et al. 2011).

$$K_n = \frac{\lambda}{r} \tag{2.63}$$

The mean-free-path λ is the average distance travelled by a moving molecule between successive collisions on pore wall or with another molecule. Knudsen number, which is given as the collision distance scaled by the pore radius, indicates the frequency of molecular-molecular and molecular-wall collisions when a molecule travels in the unit length. For ideal gas, λ is defined as follows (Civian et al. 2011).

$$\lambda = \frac{\mu}{P}\sqrt{\frac{\pi RT}{2M_w}} \tag{2.64}$$

where T is temperature, R is a universal gas constant, and M_w is molecular weight. For real gas situations, the mean-free-path λ is corrected by multiplying the compressibility factor z (Swami et al. 2012).

$$\lambda = \frac{\mu z}{P}\sqrt{\frac{\pi RT}{2M_w}} \tag{2.65}$$

Schaaf and Chambre (1961) identified five flow regimes on the basis of Knudsen number as shown in **Table 2.1**.

Table 2.1 – Flow regime identification based on Knudsen number	
Knudsen Number, Kn	Flow Regime
Kn ≤ 0.001	Viscous flow
0.001 < Kn < 0.1	Slip flow
0.1 < Kn < 10	Transition flow
Kn ≥ 10	Knudsen flow

The Darcy's law (viscous flow) is valid only in a fairly low Knudsen number range ($K_n \leq 0.001$), whereas the non-slip boundary condition is broken as Knudsen number becomes higher ($K_n > 0.001$). In the slip flow regime ($0.001 < K_n < 0.1$), the collisions between gas molecule and pore surface become more pronounced and consequently the linear flow approximation is broken down. In the transition flow ($0.1 < K_n < 10$), the additional pore surface effect plays an important role on the fluid flow, that is Knudsen diffusion. Knudsen diffusion represents the diffusive flow driven by the collisions between the molecule and pore surface, which is different from the molecular diffusion driven by the molecule-molecule collision (**Fig.2.5**), and it occurs on the porous media where the physical length r of the fluid flow path approaches comparable or smaller than the mean-free-path λ. The transition flow is identified as the combination flow contributed by the convection, slippage, and Knudsen diffusion. Some authors (Javadpour et al. 2007, Swami et al. 2012) pointed out that most of shales and many tight gas reservoirs fall in the transition flow regime. At a very high Knudsen number ($K_n \geq 10$), the fluid flow is mainly driven by Knudsen diffusion flow, not by the convective drive. This regime is not frequently encountered in shales and tight gas plays. Knudsen

flow is usually modeled by using the molecular simulation instead of the continuum flow approach.

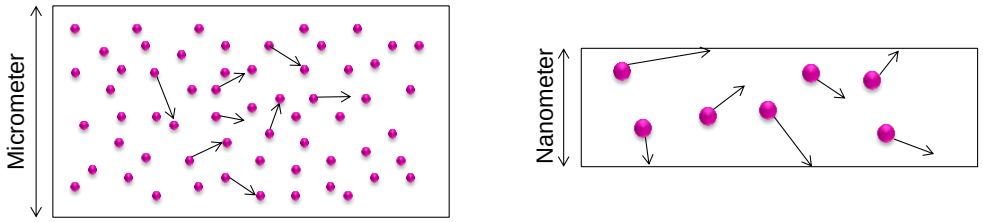

(a) Molecular Diffusion in Micro-scale Tube

(b) Knudsen Diffusion in Nano-scale Tube

Fig. 2.5 – Diffusion types in porous media.

On the basis of the above flow regime identification, we focus on the fluid flow modeling for the slip and transition flow regimes. The target Knudsen number is $0.001< K_n <10$ (**Table 2.1**). During the slip and transition flow regimes, the total mass flux J_T in nanoporous media is governed by the Convection-Knudsen diffusion equation in addition to the slip surface boundary condition.

$$J_T = J_C + J_{K_n} \tag{2.66}$$

where J_C is convective mass flux, given by the Darcy's equation with the correction of slippage effect.

$$J_C = \rho_g \frac{k_\infty}{\mu_g} F \nabla P \tag{2.67}$$

where F is the slippage factor. Brown et al. (1946) proposed a theoretical dimensionless slippage factor for slip velocity in capillary tube.

$$F = 1 + \left(\frac{8RT}{\pi M_w}\right)^{0.5} \frac{\mu_g}{Pr}\left(\frac{2}{\alpha} - 1\right) \tag{2.68}$$

where α is the tangential momentum accommodation coefficient or, simply, the part of gas molecules reflected diffusely from the pore wall relative to specular reflection. The value of α varies theoretically in the range from 0 to 1, depending upon the pore surface smoothness, gas type, temperature, and pressure (Javadpour et al. 2007). In **Eq. (2.66)**, the Knudsen diffusion mass flux J_{K_n} is given by the Fick's first law with the gas concentration difference.

$$J_{K_n} = D_m \nabla \rho_g \tag{2.69}$$

where D_m is the 'effective' Knudsen diffusion coefficient. For convenience, we use the gas density difference $\nabla \rho_g$ in **Eq. (2.69)** instead of using the gas concentration difference ∇C. Grathwohl (1998) suggested that the Knudsen diffusion coefficient is scaled based on the matrix porosity and surface tortuosity due to the complexity of the geometry of the porous media network. The approach is to consider the porous network as consisting of a certain percentage of open pores (matrix porosity) and having a degree of interconnection resulting in the actual path of the porous media longer than the straight path (tortuosity).

$$D_m = \frac{\phi_m}{\delta} D_k \tag{2.70}$$

where ϕ_m represents the matrix porosity and δ denotes the tortuosity, and D_k represents the Knudsen diffusion coefficient in a long smooth straight tube that is given by the function of mean molecular speed (Igwe 1987).

$$D_k = \frac{2r}{3}\left(\frac{8RT}{\pi M_w}\right)^{0.5} \tag{2.71}$$

Notice that the Knudsen diffusion coefficient is proportional to the pore radius and temperature. From **Eqs. (2.66)**, **(2.67)**, and **(2.69)**, the Convection-Knudsen diffusion equation for nanoporous media is written as

$$J_{Total} = \rho_g \frac{k_\infty}{\mu_g} F \nabla P + D_m \nabla \rho_g = \rho_g \frac{1}{\mu_g}\left(k_\infty F + c_g \mu_g D_m\right)\nabla P \tag{2.72}$$

where c_g is gas compressibility. In **Eq. (2.72)**, we define the apparent permeability as follows (Javadpour et al. 2007, Swami et al. 2012).

$$k_{app} = k_\infty F + c_g \mu_g D_m \tag{2.73}$$

Finally, the total mass flux (**Eq. (2.66)**) is written by the same equation form as the Darcy's law on the basis of apparent permeability.

$$J_T = \rho_g \frac{1}{\mu_g} k_{app} \nabla P \tag{2.74}$$

The Hagen-Poiseuille equation, which assumes a laminar flow in cylindrical pipe with non-slip side boundary, gives a theoretical value for the Darcy permeability k_∞.

$$k_\infty = \frac{r^2}{8} \tag{2.75}$$

If the representative shape of pore is not straight cylinder, the Darcy permeability is also corrected based on the porosity and pore geometry (tortuosity) as shown in **Eq. (2.70)** (Grathwohl 1998).

$$k_\infty = \frac{\phi_m}{\delta}\frac{r^2}{8} \tag{2.76}$$

Substituting **Eqs. (2.68)**, **(2.70)**, **(2.71)** and **(2.76)** into **Eq. (2.73)**, the apparent permeability is defined as follows.

$$k_{app} = \left(\frac{\phi_m}{\delta}\frac{r^2}{8}\right)\left[1 + \left(\frac{8RT}{\pi M_w}\right)^{0.5}\frac{\mu_g}{Pr}\left(\frac{2}{\alpha} - 1\right)\right] + c_g\mu_g\left[\frac{\phi_m}{\delta}\frac{2r}{3}\left(\frac{8RT}{\pi M_w}\right)^{0.5}\right]$$
$$= \frac{\phi_m}{\delta}\left[\frac{r^2}{8} + \left(\frac{8RT}{\pi M_w}\right)^{0.5}\frac{\mu_g r}{8P}\left(\frac{2}{\alpha} - 1\right) + \frac{2rc_g\mu_g}{3}\left(\frac{8RT}{\pi M_w}\right)^{0.5}\right] \quad (2.77)$$

The apparent permeability is proportional to the pore radius and given by the pressure, temperature, gas properties, and pore radius. The ratio of the apparent permeability to the Darcy permeability ('Permeability Ratio') is obtained by dividing **Eq. (2.77)** by **Eq. (2.76)**.

$$\frac{k_{app}}{k_\infty} = 1 + \left(\frac{8RT}{\pi M}\right)^{0.5}\frac{\mu_g}{Pr}\left(\frac{2}{\alpha} - 1\right) + \frac{16c_g\mu_g}{3r}\left(\frac{8RT}{\pi M}\right)^{0.5} \quad (2.78)$$

In above expression, we see that the apparent permeability is comprised of three dimensionless components. First term in right hand side of **Eq. (2.78)** represents the relative importance of the viscous flow (convective permeability), that is scaled to 1. Second and third terms indicate the importance of the slippage and Knudsen diffusion relative to the viscous flow, respectively. If the permeability ratio closes to 1, the pore surface effects have no impact on the mass flux (purely viscous flow). If the permeability ratio is fairly larger than 1, the fluid flow behavior is highly affected by the slippage and Knudsen diffusion. Notice that the permeability ratio is proportional to the pressure and inversely proportional to the pore size.

2.3.3 Triple-Continuum Model

Based on the pore size variation in naturally- or hydraulically-fractured shale reservoirs, the gas transport domain are divided into three distinct systems: (1) natural and hydraulic fracture networks (macro-scale porous media), (2) nanopores in matrix or organic matters (nano-scale porous media), and (3) organic bulk or Kerogen (not containing pore space). **Fig 2.6** illustrates a typical gas flow process and physical mechanisms encountered in fractured shale reservoirs. The reservoir gas is produced primarily through the fracture networks, and the other two systems, nanopores and Kerogen content act as additional gas source to the fracture system. In this research, there are three distinct sources of gas compressed in the pore spaces of the three domains, which are the free gas in fracture and nanopores, adsorbed gas on nanopore surface, and dissolved gas in organic matter bulk. For each coordinate system, the shale gas physics are incorporated as follows.

- Primary coordinate: Fracture network
    a. Fracture is the primary coordinate for fluid flow and production.
    b. Flow is governed by convective transport.
    c. Fractures are affected by rock compacted due to geomechanics effect.
- Secondary coordinate: Nanopores in organic- and inorganic-rocks
    a. Two types of gases are compressed in nanopores – free gas and adsorbed gas.
    b. Flow is governed by the convection-Knudsen diffusion.
- Tertiary coordinate: Organic bulk (Kerogen)

a. Kerogen is the hydrocarbon source and contains the dissolved gas.

b. Dissolved gas diffuses to nanopores by concentration drive.

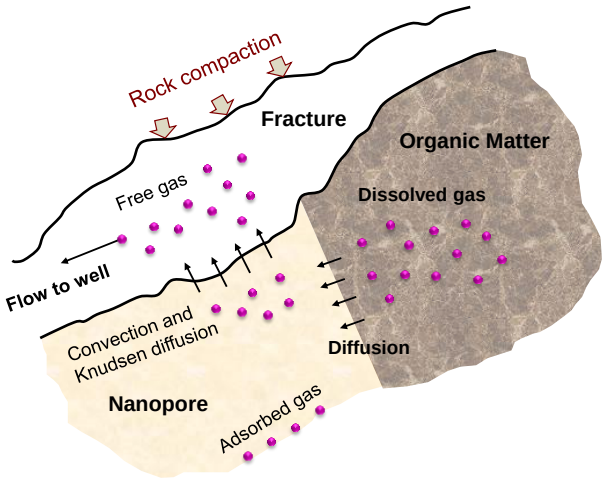

Fig. 2.6 – Gas flow process in the fractured shale reservoir.

The triple-continuum approach provides the generalized framework that is able to account for all physical effects and processes that exist in shale gas reservoirs. The numerical implementation involves the slippage and Knudsen diffusion effects, rock compaction in fractures, adsorption/diffusion, and gas diffusion from Kerogen content. **Fig. 2.7** illustrates the gas transport processes on the triple-continuum model and the connectivity among the fracture, nanopores, and Kerogen systems. The approach is similar to the DPSP model, while the one more coordinate (Kerogen) is added outside the matrix system. The inter-coordinate mass transfer between the fracture and nanopore is governed by the convection-Knudsen diffusion flow (apparent permeability).

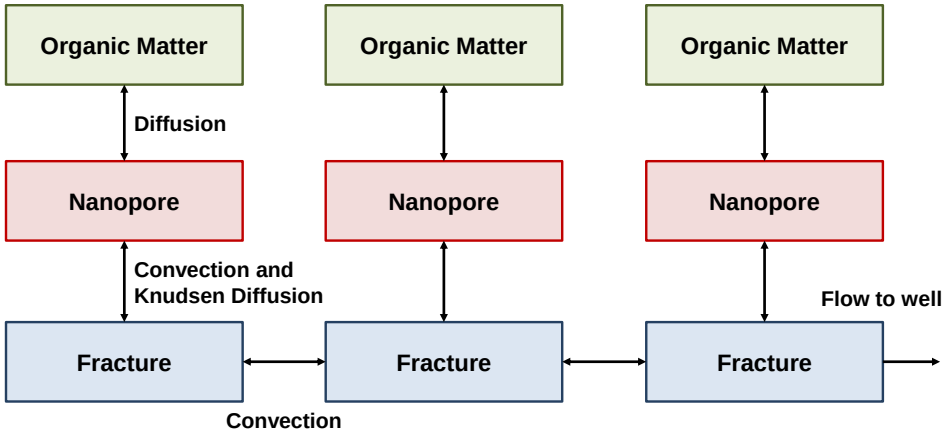

Fig. 2.7 – Illustration of the triple-continuum approach.

The mass transfer between the nanopores and Kerogen is governed by diffusive transport driven by the gas concentration difference between the nanopores (adsorbed gas) and Kerogen bulk (dissolved gas), which is given by the Fick's law of diffusion.

$$J_{KM} = -\sigma \rho_{g,sc} D_c (C_m - C_k) \tag{2.79}$$

where σ is the shape factor, $\rho_{g,sc}$ is the surface gas density, D_c is gas diffusion coefficient, C_k is gas concentration dissolved in Kerogen, and C_m is gas concentration adsorbed on the surface of nanopores. The adsorbed gas concentration on the nanopore surface C_m is given by the Langmuir isotherm model (Langmuir 1916).

$$C_m = V_L \frac{P}{P_L + P} \tag{2.80}$$

where V_L is Langmuir volume and P_L is Langmuir pressure. Notice that the Langmuir volume V_L has the units of scf/rcf. This is obtained from the bulk rock density ρ_b (gm/cc) and the adsorbed gas content V_m (scf/ton).

$$V_L = 0.031214\rho_b V_m \tag{2.81}$$

Mengal et al. (2011) suggested that the approximate values of ρ_b, V_m, and P_L in the Barnett shale are 2.38 (gm/cc), 96 (scf/ton), and 650 (psia), respectively. Hence, the Langmuir volume V_L is expected to be about 7.13 (scf/rcf).

Fig. 2.8 shows the gas flow process from organic matter bulk to nanopores. At static condition, the Kerogen gas concentration is in equilibrium with the adsorbed gas concentration. After the well production and resulting pressure depletion in the nanopore system, the equilibrium condition is disrupted due to desorption of the adsorbed gas molecules. The concentration imbalance causes the dissolved gas in the Kerogen to diffuse to the Kerogen-nanopore interface, and then the gas molecules start to be adsorbed on the pore surface.

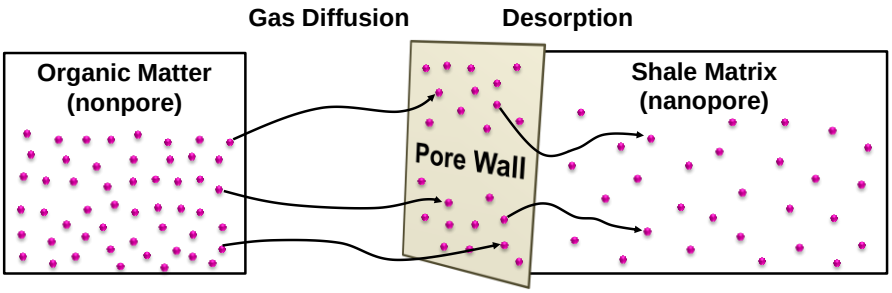

Fig. 2.8 – Gas diffusion from organic matter to nanopore.

The mass balance in the fracture system is obtained by **Eq. (2.53)** including rock compaction effects, M_ϕ and M_k and using the apparent permeability k_{app} in the matrix-fracture transfer term instead of the ordinary matrix permeability k_m.

$$\frac{\partial}{\partial t}\left(\phi_f M_\phi \rho_g\right) = \nabla \bullet \left(\rho_g \frac{M_k k_f}{\mu_g} \nabla P_f\right) - \sigma_{FM} \rho_g \frac{k_{app}}{\mu_g}\left(P_f - P_m\right) + \rho_g q_f \tag{2.82}$$

where M_ϕ and M_k represent the multipliers for porosity and permeability, respectively, and σ_{FM} denotes the shape factor of fracture-nanopore connectivity (fracture density). In this formulation, the porosity multiplier M_ϕ is given by the rock compaction table as a function of pressure instead of the conventional exponential rock compressibility function (**Eq. (2.34)**). Applying the coordinate transformation into 1-D τ-coordinate (**Eq. (2.38)**), we obtain the fracture equation along τ-coordinate as follows.

$$\begin{aligned}&\frac{\partial\left(\phi_f \rho_g\right)}{\partial t} \\ &= \frac{\phi_{f,\text{init}}}{w(\tau)} \frac{\partial}{\partial \tau}\left(w(\tau) M_k \rho_g \frac{\left(\mu_g c_t\right)_{\text{init}}}{\mu_g} \frac{\partial P_f}{\partial \tau}\right) - \sigma_{FM} \rho_g \frac{k_{app}}{\mu_g}\left(P_f - P_m\right) + \rho_g q_f\end{aligned} \tag{2.83}$$

Notice that the surface production rate q_{sf} is calculated by **Eq. (2.50).** For the nanopores system, the mass balance equation is written as

$$\frac{\partial}{\partial t}\left(\phi_m \rho_g + \rho_{g,sc} C_m\right) = \sigma_{FM} \rho_g \frac{k_{app}}{\mu_g}\left(P_f - P_m\right) - \sigma_{MK} \rho_{g,sc} D_c (C_m - C_k) \tag{2.84}$$

where $\rho_{g,sc}$ represents the gas density at standard condition (14.7 psia and 60 °F), and σ_{MK} denotes the shape factor of nanopore-Kerogen connectivity (density of nanopores in organic matter). The accumulation term in **Eq. (2.84)** contains the mass of two states of gas which are free gas compressed within pore and adsorbed gas compressed on pore surface. The first term in the right hand side of **Eq. (2.84)** represents the mass transfer between fracture and nanopore given by the convection-Knudsen diffusion flow, and the second term represents the mass transfer term between nanopore and Kerogen given by

the diffusion flow (**Eq. (2.79)**). For the Kerogen system, the mass balance equation is written as

$$\frac{\partial C_k}{\partial t} = \sigma_{MK} D_c (C_m - C_k) \tag{2.85}$$

The finite difference equation in the fracture system is

$$\begin{aligned} &T_{i-1/2}^{n+1} P_{f,i-1}^{n+1} - \left(T_{i-1/2}^{n+1} + T_{i+1/2}^{n+1}\right) P_{f,i}^{n+1} + T_{i+1/2}^{n+1} P_{f,i+1}^{n+1} \\ &\quad = \frac{w_i \Delta\tau_i}{\Delta t^{n+1}} \left[\left(\frac{M_{\phi,i}^{n+1}}{B_i^{n+1}} \right) - \left(\frac{M_{\phi,i}^{n}}{B_i^{n}} \right) \right] + \Delta\tau_i v_i \sigma \frac{k_{app,i}^{n+1}}{(B\mu)_{up}^{n+1}} \left(P_{f,i}^{n+1} - P_{m,i}^{n+1} \right) - q_{sf}^{n+1} \end{aligned} \tag{2.86}$$

where v_i is the derivative of the drainage 'bulk' volume of the grid block i as defined in **Eq. (2.57)**. The apparent permeability $k_{app,i}^{n+1}$ is calculated by **Eq. (2.77)** for each matrix block for each time-step. The finite difference equation in the matrix system is

$$\begin{aligned} &\frac{1}{\Delta t^{n+1}} \left[\left(\frac{\phi_{m,i}^{n+1}}{B_i^{n+1}} + C_{m,i}^{n+1} \right) - \left(\frac{\phi_{m,i}^{n}}{B_i^{n}} + C_{m,i}^{n} \right) \right] - \sigma \frac{k_{app,i}^{n+1}}{(B\mu)_{up}^{n+1}} \left(P_{f,i}^{n+1} - P_{m,i}^{n+1} \right) \\ &\qquad + \sigma_{MK} D_c \left(C_{m,i}^{n+1} - C_{k,i}^{n} \right) = 0 \end{aligned} \tag{2.87}$$

The finite difference equation in the Kerogen system is

$$\frac{\left(C_{k,i}^{n+1} - C_{k,i}^{n} \right)}{\Delta t^{n+1}} - \sigma_{MK} D_c \left(C_{m,i}^{n+1} - C_{k,i}^{n+1} \right) = 0 \tag{2.88}$$

The governing equations of the DTOF-based triple-continuum approach are given by **Eqs. (2.86)** - **(2.88)**, and the corresponding primary variables are the fracture pressure (P_f), matrix pressure (P_m), and Kerogen dissolved gas concentration (C_k) for each grid. The numerical simulation procedure and derivative calculations for constructing the Jacobian are described in **APPENDIX B**.

2.4 Results and Discussions

In this subchapter, three examples are presented for the validation of the single-phase DTOF-based flow simulation using 2-D and 3-D heterogeneous gas reservoir models. The model validations include the single-porosity, dual-porosity, and triple-continuum models as described in this chapter. The results of the DTOF-based simulation are compared with the predictions from a commercial blackoil simulator (Schlumberger© ECLIPSE100).

2.4.1 Single-Porosity Model

For the validation of the single-phase single-porosity model, we first present a 2-D channel-type reservoir model. The model size is 1,200 ft, 2,400 ft, and 10 ft along x, y, and z directions, respectively, and the model is comprised of 60×120 (7,200) grids. The initial reservoir pressure is 5,000 psi at equilibrium. **Fig. 2.9** shows the geological heterogeneities of the 2-D model. The permeability has the directionality among x-, y-, and z-axes (**(a)** – **(c)**), and the porosity is heterogeneously distributed (**(d)**). The formation permeability ranges from 2.3×10^{-3} to 2 md in horizontal and the porosity ranges from 0 to 5 %.

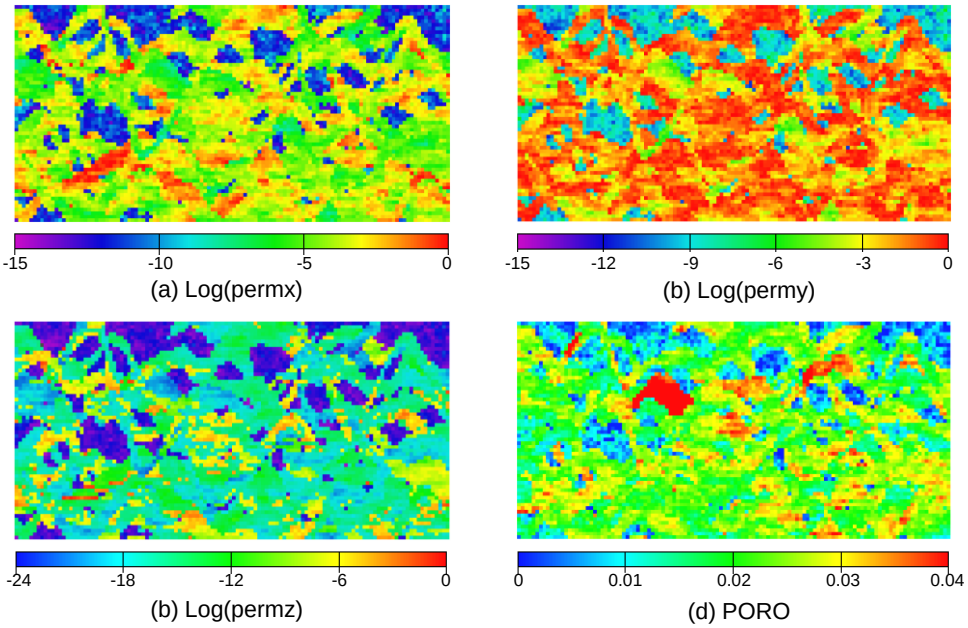

Fig. 2.9 – Distributions of the porosity and logarithmic permeability.

Before conducting a numerical simulation, we first transform the multidimensional geometric heterogeneities (geometry, porosity and permeability) into 1-D heterogeneity along the DTOF coordinate by the FMM calculation. The DTOF map is illustrated in **Fig. 2.10**. Notice that the well is vertically placed in the center of the model.

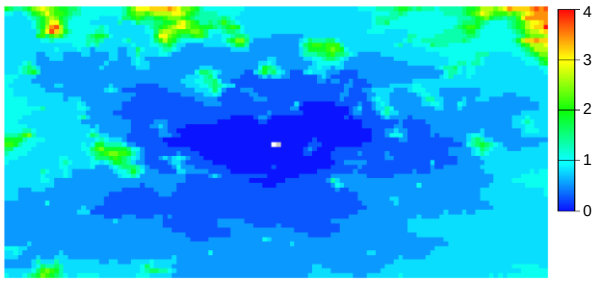

Fig. 2.10 – DTOF map in heterogeneous single-porosity model.

Fig. 2.11 shows the drainage volume curves. After the DTOF calculation, the FMM successively computes the well drainage volumes by summing up the pore volumes within the contours of DTOF along the pressure propagation trajectory (**(a)**). The drainage volume is also calculated as a function of time (**(b)**) using the following equation.

$$V_p(t) = \sum_j V_{p,j} \exp\left(-\frac{\tau_j^2}{4t}\right) \tag{2.89}$$

The drainage pore volume monotonically evolves from the well completions and finally reaches a plateau (pseudo-steady state / boundary-dominant flow) which means that the propagation front completely touches on the model outer boundaries and there is no available (propagable) pore volume anymore.

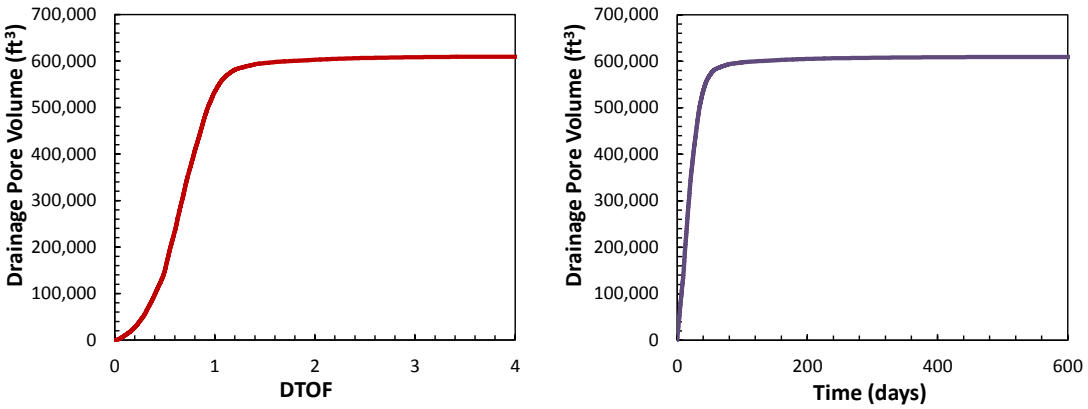

(a) Vp as a function of DTOF

(a) Vp as a function of TIME

Fig. 2.11 – Drainage pore volumes as a function of (a) DTOF and (b) Time.

Once we obtain the drainage pore volume, we successively perform a numerical simulation based on the 1-D DTOF coordinate system. **Fig. 2.12** shows the results of the DTOF-based simulation. The simulation results are compared with the commercial simulator for reference. **Fig. 2.12 (a)** is the predicted well gas production rate under a constant bottom-hole pressure constraint (3,500 psi). **Fig. 2.12 (b)** is the predicted well bottom-hole pressure under a constant gas production rate constraint (1,000 Mscf/day). The both results have a good agreement with the results of the commercial simulator.

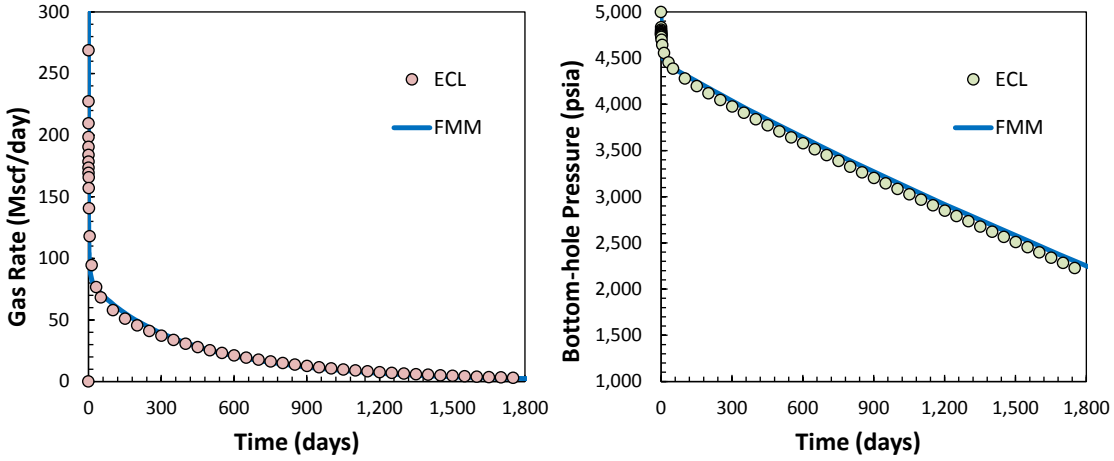

(a) Predicted gas production rate

(b) Predicted bottom-hole pressure

Fig. 2.12 – Simulation results of the (a) gas production rate and (b) bottom-hole pressure. The plot denotes the result of the commercial simulator (ECLIPSE) and the lines represents the result of the DTOF-based simulation.

During the DTOF-based flow simulation, the spatial variable (pressure) is numerically solved along the 1-D coordinate system each time-step. Because we know the DTOF values on the cell center of each Cartesian grid, the 1-D pressure solution can be linearly

mapped back on the original Cartesian model each time-step. **Fig. 2.13 (a)** and **(c)** are the pressure contours at 100 days and 300 days, respectively, calculated by the commercial simulator. **Fig. 2.13 (b)** and **(d)** are the pressure map at the corresponding time-steps calculated by the DTOF-simulation. We can see the DTOF-based simulation captures the pressure in a highly heterogeneous geological characteristics based on its 1-D coordinate.

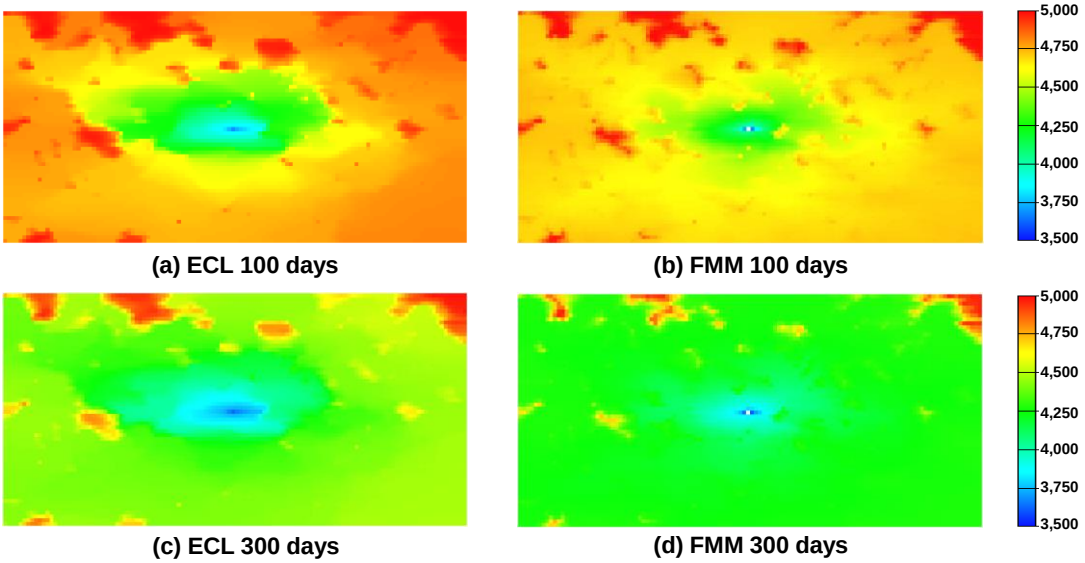

Fig. 2.13 – Pressure maps of the (a) ECLIPSE at 100 days, (b) DTOF simulation at 100 days, (c) ECLIPSE at 300 days, and (d) DTOF simulation at 300 days.

2.4.2 Dual-Porosity Model

A dual-porosity modeling is an efficient way to simplify a geological description of the complex fractured reservoirs. In this example, we demonstrate the naturally fractured gas reservoir model with a vertically completed well. The reservoir size is

1,990 ft, 1,990 ft, and 500 ft along x, y, and z directions, respectively, and the model is comprised of the total 199×199×10 grids. The first 5 layers represent the matrix system and the other 5 layers are the fracture system. These two distinct systems are connected by the convective transfer function without the diffusion and slippage effects. The initial reservoir pressure is 5,470 psi. **Fig. 2.14** shows the permeability and porosity distributions in the fracture coordinate. The fracture permeability is ranging from 0.32 to 4.93 md in x direction, 0.32 to 4.98 md in y direction, and 0.034 to 0.634 md in z direction. The fracture porosity ranges from 0.97 to 12 %.

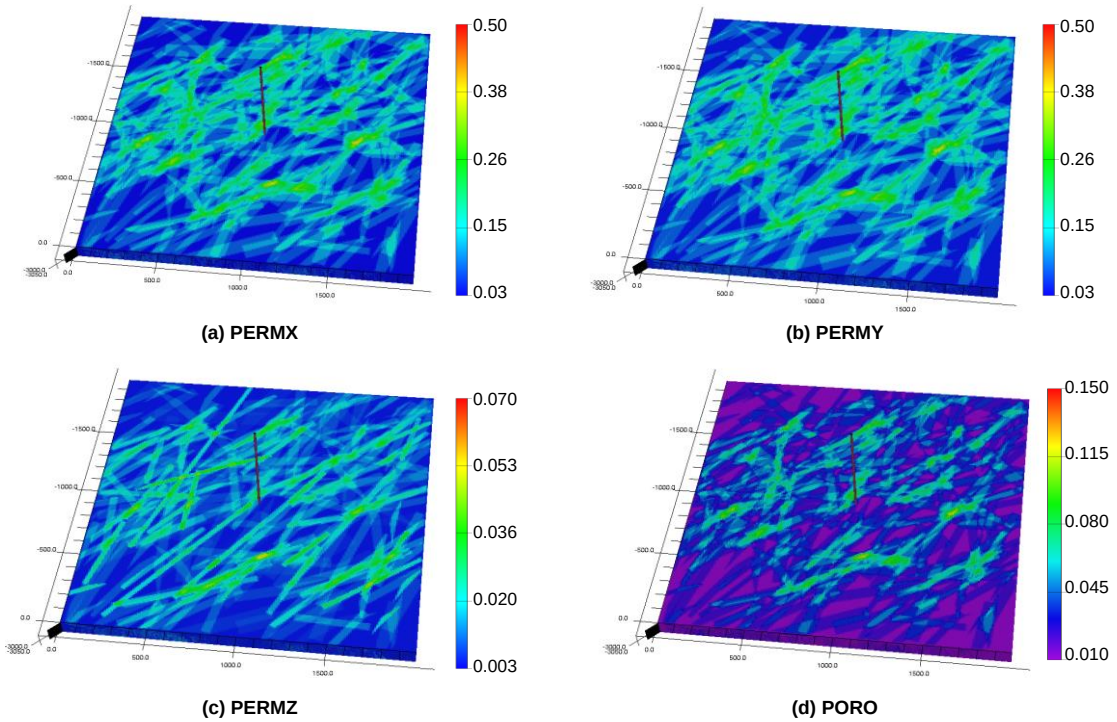

Fig. 2.14 – Distributions of the fracture permeability and porosity.

In the matrix system, the permeability and porosity are both constant (1×10^{-4} md and 10 %). The matrix rocks have a low permeability but large storage capacity relative to the fracture system. The well is vertically placed on the center of the model and completed through the five fracture layers.

In this model, the geomechanical rock compaction is considered to account for the effects of the rock deformation and compaction in the fracture space. In the conventional stratified sandstone reservoirs, geomechanical effects on its porosity and permeability are generally small and usually neglected. However, in fractured reservoirs, such geomechanical effects can be relatively large and may have a significant impact particularly in near-wellbore region due to the large pressure drawdown. The resulting rock compaction can significantly affect to the flow conductivity and the fluid storage capacity in fractures space. In this model, the rock compaction is incorporated on the pressure and porosity as shown in **Fig. 2.15**. The fracture permeability (multiplier) changes nonlinearly as a function of pressure. The porosity (multiplier) changes linearly in the pressure table instead of using the conventional exponential rock compressibility function (**Eq. (2.34)**).

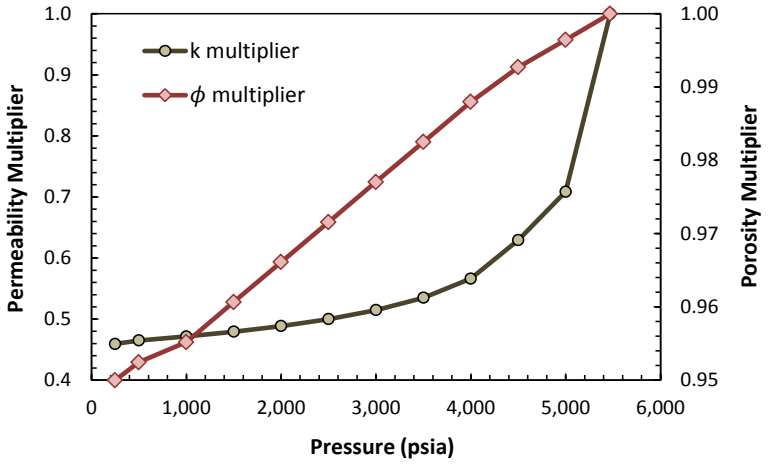

Fig. 2.15 – Rock compaction table for the fracture system.

Fig. 2.16 shows the numerical simulation results of the constant well bottom-hole pressure and constant well rate cases. **Fig. 2.16 (a)** is the predicted gas production rate under the constant bottom-hole pressure constraint (4,000 psi). In this figure, the 'case1' represents the result without the rock compaction effect, and 'case2' represents the result with the rock compaction effect. **Fig. 2.16 (b)** is the predicted bottom-hole pressure under the constant gas rate constraint (1,000 Mscf/day). It is obvious that the rock compaction effect in fractures has a significant impact on the production and bottom-hole pressure behaviors. Under the influence of the rock compaction, the rate and bottom-hole pressure rapidly declined because the fracture conductivity and storage capacity are dramatically decreased as the fracture pressure decreases.

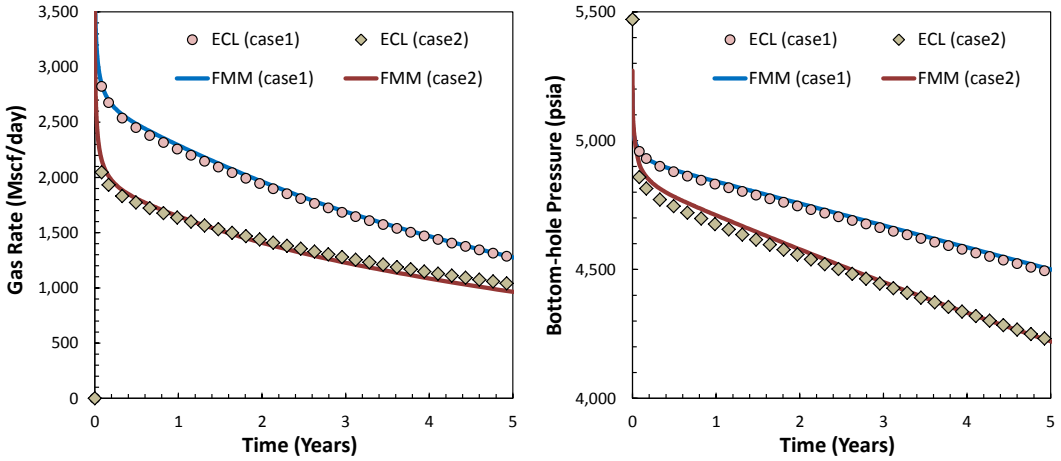

(a) Predicted Gas Production Rate (b) Predicted Bottom-hole Pressure

Fig. 2.16 – Simulation results of the (a) gas production rate and (b) bottom-hole pressure. The plots are the commercial simulator and the lines are the DTOF-based simulation. The 'case1' represents the no rock compaction model, and 'case2' denotes the rock compaction model.

2.4.3 Triple-Continuum Model

The main purpose of the triple-continuum modeling is to simulate unconventional shale gas reservoirs with taking account for all the known physical mechanisms and its characteristics. The dual-porosity model is still a reasonable approach to model such reservoirs because most shale reservoirs are essentially naturally fractured, but it is not sufficient to explain the existence of organic matters. In the triple-continuum approach, we decompose the reservoir domain into three distinct subdomains – (1) natural and hydraulic fracture networks (micropores), (2) inorganic matrix (nanopores), and (3) organic matter bulk (Kerogen). It enables us to incorporate various types of physical phenomena into each subdomain, i.e. geomechanical rock compaction in fractures, slippage and Knudsen diffusion effect in nanopores, and gas diffusion from organic matters. In this example, we present a synthetic shale gas well model stimulated

by a multistage hydraulic fracturing. The model size is 2,000 ft, 4,000 ft, and 150 ft along x, y, and z directions, respectively, and the model consists of the 200×400×90 (7,200,000) grids. The first 30 layers is the fracture domain, the second 30 layers is the nanoporous domain, and the last 30 layers is the Kerogen bulk domain. The initial reservoir pressure is 1,500 psi at equilibrium for all the domains. **Fig. 2.17** shows the fracture permeability distribution that ranges from 1×10^{-4} to 0.15 md in horizontal direction and from 1×10^{-6} to 1.5×10^{-3} md in vertical direction. The fracture porosity is assumed to be constant (1 %).

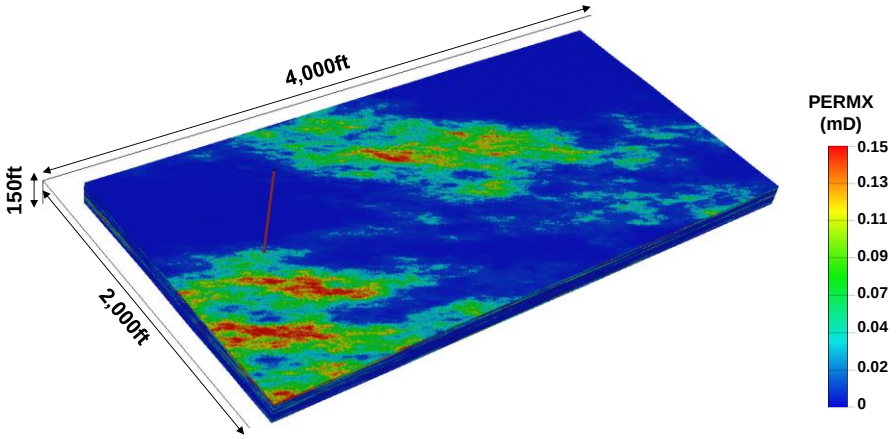

Fig. 2.17 – Horizontal permeability distribution in the fracture system.

The well is horizontally placed along y direction and completed with planar 12-stage hydraulic fractures as shown in **Fig. 2.18**. The horizontal length of the well is approximately 3,300 ft. The average fracture half-length, width, and height are 200 ft, 10 ft, and 100 ft respectively. Because of the hydraulic fracturing, the permeability is

increased by a factor of 10,000 in the stimulated grids for all the directions. The hydraulic fracture permeability ranges from 1.3 to 1,532 md in horizontal direction and from 0.013 to 15.3 md in vertical direction.

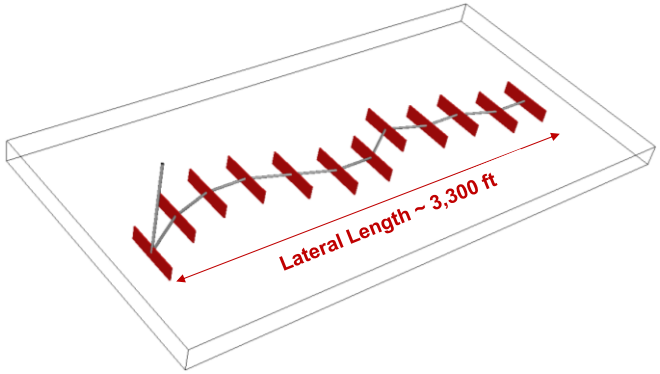

Fig. 2.18 – Horizontal well stimulated by the 12-stage hydraulic fracturing.

The reservoir properties are summarized in **Table 2.2**. In the triple-continuum model, the apparent matrix permeability is calculated using pressure, temperature, gas properties, and nanopore size as described in **Eq. (2.76)**, thus the matrix permeability is not explicitly input in the model. In **Table 2.2**, there are two shape factors that is fracture-matrix shape factor and Kerogen-nanopore shape factor. The latter one represents the density of formation porosity in inorganic- and organic-rocks. The adsorption/desorption processes are modeled by the Langmuir isotherm. This isotherm model has several assumptions.

- The adsorption equilibrium is instantaneous (only relates to pressure, not to time).

- The adsorption layer forms only monolayer at maximum.
- There are no phase transitions and surface diffusion in the adsorbed layer.

This isotherm is characterized by two parameters – Langmuir pressure and Langmuir volume. Langmuir pressure represents the pressure at which one half of the Langmuir volume can be adsorbed. Langmuir volume is defined as the maximum amount of gas that can be adsorbed to the surface of nanopores at infinite pressure. In this model, the Barnett shale gas data are used (Mengal et al. 2011) as shown in **Fig.2.19**.

Table 2.2 – Reservoir properties (3D triple-continuum model)		
Reservoir properties		
Initial pressure	(psia)	1,500
Temperature	(degF)	250
Matrix properties		
Porosity	(fraction)	0.1
Rock compressibility	(1/psi)	1×10^{-6}
Fracture-matrix shale factor	($1/ft^2$)	0.15
Langmuir pressure	(psi)	650
Langmuir volume	(scf/rcf)	7.13
Kerogen properties		
Diffusion coefficient	(ft/day)	0.02
Kerogen-matrix shape factor	($1/ft^2$)	0.15

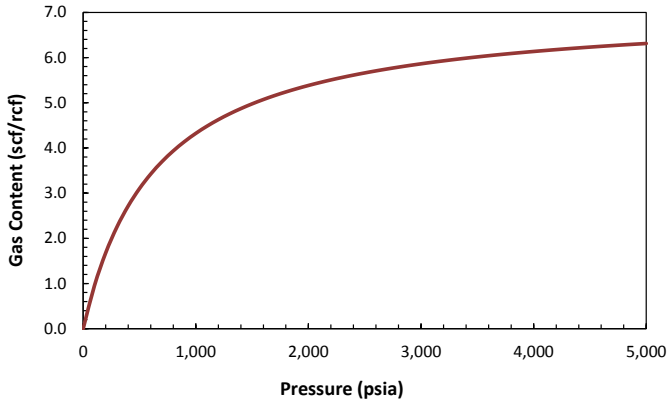

Fig. 2.19 – Langmuir isotherm model (the Barnett shale gas).

Fig. 2.20 illustrates the Knudsen number as a function of pressure and pore radius at given temperature and fluid compositions. The Knudsen number is calculated by **Eq. (2.62)** as a function of mean-free-path and pore size. When pore size is smaller than 100nm, the flow regime falls in slip or in transition flows at low pressure condition. Contrary, the viscous flow regime is appeared in micrometer pores (1,000 nm~).

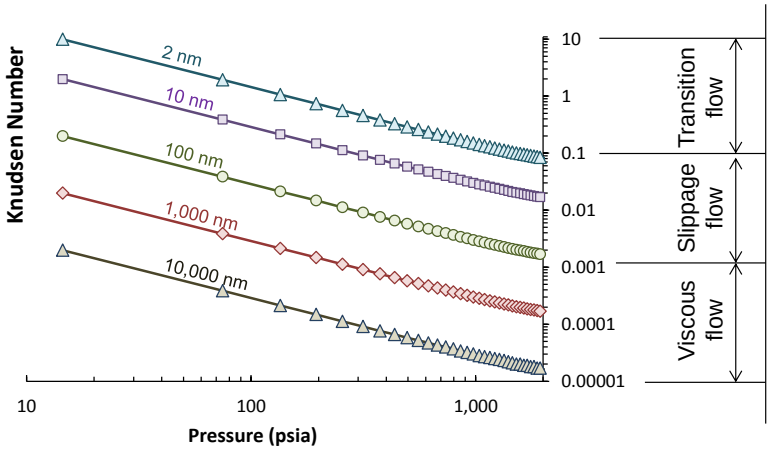

Fig. 2.20 – Knudsen number as a function of pressure and pore size at fixed gas composition and reservoir temperature (T = 250 °F).

Fig. 2.21 shows the changes of apparent gas permeability (**(a)**) and permeability ratio (**(b)**) as a function of pressure and pore size at given reservoir temperature and fluid compositions. These parameters are calculated by **Eqs. (2.76)** and **(2.77)**, respectively.

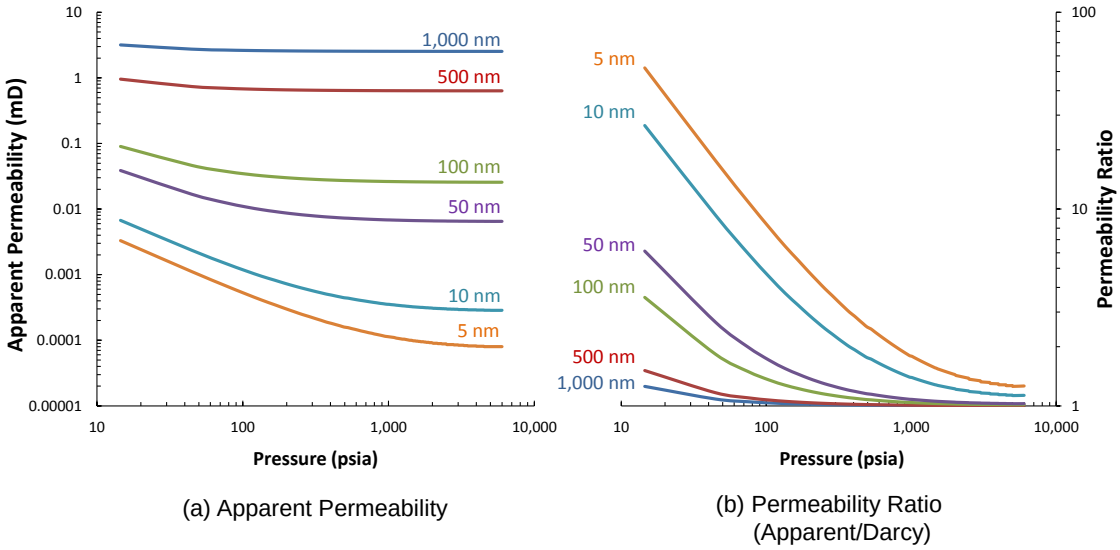

(a) Apparent Permeability

(b) Permeability Ratio (Apparent/Darcy)

Fig. 2.21 – Permeability change due to the slippage and Knudsen diffusion effects. (a) Apparent permeability and (b) Permeability ratio.

Before conducting the simulation of the triple-continuum model, we first validate this multistage hydraulic fractured model using single- and dual-porosity approaches without the shale gas effects (adsorption/desorption, slippage and Knudsen diffusion, and Kerogen diffusion terms). **Fig. 2.22 (a)** shows the simulation result of the single-porosity model that only involves the fracture system. **Fig. 2.22 (b)** is the simulation result of the dual-porosity model that involves the fracture and matrix systems. Both

models have a good agreement with the commercial simulator on the gas rate predictions.

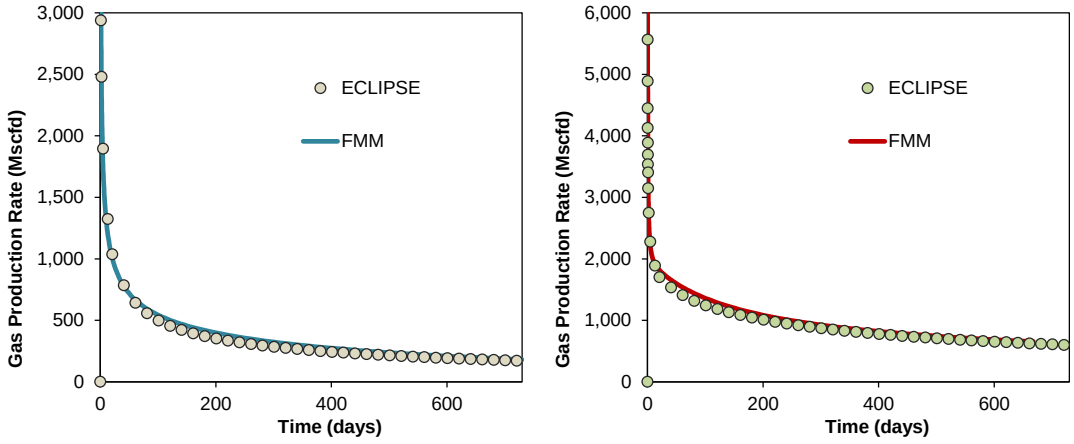

(a) Predicted Gas Production Rate on the single-porosity fracture model

(b) Predicted Gas Production Rate on the dual-porosity fracture-matrix model

Fig. 2.22 – Validation results of the (a) single-porosity model and (b) dual-porosity models. The results are compared with the ECLIPSE.

Next, we conduct the simulation of the triple-continuum model with fracture, nanopore, and Kerogen domains. We first predict the 10 years gas production rate under the constant bottom-hole pressure condition (500 psia) as shown in **Fig. 2.23**. The simulation is conducted based on several pore size conditions (100, 50, 20, 10, and 5 nm cases). The early-time production behavior significantly differs with the pore size variations which controls the matrix-fracture conductivity. The production decline rate is considerably higher in smaller pore condition, because the fracture obtains little

assistance from low-conductive smaller nanopores. After 10 days from the first production, the pore size does not make a difference on the production behavior.

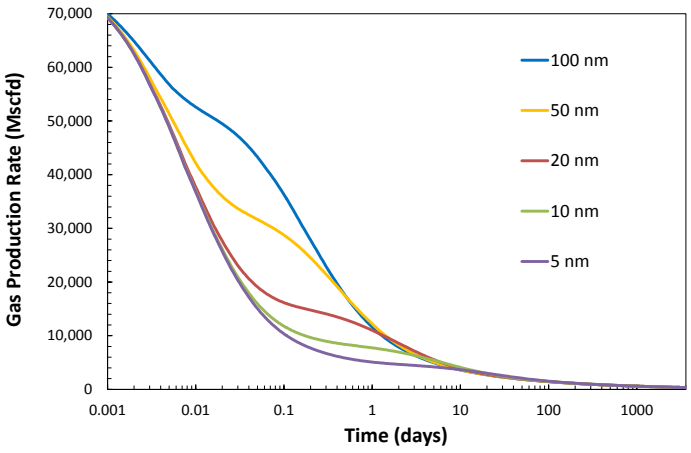

Fig. 2.23 – Gas production rates with different pore size conditions (10 years).

Fig 2.24 shows the volume transfer rate between fracture and matrix (**(a)**) and between matrix and organic matter (**(b)**). The matrix-fracture transfer responds very quickly to the pressure depletion due to its convective nature. The diffusive flow between nanopore and Kerogen proceeds slowly due to its diffusive nature.

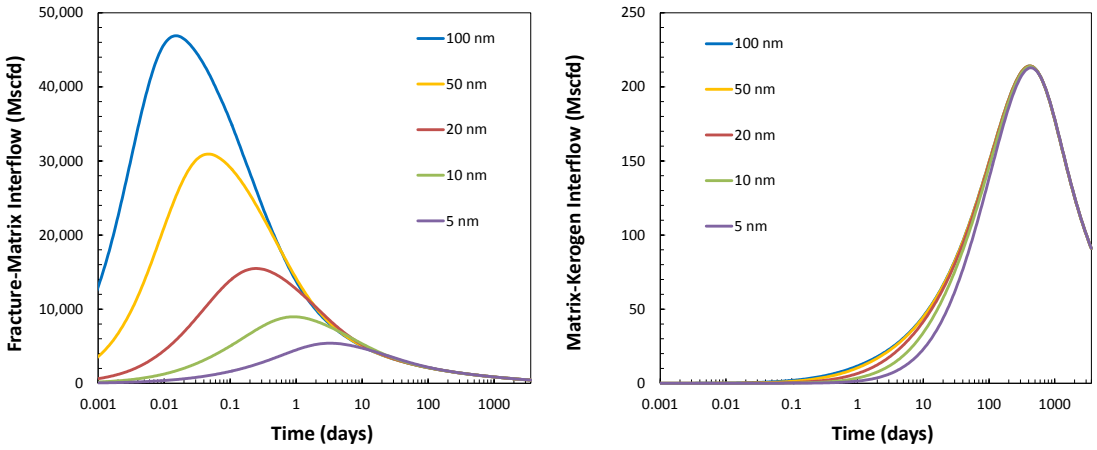

(a) Matrix-Fracture Mass Transfer

(b) Kerogen-Matrix Mass Transfer

Fig. 2.24 – Inter-coordinate fluid transfer between (a) matrix and fracture, and (b) Kerogen and matrix.

Finally, we predict the well bottom-hole pressure under the constant gas rate constraints (500 Mscf/day). Warren and Root (1963) suggested that, in dual-porosity reservoirs, they exhibit two distinct parallel pressure responses (or pseudo-pressure response). The model shows the similar behaviors to the dual-porosity model as shown in **Fig 2.25 (a)**. The first straight line represents the fracture-dominant behavior, and the second straight line represents the behavior of the dual system (fractures + nanopores). In the 100 nm case (blue line), the first straight line does not explicitly appear because the matrix instantaneously responds to the pressure drawdown due to the high conductivity between the fracture and nanopores. In contrast, the 5 nm (purple line) shows the long first straight line because of its low conductivity and the slow response of the matrix system. The pressure derivative plots are shown in **Fig. 2.25 (b)**.

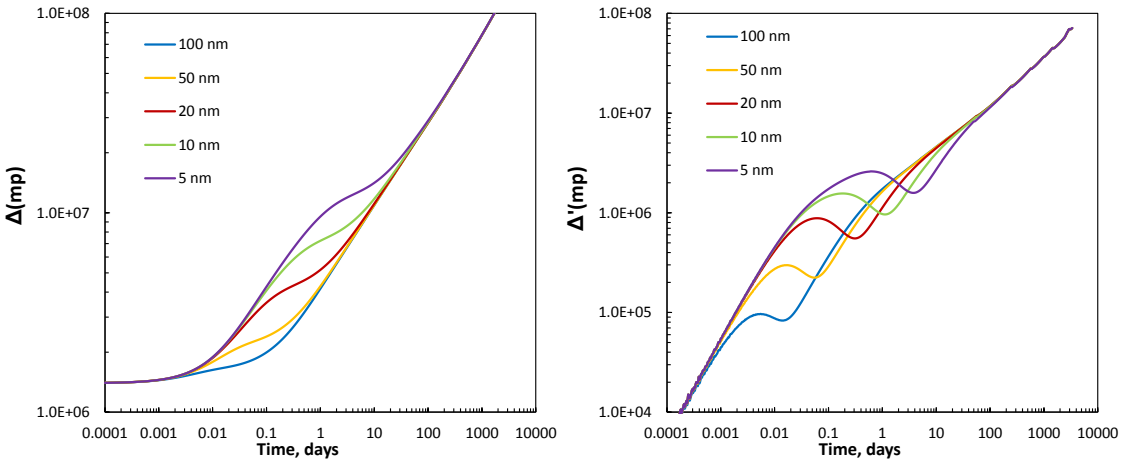

(a) Pressure Response (Pseudo-pressure)

(b) Pressure Derivative (Pseudo-pressure)

Fig. 2.25 – Simulation results of the (a) bottom-hole pressures and (b) its derivatives

The responses of the matrix and Kerogen systems are also observed by plotting the volume transfer rate between the fracture and matrix and between the matrix and Kerogen (**Fig. 2.26**). The instantaneous response can be seen in the 100 nm case (blue line), and then the smaller pores gradually activated as the pressure drawdown proceeds in the matrix system (**(a)**). Notice that the steady-state matrix-fracture transfer rate (the rate after 10 days) does not show difference among all the pore size cases. In contrast, the Kerogen system is pronounced in the late time period and essentially has no difference in the transfer rate for the pore size variations (**(b)**).

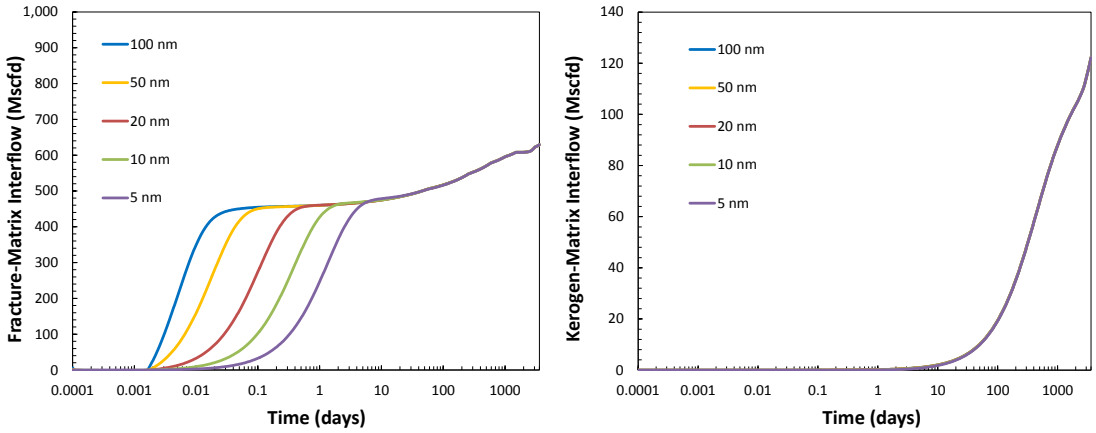

(a) Matrix-Fracture Mass Transfer (b) Kerogen-Matrix Mass Transfer

Fig. 2.26 – Inter-coordinate fluid transfer between (a) matrix and fracture, and (b) Kerogen and matrix.

2.5 Conclusions

This chapter presented the DTOF formulation and its extension to the multi-continuum modeling for single-phase fluid flow problems. The proposed approach is applicable in both compressible and slightly-compressible fluids and allows us to include complex well models (i.e. horizontal well with multistage hydraulic fractures) as well. The numerical experiments show good agreement between the proposed approach and conventional simulation method (commercial simulator). The power and versatility have been demonstrated through the model validations. The major features of this chapter are summarized as follows.

- A finite difference method is used to approximate the pressure solutions of the 1-D DTOF-based differential equations as with the conventional reservoir simulation approach. The w-function is constructed as a directional property from the drainage volume using forward, backward, and central differences.

- The DTOF-based flow simulation is less computationally demanding compared with the conventional reservoir simulation method due to the several inherent advantages of this approach. First, the Fast Marching Method is single-pass algorithm because each cell is touched essentially only once. Thus, the solution can be constructed sequentially from the small τ (source point) to large τ (usually outer boundary) along the pressure propagation path. It allows the FMM to be applied for large scale problems. Second, the multidimensional transport equations are decomposed into the series of 1-D transport equations based on the coordinate transformation. During the numerical computation, the sizes of the matrix and vector constructed for each iteration step are dramatically reduced, for example, from several millions to several hundreds. Third, in the transformed 1-D coordinate, the geological heterogeneities are integrated to only one heterogeneous parameter that is drainage volume. The complex reservoir geometries (i.e. corner point grid) are also transformed to a simple 1-D grid coordinate. Furthermore, the drainage volume is a property monotonically increasing from small τ to large τ. As a result, the grid complexities and spatial heterogeneities are considerably simplified in the DTOF formulation.
- The DTOF formulation is extended to dual-porosity modeling. The additional coordinate (matrix system) is added to the 1-D fracture system under several assumptions: (1) the FMM is performed on the fracture coordinate without consideration for the matrix system and its heterogeneities, and (2) matrix properties (permeability, porosity, an shape factor) are constant over the domain.

Also, the primary variables in the matrix system are solved along the same 1-D coordinate as the 1-D fracture system.

- We have proposed a generalized framework for the flow modeling of shale gas reservoir using the triple-continuum approach. The unconventional reservoir characteristics were comprehensively investigated by accounting for all the known physical mechanisms and its characteristics including the Knudsen diffusion and slippage effects, adsorption/diffusion in nanopore surfaces, rock compaction in fractures due to the geomechanical effect, and gas diffusion from Kerogen content. The numerical simulation results show that the apparent permeability, which governs the mass transmissibility between the fracture and nanopores, can change significantly in low bottom-hole flowing pressure conditions. The apparent permeability also shows high dependency on the matrix pore radius. The numerical results show that the matrix-fracture interaction has an impact on the early time transient behavior, while the Kerogen system is activated slowly due to its diffusive nature.

CHAPTER III

MULTIPHASE DTOF AND ITS USE IN FLOW SIMULATION

In the petroleum industry, multiphase and multicomponent flow simulations are essential for modeling fluid flow in porous media due to the fact that reservoir fluids are comprised of various types of hydrocarbon and non-hydrocarbon components. Subsurface reservoir is often saturated with multiphase fluids (oil, gas, and grand water) because of the presence of aquifer and phase transitions of the hydrocarbon components depending upon the dynamic reservoir conditions. A numerical simulation for solving this highly nonlinear differential equation problem involves linearizing and discretizing the phase or component flow equations in terms of space and time using the solution techniques (i.e. FDM, FEM, and FVM).

This chapter is organized as follows. In **Subchapter 3.1**, general mass balance equations are introduced for multiphase and multicomponent flow modeling. In this research, the fully implicit method (FIM) is used for the multiphase simulations, which means all unknown variables are simultaneously computed by solving a linear system of equations. In **Subchapter 3.2**, the concept of the diffusive time of flight is generalized for multiphase and multicomponent flow problems using the asymptotic theory (‘multiphase DTOF’). On the basis of the multiphase DTOF, the flow domain is transformed from the physical coordinate to the series of 1-D coordinate associated with the coordinate transformation of the multiphase transport equation. In **Subchapter 3.3**, capillary pressure effects are taken into account for the thermodynamic condition of two-

phase vapor-liquid equilibrium (VLE) by modifying a conventional flash calculation procedure. The conventional thermodynamic system is assumed to be macro-scale PVT cell without the consideration for the IFT and capillarity effects. These effects are especially important for simulating a vapor-liquid phase transition in confined nano-scale porous space such as shale, CBM, and tight reservoirs. The proposed formulations are validated through the numerical simulations in **Subchapter 3.4**. Finally, we make conclusions and discussions in **Subchapter 3.5**.

3.1 Introduction to Multiphase Flows

3.1.1 Three-phase Blackoil Equations

We first see the differential equations of general blackoil situation in a porous medium. The reservoir fluid is saturated with three-phase state – oil, gas, and water phases. The oil and gas phases exchange mass between them (i.e. solution gas in oil, vaporized oil in gas), while the water phase does not exchange mass with the other hydrocarbon phases. The flow equation of phase α (w, o, g) is written by the following mass balance form.

$$\frac{\partial}{\partial t}(\phi \rho_\alpha S_\alpha) = -\nabla \bullet (\rho_\alpha \mathbf{u}_\alpha) + \rho_\alpha q_\alpha \tag{3.1}$$

where $\mathbf{u}_\alpha$ is the velocity of phase α and q_α is the production or injection rate of phase α per unit volume per unit time at wellbore condition. The phase velocity is approximated by the Darcy's law with a relative permeability. For simplicity, we neglect the gravity and capillary pressure. Thus, the velocity has a linear relationship to the pressure differential.

$$\mathbf{u}_\alpha = -\mathbf{k}\frac{k_{r\alpha}}{\mu_\alpha}\nabla P \tag{3.2}$$

In a closed domain, the outer boundary is imposed as no-flow impermeable boundary. The mass conservation equation is written as follows.

$$\frac{\partial}{\partial t}(\phi\rho_\alpha S_\alpha) = \nabla \bullet \left(\rho_\alpha \frac{k_{r\alpha}}{\mu_\alpha}\mathbf{k}\nabla P\right) + \rho_\alpha q_\alpha \tag{3.3}$$

For water phase, the continuity of mass involves the mass of free water and the mass of irreducible water.

$$\frac{\partial}{\partial t}(\phi\rho_w S_w) = \nabla \bullet \left(\rho_w \frac{k_{rw}}{\mu_w}\mathbf{k}\nabla P\right) + \rho_w q_w \tag{3.4}$$

Notice that the mass density of water is defined by

$$\rho_w = \frac{\rho_{w,sc}}{B_w} \tag{3.5}$$

where $\rho_{w,sc}$ denotes the surface water density and B_w represents the formation volume factor of the water phase.

For oil phase, the continuity of mass involves the mass of oil in the oil phase and mass of oil vaporized in gas phase (condensate).

$$\begin{aligned}\frac{\partial}{\partial t}\left[\phi\left(\rho_{oo}S_o + R_v\rho_{og}S_g\right)\right] \\ = \nabla \bullet \left[\mathbf{k}\left(\rho_{oo}\frac{k_{ro}}{\mu_o} + R_v\rho_{og}\frac{k_{rg}}{\mu_g}\right)\nabla P\right] + \rho_{oo}q_o + R_v\rho_{og}q_g\end{aligned} \tag{3.6}$$

where R_v represents the vaporized oil gas ratio, ρ_{oo} denotes the mass density of oil in the oil phase, and ρ_{og} denotes the mass density of oil in gas phase.

$$\rho_{oo} = \frac{\rho_{o,sc}}{B_o}, \qquad \rho_{og} = \frac{\rho_{o,sc}}{B_g} \tag{3.7}$$

where $\rho_{o,sc}$ is surface oil density, and B_o and B_g are formation volume factor of oil and gas phase, respectively. For gas phase, the continuity of mass involves the mass of gas in the gas phase and mass of gas dissolved in oil phase (solution gas).

$$\frac{\partial}{\partial t}\left[\phi\left(\rho_{gg}S_g + R_{so}\rho_{go}S_o\right)\right] = \nabla \bullet \left[\mathbf{k}\left(\rho_{gg}\frac{k_{rg}}{\mu_g} + R_{so}\rho_{go}\frac{k_{ro}}{\mu_o}\right)\nabla P\right] + \rho_{gg}q_g + R_{so}\rho_{go}q_o \tag{3.8}$$

where R_{so} represents the solution gas oil ratio, ρ_{gg} denotes the volumetric mass density of gas in free gas phase, and ρ_{go} denotes the volumetric mass density of gas dissolved in oil phase.

$$\rho_{gg} = \frac{\rho_{g,sc}}{B_g}, \qquad \rho_{go} = \frac{\rho_{g,sc}}{B_o} \tag{3.9}$$

where $\rho_{g,sc}$ is the surface gas density.

Dividing **Eqs. (3.4)**, **(3.6)**, and **(3.8)** by **Eqs. (3.5)**, **(3.7)**, and **(3.9)**, respectively, we obtain the mass balance equation on the standard volume basis for the three-phase black oil model. The mass balance equation of water is

$$\frac{\partial}{\partial t}\left(\phi\frac{S_w}{B_w}\right) = \nabla \bullet \left(\mathbf{k}\frac{k_{rw}}{B_w\mu_w}\nabla P\right) + \frac{q_w}{B_w} \tag{3.10}$$

The mass balance equation of oil is

$$\frac{\partial}{\partial t}\left[\phi\left(\frac{S_o}{B_o} + R_v\frac{S_g}{B_g}\right)\right] = \nabla \bullet \left[\mathbf{k}\left(\frac{k_{ro}}{B_o\mu_o} + R_v\frac{k_{rg}}{B_g\mu_g}\right)\nabla P\right] + \frac{q_o}{B_o} + R_v\frac{q_g}{B_g} \tag{3.11}$$

The mass balance equation of gas is

$$\frac{\partial}{\partial t}\left[\phi\left(\frac{S_g}{B_g} + R_{so}\frac{S_o}{B_o}\right)\right] = \nabla \bullet \left[\mathbf{k}\left(\frac{k_{rg}}{B_g\mu_g} + R_{so}\frac{k_{ro}}{B_o\mu_o}\right)\nabla P\right] + \frac{q_g}{B_g} + R_{so}\frac{q_o}{B_o} \tag{3.12}$$

The additional equation is given by the saturation constraint.

$$S_w + S_o + S_g = 1 \tag{3.13}$$

Eqs. (3.10) – **(3.13)** provide the four independent equations to solve the four primary unknowns. In the three-phase transport process, the primary unknowns correspond to the pressure (P) and phase saturations (S_o, S_g, S_w). We solve the linear system of equations of this partial differential equations by linearizing and discretizing into the finite space and time.

3.1.2 Multicomponent Flow Equations

The compositional flow equations consist of $N_c + 1$ equations associated with the transport of the N_c hydrocarbon components and water. The molar mass balance equation of hydrocarbon component i is written as follows.

$$\frac{\partial}{\partial t}\left[\phi\left(x_i \xi_o S_o + y_i \xi_g S_g\right)\right] = \nabla \bullet \left[\mathbf{k}\left(x_i \xi_o \frac{k_{ro}}{\mu_o} + y_i \xi_g \frac{k_{rg}}{\mu_g}\right)\nabla P\right] + x_i \xi_o q_o + y_i \xi_g q_g \tag{3.14}$$

where x_i is the mole fraction of component i in oil phase, y_i is the mole fraction of component i in gas phase, ξ_o and ξ_g are the oil and gas molar density, respectively, and q_o and q_g are the oil and gas volumetric rate at wellbore condition, respectively.

In this research, we assume that the water phase does not exchange mass with the hydrocarbon phases. Thus, the water flow equation is given by the independent mass balance form, which has the same form with the blackoil equation (**Eq. (3.4)**). The

thermodynamic equilibrium of the hydrocarbon phases is given by the fugacity equality of liquid and vapor phases for each component.

$$f_i^L\left(P, T, x_1, \ldots, x_{N_c}\right) = f_i^V\left(P, T, y_1, \ldots, y_{N_c}\right) \tag{3.15}$$

In addition to the differential equations and fugacity equilibrium, there are two mole fraction constraints.

$$\sum_{i=1}^{N_c} x_i = 1, \qquad \sum_{i=1}^{N_c} y_i = 1 \tag{3.16}$$

In the transport process, there is one saturation constraints.

$$S_o + S_g + S_w = 1 \tag{3.17}$$

In multicomponent flow simulation, the fluid phase properties ξ_o, ξ_g, f_i^L, and f_i^V are calculated by the three-parameter Peng-Robinson Equation of State (PR-EOS). The phase viscosities, μ_o and μ_g, are successively calculated using the Lohrenz-Bray-Clark viscosity correlation based on the given phase composition and phase molar density. The procedure of the phase split (flash) calculation is described in **APPENDIX D**. If the reservoir is saturated with three-phase (oil, water, and gas), we solve the following primary unknowns.

$$P, S_o, S_g, S_w, x_1, \ldots, x_{N_c}, y_1, \ldots, y_{N_c} \tag{3.18}$$

Eqs. (3.4), and **(3.14)** – **(3.17)** provide $2N_c + 4$ independent equations for the $2N_c + 4$ unknowns (**Eq. (3.18)**). Notice that the component-based flow equation can be transformed into the phase-based flow equation from by summing up the component equations (**Eq. (3.14)**) for oil and gas phases, separately.

$$\frac{\partial}{\partial t}(\phi\xi_o S_o) = \nabla \bullet \left(\mathbf{k}\xi_o \frac{k_{ro}}{\mu_o}\nabla P\right) + x_i \xi_o q_o \tag{3.19}$$

$$\frac{\partial}{\partial t}(\phi\xi_g S_g) = \nabla \bullet \left(\mathbf{k}\xi_g \frac{k_{rg}}{\mu_g}\nabla P\right) + y_i \xi_g q_g \tag{3.20}$$

If we neglect the hydrocarbon phase interactions (i.e. solution gas, vaporized oil), the compositional flow equations (**Eqs. (3.19)** and **(3.20)**) are equivalent to the blackoil equations (**Eqs. (3.6)** and **(3.8)**). Thus, the compositional flow formulation holds the phase mass balance.

3.2 Development: DTOF-based Simulation for Multiphase Flows

3.2.1 Multiphase Diffusive Time of Flight

We generalize the DTOF from multiphase and multicomponent flow equation based on the asymptotic pressure solution as we showed the single-phase case in the previous chapter. On the basis of **Eq. (3.3)**, the general mass balance equation of phase α can be written as

$$\frac{\partial}{\partial t}(\phi\rho_\alpha S_\alpha) - \nabla(\rho_\alpha \mathbf{k}\lambda_\alpha) \bullet \nabla P - (\rho_\alpha \mathbf{k}\lambda_\alpha) \bullet \nabla^2 P = 0 \tag{3.21}$$

where λ_α is fluid mobility of phase α. The sink or source term is imposed on the inner boundary condition. Not only the blackoil equations, but the compositional equations also holds this phase transport equation by summing up all the component mass balance equation ($i = 1, \dots, N_c$) for phase α as shown in **Eqs. (3.19)** and **(3.20)**. After carrying out the time differentiation, the accumulation term in **Eq. (3.21)** is rearranged as follows.

$$\frac{\partial}{\partial t}(\phi\rho_\alpha S_\alpha) = \left(\frac{\partial \phi}{\partial P}\rho_\alpha + \phi\frac{\partial \rho_\alpha}{\partial P}\right)S_\alpha\frac{\partial P}{\partial t} + \phi\rho_\alpha\frac{\partial S_\alpha}{\partial t}$$
$$= \phi\rho_\alpha S_\alpha(c_r + c_\alpha)\frac{\partial P}{\partial t} + \phi\rho_\alpha\frac{\partial S_\alpha}{\partial t} \quad (3.22)$$

Substituting **Eq. (3.22)** into **Eq. (3.21)**, the transport equation for phase α is

$$\phi S_\alpha(c_r + c_\alpha)\frac{\partial P}{\partial t} + \phi\frac{\partial S_\alpha}{\partial t} - \frac{1}{\rho_\alpha}\nabla(\mathbf{k}\rho_\alpha\lambda_\alpha) \bullet \nabla P - (\mathbf{k}\lambda_\alpha) \bullet \nabla^2 P = 0 \quad (3.23)$$

The global mass balance equation in the domain is obtained by summing up all the phase equations (**Eq. (3.23)**).

$$\phi c_t\frac{\partial P}{\partial t} + \phi\sum\frac{\partial S_\alpha}{\partial t} - \sum\left[\frac{1}{\rho_\alpha}\nabla(\mathbf{k}\rho_\alpha\lambda_\alpha)\right] \bullet \nabla P - \mathbf{k}\lambda_t \bullet \nabla^2 P = 0 \quad (3.24)$$

where c_t is the total compressibility factor.

$$c_t = c_r + \sum S_\alpha c_\alpha \quad (3.25)$$

Notice that the saturation constraint leads

$$\sum\frac{\partial S_\alpha}{\partial t} = 0 \quad (3.26)$$

From **Eqs. (3.24)** - **Eq. (3.26)**, the pressure equation for multiphase flow is obtained as follows.

$$\phi c_t\frac{\partial P}{\partial t} - \sum\left[\frac{1}{\rho_\alpha}\nabla(\mathbf{k}\rho_\alpha\lambda_\alpha)\right] \bullet \nabla P - \mathbf{k}\lambda_t \bullet \nabla^2 P = 0 \quad (3.27)$$

We consider the equation in the frequency domain by applying a Fourier transform.

$$\phi c_t(-i\omega)\tilde{P}(\mathbf{x},\omega) - \sum\left[\frac{1}{\rho_\alpha}\nabla(\mathbf{k}\rho_\alpha\lambda_\alpha)\right] \bullet \nabla\tilde{P}(\boldsymbol{x},\omega) - \mathbf{k}\lambda_t \bullet \nabla^2\tilde{P}(\mathbf{x},\omega) = 0 \quad (3.28)$$

The leading-order solution of the pressure propagation equation is obtained using the same way as single phase flow case. As we see in the previous chapter, the asymptotic

pressure solution is expressed by **Eq. (2.14)**. However, we will generally be interested in only the leading-order solution of the infinite series of the asymptotic solution. Inserting **Eqs. (2.15)** – **(2.17)** into **Eq. (3.28)** and arranging the equation in terms of powers of $\sqrt{-i\omega}$, we obtain the following quadratic equation.

$$(\phi c_t - \mathbf{k}\lambda_t \nabla^2\tau)A_0\left(\sqrt{-i\omega}\right)^2 + \left\{\mathbf{k}\lambda_t \nabla^2\tau A_0 + 2\mathbf{k}\lambda_t \nabla\tau\nabla A_0 + \sum\left[\frac{1}{\rho_\alpha}\nabla(\mathbf{k}\rho_\alpha\lambda_\alpha)\right]\nabla\tau A_0\right\}\sqrt{-i\omega} - \left\{\sum\left[\frac{1}{\rho_\alpha}\nabla(\mathbf{k}\rho_\alpha\lambda_\alpha)\right]\nabla A_0 + \mathbf{k}\lambda_t\nabla^2 A_0\right\} = 0 \tag{3.29}$$

The equation from is very similar to that of single phase flow case as written in **Eq. (2.18)**. Consequently, the first term in **Eq. (3.29)** leads the equation for the front of pressure propagation in multiphase porous medium.

$$\mathbf{k}\lambda_t\nabla^2\tau - \phi c_t = 0 \tag{3.30}$$

Alternatively, we can rewrite **Eq. (3.30)** in the Eikonal equation form.

$$|\nabla\tau|\sqrt{\frac{\mathbf{k}\lambda_t}{\phi c_t}} = 1 \tag{3.31}$$

As a result, we can define the multiphase diffusivity.

$$\alpha_{\text{diff}} = \frac{\mathbf{k}\lambda_t}{\phi c_t} \tag{3.32}$$

In a single-phase state, λ_t simply represents the inverse of the fluid viscosity, thus **Eq. (3.32)** is equivalent to the single-phase diffusivity (**Eq. (2.21)**). In a multiphase state, the total mobility λ_t and total compressibility c_t are obtained by summing up all the saturated phase properties (i.e. oil, water, gas). In a compositional simulation, the

phase properties (i.e. density, viscosity, compressibility) are calculated using the phase split calculation (VLE flash). Therefore, the total mobility is obtained by

$$\lambda_t = \sum \frac{k_{r\alpha}}{\mu_\alpha} \tag{3.33}$$

In **Eq. (3.25)**, the isothermal compressibility of phase α is calculated by

$$c_\alpha = \frac{1}{\rho_\alpha}\frac{\partial \rho_\alpha}{\partial p} \tag{3.34}$$

The hydrocarbon phase density in **Eq. (3.34)** is computed by the flash calculation as well. However, in the blackoil simulation, the condensing and vaporizing effects in the oil and gas phases (i.e. solution gas in oil, vaporized oil in gas) must be explicitly taken into account for the calculation of density and total mobility. In such case, the oil and gas densities are calculated by accounting such phase interaction effects as follows.

$$\rho_o = \frac{\rho_{o,sc} + \rho_{g,sc} R_{so}}{B_o} \tag{3.35}$$

$$\rho_g = \frac{\rho_{g,sc} + \rho_{o,sc} R_v}{B_g} \tag{3.36}$$

In addition, the total mobility is defined by

$$\lambda_t = \sum \frac{k_{r\alpha}}{\mu_\alpha} + R_{so}\frac{k_{ro}}{\mu_o} + R_v \frac{k_{rg}}{\mu_g} \tag{3.37}$$

On the basis of **Eq. (3.32)**, we can also define the phase (partial) diffusivity by decomposing the total mobility into the sum of phase mobility.

$$\alpha_{\text{diff}} = \frac{\mathbf{k}\lambda_t}{\phi c_t} = \sum_{j=o,w,g} \frac{\mathbf{k}\lambda_j}{\phi c_t} = \sum_{j=o,w,g} \alpha_j \tag{3.38}$$

where α_j is the diffusivity of phase j.

$$\alpha_j = \frac{\mathbf{k}\lambda_j}{\phi c_t} \tag{3.39}$$

where λ_j is the mobility of phase j. In **Eq. (3.38)**, the total diffusivity is identical to the propagation speed of the pressure front in multiphase domain. Hence, the phase diffusivity is regarded as a partial speed that the pressure front propagates through the phase with.

For example, in a two-phase oil and water case, the total diffusivity is obtained by the sum of the oil and water diffusivities.

$$\alpha_{\text{diff}} = \frac{\mathbf{k}\lambda_o}{\phi c_t} + \frac{\mathbf{k}\lambda_w}{\phi c_t} = \alpha_{\text{oil}} + \alpha_{\text{water}} \tag{3.40}$$

Fig. 3.1 shows the diffusivities in two-phase oil and water domain. The initial water saturation (**(a)**) is heterogeneously distributed, while the other geological parameters (i.e. porosity, permeability) are constant over the domain. The total diffusivity (**(b)**) is given by summing the oil diffusivity (**(c)**) with the water diffusivity (**(d)**).

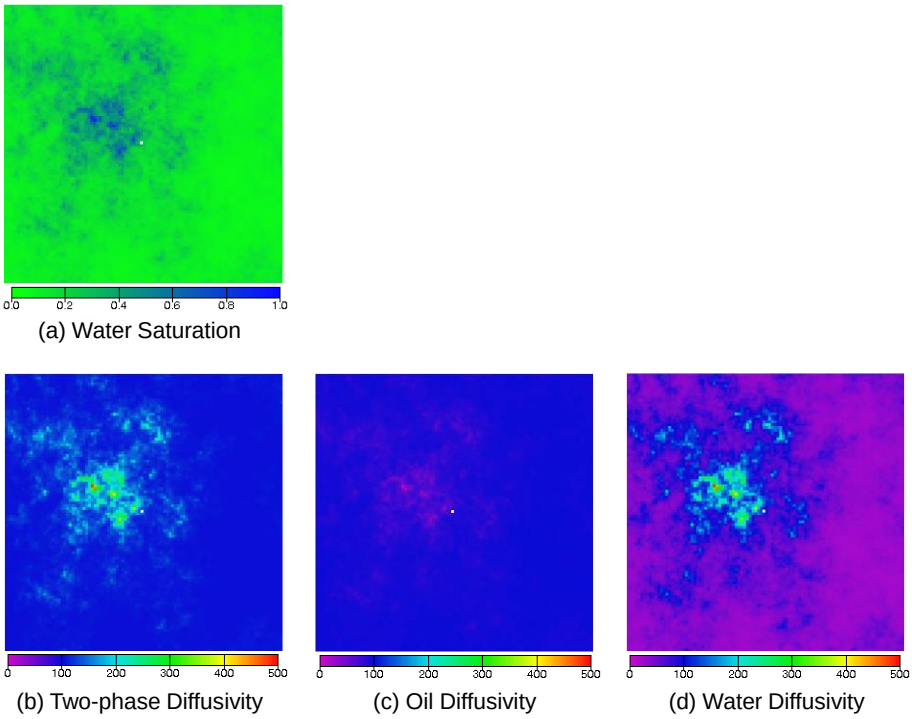

Fig. 3.1 – Diffusivity calculation in two-phase system. (a) Water saturation, (b) Total diffusivity, (c) Oil diffusivity, and (d) Water diffusivity.

Substituting **Eq. (3.40)** into **Eq. (3.31)** yields the following Eikonal equation.

$$|\nabla\tau|\sqrt{\alpha_{\text{oil}} + \alpha_{\text{water}}} = 1 \tag{3.41}$$

Notice that the phase diffusivity cannot be used for the DTOF calculation in the FMM, because the Eikonal equation form in **Eq. (3.41)** is held only when the total diffusivity is used for the DTOF calculation. However, the phase diffusivity is a good measure to know the influence of the saturation effect to the pressure propagation in multiphase domain. **Fig. 3.2** shows the DTOF map calculated using the same condition as **Fig. 3.1**. The two-phase DTOF (**(a)**) is obtained by the FMM calculation with the two-phase diffusivity. The oil-phase DTOF (**(b)**) is obtained by temporary neglecting the water-

phase diffusivity and by simply using the oil-phase diffusivity in the FMM. The water-phase DTOF (**(c)**) is also obtained in the same way. As **Eq. (3.41)** suggests, the DTOF is identical to the time when the pressure 'front' propagates through the multiphase domain with a propagation speed of total diffusivity. Therefore, **(b)** and **(c)** are obviously not true solutions.

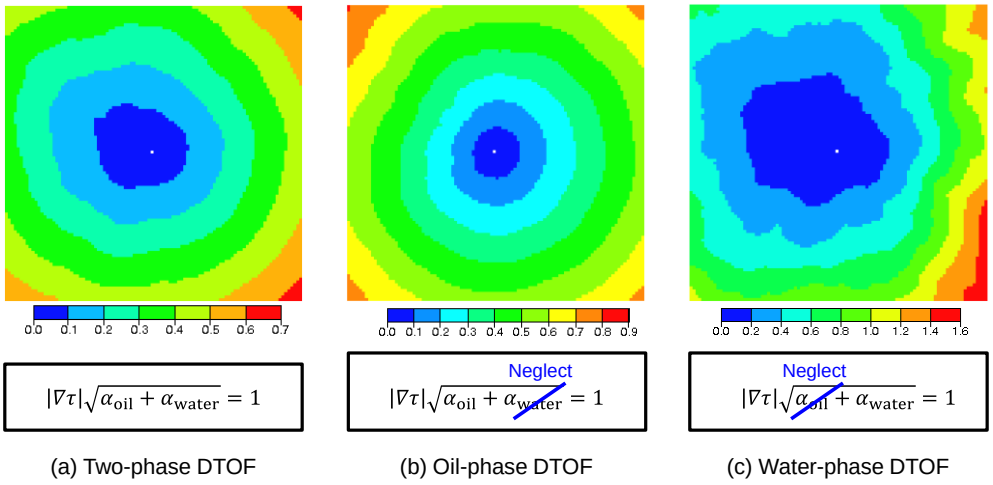

Fig. 3.2 – DTOFs in two-phase system calculated based on the (a) Two-phase diffusivity, (b) Oil-phase diffusivity, and (c) Water-phase diffusivity.

3.2.2 Coordinate Transformation

In a single-phase flow, the diffusivity equation can be transformed into the τ-coordinate using **Eq. (2.38)**. For a multiphase flow, the same coordinate transformation is applied on the multiphase flow equation using multiphase DTOF. Rearranging the Eikonal equation (**Eq. (3.30)**), absolute permeability is expressed with the relation to the DTOF.

$$\mathbf{k} = \frac{1}{|\nabla\tau|^2}\left(\frac{\phi c_t}{\lambda_t}\right)_{\text{init}} \tag{3.42}$$

Substituting **Eqs. (2.24)** and **(3.42)** into the Darcy's equation (**Eq. (3.2)**), the phase velocity is defined along the τ-coordinate under the assumption that the pressure gradient direction aligns with the τ gradient direction.

$$\mathbf{u} = -\left(\frac{\phi c_t}{\lambda_t}\right)_{\text{init}} \frac{k_{r\alpha}}{\mu_\alpha}\frac{1}{|\nabla\tau|}\frac{\partial P}{\partial \tau} \tag{3.43}$$

We take a volumetric integral of the mass balance equation of phase α (**Eq. (3.3)**) over the domain Ω.

$$\int_\Omega \frac{\partial(\phi\rho_\alpha S_\alpha)}{\partial t} dV = -\int_\Omega \nabla \bullet (\rho_\alpha \mathbf{u}_\alpha) dV \tag{3.44}$$

On the basis of **Eq. (2.27)**, the flux term (RHS) in **Eq. (3.44)** is transformed to the surface integral by applying a divergence theorem.

$$\int_\Omega \nabla \bullet (\rho_\alpha \mathbf{u}_\alpha) dV = \int_{d\Omega} (\rho_\alpha \mathbf{u}_\alpha) \bullet \vec{\mathbf{n}}\, dA = \int_{d\Omega(\tau)} (\rho_\alpha \mathbf{u}_\alpha) \bullet \frac{\nabla\tau}{|\nabla\tau|}\, dA \tag{3.45}$$

The accumulation term (LHS) in **Eq. (3.40)** is also transformed to surface integral by substituting **Eq. (2.27)**.

$$\int_\Omega \frac{\partial(\phi\rho_\alpha S_\alpha)}{\partial t} dV = \nabla\tau \int_{d\Omega(\tau)} \frac{\partial(\phi\rho_\alpha S_\alpha)}{\partial t}\frac{1}{|\nabla\tau|} dA \tag{3.46}$$

Inserting **Eqs. (3.45)** and **(3.46)** into **Eq. (3.44)**, we obtain the surface integral form of the mass balance equation of phase α.

$$\nabla\tau \int_{d\Omega(\tau)} \frac{\partial(\phi\rho_\alpha S_\alpha)}{\partial t}\frac{1}{|\nabla\tau|} dA = -\int_{d\Omega(\tau)} (\rho_\alpha \mathbf{u}_\alpha) \bullet \frac{\nabla\tau}{|\nabla\tau|}\, dA \tag{3.47}$$

Substituting the DTOF-based velocity equation (**Eq. (3.43)**) into **Eq. (3.47)** yields

$$\int_{d\Omega(\tau)} \frac{\partial(\phi\rho_\alpha S_\alpha)}{\partial t}\frac{1}{|\nabla\tau|}dA = \frac{1}{\nabla\tau}\left[\int_{d\Omega(\tau)}\left(\frac{\phi c_t}{\lambda_t}\right)_{\text{init}}\rho_\alpha\frac{k_{r\alpha}}{\mu_\alpha}\frac{\partial P}{\partial\tau}\bullet\frac{1}{|\nabla\tau|}dA\right] \tag{3.48}$$

Let $\Delta\tau \to 0$. Rearranging **Eq. (3.48)** yields

$$\int_{d\Omega(\tau)} \frac{\partial\left(M_\phi\rho_\alpha S_\alpha\right)}{\partial t}\frac{\phi_{\text{init}}}{|\nabla\tau|}dA = \frac{\partial}{\partial\tau}\left[\int_{d\Omega(\tau)}\left(\frac{c_t}{\lambda_t}\right)_{\text{init}}\rho_\alpha\frac{k_{r\alpha}}{\mu_\alpha}\frac{\partial P}{\partial\tau}\bullet\frac{\phi_{init}}{|\nabla\tau|}dA\right] \tag{3.49}$$

where M_ϕ is the exponential rock compressibility function. Based on the definition of the w-function (**Eq. (2.35)**), we rearrange **Eq. (3.49)** as

$$w(\tau)\int_{d\Omega(\tau)} \frac{\partial\left(M_\phi\rho_\alpha S_\alpha\right)}{\partial t}dA = \frac{\partial}{\partial\tau}\left[w(\tau)\int_{d\Omega(\tau)}\left(\frac{c_t}{\lambda_t}\right)_{\text{init}}\rho_\alpha\frac{k_{r\alpha}}{\mu_\alpha}\frac{\partial P}{\partial\tau}dA\right] \tag{3.50}$$

In **Eq. (3.50)**, the pressure P and phase saturation S_α are the location- and time-dependent variables. Now, we assume that P and S_α are the function of τ and t (i.e. the pressure gradient and saturation change align with the τ gradient). Therefore, we can take the terms outside the integral. The DTOF-based transport equation can be written as follows.

$$w(\tau)\frac{\partial\left(M_\phi\rho_\alpha S_\alpha\right)}{\partial t} = \frac{\partial}{\partial\tau}\left[w(\tau)\left(\frac{c_t}{\lambda_t}\right)_{\text{init}}\rho_\alpha\frac{k_{r\alpha}}{\mu_\alpha}\frac{\partial P}{\partial\tau}\right] \tag{3.51}$$

Comparing **Eq. (3.51)** with **Eq. (3.1)**, we can define the coordinate transformation for the multiphase flow equation as follows.

$$\nabla\bullet(\rho_\alpha\mathbf{u}_\alpha) \equiv -\frac{\phi_{\text{init}}}{w(\tau)}\frac{\partial}{\partial\tau}\left[w(\tau)\left(\frac{c_t}{\lambda_t}\right)_{\text{init}}\rho_\alpha\lambda_\alpha\frac{\partial P}{\partial\tau}\right] \tag{3.52}$$

The transformed flux term is very similar to the single-phase formulation (**Eq. (2.38)**). Suppose $\lambda_t = 1/\mu$ (single-phase) and $\lambda_\alpha = 1/\mu$, then **Eq. (3.52)** is equivalent to **Eq. (2.38)**. However, there is an additional constraint associated with the coordinate

transformation of the multiphase equation that the direction of the phase saturation change aligns with the τ gradient direction as well as the pressure gradient direction ($P = P(\tau, t)$ and $S_\alpha = S_\alpha(\tau, t)$).

3.2.3 DTOF-based Blackoil Model

The blackoil simulation contains up to three mass balance equations for each grid. The general equation form is described in **Eqs. (3.10)** – **(3.12)**. Thus, we apply the coordinate transformation (**Eq. (3.52)**) of the phase transport equations for the DTOF-based simulation. For water phase, the DTOF-based flow equation is written as

$$\frac{\partial}{\partial t}\left(\frac{\phi S_w}{B_w}\right) = \frac{\phi_{\text{init}}}{w(\tau)}\frac{\partial}{\partial \tau}\left[w(\tau)\left(\frac{c_t}{\lambda_t}\right)_{\text{init}}\frac{k_{rw}}{B_w\mu_w}\frac{\partial P}{\partial \tau}\right] + \frac{q_w}{B_w} \tag{3.53}$$

For oil phase, the DTOF-based flow equation is given by

$$\begin{aligned}&\frac{\partial}{\partial t}\left[\phi\left(\frac{S_o}{B_o} + R_v\frac{S_g}{B_g}\right)\right] \\ &\qquad = \frac{\phi_{\text{init}}}{w(\tau)}\frac{\partial}{\partial \tau}\left[w(\tau)\left(\frac{c_t}{\lambda_t}\right)_{\text{init}}\left(\frac{k_{ro}}{B_o\mu_o} + R_v\frac{k_{rg}}{B_g\mu_g}\right)\frac{\partial P}{\partial \tau}\right] + \frac{q_o}{B_o} + R_v\frac{q_g}{B_g}\end{aligned} \tag{3.54}$$

For gas phase, the DTOF-based flow equation is written as

$$\begin{aligned}&\frac{\partial}{\partial t}\left[\phi\left(\frac{S_g}{B_g} + R_{so}\frac{S_o}{B_o}\right)\right] \\ &\qquad = \frac{\phi_{\text{init}}}{w(\tau)}\frac{\partial}{\partial \tau}\left[w(\tau)\left(\frac{c_t}{\lambda_t}\right)_{\text{init}}\left(\frac{k_{rg}}{B_g\mu_g} + R_{so}\frac{k_{ro}}{B_o\mu_o}\right)\frac{\partial P}{\partial \tau}\right] + \frac{q_g}{B_g} + R_{so}\frac{q_o}{B_o}\end{aligned} \tag{3.55}$$

In the DTOF-based simulation, the mass balances equations of **Eqs. (3.53)** – **(3.55)** are discretized on 1-D coordinate using the finite difference scheme as illustrated in **Fig. 2.2**. From **Eqs. (3.53)** – **(3.55)**, the finite difference equation is written as follows.

The 1-D finite difference of the water flow equation is

$$T_{w,i-1/2}^{n+1}P_{i-1}^{n+1} - \left(T_{w,i-1/2}^{n+1} + T_{w,i+1/2}^{n+1}\right)P_i^{n+1} + T_{w,i+1/2}^{n+1}P_{i+1}^{n+1} = \frac{w_i\Delta\tau_i}{\Delta t^{n+1}}\left[M_{\phi,i}^{n+1}\left(\frac{S_w}{B_w}\right)_i^{n+1} - M_{\phi,i}^{n}\left(\frac{S_w}{B_w}\right)_i^{n}\right] - q_{ws}^{n+1} \tag{3.56}$$

The 1-D finite difference of the oil flow equation is

$$T_{o,i-1/2}^{n+1}P_{i-1}^{n+1} - \left(T_{o,i-1/2}^{n+1} + T_{o,i+1/2}^{n+1}\right)P_i^{n+1} + T_{o,i+1/2}^{n+1}P_{i+1}^{n+1} = \frac{w_i\Delta\tau_i}{\Delta t^{n+1}}\left[M_{\phi,i}^{n+1}\left(\frac{S_o}{B_o} + R_v\frac{S_g}{B_g}\right)_i^{n+1} - M_{\phi,i}^{n}\left(\frac{S_o}{B_o} + R_v\frac{S_g}{B_g}\right)_i^{n}\right] - q_{os}^{n+1} \tag{3.57}$$

The 1-D finite difference of the gas flow equation is

$$T_{g,i-1/2}^{n+1}P_{i-1}^{n+1} - \left(T_{g,i-1/2}^{n+1} + T_{g,i+1/2}^{n+1}\right)P_i^{n+1} + T_{g,i+1/2}^{n+1}P_{i+1}^{n+1} = \frac{w_i\Delta\tau_i}{\Delta t^{n+1}}\left[M_{\phi,i}^{n+1}\left(\frac{S_g}{B_g} + R_{so}\frac{S_o}{B_o}\right)_i^{n+1} - M_{\phi,i}^{n}\left(\frac{S_g}{B_g} + R_{so}\frac{S_o}{B_o}\right)_i^{n}\right] - q_{gs}^{n+1} \tag{3.58}$$

where i denotes the grid block number on 1-D coordinate, $T_{\alpha,i\pm1/2}^{n+1}$ represents the transmissibility of phase α of the grid i at the time $n+1$, M_ϕ is the exponential rock compressibility function (**Eq. (2.34)**), and $q_{\alpha s}^{n+1}$ denotes the surface volume production rate of phase α at the time $n+1$ which is imposed only on the first grid ($i = 1$). In **Eqs. (3.56)** – **(3.58)**, the transmissibility is defined using the phase mobility.

$$T_{\alpha,i\pm1/2}^{n+1} = \frac{w_{i\pm1/2}}{\Delta\tau_{i\pm1/2}}\left(\frac{c_t}{\lambda_t}\right)_{\text{init},i\pm1/2}\lambda_{\alpha,up}^{n+1} \tag{3.59}$$

where $\lambda_{\alpha,up}^{n+1}$ is the mobility of phase α. For each phase, the mobility is written as

$$\lambda_{w,up}^{n+1} = \left(\frac{k_{rw}}{B_w\mu_w}\right)_{up}^{n+1} \tag{3.60}$$

$$\lambda_{o,up}^{n+1} = \left(\frac{k_{ro}}{B_o\mu_o} + R_v\frac{k_{rg}}{B_g\mu_g}\right)_{up}^{n+1} \tag{3.61}$$

$$\lambda_{g,up}^{n+1} = \left(\frac{k_{rg}}{B_g \mu_g} + R_{so}\frac{k_{ro}}{B_o \mu_o}\right)_{up}^{n+1} \tag{3.62}$$

Notice that the phase mobility is determined by the up-winding scheme. In **Eq. (3.56)** – **(3.58)**, the surface production rate of phase α, $q_{\alpha s}^{n+1}$ is given by

$$q_{\alpha s}^{n+1} = \frac{w_1 \Delta\tau_1}{\phi_{\text{init}}}\frac{q_\alpha^{n+1}}{B_\alpha^{n+1}} \tag{3.63}$$

where q_α^{n+1} is the production rate of phase α per unit volume per unit time and the constant, $w_1\Delta\tau_1/\phi_{\text{init}}$ is the 'bulk' volume of the grid block $i = 1$. We rearrange **Eq. (3.63)** using the velocity equation (**Eq. (3.43)**).

$$q_{\alpha s}^{n+1} = \frac{w_1 \Delta\tau_1}{\phi_{\text{init}}}\left[\frac{1}{\Delta\tau_1}\left(\frac{\phi c_t}{\lambda_t}\right)_{\text{init},1}\lambda_{\alpha,1}^{n+1}\left(\frac{P_1^{n+1} - P_{wf}^{n+1}}{\tau_1 - \tau_{\text{well}}}\right)\right] \tag{3.64}$$

Rearranging **Eq. (3.64)**, the surface production rate of phase α is obtained as follows.

$$q_{\alpha s}^{n+1} = w_1\left(\frac{c_t}{\lambda_t}\right)_{\text{init},1}\lambda_{\alpha,1}^{n+1}\left(\frac{P_1^{n+1} - P_{wf}^{n+1}}{\tau_1 - \tau_{\text{well}}}\right) \tag{3.65}$$

In the DTOF-based blackoil simulation, **Eqs. (3.56)** – **(3.58)** are used for solving the three unknown variables ($\{P, S_w, S_g\}$ or $\{P, S_w, R_s\}$) for each grid. The simulation flow chart is illustrated in **Fig. 3.3**. The Jacobian construction and numerical calculation procedure are described in **APPENDIX C**.

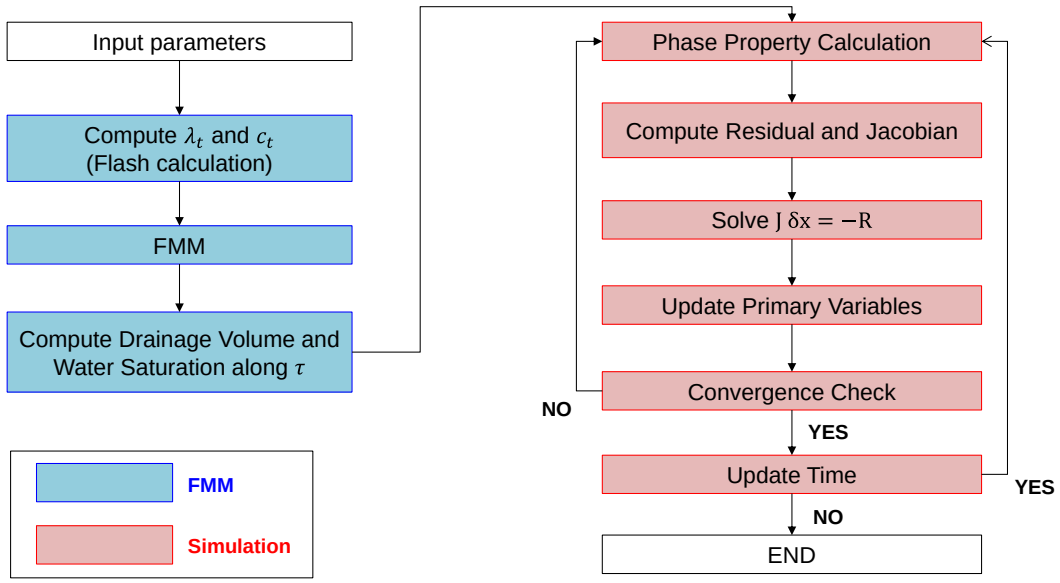

Fig. 3.3 – Flowchart of the multiphase DTOF-based simulation.

3.2.4 Dual-Porosity Blackoil Modeling based on DTOF

The blackoil dual-porosity equations are formulated by a direct extension of the single-phase dual-porosity modeling. In this approach, the fracture and matrix are treated as separate continua throughout the reservoir. As we discussed in the previous chapter, we holds some assumptions and constraints for the dual-porosity modeling on its DTOF formulation (i.e. constant matrix properties). The general mass balance equation is written as follows. The water mass balance in the fracture system is

$$\frac{\partial}{\partial t}\left(\frac{\phi_f S_{wf}}{B_w}\right) = \nabla \bullet \left(\mathbf{k}_f \lambda_w \nabla P_f\right) - \Gamma_w + \frac{q_w}{B_w} \tag{3.66}$$

where S_{wf} is the water saturation in the fracture system. The oil mass balance in the fracture system is

$$\frac{\partial}{\partial t}\left[\phi_f \left(\frac{S_{of}}{B_o} + R_v \frac{S_{gf}}{B_g}\right)\right] = \nabla \bullet \left(\mathbf{k}_f \lambda_o \nabla P_f\right) - \Gamma_o + \left(\frac{q_o}{B_o} + R_v \frac{q_g}{B_g}\right) \tag{3.67}$$

where S_{of} and S_{gf} are the oil and gas saturations in the fracture system, respectively. The gas mass balance in the fracture system is

$$\frac{\partial}{\partial t}\left[\phi_f\left(\frac{S_{gf}}{B_g}+R_{so}\frac{S_{of}}{B_o}\right)\right]=\nabla\bullet\left(\mathbf{k}_f\lambda_g\nabla P_f\right)-\Gamma_g+\left(\frac{q_g}{B_g}+R_{so}\frac{q_o}{B_o}\right) \tag{3.68}$$

In **Eqs. (3.66)** – **(3.68)**, the matrix-fracture transfer function of phase α is written as

$$\Gamma_\alpha=\sigma k_m\lambda_{\alpha,up}\left(P_f-P_m\right) \tag{3.69}$$

where σ denotes the shape factor, k_m represents the matrix permeability, and $\lambda_{\alpha,up}$ is the phase mobility defined by **Eqs. (3.60)** – **(3.62)**. The mobility is determined by the up-winding scheme. The water mass balance in the matrix system is

$$\frac{\partial}{\partial t}\left(\frac{\phi_m S_{wm}}{B_w}\right)=\Gamma_w \tag{3.70}$$

The oil mass balance in the matrix system is

$$\frac{\partial}{\partial t}\left[\phi_m\left(\frac{S_{om}}{B_o}+R_v\frac{S_{gm}}{B_g}\right)\right]=\Gamma_o \tag{3.71}$$

The gas mass balance in the matrix system is

$$\frac{\partial}{\partial t}\left[\phi_m\left(\frac{S_{gm}}{B_g}+R_{so}\frac{S_{om}}{B_o}\right)\right]=\Gamma_g \tag{3.72}$$

In the dual-porosity model, there is no mass transfer between the matrix blocks. It means that the matrix blocks are linked only through the corresponding fracture blocks and the fracture blocks provides the main flow path to the well production. As we see in the single-phase dual-porosity model, the matrix equations remain the same form even in the 1-D τ-coordinate system while the matrix properties (ϕ_m, k_m, and σ) are assumed to be a constant parameter. The coordinate transformation is applied for the fracture system

equations (**Eqs. (3.66)** – **(3.68)**) using **Eq. (3.52)**. The transformed 1-D equations are written as follows. The DTOF-based water mass balance in the fracture system is

$$\frac{\partial}{\partial t}\left(\frac{\phi_f S_{wf}}{B_w}\right) = \frac{\phi_{f,\text{init}}}{w(\tau)}\frac{\partial}{\partial \tau}\left[w(\tau)\left(\frac{c_t}{\lambda_t}\right)_{\text{init}}\lambda_w\frac{\partial P_f}{\partial \tau}\right] - \Gamma_w + \frac{q_w}{B_w} \tag{3.73}$$

The DTOF-based oil mass balance in the fracture system is

$$\begin{aligned}\frac{\partial}{\partial t}\left[\phi_f\left(\frac{S_{of}}{B_o} + R_v\frac{S_{gf}}{B_g}\right)\right] \\ = \frac{\phi_{f,\text{init}}}{w(\tau)}\frac{\partial}{\partial \tau}\left[w(\tau)\left(\frac{c_t}{\lambda_t}\right)_{\text{init}}\lambda_o\frac{\partial P_f}{\partial \tau}\right] - \Gamma_o + \frac{q_o}{B_o} + R_v\frac{q_g}{B_g}\end{aligned} \tag{3.74}$$

The DTOF-based gas mass balance in the fracture system is

$$\begin{aligned}\frac{\partial}{\partial t}\left[\phi_f\left(\frac{S_{gf}}{B_g} + R_{so}\frac{S_{of}}{B_o}\right)\right] \\ = \frac{\phi_{f,\text{init}}}{w(\tau)}\frac{\partial}{\partial \tau}\left[w(\tau)\left(\frac{c_t}{\lambda_t}\right)_{\text{init}}\lambda_g\frac{\partial P_f}{\partial \tau}\right] - \Gamma_g + \frac{q_g}{B_g} + R_{so}\frac{q_o}{B_o}\end{aligned} \tag{3.75}$$

In **Eqs. (3.73)** – **(3.75)**, $w(\tau)/\phi_{f,\text{init}}$ represents the drainage 'bulk' volume v_i in the fracture system, that is directly computed in the FMM. The finite difference equations of the fracture system are written as follows.

The 1-D finite difference of the water equation in the fracture system is

$$\begin{aligned}T_{wf,i-1/2}^{n+1}P_{f,i-1}^{n+1} - \left(T_{wf,i-1/2}^{n+1} + T_{wf,i+1/2}^{n+1}\right)P_{f,i}^{n+1} + T_{wf,i+1/2}^{n+1}P_{f,i+1}^{n+1} \\ = \frac{w_i\Delta\tau_i}{\Delta t^{n+1}}\left[M_{\phi,i}^{n+1}\left(\frac{S_{wf}}{B_w}\right)_i^{n+1} - M_{\phi,i}^{n}\left(\frac{S_{wf}}{B_w}\right)_i^{n}\right] \\ + v_i\Delta\tau_i\sigma k_m\lambda_{w,up}^{n+1}\left(P_{f,i}^{n+1} - P_{m,i}^{n+1}\right) - q_{ws}^{n+1}\end{aligned} \tag{3.76}$$

The 1-D finite difference of the oil equation in the fracture system is

$$T_{of,i-1/2}^{n+1}P_{f,i-1}^{n+1} - \left(T_{of,i-1/2}^{n+1} + T_{of,i+1/2}^{n+1}\right)P_{f,i}^{n+1} + T_{of,i+1/2}^{n+1}P_{f,i+1}^{n+1}$$

$$= \frac{w_i\Delta\tau_i}{\Delta t^{n+1}}\left[M_{\phi,i}^{n+1}\left(\frac{S_{of}}{B_o} + R_v\frac{S_{gf}}{B_g}\right)_i^{n+1} - M_{\phi,i}^{n}\left(\frac{S_{of}}{B_o} + R_v\frac{S_{gf}}{B_g}\right)_i^{n}\right] \tag{3.77}$$

$$+v_i\Delta\tau_i\sigma k_m\lambda_{o,up}^{n+1}\left(P_{f,i}^{n+1} - P_{m,i}^{n+1}\right) - q_{os}^{n+1}$$

The 1-D finite difference of the gas equation in the fracture system is

$$T_{gf,i-1/2}^{n+1}P_{f,i-1}^{n+1} - \left(T_{gf,i-1/2}^{n+1} + T_{gf,i+1/2}^{n+1}\right)P_{f,i}^{n+1} + T_{gf,i+1/2}^{n+1}P_{f,i+1}^{n+1}$$

$$= \frac{w_i\Delta\tau_i}{\Delta t^{n+1}}\left[M_{\phi,i}^{n+1}\left(\frac{S_{gf}}{B_g} + R_{so}\frac{S_{of}}{B_o}\right)_i^{n+1} - M_{\phi,i}^{n}\left(\frac{S_{gf}}{B_g} + R_{so}\frac{S_{of}}{B_o}\right)_i^{n}\right] \tag{3.78}$$

$$+v_i\Delta\tau_i\sigma k_m\lambda_{g,up}^{n+1}\left(P_{f,i}^{n+1} - P_{m,i}^{n+1}\right) - q_{gs}^{n+1}$$

In **Eqs. (3.76) – (3.78)**, the phase production rate $q_{\alpha s}^{n+1}$ is calculated by **Eq. (3.65)**. The finite difference equations of the matrix system are written as follows. The 1-D finite difference of the water equation in the matrix system is

$$\frac{1}{\Delta t^{n+1}}\left[\phi_{m,i}^{n+1}\left(\frac{S_{wm}}{B_w}\right)_i^{n+1} - \phi_{m,i}^{n}\left(\frac{S_{wm}}{B_w}\right)_i^{n}\right] = \sigma k_m\lambda_{w,up}^{n+1}\left(P_{f,i}^{n+1} - P_{m,i}^{n+1}\right) \tag{3.79}$$

The 1-D finite difference of the oil equation in the fracture system is

$$\frac{1}{\Delta t^{n+1}}\left[\phi_{m,i}^{n+1}\left(\frac{S_{om}}{B_o} + R_v\frac{S_{gm}}{B_g}\right)_i^{n+1} - \phi_{m,i}^{n}\left(\frac{S_{om}}{B_o} + R_v\frac{S_{gm}}{B_g}\right)_i^{n}\right] \tag{3.80}$$

$$= \sigma k_m\lambda_{o,up}^{n+1}\left(P_{f,i}^{n+1} - P_{m,i}^{n+1}\right)$$

The 1-D finite difference of the gas equation in the fracture system is

$$\frac{1}{\Delta t^{n+1}}\left[\phi_{m,i}^{n+1}\left(\frac{S_{gm}}{B_g} + R_{so}\frac{S_{om}}{B_o}\right)_i^{n+1} - \phi_{m,i}^{n}\left(\frac{S_{gm}}{B_g} + R_{so}\frac{S_{om}}{B_o}\right)_i^{n}\right] \tag{3.81}$$

$$= \sigma k_m\lambda_{g,up}^{n+1}\left(P_{f,i}^{n+1} - P_{m,i}^{n+1}\right)$$

In the DTOF-based blackoil dual-porosity simulation, the above six finite difference equations (**Eqs. (3.76)** – **(3.81)**) are used for solving the corresponding six unknown variables ($\{P_f, S_{wf}, S_{gf}\}$ or $\{P_f, S_{wf}, R_{sf}\}$ in the fracture system, and $\{P_m, S_{wm}, S_{gm}\}$ or $\{P_m, S_{wm}, R_{sm}\}$ in the matrix system) for each τ grid. In addition, the following conditions must be satisfied during the simulation.

(1) The DTOF is characterized by the fracture heterogeneity using the FMM.

(2) At the initial state, the saturation distribution in the matrix system is uniform.

(3) During the 1-D numerical simulation, the matrix pressure and saturations are solved along the τ-coordinate.

(4) The matrix geometric parameters (k_m, ϕ_m, and σ) are constant.

The numerical procedure and derivative calculations for constructing the Jacobian is described in **APPENDIX C**.

3.2.5 DTOF-based Compositional Model

The compositional simulation is comprised of the sets of the $N_c + 1$ mass balance equations and N_c fugacity equilibrium relations (total $2N_c + 1$ primary equations) and the corresponding $2N_c + 1$ primary variables (i.e. pressure, saturations, and oil and gas compositions) for each grid. The general mass balance equations are described in **Eqs. (3.4)** and **(3.14)**. We apply the coordinate transformation (**Eq. (3.52)**) on the component transport equations. For hydrocarbon component j, the DTOF-based mass balance equation is written as

$$\frac{\partial}{\partial t}\left[\phi\left(x_j\xi_o S_o + y_j\xi_g S_g\right)\right] = \frac{\phi_{\text{init}}}{w(\tau)}\frac{\partial}{\partial \tau}\left[w(\tau)\left(\frac{c_t}{\lambda_t}\right)_{init}\left(x_j\xi_o\frac{k_{ro}}{\mu_o} + y_j\xi_g\frac{k_{rg}}{\mu_g}\right)\frac{\partial P}{\partial \tau}\right] + \tilde{q}_j \tag{3.82}$$

where $\tilde{q}_j^{n+1}$ is the molar production rate of component j per unit volume per unit time. Notice that the mass balance of water is given by the same equation as blackoil formulation (**Eq. (3.53)**). The finite difference equation of **Eq. (3.82)** is obtained by

$$T_{j,i-1/2}^{n+1}P_{i-1}^{n+1} - \left(T_{j,i-1/2}^{n+1} + T_{j,i+1/2}^{n+1}\right)P_i^{n+1} + T_{j,i+1/2}^{n+1}P_{i+1}^{n+1} = \frac{w_i\Delta\tau_i}{\Delta t^{n+1}}\left[M_{\phi,i}^{n+1}\left(x_j\xi_o S_o + y_j\xi_g S_g\right)_i^{n+1} - M_{\phi,i}^{n}\left(x_j\xi_o S_o + y_j\xi_g S_g\right)_i^{n}\right] - \tilde{q}_{wj}^{n+1} \tag{3.83}$$

where $T_{j,i\pm1/2}^{n+1}$ denotes the transmissibility of component j, M_j denotes the molar mass of component j, and $\tilde{q}_{wj}$ is the molar production rate of component j on the well which is imposed only on the first grid ($i = 1$). The molar mass of component j, M_j is defined by

$$M_j = x_j\xi_o S_o + y_j\xi_g S_g \tag{3.84}$$

Therefore, the overall component of the component j is obtained by the molar based calculation.

$$z_j = \frac{M_j}{\sum M_j} = \frac{x_j\xi_o S_o + y_j\xi_g S_g}{\xi_o S_o + \xi_g S_g} \tag{3.85}$$

The transmissibility of component j is defined by

$$T_{j,i\pm1/2}^{n+1} = \frac{w_{i\pm1/2}}{\Delta\tau_{i\pm1/2}}\left(\frac{c_t}{\lambda_t}\right)_{\text{init},i\pm1/2}\left(x_j\xi_o\frac{k_{ro}}{\mu_o} + y_j\xi_g\frac{k_{rg}}{\mu_g}\right)_{up}^{n+1} \tag{3.86}$$

In **Eq. (3.83)**, the molar production rate of component j is given by

$$\tilde{q}_{wj}^{n+1} = \frac{w_1 \Delta\tau_1}{\phi_{\text{init}}} \tilde{q}_j^{n+1} \tag{3.87}$$

where $\tilde{q}_j^{n+1}$ is given by the velocity equation (**Eq. (3.39)**).

$$\tilde{q}_{wj}^{n+1} = \frac{w_1 \Delta\tau_1}{\phi_{\text{init}}} \left[\frac{1}{\Delta\tau_1} \left(\frac{\phi c_t}{\lambda_t} \right)_{\text{init},1} \left(x_j \xi_o \frac{k_{ro}}{\mu_o} + y_j \xi_g \frac{k_{rg}}{\mu_g} \right)_1^{n+1} \left(\frac{P_1^{n+1} - P_{wf}^{n+1}}{\tau_1 - \tau_{\text{well}}} \right) \right] \tag{3.88}$$

Rearranging **Eq. (3.88)**, the molar production rate of component j is

$$\tilde{q}_{wj}^{n+1} = w_1 \left(\frac{c_t}{\lambda_t} \right)_{\text{init},1} \left(x_j \xi_o \frac{k_{ro}}{\mu_o} + y_j \xi_g \frac{k_{rg}}{\mu_g} \right)_1^{n+1} \left(\frac{P_1^{n+1} - P_{wf}^{n+1}}{\tau_1 - \tau_{\text{well}}} \right) \tag{3.89}$$

In addition, the molar production rate of phase α is obtained by summing up all the component production rate (**Eq. (3.89)**) for each phase, separately.

$$\tilde{q}_{wj}^{n+1} = w_1 \left(\frac{c_t}{\lambda_t} \right)_{\text{init},1} \left(\xi_\alpha \frac{k_{r\alpha}}{\mu_\alpha} \right)_1^{n+1} \left(\frac{P_1^{n+1} - P_{wf}^{n+1}}{\tau_1 - \tau_{\text{well}}} \right) \tag{3.90}$$

Notice that **Eqs. (3.89)** and **(3.90)** are the molar production rate at the wellbore. On the wellbore condition, the oil phase will contain the free oil and solution gas as well as the gas phase contained in the free gas and vaporized oil. The surface oil and gas volumetric rates are obtained by flashing the wellbore phase compositions ($\{x_i\}$ and $\{y_i\}$) into the surface condition (14.6 psia and 60 °F) as illustrated in **Fig. 3.4**.

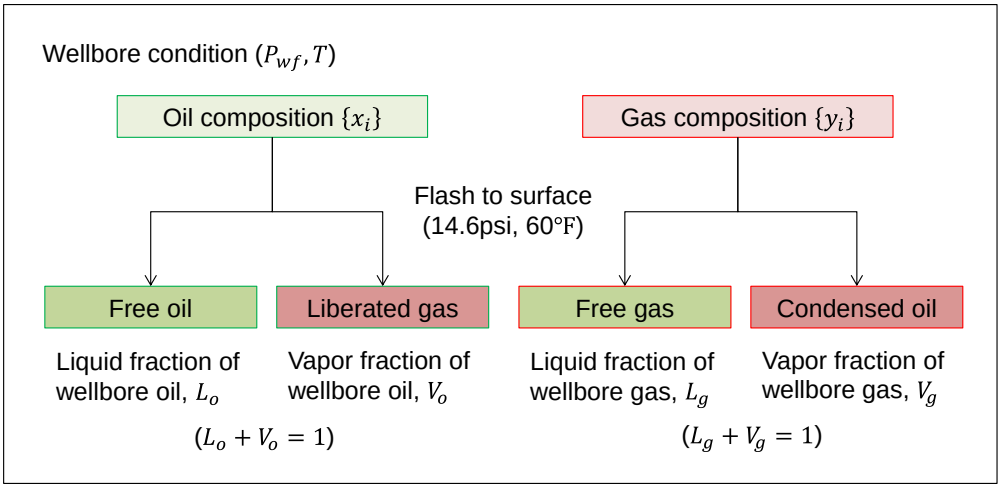

Fig. 3.4 – Calculation of the surface condition using the flash.

Suppose $\tilde{q}_o$ and $\tilde{q}_g$ are the molar production rate of oil and gas phase at the wellbore, respectively. Flashing the wellbore oil to surface condition, we obtain the liquid and vapor molar fractions of the wellbore oil, L_o and V_o, and the liquid and vapor molar densities at the surface condition, $\xi_{oo,sc}$ and $\xi_{go,sc}$. At the surface conditions, the wellbore oil becomes free oil and liberated gas with the molar fraction of L_o and V_o, respectively. The standard volume oil (free oil) production rate from the wellbore oil is

$$q_{oo,sc} = \frac{L_o}{\xi_{oo,sc}} \tilde{q}_o \tag{3.91}$$

The standard volume gas (liberated gas) production rate from the wellbore oil is

$$q_{go,sc} = \frac{V_o}{\xi_{go,sc}} \tilde{q}_o \tag{3.92}$$

In contrast, flashing the wellbore gas to surface condition, we obtain the liquid and vapor phase fractions of the wellbore gas, L_g and V_g, and the liquid and vapor molar densities at the surface condition, $\xi_{og,sc}$ and $\xi_{gg,sc}$. At the surface condition, the wellbore gas

becomes the free gas and condensate with the molar fraction of V_g and L_g, respectively. The standard volume gas (free gas) production rate from the wellbore gas is

$$q_{gg,sc} = \frac{V_g}{\xi_{gg,sc}} \tilde{q}_g \tag{3.93}$$

The standard volume oil (condensate) production rate from the wellbore gas is

$$q_{og,sc} = \frac{L_g}{\xi_{og,sc}} \tilde{q}_g \tag{3.94}$$

Therefore, the standard volume production rate for oil and gas phases at surface condition, q_{os} and q_{gs} are calculated by

$$q_{os} = q_{oo,sc} + q_{og,sc} \tag{3.95}$$

$$q_{gs} = q_{go,sc} + q_{gg,sc} \tag{3.96}$$

In addition, the mass production rate of the component j, $q_{j,mass}$ is given by

$$q_{j,mass} = M_{w,j}\left(x_j \tilde{q}_o + y_j \tilde{q}_g\right) \tag{3.97}$$

where x_j and y_j are the phase compositions at the wellbore condition, and $M_{w,j}$ is the molecular weight of the component j. The surface volume rate of the component j is

$$q_{j,sc} = \frac{x_j}{\xi_{o,sc}} \tilde{q}_o + \frac{y_j}{\xi_{g,sc}} \tilde{q}_g \tag{3.98}$$

where $\xi_{o,sc}$ and $\xi_{g,sc}$ are obtained by flashing the overall component $\{z_i\}$ (**Eq. (3.85)**) from the wellbore condition to the surface condition.

In the three-phase condition, the primary equations solved are **Eqs. (3.15)**, **(3.56)** and **(3.83)** for each grid, that is total $2N_c + 1$ equations. If the oil or gas saturation is zero or water does not exist at the grid block, the number of primary equations changes

(i.e. if the grid is saturated with oil and water, we only calculate **Eqs. (3.56)** and **(3.83)** to solve for pressure, water saturation, and oil compositions). The number of phases in each grid block must be identified prior to constructing a residual vector and Jacobian matrix as summarized in **Table 3.1**. The numerical simulation procedure and derivative calculations for constructing the Jacobian are described in **APPENDIX E**.

Table 3.1 – Primary equations and variables in compositional model

No.	Phases	Number	Primary Equations	Primary Variables
1	Oil	N_c	Eq. (3.83)	$P, x_2, \dots, x_{N_c}$
2	Gas	N_c	Eq. (3.83)	$P, y_2, \dots, y_{N_c}$
3	Oil / Water	$N_c + 1$	Eqs. (3.56) & (3.83)	$P, S_w, x_2, \dots, x_{N_c}$
4	Gas / Water	$N_c + 1$	Eqs. (3.56) & (3.83)	$P, S_w, y_2, \dots, y_{N_c}$
5	Oil / Gas	N_c	Eqs. (3.56) & (3.83)	$P, S_g, x_2, \dots, x_{N_c}$ $y_2, \dots, y_{N_c}$
6	Oil / Gas / Water	$2N_c + 1$	Eqs. (3.15), (3.56), & (3.83)	$P, S_w, S_g, x_2, \dots, x_{N_c}$ $y_2, \dots, y_{N_c}$

3.3 Approach: Phase Behavior in Confined Environments

3.3.1 Capillarity Effects on Thermodynamic Equilibrium

The conventional vapor-liquid equilibrium calculation is usually carried out with the assumption that the vapor-liquid interface is flat with the contact angle of 90° and the capillary pressure has no influence on the static phase equilibrium. This assumption is valid for the phase behavior on the macro-scale porous space (i.e. PVT cell). But, in micro to nano-scale porous media (i.e. shale), the vapor-liquid interface has a non-flat

curvature, which causes the vapor and liquid phases to have a different pressure due to the capillarity effect. **Fig. 3.5** illustrates the schematics of the vapor-liquid equilibrium in the closed system.

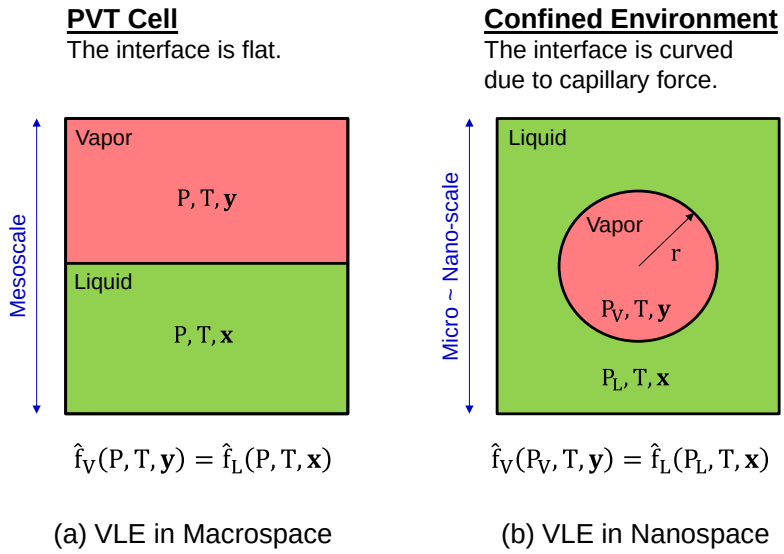

Fig. 3.5 – Illustrations of the phase equilibrium in (a) PVT cell and (b) confined system.

Shapiro et al. (2001) investigated the capillary pressure effect on the phase behavior. They showed a theoretical thermodynamic relation of the vapor-liquid two phase state in small-scale pore space and the flash calculation procedure with accounting for the capillary pressure effect. Qi et al. (2007) investigated an interfacial tension (IFT) effect on the condensate dropout in the low-permeability gas condensate reservoir. They concluded that, under the capillary pressure effects, the retrograde process is enhanced and the condensate dropout increases during the pressure depletion. Nojabaei et al.

(2013) observed the produced gas oil ratio on the Bakken shale oil wells, which is inconsistent with the prediction result of the Bakken oil sample. They reported that the operational flowing bottom-hole pressures in the Bakken shale wells were far below the predicted bubble-point pressure for a long time period, and they have not observed any increase of the produced GOR. They also showed the shift of the oil properties (density, viscosity, saturation pressures) of the Bakken shale oil sample by incorporating the capillary pressure on the VLE flash calculation, and concluded that, if the bubble-point pressure is suppressed due to the capillary pressure, the reservoir pressure can exceed the bubble-point pressure.

In a small-scale confined system (i.e. nanometers), the multiphase thermodynamic equilibrium is achieved by letting each phase having a different pressure. For the vapor-liquid equilibrium, the fugacity relation is expressed by

$$f_i^L\left(P^L, T, x_1, \dots, x_{N_c}\right) = f_i^V\left(P^V, T, y_1, \dots, y_{N_c}\right) \tag{3.99}$$

where P^L and P^V are the liquid and vapor phase pressure, respectively. The differential pressure between the liquid and vapor phases is defined by the capillary pressure. In this study, the capillary pressure is given on the basis of the Young-Laplace equation.

$$P^V - P^L = P_{cgo} = \frac{2\sigma}{r} \tag{3.100}$$

where P_{cgo} is the capillary pressure between oil and gas phases and r is the pore radius. In **Eq. (3.100)**, we assume that the shape of the vapor-liquid interface is a sphere ($\theta = 0°$), thus, we have that $\cos\theta = 1$.

At the dew-point condition, we have

$$y_i = z_i \quad \text{for} \quad i = 1, \dots, N_c \tag{3.101}$$

whereas at the bubble-point condition, we have

$$x_i = z_i \quad \text{for} \quad i = 1, \dots, N_c \tag{3.102}$$

The surface tension σ between the oil and gas phases is calculated by the Macleod-Sugden correlation (Whitson 1989).

$$\sigma = \left[\sum_{i=1}^{N_c} \varphi_i \left(\xi_o x_i - \xi_g y_i\right)\right]^4 \tag{3.103}$$

where φ_i is the parachor of component i. Considering **Eq. (3.99)**, the fugacity of component i is calculated as follows.

$$f_i^L = x_i P^L \phi_i^L \tag{3.104}$$

$$f_i^V = y_i P^V \phi_i^V \tag{3.105}$$

Once f_i^L, f_i^V, P^L, and P^V are obtained at current iteration step, the K-values are updated by the successive substitution method (SSM).

$$K_i^{new} = \frac{\phi_i^L}{\phi_i^V} = \frac{f_i^L}{f_i^V}\frac{y_i}{x_i}\frac{P^V}{P^L} = \frac{f_i^L}{f_i^V}\frac{P^V}{P^L}K_i^{old} \tag{3.106}$$

where K_i^{new} is the new K-values for next iteration step and K_i^{old} is the old K-values at previous iteration step. The procedure of the modified VLE flash is illustrated in **Fig. 3.6**. In this procedure, the calculation is repeated until the fugacity and capillary pressure satisfy the convergence criteria. The tolerance is 10^{-6} (psia) for the maximum updates in the capillary pressure. Notice that the initial guess of P_c is given by $P_c = 0$.

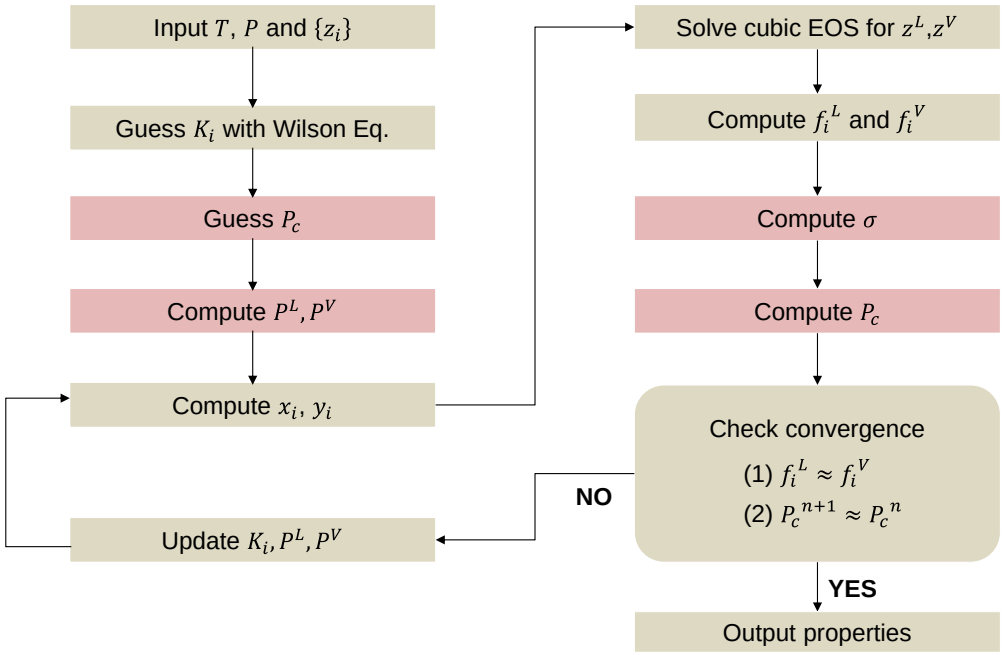

Fig. 3.6 – Modified VLE flash procedure with oil-gas capillary pressure.

3.3.2 Shift of Saturation Pressure in Shale Reservoirs

We present two examples for the modified VLE flash calculation using actual shale reservoir samples – the Bakken shale oil sample and the shale gas reservoir sample in west Texas. **Fig. 3.7** shows the change of the capillary pressure under the influences of the pore radius and reservoir pressure. After the iterative flash calculation, the surface tension and capillary pressure are successively calculated using the Young-Laplace equation (**Eq. (3.100)**) and Macleod-Sugden correlation (**Eq. (3.103)**), respectively. In smaller pore radius, the capillary pressure becomes several thousand psi. In the Bakken sample, 1 nm pore has about 2,500 psia of the capillary pressure at the reservoir pressure of 1,000 psia. In the gas sample, 1 nm pore has approximately 1,500 psia of the capillary pressure at the reservoir pressure of 1,000 psia.

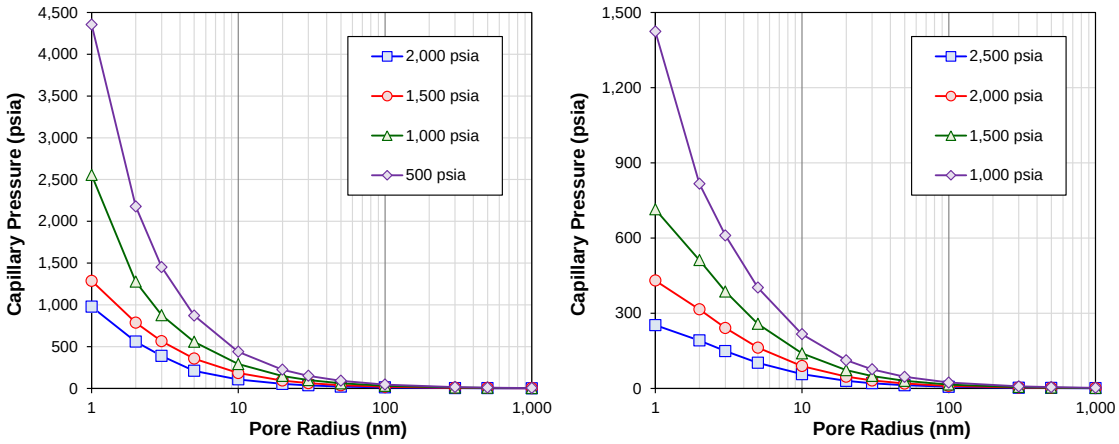

(a) Bakken Oil Sample at 150°F

(b) Shale Gas Sample at 200°F

Fig. 3.7 – Capillary pressures of the (a) Bakken oil shale sample and (b) Shale gas sample.

The saturation pressures are computed by the negative flash procedure. At the bubble-point pressure, the liquid phase holds **Eq. (3.102)**, while the vapor phase holds **Eq. (3.101)** at the dew-point pressure. The saturation pressures are iteratively computed using the standard Newton-Raphson method. The procedure is described in **APPENDIX D**. **Fig. 3.8** shows the shift of the bubble-point pressure and gas saturation profile of the Bakken shale oil sample as a function of the pore size and reservoir temperature. In **Fig. 3.8 (a)**, we see that the bubble-point pressure is decreased as the pore size becomes smaller in all the simulated temperature conditions (150 – 300 °F). In the pore size range from 1,000 nm (1 μm) to 50 nm (0.05 μm), the bubble-point pressures are nearly constant because the capillary pressure effects are negligible in such large pores. Below the pore size of 50 nm, the bubble-point pressures are gradually decreased as the capillary pressure rapidly increases. The bubble-point pressure at the pore radius of 1 nm is approximately 1,000 – 1,500 psi lower than that in the micrometer pore. The declining

trend of this bubble-point pressure is consistent with the capillary pressure change as shown in **Fig. 3.7 (a)**. Because the capillary pressure becomes fairly large below the pore size of 10 nm, the bubble-point pressure is considerably suppressed in such pore size conditions. **Fig. 3.8 (b)** shows the simulation results of the liberation profile of the solution gas during the constant composition pressure depletion (CCE) at the temperature of 250 °F. For each specified pore size condition, the gas begins to liberate at each bubble-point pressure. The solution gas liberates first in the largest pore (100 nm), and then the PVT cell is saturated with 100% gas first in the smallest pore (2 nm).

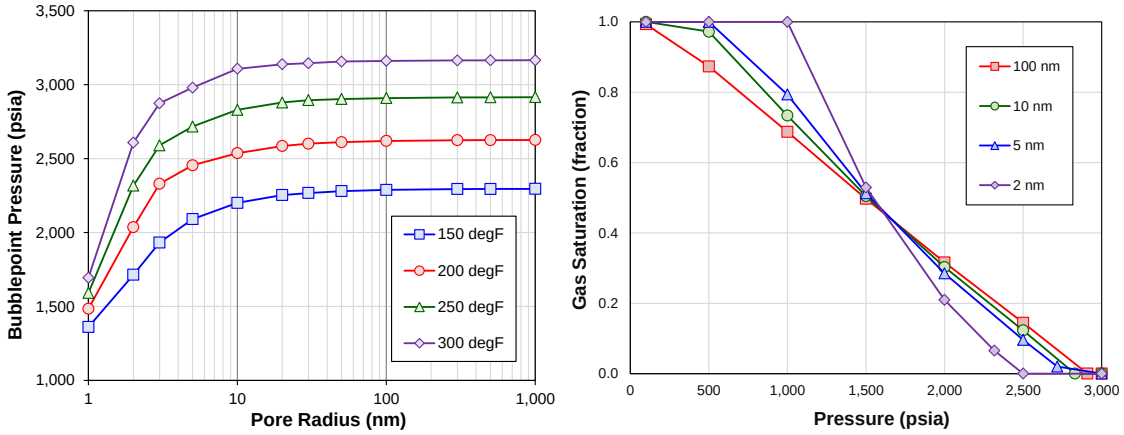

(a) Shift of Bubble-point Pressures (b) Gas Saturation at 250°F

Fig. 3.8 – Simulation results of the Bakken oil sample at constant composition. (a) Shift of bubble-point pressure and (b) Gas liberation processes in confined system.

Fig. 3.9 shows the shift of the dew-point pressure and liquid saturation of the shale gas sample as a function of the pore size and reservoir temperature. In contrast to the bubble-point system, we see that the dew-point pressure is increased as the pore size becomes smaller. In the pore size range from 1,000 nm to 100 nm, the dew-point pressures are

nearly constant because the capillary pressure is negligible. Below the pore size of 100 nm, the dew-point pressures gradually increase as the capillary pressure rapidly increases. The dew-point pressure in the pore radius of 1 nm is approximately 100 – 500 psi higher than that in the micrometer pore. Thus, the capillary pressure makes the saturation pressure increase in the dew-point system (gas reservoirs). **Fig. 3.9 (b)** shows the simulation results of the condensate dropout during the constant composition pressure depletion (CCE) at the reservoir temperature of 260 °F. For each pore size condition, the condensate begins to drop from the gas phase at each dew-point pressure. The condensate drops first in the smallest pore (2 nm), and then the PVT cell is saturated with 100 % gas first in the smallest pore again.

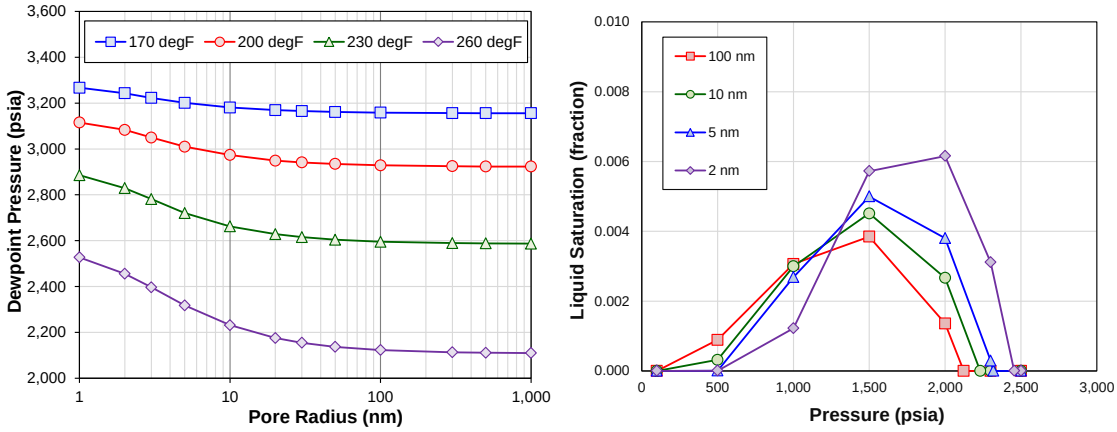

(a) Shift of Dew-point Pressures

(b) Liquid Saturation at 260°F

Fig. 3.9 – Simulation results of the shale gas sample at constant composition. (a) Shift of dew-point pressure and (b) Liquid dropout in confined system.

The shift of the confined vapor-liquid phase behavior is completely different between the bubble-point system (shale oil reservoirs) and dew-point system (shale gas reservoirs) on the modified flash calculation. In general perspective, the saturation pressure is reached first in the larger pores in the bubble-point system, whereas this achieved first in the smaller pores in the dew-point system.

3.4 Results and Discussions

The blackoil and compositional simulation results are presented using 1-D, 2-D, and 3-D models. The validations include a three-phase dual-porosity blackoil model and confined shale oil compositional model with the modified phase behavior calculation as well. The simulation results are compared with the results from a commercial simulator.

3.4.1 Two-phase Oil-Water Model (1-D Heterogeneous)

For the multiphase DTOF-based simulation, we start the model validation from the 1-D two-phase oil and water example. The model consists of the 100 x 1 x 1 grids with a production well placed at the left edge of the model. The porosity and permeability are constant (1mD and 0.1 %). The initial water saturation is heterogeneously distributed on the Cartesian model as illustrated in **Fig. 3.10**.

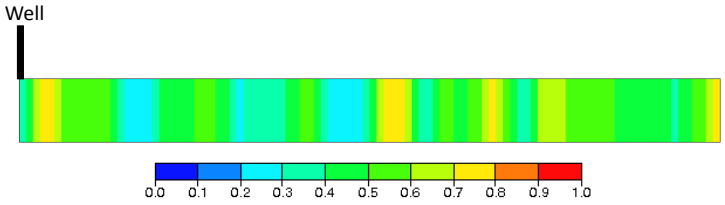

Fig. 3.10 – 1-D water saturation distribution at initial state.

The concept of the coordinate transformation is illustrated in **Fig. 3.11**. The Cartesian 100 grids are transformed into the 1-D 100 grids along the τ-coordinate. The minimum tau (τ_1) corresponds to the first τ-contour neighboring the wellbore, and the maximum tau (τ_{100}) is identical to the last τ-contour touching the outer boundary. The τ grids are uniformly discretized in this problem.

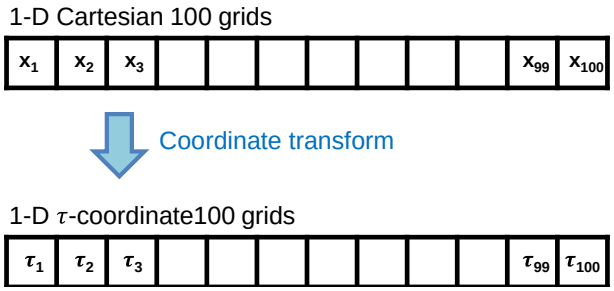

Fig. 3.11 – Transformation of the 1-D uniform grid from the (a) Cartesian to (b) DTOF.

First, we perform the FMM to calculate the drainage 'pore' volumes and the corresponding 'water' volumes along the τ-coordinate. In multiphase flow problems, the diffusivity (propagation speed) is given by **Eq. (3.32)** for each node. As shown in **Fig.3.12**, the evolution of the drainage 'pore' volume (red line) has a nearly linear trend due to the uniform porosity distribution, while the growth of the drainage 'water' volume (blue line) deviates from the linear line due to the heterogeneous water saturation distribution. Notice that the both drainage 'pore' and 'water' volumes are monotonically increasing property propagated from the wellbore along the τ-coordinate.

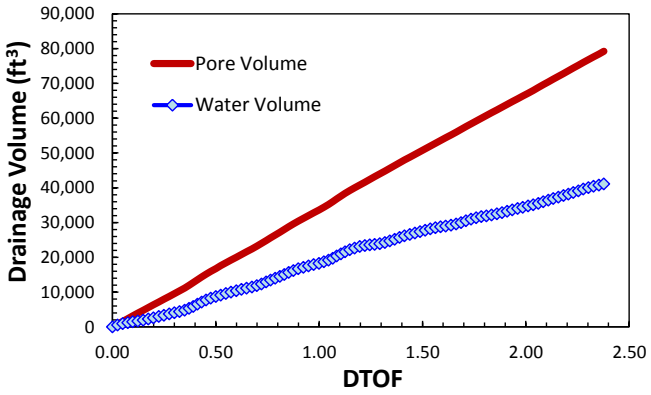

Fig. 3.12 – Drainage 'pore' and 'water' volumes along τ-cordinate.

Once the drainage 'pore' and 'water' volumes are obtained, the water saturations can be estimated along the τ-coordinate using a first-order backward difference.

$$S_{w,i} = \frac{V_{w,i} - V_{w,i-1}}{V_{p,i} - V_{p,i-1}} \tag{3.107}$$

where i denotes the number of the τ-contour, and $V_{w,i}$ and $V_{p,i}$ represent the 'water' and 'pore' volumes of the contour i, respectively. The drainage 'pore' volume $V_{p,i}$ is calculated by summating the 'pore' volume inside the contour i.

$$V_{p,i} = \sum_j \left(V_{b,j}\phi_j\right) \tag{3.108}$$

where the grid j has smaller DTOF than the grid i. The corresponding 'water' volume $V_{p,i}$ is calculated by

$$V_{w,i} = \sum_j \left(V_{b,j}\phi_j S_{w,j}\right) \tag{3.109}$$

On the basis of **Eq. (3.106)**, the initial water saturation is can be calculated along the τ-coordinate as shown in **Fig. 3.13**. This transformed 1-D water saturation is used as initial water saturation in the DTOF-based simulation.

Finally, the simulation results are shown in **Fig. 3.14**. The production rates are calculated under the constant bottom-hole pressure constraints (3,500 psia).

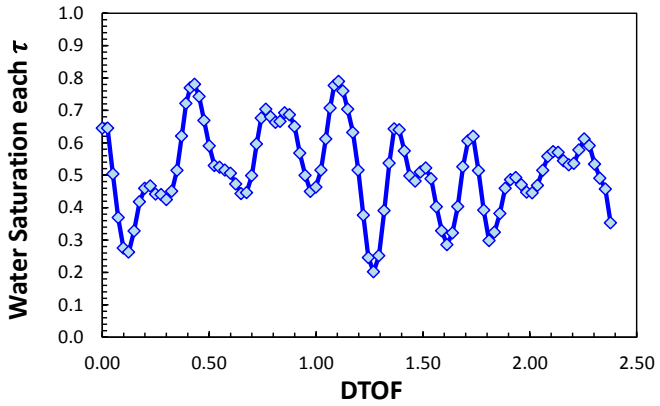

Fig. 3.13 – 1-D water saturation distribution along the τ-coordinate.

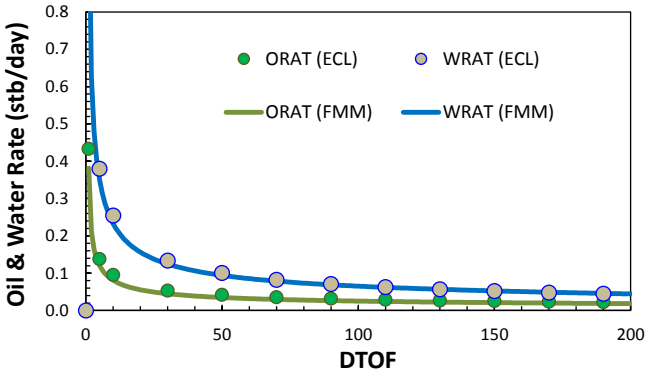

Fig. 3.14 – Simulation results. The results are compared with the ECLIPSE.

The pressure and water saturation distributions are also compared with the commercial simulator at the initial and final time-step (200 days) as shown in **Fig. 3.15**. Because this is the primary depletion problem with single production well, the saturation change is much smaller than the change of the reservoir pressure.

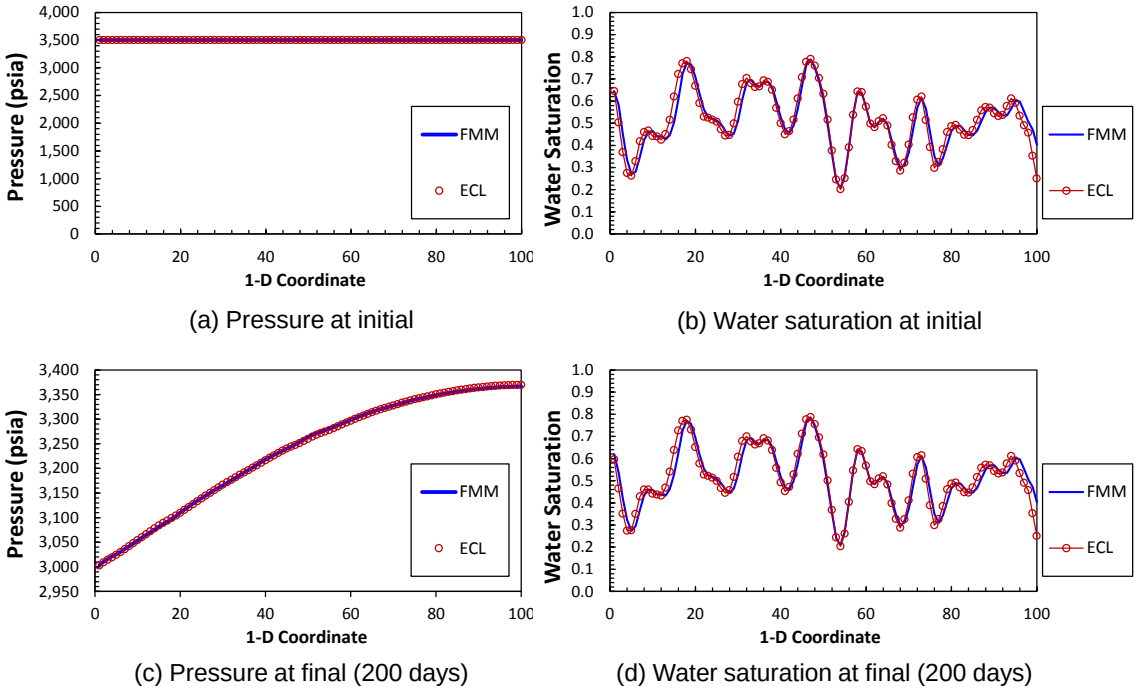

(a) Pressure at initial

(b) Water saturation at initial

(c) Pressure at final (200 days)

(d) Water saturation at final (200 days)

Fig. 3.15 – Pressure and saturation comparisons on the 1-D grids.

3.4.2 Three-phase Blackoil Model (2-D Heterogeneous)

Next, we show the heterogeneous 2-D model saturated with three-phase water, oil, and gas. The permeability is heterogeneously distributed as shown in **Fig. 3.16 (a)**. The production well is vertically placed on the center of the model. The calculated DTOF map is shown in **Fig. 3.16 (b)**.

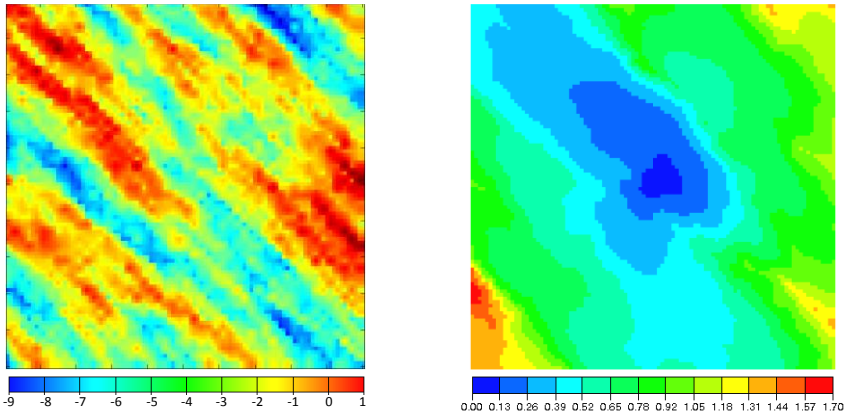

(a) Log permeability distribution **(b) Three-phase DTOF**

Fig. 3.16 – Permeability and DTOF maps in the heterogeneous 2-D model.

The other reservoir parameters are summarized in **Table 3.2**. In addition to the free oil and gas, there is solution gas in oil phase as well. The oil, water, and gas saturations are uniformly distributed at initial condition.

Table 3.2 – Reservoir parameters (2-D heterogeneous model)		
Grid Number	[-]	100 x 100 x 1
Grid Size	[ft]	100 x 100 x 50
Porosity	[fraction]	0.2
Initial Water Saturation	[fraction]	0.3
Initial Gas Saturation	[fraction]	0.2
Initial Solution GOR	[Mscf/stb]	1.713
Initial Pressure	[psia]	5,000
Bottom-hole Pressure	[psia]	3,000

The drainage volumes are calculated after the FMM as shown in **Fig. 3.17 (a)**. Because the reservoir is saturated with oil, gas, and water, the phase drainage volumes

are calculated in order to obtain the water and gas saturations along the 1-D τ-coodinate based on the same way as the previous example. As illustrated in **Fig. 3.17 (b)**, the resulting transformed water and gas saturation distributions are uniform along the τ-coordinate due to the constant initial saturation input. The production rates are predicted under the constant bottom-hole pressure (3,000 psi) as shown in **Fig. 3.18**.

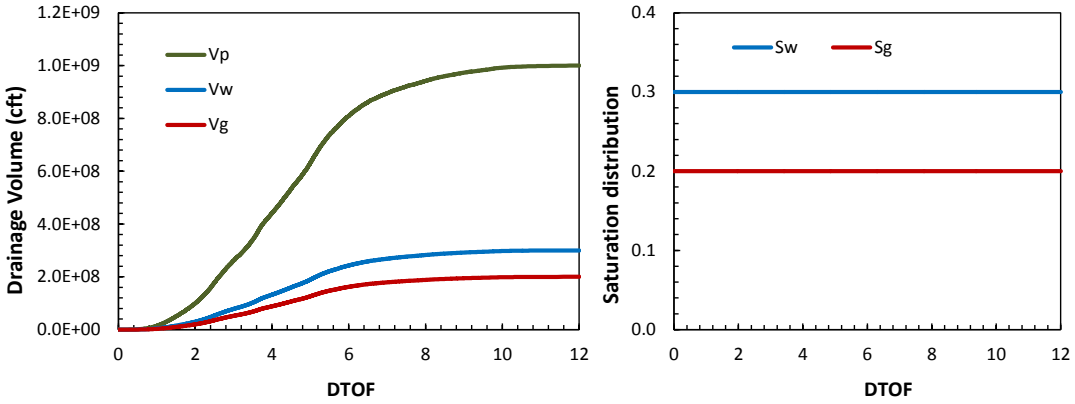

(a) Drainage volumes (pore, water, and gas) (b) Saturation distribution along τ

Fig. 3.17 – Drainage volume and saturation distribution along the τ-coordinate.

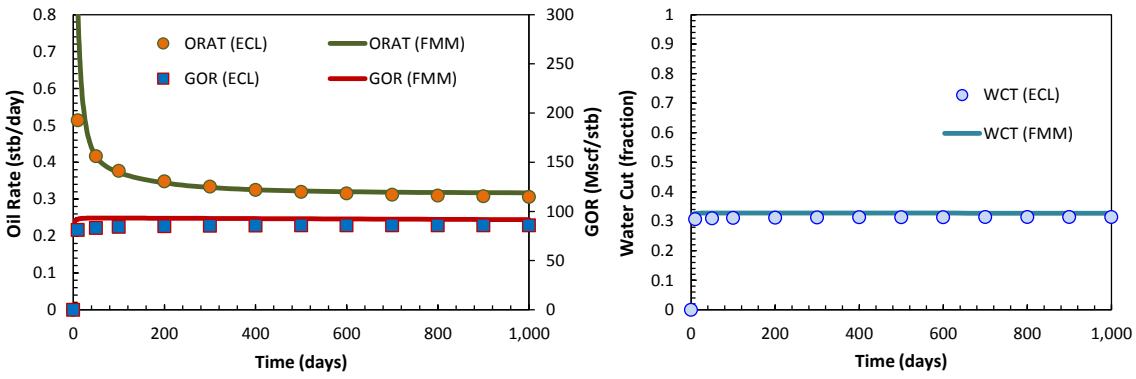

(a) Oil Rate and GOR (b) Water Cut

Fig. 3.18 – Simulation results of the 2-D three-phase model.

3.4.3 Three-phase Blackoil Model (3-D Dual-Porosity)

In this example, the naturally fractured reservoir model is used as described in **Fig. 2.13**. The saturation distribution is same as the previous example. First, we show the simulation results under the constant bottom-hole pressure constraint (4,000 psia) as shown in **Fig.3.19**.

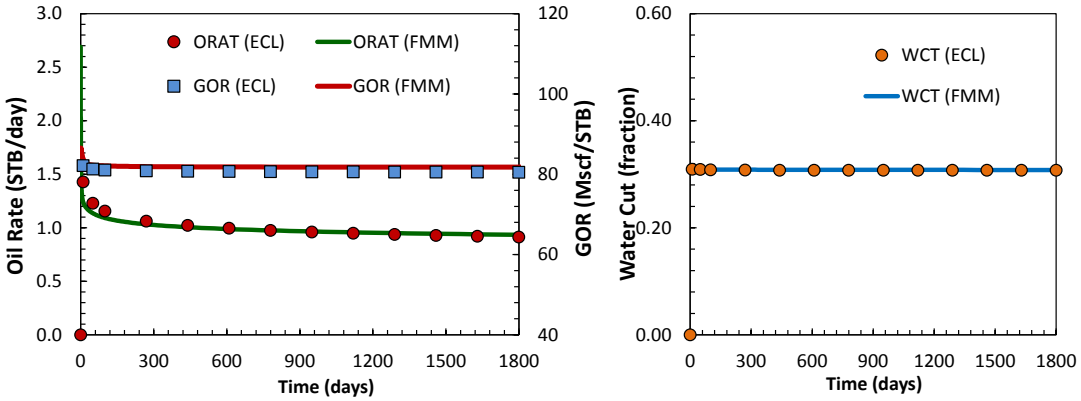

(a) Oil Rate and GOR (b) Water Cut

Fig. 3.19 – Simulation results at the constant bottom-hole pressure. (a) Oil rate and GOR, and (b) Water cut.

Next, we show the simulation results under the constant oil rate (1 stb/day) as shown in **Fig. 3.20**. The both cases have a good agreement with the commercial simulator.

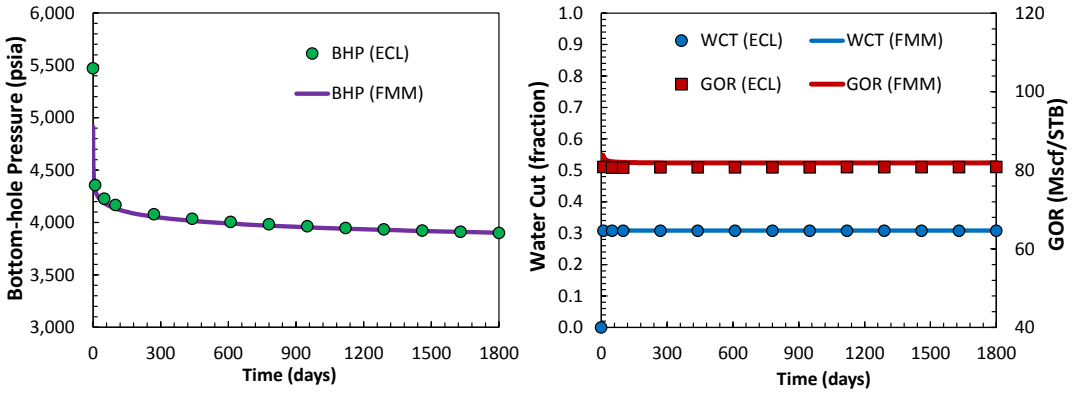

(a) Bottom-hole Pressure (b) Water Cut and GOR

Fig. 3.20 – Simulation result at the constant oil rate. (a) BHP and (b) GOR and Water cut.

3.4.4 Compositional Model (2-D Homogeneous)

The reservoir parameters are shown in **Table 3.3**. The geological heterogeneities and water saturation are uniformly distributed at the initial condition. Notice that the initial oil and gas saturations are given by the flash calculation in the compositional simulation.

Table 3.3 – Reservoir parameters (2-D homogeneous model)		
Grid Number	[-]	596 x 596 x 1
Grid Size	[ft]	10 x 10 x 10
Permeability	[mD]	1
Porosity	[fraction]	0.1
Water Saturation	[fraction]	0.1
Initial Pressure	[psia]	2,000
Bottom-hole Pressure	[psia]	800

The fluid model used in the compositional model validations is the Bakken oil sample composition (Nobabaei et al. 2013) as summarized in **Table 3.4**.

Table 3.4 – Bakken oil composition (Nojabaei et al. 2013)

Component	Molar Fraction	MW (lb/lb-mol)	Pcrit (psia)	Tcrit (degR)
C1	0.36736	16.535	655.02	335.336
C2	0.14885	30.433	721.99	549.969
C3	0.09334	44.097	615.76	665.970
C4	0.05751	58.124	546.46	759.208
C5-C6	0.06406	78.295	461.29	875.479
C7-C12	0.15854	120.562	363.34	1053.250
C13-C21	0.07330	220.716	249.61	1332.095
C22-C80	0.03704	443.518	190.12	1844.491

Because of the homogeneity of the model, the contour of the multiphase DTOF forms a circle centered on the well. The DTOF calculated by the FMM are shown in **Fig. 3.21**.

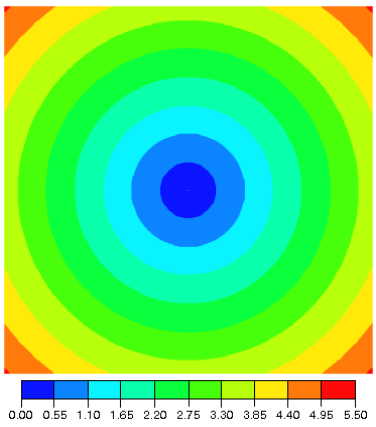

Fig. 3.21 – Three-phase DTOF in the homogeneous 2-D model

The production behavior is shown in **Fig. 3.22**. The well is placed at the center of the model and controlled by the constant bottom-hole pressure (800 psi).

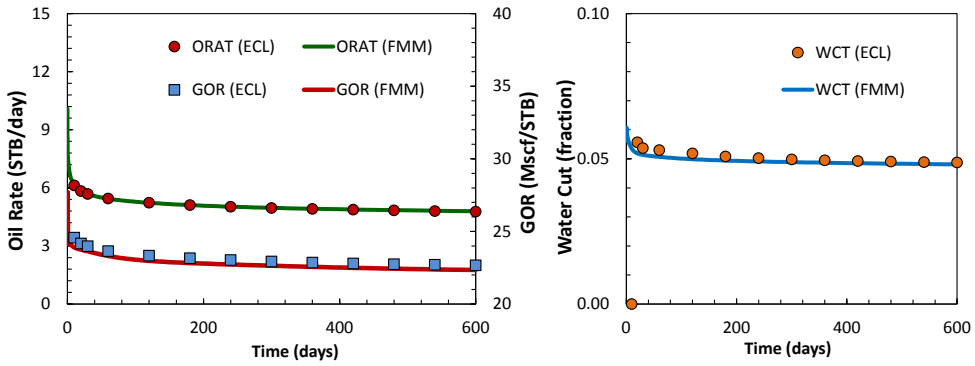

(a) Oil Rate and GOR (b) Water Cut

Fig. 3.22 – Simulation results of the (a) oil rate and GOR, and (b) water cut.

The pressure and gas saturation profiles are compared with the commercial simulator as illustrated in **Figs. 3.23** and **3.24**, respectively. Although the DTOF-based simulation has a good agreement with the commercial simulator, the difference can be seen in the gas saturation profile at 600 days. The commercial simulator shows the numerical dispersion effect along the axis directions. Notice that the numerical dispersion in the DTOF-based simulation is aligned with 1-D coordinate.

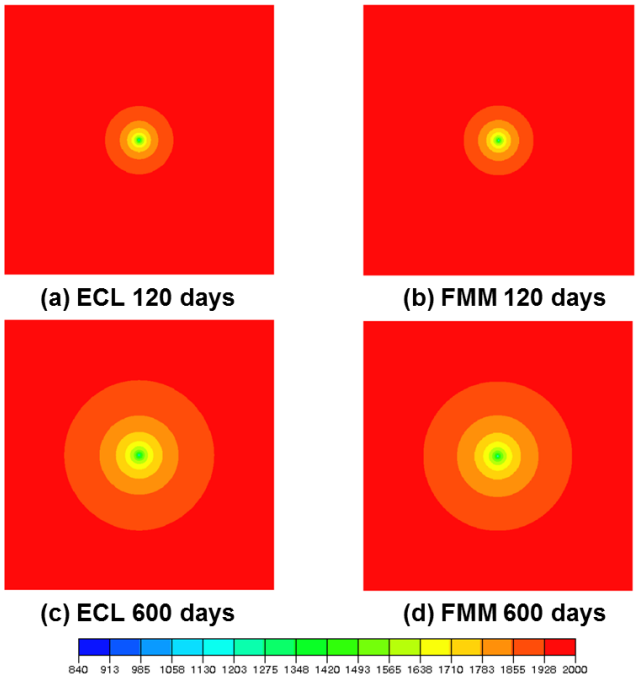

Fig. 3.23 – Comparison of the pressure profile between the commercial simulator (ECLIPSE) and DTOF-based simulation (FMM)

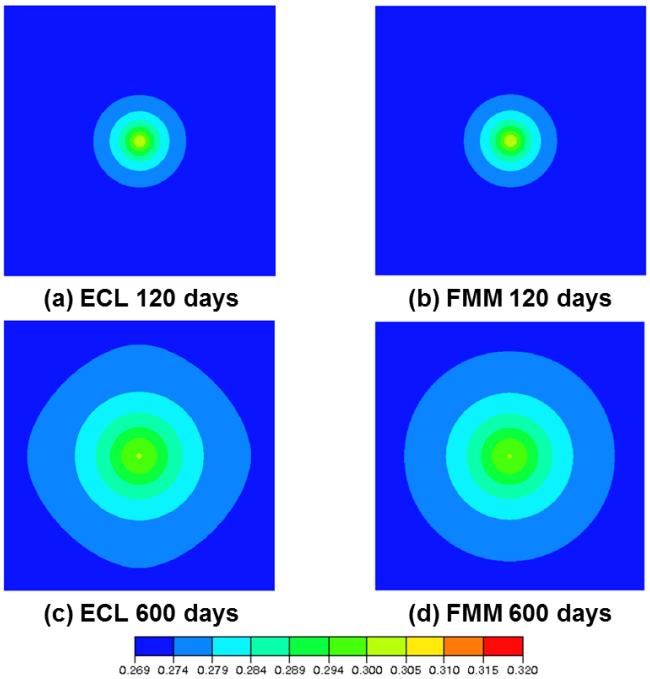

Fig. 3.24 – Comparison of the gas saturation profile between the commercial simulator (ECLIPSE) and DTOF-based simulation (FMM)

3.4.5 Compositional Model (2-D Heterogeneous)

In this model, the permeability is heterogeneously distributed as shown in **Fig. 3.25**. All the other reservoir parameters are the same as the previous homogeneous case as shown in **Table. 3.3**. The DTOF contour is aligned with the permeability contour. The production rates are shown in **Fig. 3.26**. The pressure and saturation profiles are compared with the commercial simulator as illustrated in **Figs. 3.27** and **3.28**, respectively.

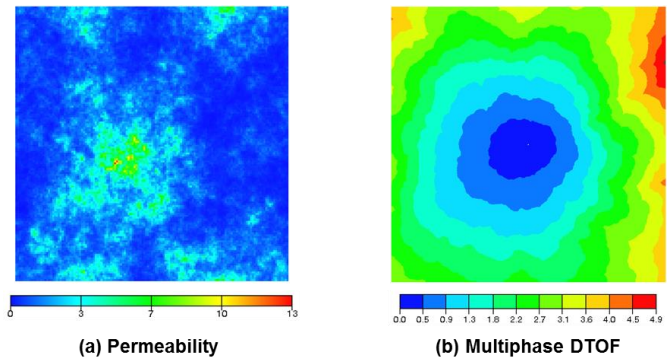

Fig. 3.25 – Distributions of (a) permeability and (b) DTOF in the 2-D heterogeneous model

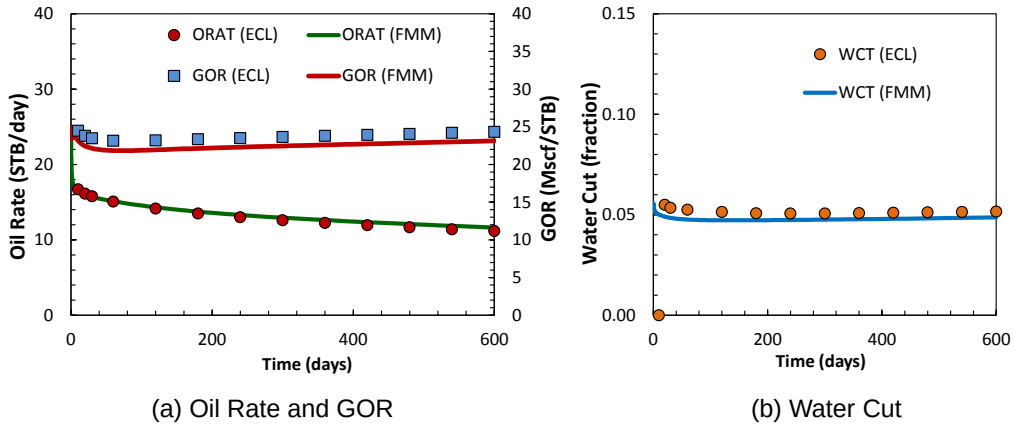

Fig. 3.26 – Simulation results of the (a) oil rate and GOR, and (b) water cut.

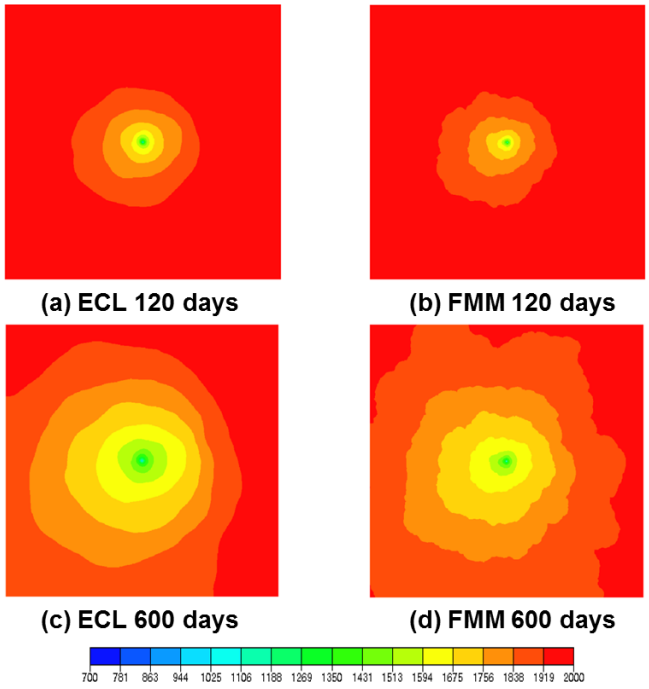

Fig. 3.27 – Comparison of the pressure profile between the commercial simulator (ECLIPSE) and DTOF-based simulation (FMM)

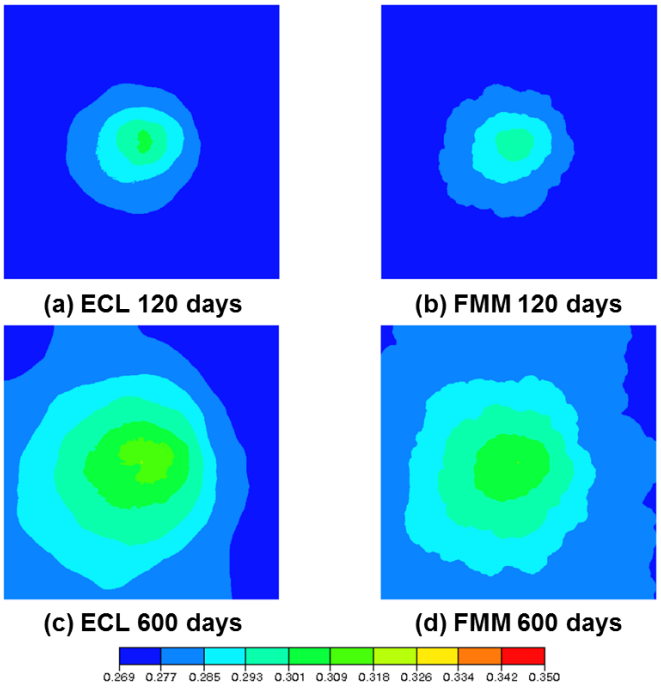

Fig. 3.28 – Comparison of the gas saturation profile between the commercial simulator (ECLIPSE) and DTOF-based simulation (FMM)

3.4.6 Compositional Model (3-D Confined Shale Oil)

In this 3-D model, the modified phase behavior calculation is used in the compositional simulation. We use a single representative pore size as input in the reservoir model for the fugacity and phase property calculations. The reservoir parameters are summarized in **Table 3.5**. The reservoir permeability and porosity are heterogeneously distributed as shown in **Fig. 3.29**. The natural fractures are stochastically distributed in the model.

Table 3.5 – Reservoir parameters (3-D confined model)		
Grid Number	[-]	596 x 596 x 1
Grid Size	[ft]	10 x 10 x 10
Permeability	[mD]	1
Porosity	[fraction]	0.1
Water Saturation	[fraction]	0.1
Initial Pressure	[psia]	2,000
Bottom-hole Pressure	[psia]	800

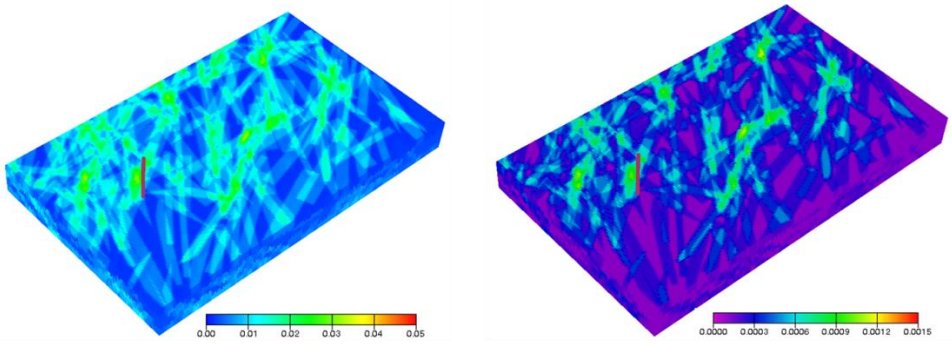

(a) Permeability distribution (b) Porosity distribution

Fig. 3.29 – Distributions of the (a) Permeability and (b) Porosity in the 3-D naturally fractured reservoir model

The well is horizontally drilled and completed at the equally-spaced four grid blocks as illustrated in **Fig. 3.30**.

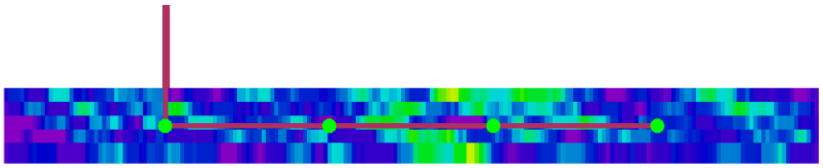

Fig. 3.30 – Vertical section of the fractured model

First, we perform a numerical simulation with conventional VLE flash calculation (no capillarity on phase equilibrium). The production rates are shown in **Fig. 3.31**. The results have a good agreement with the commercial simulator.

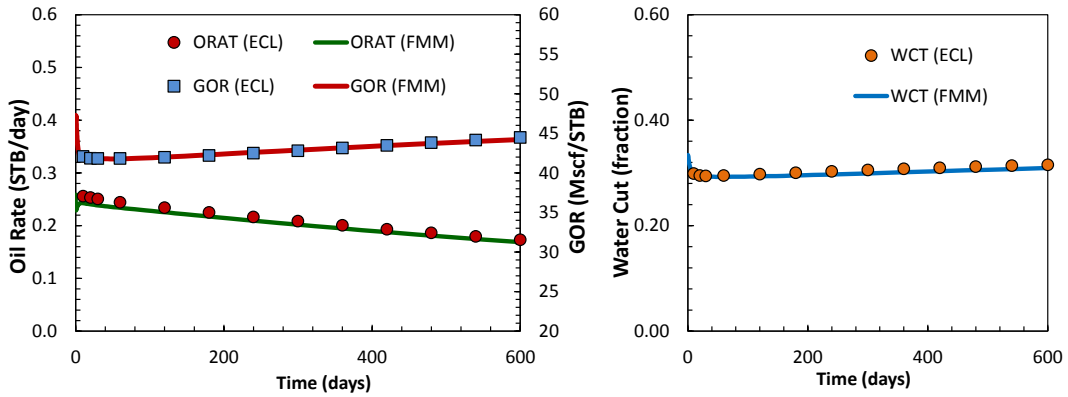

(a) Oil Rate and GOR (b) Water Cut

Fig. 3.31 – Simulation results of the (a) oil rate and GOR, and (b) water cut. The production behaviors are predicted without the capillarity on the phase equilibrium

Next, we incorporate the capillary pressure in the compositional simulation. Notice that pore size is used only for capillary pressure calculation, not for permeability correction. Also, the capillary pressure is used only for the fugacity and phase property calculations, as shown in **Fig. 3.6**, not for the transmissibility calculation. There are three pore size conditions – (1) unconfined (no capillarity), (2) confined in 10 nm pore, and (3) confined in 8 nm. The GOR behaviors are shown in **Fig. 2.32**. The GOR shift is clearly observed in the confined environments. In small pore size condition, the produced GOR is decreased due to the bubble-point suppression effect.

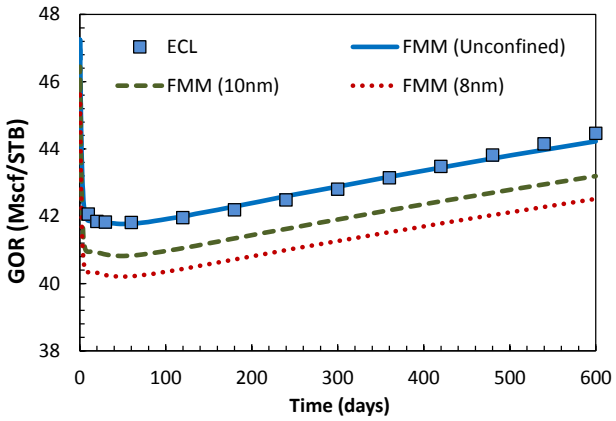

Fig. 3.32 – Predicted GOR behavior in the confined system. The blue line represents the GOR in unconfined (macro-scale) pore, the green dot line denotes the GOR in 10 nm pore, and the red dot line represents the GOR in 8 nm pore.

The oil and gas production rates are shown in **Fig. 3.33**. The shift of the produced GOR is associated by the large decrease of gas production rate relative to oil production rate.

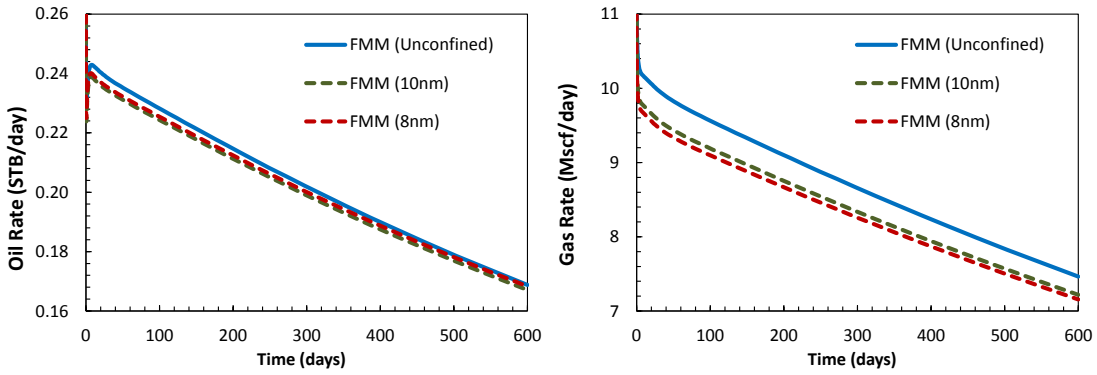

(a) Oil production rate (b) Gas production rate

Fig. 3.33 – Simulation results of the (a) oil rate and (b) gas rate in the confined reservoirs.

Fig. 3.34 shows the distributions of oil saturation and pressure along the τ-coordinate. The oil saturation is increased in the small pore space, while the reservoir pressure is not much affected by the pore size condition.

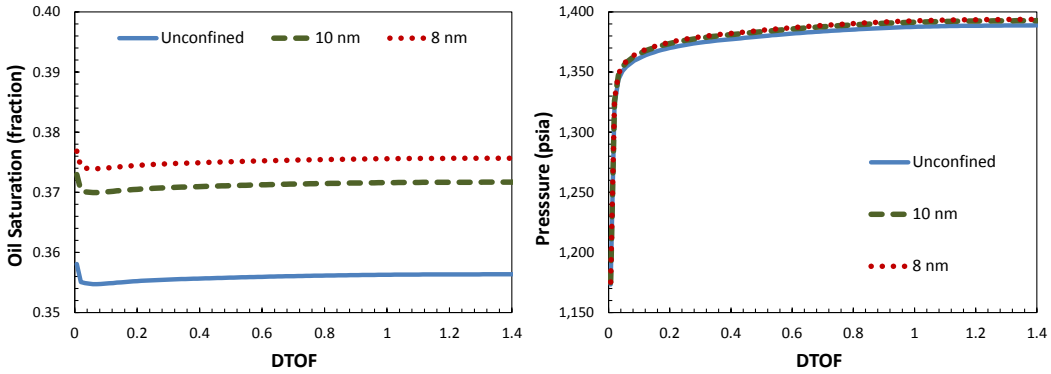

(a) Oil saturation along τ-coordinate (b) Pressure along τ-coordinate

Fig. 3.34 – Simulated distributions of the (a) oil saturation and (b) reservoir pressure along the τ-coordinate at the final simulation step (600 days).

Fig. 2.35 shows the distributions of oil and gas molar densities along the τ-coordinate. The oil molar density becomes heavier as the pore size becomes smaller, while the gas molar density becomes lighter in such condition.

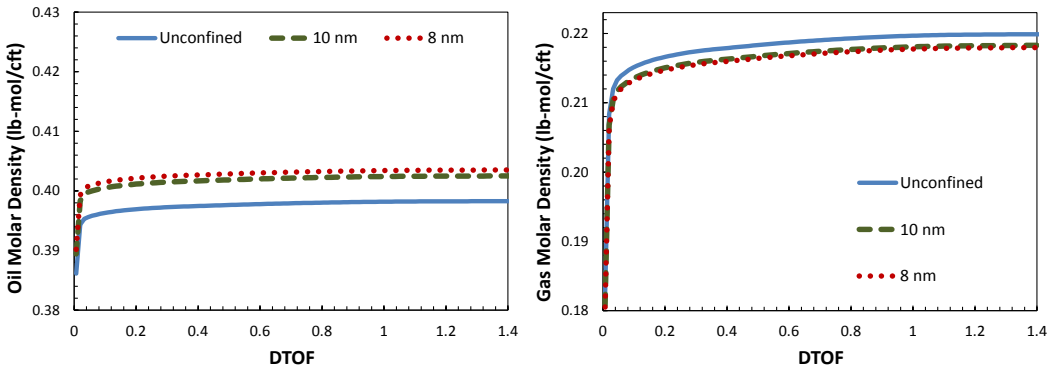

(a) Oil molar density along τ-coordinate

(b) Gas molar density along τ-coordinate

Fig. 3.35 – Simulated distributions of the (a) oil molar density and (b) gas molar density along the τ-coordinate at the final simulation step (600 days).

The confined environment causes the mobility change of the oil and gas phases due to its high capillarity effect. In the bubble-point system (oil reservoir), the relative oil volume is increased as shown in **Fig. 3.34** but the oil phase becomes heavier at the reservoir condition as illustrated in **Fig. 3.35**, while the relative gas volume is decreased but it becomes easy to move due to the gas density reduction.

3.5 Conclusions

In this chapter, we have developed the DTOF theory for multiphase and multicomponent flow simulations and established the numerical algorithms. The fully implicit method is used as a solution technique for both blackoil and compositional

simulations, and then the primary variables are solved simultaneously on the 1-D coordinate. The DTOF-based blackoil simulation is also extended to dual-porosity model. The numerical experiments show good agreement between the proposed approach and commercial simulator. The major features of this chapter are summarized as follows.

- A multiphase DTOF is derived by introducing the asymptotic theory to phase mass balance equation. The equation form is similar to the single-phase DTOF. In multiphase models, the diffusivity is calculated using total mobility and total compressibility for each grid.
- The coordinate transformation is applied to the mass balance equation in each phase using similar approach to the single-phase equation. In this research, the transformed phase flow equation is not linearized in terms of pressure, which forces the saturation contours to align with the pressure contours. Thus, we can employ a fully implicit method to solve pressure and saturation simultaneously on the same τ-coordinate under the assumption. In reality, pressure and saturation have a different behavior each other because the saturation is a hyperbolic property whereas the pressure has a parabolic nature. But the difference of the two properties can be mitigated when there is only single well and the properties cylindrically change from the well. If the profile deviates significant between pressure and saturation, the constraint can be removed by using the linearized pressure equation in the coordinate transformation. The resulting 1-D pressure equation will be aligned with the τ-coordinate, but the

saturation equation is not. In this case, the pressure and saturation are solved separately on different coordinates based on IMPES approach (i.e. solve pressure equation on 1-D DTOF coordinate, and then solve saturation equation along 1-D streamlines). Additional research is needed for this problem.

- In the nanoporous confined system, the vapor-liquid phase behavior significantly differs from that in conventional micro-scale system (PVT cell). The bubble-point pressure is suppressed in nanoporous space due to the capillary pressure effect, whereas the dew-point pressure is increased. This modified phase equilibrium calculation has been incorporated on the compositional simulation model for the simulation of nanoporous confined reservoirs. In the numerical model experiments, we observed that the produced GOR is suppressed as the pore size becomes smaller, which is consistent with the observations in the Bakken shale oil field.

CHAPTER IV

CONCLUSIONS AND RECOMMENDATIONS

4.1 Conclusions

This research is focused on the developments of the DTOF theory for multipurpose reservoir simulation.

In **Chapter II**, the 1-D transport equation is applied to single-phase flow simulation and extended to the dual-porosity and triple-continuum modeling without any change in the conventional FMM calculation. We also proposed a generalized framework for modeling hydraulically fractured shale gas reservoirs incorporating all the known physical mechanisms into the three distinct coordinates based on the triple-continuum approach. Particularly, an in-depth study has been done for modeling the gas permeability changes in naoporous media due to the slippage and Knudsen diffusion effects, which governs the mass transmissibility between the fracture and matrix systems.

In **Chapter III**, the DTOF theory is generalized to multiphase and multicomponent flow problems. The approach is analogous to the single-phase DTOF, but the saturation effects are pronounced on the FMM calculation and numerical simulations. The numerical solution technique follows the conventional fully implicit simulation, but the substantial time-saving is possible by reducing the matrix dimension and number of flash calculations. The versatility and applicability of the DTOF theory have been demonstrated though the blackoil and compositional simulations. The

compositional simulation has been applied including the phase behavior in confined environment by introducing the capillary pressure in the vapor-liquid equilibrium calculation. The numerical model result shows a good agreement with the actual GOR behavior in real shale oil field.

4.2 Recommendations

There are several recommendations that can be made as follows.

4.2.1 Gravity and Capillarity Effects

In this research, the gravity and capillarity forces are neglected in the FMM calculation and successive DTOF-based numerical simulation. These two forces have the following effects on the numerical modeling.

- The equilibrium state at initial reservoir condition (i.e. gas-oil/oil-water contact, compositional grading) is determined by the pressure gradient, capillarity effect, and geothermal gradient. In the current FMM, the capillary and gravity forces are not taken into account for the initial diffusivity calculation. This results in the following assumptions required in the FMM calculation.
    a. In a single-phase model, we assume a uniform initial reservoir pressure over the domain (no gravity effect). Thus, the reservoir is in equilibrium with a uniform viscosity and compressibility at the initial condition.
    b. In a multiphase model, we assume a uniform initial reservoir pressure over the domain (no gravity/no capillary effects). But the heterogeneity of the initial saturation distribution is accounted on the FMM calculation.

c. In a compositional model, we assume a uniform initial reservoir pressure (no gravity/no capillary effects) and uniform initial compositional distribution (no compositional grading) over the domain. The heterogeneity of the initial water saturation is accounted for the FMM calculation.

- Due to the assumption that pressure and saturation contours are aligned with the τ contour, we cannot directly account for a different phase pressure, which can cause the different pressure contour for each phase, in the DTOF formulation and simulations. Thus, an additional treatment is required to account for the capillary and gravity effects as the streamline simulation incorporate these forces using the operator splitting. Notice that the operator splitting cannot be used in the DTOF formulation, because we need to incorporate the gravity and capillarity in the convective flux term.

4.2.2 IMPES Approach

The current DTOF-based multiphase simulation adopts the fully implicit method to solve pressure, saturation, and mole fractions simultaneously on the 1-D DTOF coordinate. This approach forces saturation to have the same contour with pressure, because, during the coordinate transformation, we make an assumption that the variables, P and S, are the function of τ and t. The constraint can be removed by using the linearized pressure equation in the coordinate transformation and by making an assumption that the pressure is the function of τ and t in the 1-D transformed pressure equation. Thus, the saturation contour is not necessarily aligned with the τ-coordinate in

this case. Furthermore, a full 1-D solution can be obtained by combining the pressure solution on the DTOF with the saturation solution on the CTOF.

4.2.3 Dual-Porosity Compositional Model

The DTOF-based formulation can be extended to the dual-porosity compositional simulation. The approach is similar to the single-phase and blackoil models as we presented. The dual-porosity equation follows the Warren and Root pseudo-steady state type. A compositional dual-porosity equation is written as follows. The water equation in the fracture system is

$$\frac{\partial(\phi_f \rho_w S_{wf})}{\partial t} = \nabla \bullet (\mathbf{k}_f \lambda_{wf} \nabla P_f) - \rho_w \Gamma_w + \rho_w q_{wf} \tag{4.1}$$

where Γ_w is the matrix-fracture transfer function for water. The component equation in the fracture system is

$$\frac{\partial(\phi_f m_i)}{\partial t} = \nabla \bullet (\mathbf{k}_f \lambda_{if} \nabla P_f) - \rho_i \Gamma_i + \tilde{q}_{if} \tag{4.2}$$

where m_i denotes the component molar mass, λ_{if} represents the component mobility, and Γ_i denotes the matrix-fracture mass transfer of component i ($i = 1, \dots, N_c$). Notice that the component flow equation is molar-basis formulation and $\tilde{q}_{if}$ represents the component molar production rate. The transfer function is defined by the Darcy like expression with the up-winding mobility.

$$\Gamma_i = \sigma k_m \lambda_{i,up} (P_f - P_m) \tag{4.3}$$

The water equation in the matrix system is

$$\frac{\partial(\phi_m \rho_w S_{wm})}{\partial t} = \rho_w \Gamma_w \tag{4.4}$$

Notice that we assume the constant matrix porosity. The component equation in the matrix system is

$$\frac{\partial(\phi_m m_i)}{\partial t} = \Gamma_i \tag{4.5}$$

The coordinate transformation from the physical space to the 1D τ-coordinate (**Eq. (3.48)**) leads the following fracture equations. The water equation in the fracture system is

$$\frac{\partial\left(\phi_f \rho_w S_{wf}\right)}{\partial t} = \frac{\phi_f}{w(\tau)}\frac{\partial}{\partial \tau}\left[w(\tau)\left(\frac{c_t}{\lambda_t}\right)_{\text{init}} \lambda_{wf}\frac{\partial P_f}{\partial \tau}\right] - \rho_w \Gamma_w + \rho_w q_{wf} \tag{4.6}$$

The component equation in the fracture system is

$$\frac{\partial\left(\phi_f m_i\right)}{\partial t} = \frac{\phi_f}{w(\tau)}\frac{\partial}{\partial \tau}\left[w(\tau)\left(\frac{c_t}{\lambda_t}\right)_{\text{init}} \lambda_{if}\frac{\partial P_f}{\partial \tau}\right] - \Gamma_i + \tilde{q}_{if} \tag{4.7}$$

In the DTOF-based compositional simulation, **Eqs. (4.6)** and **(4.7)** are the governing equation in the fracture system as well as **Eqs. (4.4)** and **(4.5)** are the governing equation in the matrix system.

4.2.4 Data Integration and Optimization

In the reservoir engineering field, the production data integration and field optimization are essentially important to better characterize the reservoir heterogeneity and to improve the oil recovery with minimum cost. The streamline simulation offers a unique advantage for such problems by calculating the sensitivity coefficients along the 1D coordinate efficiently. The DTOF-based flow simulation is also applicable to such problems using an analogy of the streamline simulation. One possible method is based on the combinational use of the Adjoint method and travel time sensitivity calculation.

The Adjoint method is traditionally applied in the numerical reservoir simulation and is regarded as one of the most efficient approach to compute sensitivity coefficients. The application of the Adjoint method in the DTOF formulation leads the sensitivity along the 1-D coordinate (i.e. the sensitivity of bottom-hole pressure with respect to the drainage volume). For future use, the all derivations are attached in **APPENDIX F**.

REFERENCES

Aguilera, R. 2010. Flow Units: From Conventional to Tight Gas to Shale Gas Reservoirs. Paper SPE-132845 presented at the Trinidad and Tobago Energy Resource Conference, Port of Spain, Trinidad, 27-30 June.

Arogundate, O., and Sohrabi, M. 2012. A Review of Resent Developments and Challenges in Shale Gas Recovery. Paper SPE-160869 presented at the SPE Saudi Arabia Section Technical Symposium and Exhibition, Al-Khobar, Saudi Arabia, 8-11 April.

Barenblatt, G.E., Zheltov, I.P., and Kochina, I.N. 1960. Basic Concepts in the Theory of Seepage of Homogeneous Liquids in Fissured Rocks. *Journal of Applied Mathematics and Mechanics* **24** (5): 1286-1303.

Biswas, D. 2011. Shale Gas Predictive Model (SGPM) – An Alternative Approach to Predict Shale Gas Production. Paper SPE-148491 presented at the Eastern Regional Meeting, Columbus, Ohio, USA, 17-19 August.

Blair, P.M. 1964. Calculation of Oil Displacement by Countercurrent Water Imbibition. *Society of Petroleum Engineers Journal* **4** (3): 195-202.

Brown, G.P., Dinardo, A., Cheng, G.K., and Sherwood, T.K. 1946. The Flow of Gases in Pipes at Low Pressures. *Journal of Applied Physics* **17** (10): 802-813.

Browning, J., Ikonnikova, S., Gulen, G., and Tinker, S.W. 2013. Barnett Shale Production Outlook. *SPE Economics & Management* **5** (3): 89-104.

Chen, W.H., Gavalas, G.R., Seinfeld, J.H., and Wasserman, M.L. 1974. A New Algorithm for Automatic History Matching. *Society of Petroleum Engineers Journal* **14** (6): 593-608.

Civian, F. 2010. Effective Correlation of Apparent Gas Permeability in Tight Porous Media. *Transport in Porous Media* **82** (2): 375-384.

Civian, F., Rai, C.S., and Sondergeld, C.H. 2011. Shale-Gas Permeability and Diffusivity Inferred by Improved Formulation of Relevant Retention and Transport Mechanisms. *Transport in Porous Media* **86** (3): 925-944.

Coats, K.H. 1980. An Equation of State Compositional Model. *Society of Petroleum Engineers Journal* **20** (5): 363-376.

Cerveny, V., Molotkov, I.A., and Psensik, I. 1978. *The Ray Method in Seismology*. Charles University Press, Prague.

Curtis, M.E., Sondergeld, C.H., and Rai, C.S. 2012. The Development of Organic Porosity in the Woodford Shale Related to Thermal Maturity. Paper SPE-160158 presented at the SPE Annual Technical Conference and Exhibition, San Antonio, Texas, USA, 8-10 October.

Datta-Gupta, A., Kulkarni, K.N., Yoon, S., and Vasco, D.W. 2001. Streamlines, Ray Tracing and Production Tomography: Generalization to Compressible Flow. *Petroleum Geoscience* **7**: 75-86.

Datta-Gupta, A., and King, M.J. 2007. *Streamline Simulation: Theory and Practice*. Society of Petroleum Engineers, Richardson, Texas.

Datta-Gupta, A., Xie, J., Gupta, N., King, M.J., and Lee W.J. 2011. Radius of Investigation and its Generalization to Unconventional Reservoirs. *Journal of Petroleum Technology* **63** (7): 52-55.

Dean, R.H., and Lo, L.L. 1988. Simulations of Naturally Fractured Reservoirs. *SPE Reservoir Engineering* **3** (2): 638-648.

Dijkstra, E.W. 1959. A Note on Two Problems in Connection with Graphs. *Numerische Mathematik* **1**: 269-271.

Ertekin, T., King, G.R., and Schwerer, F.C. 1986. Dynamic Gas Slippage: A Unique Dual-Mechanism Approach to the Flow of Gas in Tight Formations. *SPE Formation Evaluation* **1** (1): 43-52.

Florence, F.A., Rushing, J.A., Newsham, K.E., and Blasingame, T.A. 2007. Improved Permeability Prediction Relations for Low-Permeability Sands. Paper SPE-107054 presented at the SPE Rocky Mountain Oil & Gas Technology Symposium, Denver, Colorado, USA, 16-18 April.

Grathwohl, P. 1998. *Diffusion in Natural Porous Media: Contaminant Transport, Sorption/Desorption and Dissolution Kinetics*. Springer Publishers, UK.

Igwe, G.J.I. 1985. Gas Transport Mechanism and Slippage Phenomenon in Porous Media. Paper SPE-16479 available from SPE, Richardson, Texas.

Javadpour, F., Fisher, D., and Unsworth, M. 2007. Nanoscale Gas Flow in Shale Gas Sediments. *Journal of Canadian Petroleum Technology* **46** (10): 55-61.

Javadpour, F. 2010. Nanoscale and Apparent Permeability of Gas Flow in Mudrocks (Shale and Siltstone). *Journal of Canadian Petroleum Technology* **48** (8): 16-21.

Jones, F.O., and Owens, W.W. 1980. A Laboratory Study of Low-Permeability Gas Sands. *Journal of Petroleum Technology* **32** (9): 1631-1640.

Kazemi, H., Merrill, L.S., Porterfield, K.L., and Zeman, P.R. 1976. Numerical Simulation of Water-Oil Flow in Naturally Fractured Reservoir. *Society of Petroleum Engineers Journal* **16** (6): 317-326.

Kazemi, H., and Merrill, L.S. 1979. Numerical Simulation of Water Imbibition in Fractured Cores. *Society of Petroleum Engineers Journal* **19** (3): 175-182.

Klinkenberg, L.J. 1941. The Permeability of Porous Media to Liquid and Gases. *API Drilling and production Practice*, 200-213.

Kuila, U., and Prasad, M. 2011. Surface Area and Pore-size Distribution in Clays and Shales. Paper SPE-146869 presented at the SPE Annual Technical Conference and Exhibition, Denver, Colorado, USA, 30 October-2 November.

Langmuir, I. 1916. The Constitution and Fundamental Properties of Solids and Liquids Part I. Solids. *Journal of the American Chemical Society* **38** (11): 2221-2295.

Lee, W.J. 1982. *Well Testing*. Society of Petroleum Engineers, Richardson, Texas.

Li, R., Reynolds, A.C., and Oliver, D.S. 2003. History Matching of Three-Phase Flow Production Data. *Society of Petroleum Enginners Journal* **8** (4): 328-340.

Michel, G.G., Sigal, R.F., Civan, F., and Devegowda, D. 2011. Parametric Investigation of Shale Gas Production Considering Nano-Scale Pore Size Distribution, Formation Factor, and Non-Darcy Flow Mechanisms. Paper SPE-147438 presented at the SPE Annual Technical Conference and Exhibition, Denver, Colorado, USA, 30 October-2 November.

Mengal, S.A., and Wattenbarger, R.A. 2011. Accounting for Adsorbed Gas in Shale Gas Reservoirs. Paper SPE-141085 presented at the SPE Middle East Oil and Gas Show and Conference, Manama, Bahrain, 21-24 March.

Nelson, P.H. 2009. Pore-throat Sizes in Sandstones, Tight Sandstones, and Shales. *AAPG Bulletin* **93** (3): 329-340.

Nojabaei, B., Johns, R.T., and Chu, L. 2013. Effect of Capillary Pressure on Phase Behavior in Tight Rocks and Shales. *SPE Reservoir Evaluation & Engineering* **16** (3): 281-289.

Qi, Z., Liang, B., Deng, R., Du, Z., Wang, S., and Zhao, W. 2007. Phase Behavior Study in the Deep Gas-Condensate Reservoir with Low Permeability. Paper SPE-

107315 presented at the SPE Europec/EAGE Annual Conference and Exhibition, London, UK, 11-14 June.

Sakhaee-Pour, A., and Bryant, S.L. 2012. Gas Permeability of Shale. *SPE Reservoir Evaluation & Engineering* **15** (4): 401-409.

Sampath, C.W, and Keighin, K. 1982. Factors Affecting Gas Slippage in Tight Sandstones of Cretaceous Age in the Uinta Basin. *Journal of Petroleum Technology* **34** (11): 2715-2720.

Schaaf, S.A., and Chambre, P.L. 1961. *Flow of Rarefied Gases*. Princeton University Press, New Jersey.

Sethian, J.A. 1996. *Level Set Method*. Cambridge University Press, New York City.

Sethian, J.A. 1999. *Level Set Methods and Fast Marching Methods*. Cambridge University Press, New York City.

Shapiro, A.A., and Stenby, E.H. 2001. Thermodynamics of the Multicomponent Vapor-Liquid Equilibrium under Capillary Pressure Difference. *Fluid Phase Equilibria* **178** (1-2): 17-32.

Swami, V., Clarkson, C.R., and Settari, A.T. 2012. Non Darcy Flow in Shale Nanopores: Do We Have a Final Answer?. Paper SPE-162665 presented at the SPE Canadian Unconventional Resource Conference, Calgary, Canada, 30 October-1 November.

U.S. Energy Information Administration. 2013. *Annual Energy Outlook 2013 with Projections to 2040*, http://www.eia.gov/forecasts/aeo/pdf/0383(2013).pdf.

Vasco, D.W., and Datta-Gupta, A. 1999. Asymptotic Solutions for Solute Transport: A Formalism for Tracer Tomography. *Water Resource Research* **35** (1): 1-16.

Vasco, D.W., Keers, H., and Karasaki, K. 2000. Estimation of Reservoir Properties Using Transient Pressure Data: An Asymptotic Approach. *Water Resource Research* **36** (12): 3447-3465.

Vasco, D.W., and Finsterle, S. 2004. Numerical Trajectory Calculations for the Efficient Inversion of Transient Flow and Tracer Observations. *Water Resource Research* **40** (1) W01507.

Virieux, J., Flores-Luna, C., and Gilbert, D. 1994. Asymptotic Theory for Diffusive Electromagnetic Imaging. *Geophysical Journal International* **119** (3): 857-868.

Warren, J.E. and Root, P.J. 1963. The Behavior of Naturally Fractured Reservoirs. *Society of Petroleum Engineers Journal* **3** (3): 245-255.

Whitson, C.H. and Michelsen, M.L. 1989. The Negative Flash. *Fluid Phase Equilibria* **53**: 51-71.

Wu, Z., Reynolds, A.C., and Oliver, D.S. 1999. Conditioning Geostatistical Models to Two-Phase Production Data. *Society of Petroleum Enginners Journal* **4** (2): 142-155.

Yamamoto, R.H., Padgett, J.B., Ford, W.T., and Boubeguira, A. 1971. Compositional Reservoir Simulator for Fissured Systems - The Single-Block Model. *Society of Petroleum Engineers Journal* **11** (2): 113-128.

Zhang, Y., Bansal, N., Fujita, Y., Datta-Gupta, A., King, M.J., and Sankaran, S. 2014. From Streamline to Fast Marching: Rapid Simulation and Performance Assessment of Shale Gas Reservoirs Using Diffusive Time of Flight as a Spatial Coordinate. Paper SPE-168997 presented at the SPE Unconventional Resource Conference, The woodlands, Texas, USA, 1-3 April.

APPENDIX A

GENERALIZATION OF DTOF FORMULATION TO ANISOTROPIC MEDIUM

A.1 Coordinate Transformation into the DTOF Space

The general diffusivity equation is given by

$$\phi c_t \frac{\partial P}{\partial t} + \nabla \bullet \vec{u} = 0 \tag{A.1}$$

where $\vec{u}$ is the Darcy velocity with an anisotropic permeability $\vec{\vec{k}}$.

$$\vec{u} = -\frac{1}{\mu}\vec{\vec{k}} \bullet \nabla P \tag{A.2}$$

Suppose the flow domain is given by the closed finite permeable media with a source or sink point (inner boundary). When the fluid flow takes place only by the convective transport, the fluid particle moves along the pressure gradient direction.

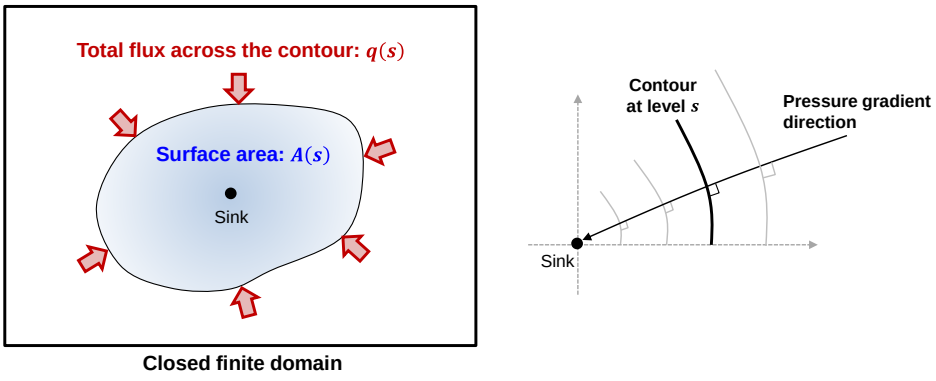

Fig. A.1 – Pressure contour map and fluid path along the pressure difference.

Furthermore, in the primary depletion stage, the evolution of the fluid flow proceeds outwardly from the sink/source point and is given by the gradient of the series of the non-overlapping contour surfaces (pressure contours). The direction of the convective fluid transport is identical to the gradient direction of the contour surface, ∇s, as shown in **Fig. A.1**. Therefore, the flux coordinate is transformed from the physical space to the series of surface contours.

$$\nabla \bullet \vec{u} \equiv -\frac{1}{A(s)}\frac{\partial q}{\partial s} \tag{A.3}$$

where $A(s)$ is the surface area of the contour and q is the total flux across the surface contour. Substituting **Eq. (A.3)** into **Eq. (A.1)**, we obtain the diffusivity equation as follows.

$$\phi c_t \frac{\partial P}{\partial t} - \frac{1}{A(s)}\frac{\partial q}{\partial s} = 0 \tag{A.4}$$

On the contour surface, the total flux is given by

$$q(s,t) = -A(s)\hat{s} \bullet \vec{u} \tag{A.5}$$

where $\hat{s}$ denotes a normal vector. Consider the drainage pore volume inside the contour surface.

$$V_p(s) = \int_0^s \phi(s')A(s')ds' \tag{A.6}$$

Differentiating **Eq. (A.6)**, we obtain the surface area of the contour.

$$A(s) = \frac{1}{\phi(s)}\frac{dV_p}{ds} \tag{A.7}$$

or, we have

$$A(s)ds = \frac{1}{\phi(s)} dV_p \tag{A.8}$$

Inserting **Eqs. (A.2)** and **(A.8)** into **Eq. (A.5)**, we obtain

$$q(s,t) = \frac{1}{\phi(s)} \nabla V_p \frac{1}{\mu} \vec{\vec{k}} \bullet \nabla P \tag{A.9}$$

Now we approximate the trajectory s by the trajectory of the pressure front propagation, τ. On the transient flow conditions, the pressure propagation trajectory is strictly given by the seismic ray equation and not necessarily aligned with the streamline. The gradient direction of the surface contour, ∇s is replaced by the gradient direction of the diffusive time of flight, $\nabla \tau$.

$$q(\tau,t) = \frac{1}{\phi\mu} \frac{\partial V_p}{\partial \tau} \left(\nabla \tau \bullet \vec{\vec{k}} \bullet \nabla \tau \right) \frac{\partial P}{\partial \tau} \tag{A.10}$$

From the Eikonal equation, we have the following relationship.

$$\nabla \tau \bullet \vec{\vec{k}} \bullet \nabla \tau = (\phi \mu c_t)_{\text{init}} \tag{A.11}$$

Notice that the Fast Marching Method is performed to solve for the DTOF τ on the initial reservoir state (i.e. the porosity, total compressibility, and fluid viscosity at the initial condition). Substituting **Eq. (A.11)** into **Eq. (A.10)**, we obtain the flux equation along τ.

$$q(\tau,t) = \frac{(\mu c_t)_{\text{init}}}{\mu} \frac{\partial V_p}{\partial \tau} \frac{\partial P}{\partial \tau} \tag{A.12}$$

Now, we define the w-function as follows.

$$w(\tau) = \frac{\partial V_p}{\partial \tau} \tag{A.13}$$

Substituting **Eqs. (A.7)** and **(A.12)** into **Eq. (A.3)**, we define the coordinate transformation as follows.

$$\nabla \bullet \vec{u} \equiv -\frac{\phi}{w(\tau)}\frac{\partial}{\partial \tau}\left(\frac{(\mu c_t)_{\text{init}}}{\mu} w(\tau)\frac{\partial P}{\partial \tau}\right) \tag{A.14}$$

A.2 Inner Boundary Condition

At inner boundary ($\tau = \tau_w$), the well production rate is given by **Eq. (A.12)**.

$$q_w(t) = \frac{(\mu c_t)_{\text{init}}}{\mu}\frac{\partial V_p}{\partial \tau}\frac{\partial P}{\partial \tau}\bigg|_{\tau=\tau_w} \tag{A.15}$$

Eq. (A.15) is approximated by the first-order finite difference method.

$$q_w(t) = \frac{(\mu c_t)_{\text{init}}}{\mu(P_1)}\left(\frac{V_{p,1} - V_{p,w}}{\tau_1 - \tau_w}\right)\left(\frac{P_1 - P_w}{\tau_1 - \tau_w}\right) \tag{A.16}$$

where q_w represents the production rate at the wellbore condition. The surface rate is obtained by dividing Eq. (A.15) by the formation volume factor. Notice that the drainage volume at wellbore ($V_{p,w}$) is zero. The fluid viscosity is given by the upstream weighting.

APPENDIX B

CONSTRUCTION OF JACOBIAN FOR SINGLE-PHASE FLOWS

B.1 Derivatives of Finite Difference Equation

The sets of finite difference equations are iteratively solved by using the Newton-Raphson method. In this approach, the Jacobian matrix is constructed by differentiating the finite difference equations by the primary variables. Based on the 1-D discretization, the Jacobian forms a sparse tridiagonal matrix as shown in **Fig. B.1**. Notice that, in the rate-specified case, some non-zero values are entered in non-tridiagonal elements due to the well conditioning. The details are discussed later.

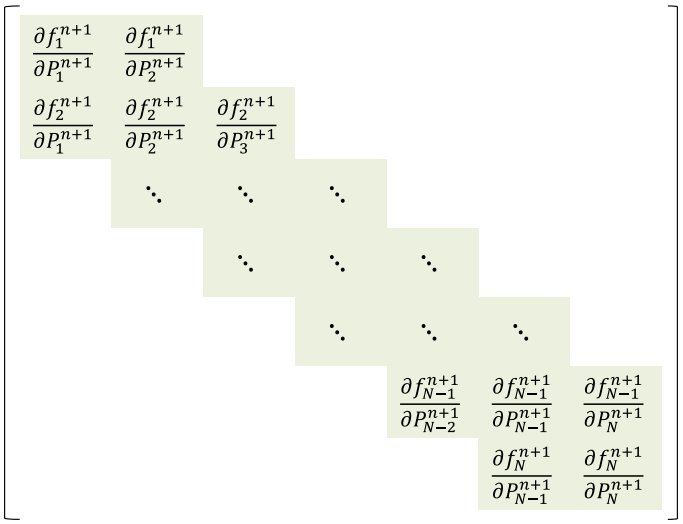

Fig. B.1 – Jacobian of the single-phase single-porosity model

On the basis of **Eq. (2.47)**, the finite difference equation of the grid i at the time-step $n+1$ is written as follows.

$$f_i^{n+1} = F_i^{n+1} - A_i^{n+1} + A_i^n + W_i^{n+1} = 0 \tag{B.1}$$

where F_i^{n+1} is the flux term, A_i^{n+1} and A_i^n are the accumulation terms, and W_i^{n+1} is the well term. Because the well is imposed on the inner boundary, this term is appeared only on the first grid ($i = 1$).

In a single-phase model, the primary variables correspond to the grid pressures P_i ($M \times 1$ vector). The diagonal terms of the Jacobian are obtained by differentiating **Eq. (B.1)** by the pressure of grid i.

$$\frac{\partial f_i^{n+1}}{\partial P_i^{n+1}} = \frac{\partial F_i^{n+1}}{\partial P_i^{n+1}} - \frac{\partial A_i^{n+1}}{\partial P_i^{n+1}} + \frac{\partial W_i^{n+1}}{\partial P_i^{n+1}} \tag{B.2}$$

The derivatives in **Eq. (B.2)** are analytically calculated in this study. The notations of the equation follow **Eq. (2.47)**. The derivative of the flux term in **Eq. (B.2)** is

$$\frac{\partial F_i^{n+1}}{\partial P_i^{n+1}} = \frac{\partial T_{i-1/2}^{n+1}}{\partial P_i^{n+1}}(P_{i-1}^{n+1} - P_i^{n+1}) + \frac{\partial T_{i+1/2}^{n+1}}{\partial P_i^{n+1}}(P_{i+1}^{n+1} - P_i^{n+1}) - \left(T_{i-1/2}^{n+1} + T_{i+1/2}^{n+1}\right) \tag{B.3}$$

In the transmissibility, flow mobility (i.e. viscosity, FVF) is determined by up-winding. If the upstream grid is i, that means the flow mobility is the function of the pressure of the grid i, the derivatives of the transmissibility in **Eq. (B.3)** are

$$\frac{\partial T_{i\pm1/2}^{n+1}}{\partial P_i^{n+1}} = \frac{w_{i\pm1/2}(\mu c_t)_{\mathrm{init},i\pm1/2}}{\Delta\tau_{i\pm1/2}} w_{i\pm1/2}(\mu c_t)_{\mathrm{init},i\pm1/2} \frac{\partial}{\partial P_i^{n+1}} \left(\frac{1}{B\mu}\right)_i^{n+1} \tag{B.4}$$

The derivative of the flow mobility in **Eq. (B.4)** is

$$\frac{\partial}{\partial P_i^{n+1}}\left(\frac{1}{B\mu}\right)_i^{n+1} = -\frac{1}{B_i^{n+1}\mu_i^{n+1^2}}\frac{\partial \mu_i^{n+1}}{\partial P_i^{n+1}} - \frac{1}{B_i^{n+1^2}\mu_i^{n+1}}\frac{\partial B_i^{n+1}}{\partial P_i^{n+1}} \tag{B.5}$$

If the upstream grid is the neighbor grid, that means the flow mobility is not related to the pressure of the grid i, the derivatives of the transmissibility in **Eq. (B.3)** are zero.

$$\frac{\partial T_{i-1/2}^{n+1}}{\partial P_i^{n+1}} = 0, \quad \frac{\partial T_{i+1/2}^{n+1}}{\partial P_i^{n+1}} = 0 \tag{B.6}$$

The derivative of the accumulation term in **Eq. (B.2)** is

$$\frac{\partial A_i^{n+1}}{\partial P_i^{n+1}} = \frac{w_i \Delta\tau_i}{\Delta t^{n+1}}\left(\frac{1}{B_i^{n+1}}\frac{\partial M_{\phi,i}^{n+1}}{\partial P_i^{n+1}} - \frac{M_{\phi,i}^{n+1}}{B_i^{n+1^2}}\frac{\partial B_i^{n+1}}{\partial P_i^{n+1}}\right) \tag{B.7}$$

where M_ϕ is the exponential rock compressibility function ($M_{c_r} = e^{c_r(P-P_i)}$). Its derivative is

$$\frac{\partial M_{c_r,i}^{n+1}}{\partial P_i^{n+1}} = c_r e^{c_r(P-P_i)} \tag{B.8}$$

The derivative of the well term in **Eq. (B.2)** is appeared at $i = 1$. This is calculated by differentiating **Eq. (2.50)**.

$$\frac{\partial W_i^{n+1}}{\partial P_i^1} = \frac{w_1(\mu c_t)_{\text{init},1}}{\tau_1 - \tau_{\text{well}}}\left[\left(\frac{1}{B\mu}\right)_1^{n+1} + \frac{\partial}{\partial P_1^{n+1}}\left(\frac{1}{B\mu}\right)_1^{n+1}\left(P_1^{n+1} - P_{wf}^{n+1}\right)\right] \tag{B.9}$$

The off-diagonal terms of the Jacobian are obtained by differentiating the finite difference equation (**Eq. (B.1)**) by the pressure of the neighbor grids.

$$\frac{\partial f_i^{n+1}}{\partial P_{i\pm1}^{n+1}} = \frac{\partial F_i^{n+1}}{\partial P_{i\pm1}^{n+1}} - \frac{\partial A_i^{n+1}}{\partial P_{i\pm1}^{n+1}} + \frac{\partial W_i^{n+1}}{\partial P_{i\pm1}^{n+1}} \tag{B.10}$$

Notice that the derivatives of the non-flux term in **Eq. (B.10)** equal zero.

$$\frac{\partial A_i^{n+1}}{\partial P_{i\pm1}^{n+1}} = 0, \quad \frac{\partial W_i^{n+1}}{\partial P_{i\pm1}^{n+1}} = 0 \tag{B.11}$$

The derivatives of the flux term in **Eq. (B.10)** is

$$\frac{\partial F_i^{n+1}}{\partial P_{i-1}^{n+1}} = T_{i-1/2}^{n+1} + \frac{\partial T_{i-1/2}^{n+1}}{\partial P_{i-1}^{n+1}}(P_{i-1}^{n+1} - P_i^{n+1}) \tag{B.12}$$

$$\frac{\partial F_i^{n+1}}{\partial P_{i+1}^{n+1}} = T_{i+1/2}^{n+1} + \frac{\partial T_{i+1/2}^{n+1}}{\partial P_{i+1}^{n+1}}(P_{i+1}^{n+1} - P_i^{n+1}) \tag{B.13}$$

If the upstream grid corresponds to i, the derivatives of the transmissibility in **Eqs. (B.12)** and **(B.13)** are zero.

$$\frac{\partial T_{i-1/2}^{n+1}}{\partial P_{i-1}^{n+1}} = 0, \quad \frac{\partial T_{i+1/2}^{n+1}}{\partial P_{i+1}^{n+1}} = 0 \tag{B.14}$$

If the upstream grid is neighbor grid ($i \pm 1$), the derivatives of the transmissibility in **Eq. (B.3)** are

$$\frac{\partial T_{i-1/2}^{n+1}}{\partial P_{i-1}^{n+1}} = \frac{w_{i-1/2}(\mu c_t)_{\text{init},i-1/2}}{\Delta\tau_{i-1/2}} w_{i-1/2}(\mu c_t)_{\text{init},i-1/2} \frac{\partial}{\partial P_{i-1}^{n+1}} \left(\frac{1}{B\mu}\right)_{i-1}^{n+1} \tag{B.15}$$

$$\frac{\partial T_{i+1/2}^{n+1}}{\partial P_{i+1}^{n+1}} = \frac{w_{i+1/2}(\mu c_t)_{\text{init},i+1/2}}{\Delta\tau_{i+1/2}} w_{i+1/2}(\mu c_t)_{\text{init},i+1/2} \frac{\partial}{\partial P_{i+1}^{n+1}} \left(\frac{1}{B\mu}\right)_{i+1}^{n+1} \tag{B.16}$$

Hence, the diagonal term of the Jacobian is constructed by using **Eqs. (B.3)**, **(B.7)**, and **(B.9)** as well as the off-diagonal term is constructed with **Eqs. (B.12)** and **(B.13)**.

B.2 Implicit BHP Calculation

If the bottom-hole pressure is specified, we can explicitly calculate the production rate using the well equation (**Eq. (2.50)**). If the production rate is specified, we implicitly solve the bottom-hole pressure during the Newton iteration. In such case, the primary variable consists of a $(M+1) \times 1$ vactor.

$$\mathbf{y}^{n+1} = \left[P_1^{n+1}, P_2^{n+1}, \dots, P_M^{n+1}, P_{wf}^{n+1}\right]^T \tag{B.17}$$

In addition to the finite difference equations, the well governing equation, that is the well residual equation (R_w) is imposed on the residual.

$$\mathbf{R}^{n+1} = [f_1^{n+1}, f_2^{n+1}, \dots, f_M^{n+1}, R_w^{n+1}]^T \tag{B.18}$$

The residual consists of a $(M+1) \times 1$ vactor. The well residual term R_w^{n+1} is obtained by rearranging **Eq. (2.50)**.

$$R_w^{n+1} = w_1 (\mu c_t)_{\text{init},i\pm\frac{1}{2}} \left(\frac{1}{B\mu}\right)_1^{n+1} \left(\frac{P_1^{n+1} - P_{wf}^{n+1}}{\tau_1 - \tau_{\text{well}}}\right) - q_s^{n+1} \tag{B.19}$$

The Jacobian consists of a $(M+1) \times (M+1)$ matrix as shown in **Fig. B.2**.

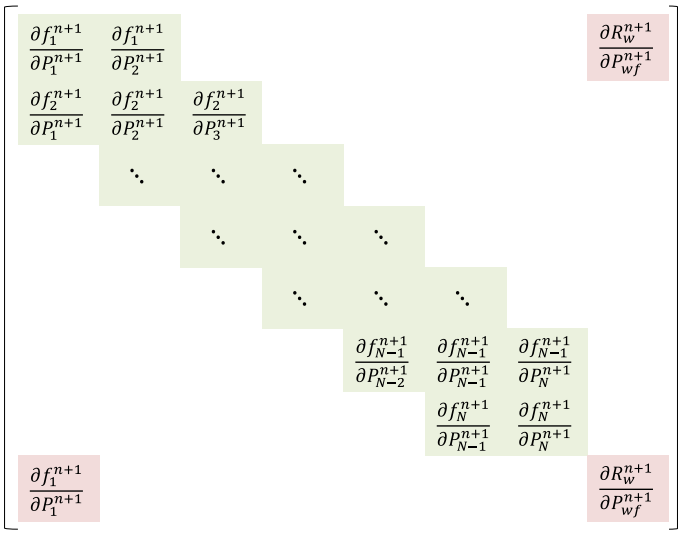

Fig. B.2 – Jacobian of the single-phase single-porosity model with well residual terms

Notice that the production rate is specified, thus this is a fixed value. The elements constructed in the Jacobian are the following three derivatives.

$$\frac{\partial f_1^{n+1}}{\partial P_{wf}^{n+1}}, \frac{\partial R_w^{n+1}}{\partial P_1^{n+1}}, \frac{\partial R_w^{n+1}}{\partial P_{wf}^{n+1}} \tag{B.20}$$

The derivative of the finite difference equation of the first grid with respect to P_{wf} is

$$\frac{\partial f_1^{n+1}}{\partial P_{wf}^{n+1}} = \frac{w_1(\mu c_t)_{\text{init},1}}{\tau_1 - \tau_{\text{well}}} \left(\frac{1}{B\mu}\right)_1^{n+1} \tag{B.21}$$

The derivative of the well residual term with respect to P_1 is given by

$$\frac{\partial R_w^{n+1}}{\partial P_1^{n+1}} = \frac{w_1(\mu c_t)_{\text{init},1}}{\tau_1 - \tau_{\text{well}}} \left[\left(\frac{1}{B\mu}\right)_1^{n+1} + \frac{\partial}{\partial P_1^{n+1}} \left(\frac{1}{B\mu}\right)_1^{n+1} \left(P_1^{n+1} - P_{wf}^{n+1}\right) \right] \tag{B.22}$$

The derivative of the well residual term with respect to P_1 is given by

$$\frac{\partial R_w^{n+1}}{\partial P_{wf}^{n+1}} = -\frac{w_1(\mu c_t)_{\text{init},1}}{\tau_1 - \tau_{\text{well}}} \left(\frac{1}{B\mu}\right)_1^{n+1} \tag{B.23}$$

B.3 Derivatives in Dual-Porosity Model

In the dual-porosity model, there are two types of finite difference equations. One is the discretized flow equation of the fracture grids. Another one is the discretized flow equation of the matrix grids. These are simply expressed as follows.

$$f_{f,i}^{n+1} = F_{f,i}^{n+1} - A_{f,i}^{n+1} + A_{f,i}^{n} + W_{f,i}^{n+1} - v_i \Delta\tau_i F_{FM,i}^{n+1} = 0 \tag{B.24}$$

$$f_{m,i}^{n+1} = -A_{m,i}^{n+1} + A_{m,i}^{n} + F_{FM,i}^{n+1} = 0 \tag{B.25}$$

where $v_i \Delta\tau_i$ represents the 'bulk' volume of the grid block i. The fracture-matrix transfer term $F_{FM,i}^{n+1}$ is defined by

$$F_{FM,i}^{n+1} = \sigma k_m \left(\frac{1}{B\mu}\right)_{up}^{n+1} \left(P_{f,i}^{n+1} - P_{m,i}^{n+1}\right) \tag{B.26}$$

Notice that the shape factor σ and the matrix permeability k_m are the uniform parameter throughout all the grid blocks. **Eq. (B.24)** corresponds to **Eq. (2.60)** as well as **Eq.**

(B.25) corresponds to **Eq. (2.62)**. The primary variable is the fracture pressure and the matrix pressure ($2M \times 1$ vector).

$$\mathbf{y}^{n+1} = \left[P_{f,1}^{n+1}, P_{f,2}^{n+1}, \dots, P_{f,M}^{n+1}, P_{m,1}^{n+1}, P_{m,2}^{n+1}, \dots, P_{m,M}^{n+1}\right]^T \tag{B.27}$$

The residual term is comprised of the finite difference equations of the fracture grids (**Eq. (B.24)**) and of the matrix grids (**Eq. (B.25)**) ($2M \times 1$ vector).

$$\mathbf{R}^{n+1} = \left[f_{f,1}^{n+1}, f_{f,2}^{n+1}, \dots, f_{f,M}^{n+1}, f_{m,1}^{n+1}, f_{m,2}^{n+1}, \dots, f_{m,M}^{n+1}\right]^T \tag{B.28}$$

Hence, the Jacobian is obtained by differentiating **Eq. (B.28)** by **Eq. (B.27)** ($2M \times 2M$ matrix). The matrix form is shown in **Fig. B.3**.

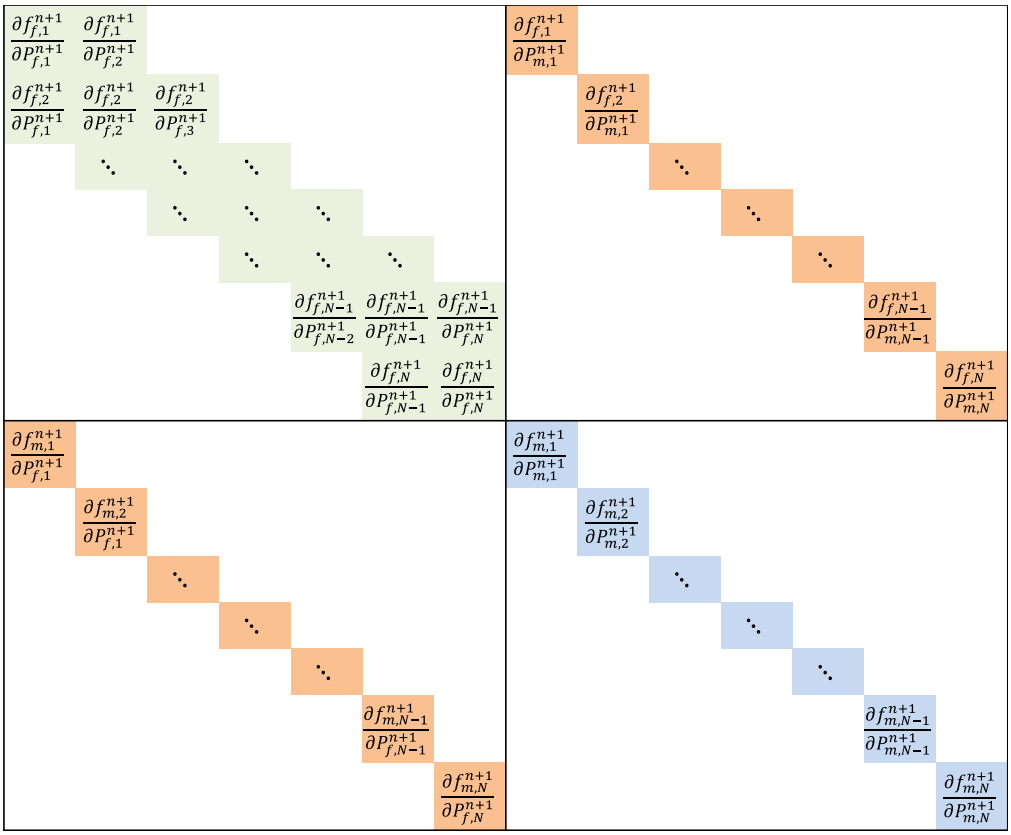

Fig. B.3 – Jacobian of the single-phase dual-porosity model

The resulting Jacobian elements are classified to four types of the derivatives.

(1) The derivative of fracture eq. (f_f) with respect to fracture pressure (P_f)

(2) The derivative of fracture eq. (f_f) with respect to matrix pressure (P_m)

(3) The derivative of matrix eq. (f_m) with respect to fracture pressure (P_f)

(4) The derivative of matrix eq. (f_m) with respect to matrix pressure (P_m)

Based on **Eqs. (B.27)** and **(B.28)**, these derivatives can be written as follows.

$$\frac{\partial f_{f,i}^{n+1}}{\partial P_{f,i}^{n+1}} = \frac{\partial F_{f,i}^{n+1}}{\partial P_{f,i}^{n+1}} - \frac{\partial A_{f,i}^{n+1}}{\partial P_{f,i}^{n+1}} + \frac{\partial W_{f,i}^{n+1}}{\partial P_{f,i}^{n+1}} - v_i \Delta\tau_i \frac{\partial F_{FM,i}^{n+1}}{\partial P_{f,i}^{n+1}} \tag{B.29}$$

$$\frac{\partial f_{f,i}^{n+1}}{\partial P_{f,i\pm1}^{n+1}} = \frac{\partial F_{f,i}^{n+1}}{\partial P_{f,i\pm1}^{n+1}} \tag{B.30}$$

$$\frac{\partial f_{f,i}^{n+1}}{\partial P_{m,i}^{n+1}} = -v_i \Delta\tau_i \frac{\partial F_{FM,i}^{n+1}}{\partial P_{m,i}^{n+1}} \tag{B.31}$$

$$\frac{\partial f_{m,i}^{n+1}}{\partial P_{f,i}^{n+1}} = \frac{\partial F_{FM,i}^{n+1}}{\partial P_{f,i}^{n+1}} \tag{B.32}$$

$$\frac{\partial f_{m,i}^{n+1}}{\partial P_{m,i}^{n+1}} = -\frac{\partial A_{m,i}^{n+1}}{\partial P_{m,i}^{n+1}} + \frac{\partial F_{FM,i}^{n+1}}{\partial P_{m,i}^{n+1}} \tag{B.33}$$

The upper left part ($M \times M$ matrix) in **Fig B.3** is comprised of **Eq. (B.29)** (diagonal term) and **Eq. (B.30)** (off-diagonal term). The upper right and the lower left parts ($M \times M$ matrices) in **Fig B.3** are the diagonal matrix given by **Eq. (B.31)** and **(B.32)**, respectively. The lower right part ($M \times M$ matrix) is also the diagonal matrix obtained by **Eq. (B.33)**.

In **Eq. (B.29)**, the first partial derivative in the right hand side is calculated using **Eq. (B.3)**. The second derivative is obtained by **Eq. (B.7)**. The third derivative is given by

Eq. (B.9). The forth derivative is calculated by differentiating the fracture-matrix transfer term (**Eq. (2.61)**) by the fracture pressure.

$$\frac{\partial F_{FM,i}^{n+1}}{\partial P_{f,i}^{n+1}} = \sigma k_m \left[\left(\frac{1}{B\mu}\right)_{up}^{n+1} + \frac{\partial}{\partial P_{f,i}^{n+1}} \left(\frac{1}{B\mu}\right)_{up}^{n+1} \left(P_{f,i}^{n+1} - P_{m,i}^{n+1}\right) \right] \tag{B.34}$$

The upstream direction is determined by comparing the fracture pressure and matrix pressure of the grid i. If the fracture pressure is larger than the matrix pressure ($P_{f,i}^{n+1} > P_{m,i}^{n+1}$), the derivative of the flow mobility in **Eq. (B.34)** is

$$\frac{\partial}{\partial P_{f,i}^{n+1}} \left(\frac{1}{B\mu}\right)_{up}^{n+1} = -\frac{1}{B_i^{n+1}\mu_i^{n+1^2}} \frac{\partial \mu_i^{n+1}}{\partial P_{f,i}^{n+1}} - \frac{1}{B_i^{n+1^2}\mu_i^{n+1}} \frac{\partial B_i^{n+1}}{\partial P_{f,i}^{n+1}} \tag{B.35}$$

In contrast, if the fracture pressure is larger than the matrix pressure ($P_{f,i}^{n+1} > P_{m,i}^{n+1}$), the derivative of the mobility is zero.

The partial derivative of **Eq. (B.30)** is given by **Eqs. (B.12)** and **(B.13)**. The partial derivative in the right hand side of **Eq. (B.31)** is calculated by

$$\frac{\partial F_{FM,i}^{n+1}}{\partial P_{m,i}^{n+1}} = \sigma k_m \left[-\left(\frac{1}{B\mu}\right)_{up}^{n+1} + \frac{\partial}{\partial P_{m,i}^{n+1}} \left(\frac{1}{B\mu}\right)_{up}^{n+1} \left(P_{f,i}^{n+1} - P_{m,i}^{n+1}\right) \right] \tag{B.36}$$

The derivative of the flow mobility in **Eq. (B.36)** follows the up-winding scheme.

The first partial derivative of the right hand side of **Eq. (B.33)** is given by

$$\frac{\partial A_{m,i}^{n+1}}{\partial P_{m,i}^{n+1}} = \frac{1}{\Delta t^{n+1}} \left(\frac{1}{B_i^{n+1}} \frac{\partial \phi_m^{n+1}}{\partial P_{m,i}^{n+1}} - \frac{\phi_m^{n+1}}{B_i^{n+1^2}} \frac{\partial B_i^{n+1}}{\partial P_{m,i}^{n+1}} \right) \tag{B.37}$$

where the derivative of the matrix porosity with respect to the matrix pressure is

$$\frac{\partial \phi_m^{n+1}}{\partial P_{m,i}^{n+1}} = \frac{\partial}{\partial P_{m,i}^{n+1}} \left(\phi_m^0 \exp\left[c_r\left(P_{m,i}^{n+1} - P_{ref}\right)\right]\right) = c_r \phi_m^0 \tag{B.38}$$

where ϕ_m^0 is the matrix porosity at the reference pressure. If the production rate is specified, we impose the well residual term in the residual vector to implicitly solve the bottom-hole pressure. In the dual-porosity case, the well residual equation is added in the Jacobian as shown in **Fig. B.4**. Because the well is placed on the fracture coordinate only, the well residual term is calculated using the same equation with the single-porosity model (**Eq. (B.19)**). The derivatives in the Jacobian is given by **Eqs. (B.21)** – **(B.23)**.

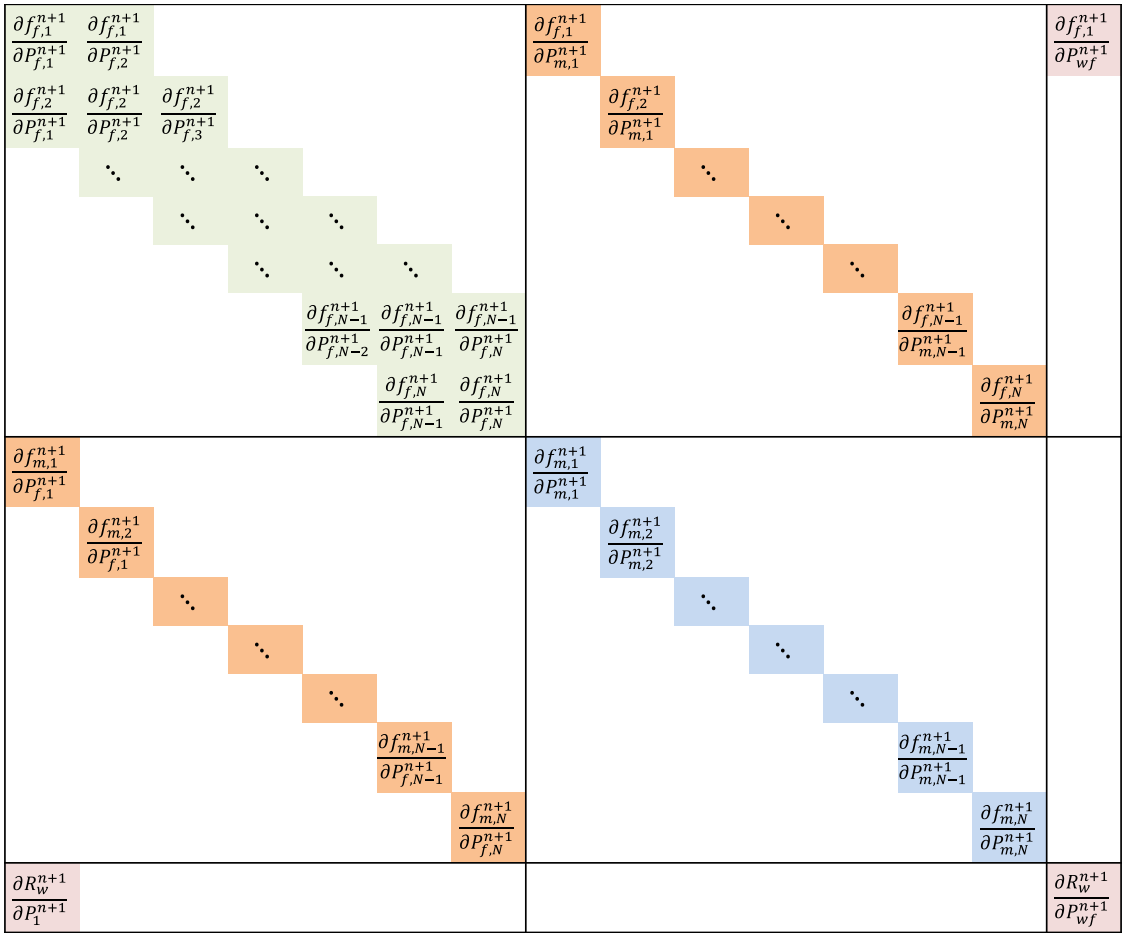

Fig. B.4 – Jacobian of the single-phase dual-porosity model with well residual terms

B.4 Derivatives in Triple-Continuum Model

In the triple-continuum model, we solve three primary variables – fracture pressure P_f, matrix pressure P_m, and gas concentration in the organic matter C_k. The coordinate is tripled as shown in **Fig. 2.6** and the resulting governing equations are divided into the three types of the finite difference equations.

$$f_{f,i}^{n+1} = F_{f,i}^{n+1} - A_{f,i}^{n+1} + A_{f,i}^{n} + W_{f,i}^{n+1} - v_i \Delta\tau_i F_{FM,i}^{n+1} = 0 \tag{B.39}$$

$$f_{m,i}^{n+1} = -A_{m,i}^{n+1} + A_{m,i}^{n} + F_{FM,i}^{n+1} - F_{MK,i}^{n+1} = 0 \tag{B.40}$$

$$f_{k,i}^{n+1} = -A_{k,i}^{n+1} + A_{m,i}^{n} + F_{MK,i}^{n+1} = 0 \tag{B.41}$$

Where $v_i \Delta\tau_i$ represents the 'bulk' volume of the grid block i. The matrix-Kerogen diffusive transfer term $F_{MK,i}^{n+1}$ is defined by

$$F_{MK,i}^{n+1} = \sigma_{MK} D_c \left(C_{m,i}^{n+1} - C_{k,i}^{n+1} \right) \tag{B.42}$$

Notice that the shape factor σ_{MK} and the diffusion coefficient D_c are the uniform parameter throughout all the grid blocks. The gas concentration of the matrix grid $C_{m,i}$ is given by the Langmuir adsorption isotherm (**Eq. (2.80)**). **Eq. (B.39)** corresponds to the fracture finite difference equation (**Eq. (2.86)**). **Eq. (B.40)** represents the discretized matrix equation (**Eq. (2.87)**). **Eq. (B.41)** expresses the Kerogen finite difference equation (**Eq. (2.88)**). The primary solution vector consists of a $3M \times 1$ vector.

$$\mathbf{y}^{n+1} = \left[P_{f,1}^{n+1}, P_{f,2}^{n+1}, \dots, P_{f,M}^{n+1}, P_{m,1}^{n+1}, P_{m,2}^{n+1}, \dots, P_{m,M}^{n+1}, C_{k,1}^{n+1}, C_{k,2}^{n+1}, \dots, C_{k,M}^{n+1} \right]^T \tag{B.43}$$

The residual term is comprised of the following equations ($3M \times 1$ vector).

$$\mathbf{R}^{n+1} = \left[f_{f,1}^{n+1}, f_{f,2}^{n+1}, \dots, f_{f,M}^{n+1}, f_{m,1}^{n+1}, f_{m,2}^{n+1}, \dots, f_{m,M}^{n+1}, f_{k,1}^{n+1}, f_{k,2}^{n+1}, \dots, f_{k,M}^{n+1} \right]^T \tag{B.44}$$

Hence, the Jacobian is obtained by differentiating **Eq. (B.43)** by **Eq. (B.42)** ($3M \times 3M$ matrix). The matrix form is shown in **Fig. B.5**.

The resulting Jacobian elements are classified to four types of the derivatives.

(1) The derivative of fracture eq. (f_f) with respect to fracture pressure (P_f)

(2) The derivative of fracture eq. (f_f) with respect to matrix pressure (P_m)

(3) The derivative of fracture eq. (f_f) with respect to Kerogen gas density (C_k)

(4) The derivative of matrix eq. (f_m) with respect to fracture pressure (P_f)

(5) The derivative of matrix eq. (f_m) with respect to matrix pressure (P_m)

(6) The derivative of matrix eq. (f_m) with respect to Kerogen gas density (C_k)

(7) The derivative of Kerogen eq. (f_k) with respect to fracture pressure (P_f)

(8) The derivative of Kerogen eq. (f_k) with respect to matrix pressure (P_m)

(9) The derivative of Kerogen eq. (f_k) with respect to Kerogen gas density (C_k)

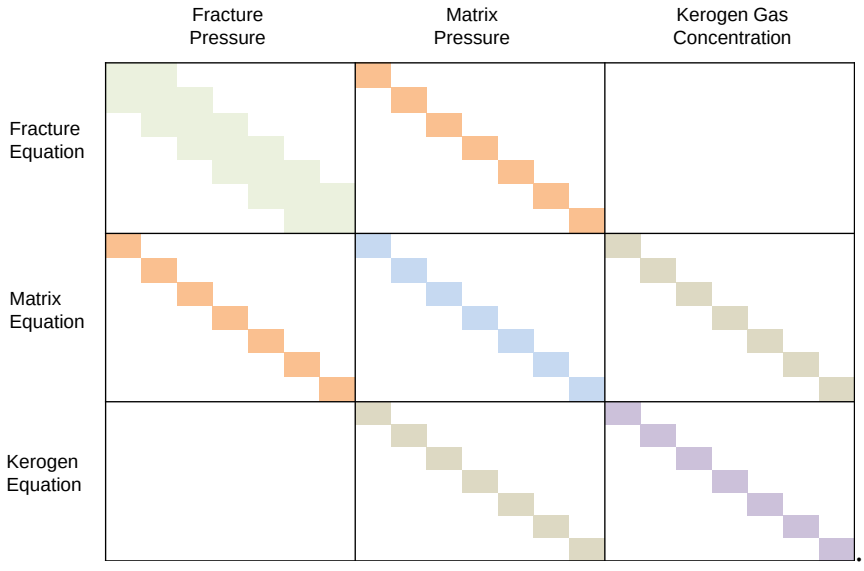

Fig. B.5 – Jacobian of the single-phase triple-continuum model

Each matrix element of the Jacobian is calculated as follows.

$$\frac{\partial f_{f,i}^{n+1}}{\partial P_{f,i}^{n+1}} = \frac{\partial F_{f,i}^{n+1}}{\partial P_{f,i}^{n+1}} - \frac{\partial A_{f,i}^{n+1}}{\partial P_{f,i}^{n+1}} + \frac{\partial W_{f,i}^{n+1}}{\partial P_{f,i}^{n+1}} - v_i \Delta\tau_i \frac{\partial F_{FM,i}^{n+1}}{\partial P_{f,i}^{n+1}} \tag{B.45}$$

$$\frac{\partial f_{f,i}^{n+1}}{\partial P_{f,i\pm1}^{n+1}} = \frac{\partial F_{f,i}^{n+1}}{\partial P_{f,i\pm1}^{n+1}} \tag{B.46}$$

$$\frac{\partial f_{f,i}^{n+1}}{\partial P_{m,i}^{n+1}} = -v_i \Delta\tau_i \frac{\partial F_{FM,i}^{n+1}}{\partial P_{m,i}^{n+1}} \tag{B.47}$$

$$\frac{\partial f_{f,i}^{n+1}}{\partial C_{k,i}^{n+1}} = 0 \tag{B.48}$$

$$\frac{\partial f_{m,i}^{n+1}}{\partial P_{f,i}^{n+1}} = \frac{\partial F_{FM,i}^{n+1}}{\partial P_{f,i}^{n+1}} \tag{B.49}$$

$$\frac{\partial f_{m,i}^{n+1}}{\partial P_{m,i}^{n+1}} = -\frac{\partial A_{m,i}^{n+1}}{\partial P_{m,i}^{n+1}} + \frac{\partial F_{FM,i}^{n+1}}{\partial P_{m,i}^{n+1}} - \frac{\partial F_{MK,i}^{n+1}}{\partial P_{m,i}^{n+1}} \tag{B.50}$$

$$\frac{\partial f_{m,i}^{n+1}}{\partial C_{k,i}^{n+1}} = -\frac{\partial F_{MK,i}^{n+1}}{\partial C_{k,i}^{n+1}} \tag{B.51}$$

$$\frac{\partial f_{k,i}^{n+1}}{\partial P_{f,i}^{n+1}} = 0 \tag{B.52}$$

$$\frac{\partial f_{k,i}^{n+1}}{\partial P_{m,i}^{n+1}} = \frac{\partial F_{MK,i}^{n+1}}{\partial P_{m,i}^{n+1}} \tag{B.53}$$

$$\frac{\partial f_{k,i}^{n+1}}{\partial C_{k,i}^{n+1}} = -\frac{\partial A_{k,i}^{n+1}}{\partial C_{k,i}^{n+1}} + \frac{\partial F_{MK,i}^{n+1}}{\partial C_{k,i}^{n+1}} \tag{B.54}$$

Notice that all the derivatives in **Eqs. (B.45)** – **(B.54)** are given in the previous dual-porosity model except for the following four derivatives.

In **Eq. (B.50)**, the derivative of the matrix accumulation term with respect to the matrix pressure is

$$\frac{\partial A_{m,i}^{n+1}}{\partial P_{m,i}^{n+1}} = \frac{1}{\Delta t^{n+1}}\left(\frac{1}{B_i^{n+1}}\frac{\partial \phi_m^{n+1}}{\partial P_{m,i}^{n+1}} - \frac{\phi_m^{n+1}}{B_i^{n+1^2}}\frac{\partial B_i^{n+1}}{\partial P_{m,i}^{n+1}} + \frac{\partial C_{m,i}^{n+1}}{\partial P_{m,i}^{n+1}}\right) \tag{B.55}$$

where the derivative of the matrix gas concentration with respect to the matrix pressure is

$$\frac{\partial C_{m,i}^{n+1}}{\partial P_{m,i}^{n+1}} = -\frac{V_L P_L}{\left(P_L + P_{m,i}^{n+1}\right)^2} \tag{B.56}$$

In **Eqs. (B.50)** and **(B.53)**, the derivative of the matrix-Kerogen transfer term with respect to the matrix pressure is

$$\frac{\partial F_{MK,i}^{n+1}}{\partial P_{m,i}^{n+1}} = \sigma_{MK} D_c \frac{\partial C_{m,i}^{n+1}}{\partial P_{m,i}^{n+1}} \tag{B.57}$$

In **Eqs. (B.51)** and **(B.54)**, the derivative of the matrix-Kerogen transfer term with respect to the Kerogen gas concentration is

$$\frac{\partial F_{MK,i}^{n+1}}{\partial C_{k,i}^{n+1}} = -\sigma_{MK} D_c \tag{B.58}$$

In **Eqs. (B.54)**, the derivative of the Kerogen accumulation term with respect to the Kerogen gas concentration is

$$\frac{\partial A_{k,i}^{n+1}}{\partial C_{k,i}^{n+1}} = \frac{1}{\Delta t^{n+1}} \tag{B.59}$$

APPENDIX C

CONSTRUCTION OF JACOBIAN FOR BLACKOIL FLOWS

C.1 Derivatives of Finite Difference Equation

In a three-phase blackoil simulation, there are three finite difference equations and the corresponding three primary variables in each grid. The primary variables are simultaneously solved using the fully implicit method (FIM) in this study. The finite difference equations are written as follows.

$$f_{w,i}^{n+1} = F_{w,i}^{n+1} - A_{w,i}^{n+1} + A_{w,i}^{n} + W_{w,i}^{n+1} = 0 \tag{C.1}$$

$$f_{o,i}^{n+1} = F_{o,i}^{n+1} - A_{o,i}^{n+1} + A_{o,i}^{n} + W_{o,i}^{n+1} = 0 \tag{C.2}$$

$$f_{g,i}^{n+1} = F_{g,i}^{n+1} - A_{g,i}^{n+1} + A_{g,i}^{n} + W_{g,i}^{n+1} = 0 \tag{C.3}$$

Eqs. (C.1) – **(C.3)** corresponds to **Eqs. (3.56)** – **(3.58)**, respectively. The Jacobian forms a block-tridiagonal matrix as shown in **Fig. C.1**.

$$\begin{bmatrix} \mathbf{A}_1^{n+1} & \mathbf{B}_1^{n+1} & & & & & \\ \mathbf{C}_2^{n+1} & \mathbf{A}_2^{n+1} & \mathbf{B}_2^{n+1} & & & & \\ & \ddots & \ddots & \ddots & & & \\ & & \ddots & \ddots & \ddots & & \\ & & & \ddots & \ddots & \ddots & \\ & & & & \mathbf{C}_{N-1}^{n+1} & \mathbf{A}_{N-1}^{n+1} & \mathbf{B}_{N-1}^{n+1} \\ & & & & & \mathbf{C}_N^{n+1} & \mathbf{A}_N^{n+1} \end{bmatrix}$$

Fig. C.1 – Jacobian of the multiphase single-porosity model

In the Jacobian, the elements in the block-tridiagonal band consist of a 3×3 matrix as shown in **Fig. C.2**.

$$\boldsymbol{A_i} = \begin{bmatrix} \frac{\partial f_{w,i}}{\partial P_i} & \frac{\partial f_{w,i}}{\partial S_{w,i}} & \frac{\partial f_{w,i}}{\partial S_{g,i}} \\ \frac{\partial f_{o,i}}{\partial P_i} & \frac{\partial f_{o,i}}{\partial S_{w,i}} & \frac{\partial f_{o,i}}{\partial S_{g,i}} \\ \frac{\partial f_{g,i}}{\partial P_i} & \frac{\partial f_{g,i}}{\partial S_{w,i}} & \frac{\partial f_{g,i}}{\partial S_{g,i}} \end{bmatrix} \quad \boldsymbol{B_i} = \begin{bmatrix} \frac{\partial f_{w,i}}{\partial P_{i+1}} & \frac{\partial f_{w,i}}{\partial S_{w,i+1}} & \frac{\partial f_{w,i}}{\partial S_{g,i+1}} \\ \frac{\partial f_{o,i}}{\partial P_{i+1}} & \frac{\partial f_{o,i}}{\partial S_{w,i+1}} & \frac{\partial f_{o,i}}{\partial S_{g,i+1}} \\ \frac{\partial f_{g,i}}{\partial P_{i+1}} & \frac{\partial f_{g,i}}{\partial S_{w,i+1}} & \frac{\partial f_{g,i}}{\partial S_{g,i+1}} \end{bmatrix} \quad \boldsymbol{C_i} = \begin{bmatrix} \frac{\partial f_{w,i}}{\partial P_{i-1}} & \frac{\partial f_{w,i}}{\partial S_{w,i-1}} & \frac{\partial f_{w,i}}{\partial S_{g,i-1}} \\ \frac{\partial f_{o,i}}{\partial P_{i-1}} & \frac{\partial f_{o,i}}{\partial S_{w,i-1}} & \frac{\partial f_{o,i}}{\partial S_{g,i-1}} \\ \frac{\partial f_{g,i}}{\partial P_{i-1}} & \frac{\partial f_{g,i}}{\partial S_{w,i-1}} & \frac{\partial f_{g,i}}{\partial S_{g,i-1}} \end{bmatrix}$$

(a) Diagonal element (b) Upper non-diagonal element (c) Lower non-diagonal element

Fig. C.2 – Block diagonal elements in the Jacobian

The elements described in **Fig. C.2** are obtained by differentiating **Eqs. (C.1)** – **(C.3)** by the pressure (P_i^{n+1}), water saturation ($S_{w,i}^{n+1}$), and gas saturation ($S_{g,i}^{n+1}$) of grid i.

$$\frac{\partial f_{\alpha,i}^{n+1}}{\partial P_i^{n+1}} = \frac{\partial F_{\alpha,i}^{n+1}}{\partial P_i^{n+1}} - \frac{\partial A_{\alpha,i}^{n+1}}{\partial P_i^{n+1}} + \frac{\partial W_{\alpha,i}^{n+1}}{\partial P_i^{n+1}} \tag{C.4}$$

$$\frac{\partial f_{\alpha,i}^{n+1}}{\partial S_{w,i}^{n+1}} = \frac{\partial F_{\alpha,i}^{n+1}}{\partial S_{w,i}^{n+1}} - \frac{\partial A_{\alpha,i}^{n+1}}{\partial S_{w,i}^{n+1}} + \frac{\partial W_{\alpha,i}^{n+1}}{\partial S_{w,i}^{n+1}} \tag{C.5}$$

$$\frac{\partial f_{\alpha,i}^{n+1}}{\partial S_{g,i}^{n+1}} = \frac{\partial F_{\alpha,i}^{n+1}}{\partial S_{g,i}^{n+1}} - \frac{\partial A_{\alpha,i}^{n+1}}{\partial S_{g,i}^{n+1}} + \frac{\partial W_{\alpha,i}^{n+1}}{\partial S_{g,i}^{n+1}} \tag{C.6}$$

where α is phase ($\alpha = o, w, g$). When the grid pressure is lower than the bubble-point pressure ($P_i^{n+1} < P_b$), the free gas phase does not exist in the grid ($S_{g,i}^{n+1} = 0$), whereas the oil phase contains the solution gas ($R_{s,i}^{n+1} > 0$). In such situations, we change the

primary variable from gas saturation ($S_{g,i}^{n+1}$) to solution gas ratio ($R_{s,i}^{n+1}$). Thus **Eq. (C.6)** is replaced by the following partial differential equation.

$$\frac{\partial f_{\alpha,i}^{n+1}}{\partial R_{s,i}^{n+1}} = \frac{\partial F_{\alpha,i}^{n+1}}{\partial R_{s,i}^{n+1}} - \frac{\partial A_{\alpha,i}^{n+1}}{\partial R_{s,i}^{n+1}} + \frac{\partial W_{\alpha,i}^{n+1}}{\partial R_{s,i}^{n+1}} \tag{C.7}$$

The derivatives of the flux term in **Eqs. (C.4)** – **(C.7)** are

$$\frac{\partial F_{\alpha,i}^{n+1}}{\partial P_i^{n+1}} = \frac{\partial T_{\alpha,i-1/2}^{n+1}}{\partial P_i^{n+1}}(P_{i-1}^{n+1} - P_i^{n+1}) + \frac{\partial T_{\alpha,i+1/2}^{n+1}}{\partial P_i^{n+1}}(P_{i+1}^{n+1} - P_i^{n+1}) - \left(T_{\alpha,i-1/2}^{n+1} + T_{\alpha,i+1/2}^{n+1}\right) \tag{C.8}$$

$$\frac{\partial F_{\alpha,i}^{n+1}}{\partial S_{w,i}^{n+1}} = \frac{\partial T_{\alpha,i-1/2}^{n+1}}{\partial S_{w,i}^{n+1}}(P_{i-1}^{n+1} - P_i^{n+1}) + \frac{\partial T_{\alpha,i+1/2}^{n+1}}{\partial S_{w,i}^{n+1}}(P_{i+1}^{n+1} - P_i^{n+1}) \tag{C.9}$$

$$\frac{\partial F_{\alpha,i}^{n+1}}{\partial S_{g,i}^{n+1}} = \frac{\partial T_{\alpha,i-1/2}^{n+1}}{\partial S_{g,i}^{n+1}}(P_{i-1}^{n+1} - P_i^{n+1}) + \frac{\partial T_{\alpha,i+1/2}^{n+1}}{\partial S_{g,i}^{n+1}}(P_{i+1}^{n+1} - P_i^{n+1}) \tag{C.10}$$

$$\frac{\partial F_{\alpha,i}^{n+1}}{\partial R_{s,i}^{n+1}} = \frac{\partial T_{\alpha,i-1/2}^{n+1}}{\partial R_{s,i}^{n+1}}(P_{i-1}^{n+1} - P_i^{n+1}) + \frac{\partial T_{\alpha,i+1/2}^{n+1}}{\partial R_{s,i}^{n+1}}(P_{i+1}^{n+1} - P_i^{n+1}) \tag{C.11}$$

where the derivatives of the phase transmissibility in **Eqs. (C.8)** – **(C.11)** are

$$\frac{\partial T_{\alpha,i\pm1/2}^{n+1}}{\partial P_i^{n+1}} = \frac{w_{i\pm1/2}}{\Delta\tau_{i\pm1/2}}\left(\frac{c_t}{\lambda_t}\right)_{\text{init},i\pm1/2}\frac{\partial \lambda_{\alpha,up}^{n+1}}{\partial P_i^{n+1}} \tag{C.12}$$

$$\frac{\partial T_{\alpha,i\pm1/2}^{n+1}}{\partial S_{w,i}^{n+1}} = \frac{w_{i\pm1/2}}{\Delta\tau_{i\pm1/2}}\left(\frac{c_t}{\lambda_t}\right)_{\text{init},i\pm1/2}\frac{\partial \lambda_{\alpha,up}^{n+1}}{\partial S_{w,i}^{n+1}} \tag{C.13}$$

$$\frac{\partial T_{\alpha,i\pm1/2}^{n+1}}{\partial S_{g,i}^{n+1}} = \frac{w_{i\pm1/2}}{\Delta\tau_{i\pm1/2}}\left(\frac{c_t}{\lambda_t}\right)_{\text{init},i\pm1/2}\frac{\partial \lambda_{\alpha,up}^{n+1}}{\partial S_{g,i}^{n+1}} \tag{C.14}$$

$$\frac{\partial T_{\alpha,i\pm1/2}^{n+1}}{\partial R_{s,i}^{n+1}} = \frac{w_{i\pm1/2}}{\Delta\tau_{i\pm1/2}}\left(\frac{c_t}{\lambda_t}\right)_{\text{init},i\pm1/2}\frac{\partial \lambda_{\alpha,up}^{n+1}}{\partial R_{s,i}^{n+1}} \tag{C.15}$$

If the upstream grid is the neighbor grid, the derivatives of the phase mobility in **Eqs. (C.12) - (C.15)** are zero.

$$\frac{\partial \lambda_{\alpha,i\pm1}^{n+1}}{\partial P_i^{n+1}} = 0, \quad \frac{\partial \lambda_{\alpha,i\pm1}^{n+1}}{\partial S_{w,i}^{n+1}} = 0, \quad \frac{\partial \lambda_{\alpha,i\pm1}^{n+1}}{\partial S_{g,i}^{n+1}} = 0, \quad \frac{\partial \lambda_{\alpha,i\pm1}^{n+1}}{\partial R_{s,i}^{n+1}} = 0 \tag{C.16}$$

If the upstream grid is i, the derivatives of the phase transmissibility in **Eqs. (C.12) - (C.15)** are

$$\frac{\partial \lambda_{w,i}^{n+1}}{\partial P_i^{n+1}} = -\frac{k_{rw,i}^{n+1}}{B_{w,i}^{n+1^2}\mu_{w,i}^{n+1}}\frac{\partial B_{w,i}^{n+1}}{\partial P_i^{n+1}} - \frac{k_{rw,i}^{n+1}}{B_{w,i}^{n+1}\mu_{w,i}^{n+1^2}}\frac{\partial \mu_{w,i}^{n+1}}{\partial P_i^{n+1}} \tag{C.17}$$

$$\frac{\partial \lambda_{w,i}^{n+1}}{\partial S_{w,i}^{n+1}} = \frac{1}{B_{w,i}^{n+1}\mu_{w,i}^{n+1}}\frac{\partial k_{rw,i}^{n+1}}{\partial S_{w,i}^{n+1}} \tag{C.18}$$

$$\frac{\partial \lambda_{w,i}^{n+1}}{\partial S_{g,i}^{n+1}} = 0 \tag{C.19}$$

$$\frac{\partial \lambda_{w,i}^{n+1}}{\partial R_{s,i}^{n+1}} = 0 \tag{C.20}$$

$$\begin{aligned}\frac{\partial \lambda_{o,i}^{n+1}}{\partial P_i^{n+1}} = &-\frac{k_{ro,i}^{n+1}}{B_{o,i}^{n+1^2}\mu_{o,i}^{n+1}}\frac{\partial B_{o,i}^{n+1}}{\partial P_i^{n+1}} - \frac{k_{ro,i}^{n+1}}{B_{o,i}^{n+1}\mu_{o,i}^{n+1^2}}\frac{\partial \mu_{o,i}^{n+1}}{\partial P_i^{n+1}} + \frac{\partial R_{v,i}^{n+1}}{\partial P_i^{n+1}}\frac{k_{rg,i}^{n+1}}{B_{g,i}^{n+1}\mu_{g,i}^{n+1}} \\ &- R_{v,i}^{n+1}\left(\frac{k_{rg,i}^{n+1}}{B_{g,i}^{n+1^2}\mu_{g,i}^{n+1}}\frac{\partial B_{g,i}^{n+1}}{\partial P_i^{n+1}} + \frac{k_{rg,i}^{n+1}}{B_{g,i}^{n+1}\mu_{g,i}^{n+1^2}}\frac{\partial \mu_{g,i}^{n+1}}{\partial P_i^{n+1}}\right)\end{aligned} \tag{C.21}$$

$$\frac{\partial \lambda_{o,i}^{n+1}}{\partial S_{w,i}^{n+1}} = \frac{1}{B_{o,i}^{n+1}\mu_{o,i}^{n+1}}\frac{\partial k_{ro,i}^{n+1}}{\partial S_{w,i}^{n+1}} + R_{v,i}^{n+1}\frac{1}{B_{g,i}^{n+1}\mu_{g,i}^{n+1}}\frac{\partial k_{rg,i}^{n+1}}{\partial S_{w,i}^{n+1}} \tag{C.22}$$

$$\frac{\partial \lambda_{o,i}^{n+1}}{\partial S_{g,i}^{n+1}} = \frac{1}{B_{o,i}^{n+1}\mu_{o,i}^{n+1}}\frac{\partial k_{ro,i}^{n+1}}{\partial S_{g,i}^{n+1}} + R_{v,i}^{n+1}\frac{1}{B_{g,i}^{n+1}\mu_{g,i}^{n+1}}\frac{\partial k_{rg,i}^{n+1}}{\partial S_{g,i}^{n+1}} \tag{C.23}$$

$$\frac{\partial \lambda_{o,i}^{n+1}}{\partial R_{s,i}^{n+1}} = 0 \tag{C.24}$$

$$\frac{\partial \lambda_{g,i}^{n+1}}{\partial P_i^{n+1}} = -\frac{k_{rg,i}^{n+1}}{{B_{g,i}^{n+1}}^2 \mu_{g,i}^{n+1}} \frac{\partial B_{g,i}^{n+1}}{\partial P_i^{n+1}} - \frac{k_{rg,i}^{n+1}}{B_{g,i}^{n+1} {\mu_{g,i}^{n+1}}^2} \frac{\partial \mu_{g,i}^{n+1}}{\partial P_i^{n+1}} + \frac{\partial R_{s,i}^{n+1}}{\partial P_i^{n+1}} \frac{k_{ro,i}^{n+1}}{B_{o,i}^{n+1} \mu_{o,i}^{n+1}} - R_{s,i}^{n+1} \left(\frac{k_{ro,i}^{n+1}}{{B_{o,i}^{n+1}}^2 \mu_{o,i}^{n+1}} \frac{\partial B_{o,i}^{n+1}}{\partial P_i^{n+1}} + \frac{k_{ro,i}^{n+1}}{B_{o,i}^{n+1} {\mu_{o,i}^{n+1}}^2} \frac{\partial \mu_{o,i}^{n+1}}{\partial P_i^{n+1}} \right) \tag{C.25}$$

$$\frac{\partial \lambda_{g,i}^{n+1}}{\partial S_{w,i}^{n+1}} = \frac{1}{B_{g,i}^{n+1} \mu_{g,i}^{n+1}} \frac{\partial k_{rg,i}^{n+1}}{\partial S_{w,i}^{n+1}} + R_{s,i}^{n+1} \frac{1}{B_{o,i}^{n+1} \mu_{o,i}^{n+1}} \frac{\partial k_{ro,i}^{n+1}}{\partial S_{w,i}^{n+1}} \tag{C.26}$$

$$\frac{\partial \lambda_{g,i}^{n+1}}{\partial S_{g,i}^{n+1}} = \frac{1}{B_{g,i}^{n+1} \mu_{g,i}^{n+1}} \frac{\partial k_{rg,i}^{n+1}}{\partial S_{g,i}^{n+1}} + R_{s,i}^{n+1} \frac{1}{B_{o,i}^{n+1} \mu_{o,i}^{n+1}} \frac{\partial k_{ro,i}^{n+1}}{\partial S_{g,i}^{n+1}} \tag{C.27}$$

$$\frac{\partial \lambda_{g,i}^{n+1}}{\partial R_{s,i}^{n+1}} = \frac{k_{ro,i}^{n+1}}{B_{o,i}^{n+1} \mu_{o,i}^{n+1}} \tag{C.28}$$

For each phase, the derivatives of the accumulation in **Eqs. (C.4)** – **(C.7)** are

$$\frac{\partial A_{w,i}^{n+1}}{\partial P_i^{n+1}} = \frac{w_i \Delta \tau_i}{\Delta t^{n+1}} \left(\frac{\partial M_{\phi,i}^{n+1}}{\partial P_i^{n+1}} \frac{S_{w,i}^{n+1}}{B_{w,i}^{n+1}} - M_{\phi,i}^{n+1} \frac{S_{w,i}^{n+1}}{{B_{w,i}^{n+1}}^2} \frac{\partial B_{w,i}^{n+1}}{\partial P_i^{n+1}} \right) \tag{C.29}$$

$$\frac{\partial A_{w,i}^{n+1}}{\partial S_{w,i}^{n+1}} = \frac{w_i \Delta \tau_i}{\Delta t^{n+1}} \left(M_{\phi,i}^{n+1} \frac{1}{B_{w,i}^{n+1}} \right) \tag{C.30}$$

$$\frac{\partial A_{w,i}^{n+1}}{\partial S_{g,i}^{n+1}} = 0 \tag{C.31}$$

$$\frac{\partial A_{w,i}^{n+1}}{\partial R_{s,i}^{n+1}} = 0 \tag{C.32}$$

$$\frac{\partial A_{o,i}^{n+1}}{\partial P_i^{n+1}} = \frac{w_i \Delta\tau_i}{\Delta t^{n+1}} \left[\frac{\partial M_{\phi,i}^{n+1}}{\partial P_i^{n+1}} \left(\frac{S_{o,i}^{n+1}}{B_{o,i}^{n+1}} + R_{v,i}^{n+1} \frac{S_{g,i}^{n+1}}{B_{g,i}^{n+1}} \right) \right.$$

$$- M_{\phi,i}^{n+1} \left(\frac{S_{o,i}^{n+1}}{{B_{o,i}^{n+1}}^2} \frac{\partial B_{o,i}^{n+1}}{\partial P_i^{n+1}} - \frac{\partial R_{v,i}^{n+1}}{\partial P_i^{n+1}} \frac{S_{g,i}^{n+1}}{B_{g,i}^{n+1}} \right. \tag{C.33}$$

$$\left. \left. + R_{v,i}^{n+1} \frac{S_{g,i}^{n+1}}{{B_{g,i}^{n+1}}^2} \frac{\partial B_{g,i}^{n+1}}{\partial P_i^{n+1}} \right) \right]$$

$$\frac{\partial A_{o,i}^{n+1}}{\partial S_{w,i}^{n+1}} = -\frac{w_i \Delta\tau_i}{\Delta t^{n+1}} \left(M_{\phi,i}^{n+1} \frac{1}{B_{o,i}^{n+1}} \right) \tag{C.34}$$

$$\frac{\partial A_{o,i}^{n+1}}{\partial S_{g,i}^{n+1}} = -\frac{w_i \Delta\tau_i}{\Delta t^{n+1}} \left(M_{\phi,i}^{n+1} \frac{1}{B_{o,i}^{n+1}} \right) \tag{C.35}$$

$$\frac{\partial A_{o,i}^{n+1}}{\partial R_{s,i}^{n+1}} = 0 \tag{C.36}$$

$$\frac{\partial A_{g,i}^{n+1}}{\partial P_i^{n+1}} = \frac{w_i \Delta\tau_i}{\Delta t^{n+1}} \left[\frac{\partial M_{\phi,i}^{n+1}}{\partial P_i^{n+1}} \left(\frac{S_{g,i}^{n+1}}{B_{g,i}^{n+1}} + R_{s,i}^{n+1} \frac{S_{o,i}^{n+1}}{B_{o,i}^{n+1}} \right) \right.$$

$$- M_{\phi,i}^{n+1} \left(\frac{S_{g,i}^{n+1}}{{B_{g,i}^{n+1}}^2} \frac{\partial B_{g,i}^{n+1}}{\partial P_i^{n+1}} - \frac{\partial R_{s,i}^{n+1}}{\partial P_i^{n+1}} \frac{S_{o,i}^{n+1}}{B_{o,i}^{n+1}} \right. \tag{C.37}$$

$$\left. \left. + R_{s,i}^{n+1} \frac{S_{o,i}^{n+1}}{{B_{o,i}^{n+1}}^2} \frac{\partial B_{o,i}^{n+1}}{\partial P_i^{n+1}} \right) \right]$$

$$\frac{\partial A_{g,i}^{n+1}}{\partial S_{w,i}^{n+1}} = -\frac{w_i \Delta\tau_i}{\Delta t^{n+1}} \left[M_{\phi,i}^{n+1} \left(R_{s,i}^{n+1} \frac{1}{B_{o,i}^{n+1}} \right) \right] \tag{C.38}$$

$$\frac{\partial A_{g,i}^{n+1}}{\partial S_{g,i}^{n+1}} = \frac{w_i \Delta\tau_i}{\Delta t^{n+1}} \left[M_{\phi,i}^{n+1} \left(\frac{1}{B_{g,i}^{n+1}} - R_{s,i}^{n+1} \frac{1}{B_{o,i}^{n+1}} \right) \right] \tag{C.39}$$

$$\frac{\partial A_{g,i}^{n+1}}{\partial R_{s,i}^{n+1}} = \frac{w_i \Delta\tau_i}{\Delta t^{n+1}} \left[M_{\phi,i}^{n+1} \left(\frac{S_{o,i}^{n+1}}{B_{o,i}^{n+1}} \right) \right] \tag{C.40}$$

The derivative of the well term in **Eqs. (C.4)** – **(C.7)** is imposed on the first grid.

$$\frac{\partial W_{\alpha,1}^{n+1}}{\partial P_1^{n+1}} = w_1 \left(\frac{c_t}{\lambda_t}\right)_{\text{init},1} \left[\lambda_{\alpha,1}^{n+1}\left(\frac{1}{\tau_1 - \tau_{\text{well}}}\right) + \frac{\partial \lambda_{\alpha,1}^{n+1}}{\partial P_1^{n+1}}\left(\frac{P_1^{n+1} - P_{wf}^{n+1}}{\tau_1 - \tau_{\text{well}}}\right)\right] \tag{C.41}$$

$$\frac{\partial W_{\alpha,1}^{n+1}}{\partial S_{w,1}^{n+1}} = w_1 \left(\frac{c_t}{\lambda_t}\right)_{\text{init},1} \frac{\partial \lambda_{\alpha,1}^{n+1}}{\partial S_{w,1}^{n+1}}\left(\frac{P_1^{n+1} - P_{wf}^{n+1}}{\tau_1 - \tau_{\text{well}}}\right) \tag{C.42}$$

$$\frac{\partial W_{\alpha,1}^{n+1}}{\partial S_{g,1}^{n+1}} = w_1 \left(\frac{c_t}{\lambda_t}\right)_{\text{init},1} \frac{\partial \lambda_{\alpha,1}^{n+1}}{\partial S_{g,1}^{n+1}}\left(\frac{P_1^{n+1} - P_{wf}^{n+1}}{\tau_1 - \tau_{\text{well}}}\right) \tag{C.43}$$

$$\frac{\partial W_{\alpha,1}^{n+1}}{\partial R_{s,1}^{n+1}} = w_1 \left(\frac{c_t}{\lambda_t}\right)_{\text{init},1} \frac{\partial \lambda_{\alpha,1}^{n+1}}{\partial R_{s,1}^{n+1}}\left(\frac{P_1^{n+1} - P_{wf}^{n+1}}{\tau_1 - \tau_{\text{well}}}\right) \tag{C.44}$$

In **Eqs. (C.41)** – **(C.44)**, the derivatives of the phase mobility are obtained using **Eqs. (C.17)** – **(C.28)**.

Similarly, the off-diagonal blocks in the Jacobian also consist of a 3×3 matrix as shown in **Fig. C.2**. The off-diagonal terms are obtained by differentiating the finite difference equations (**Eqs. (C.1) – (C.3)**) by the primary variables of the neighbor grids.

$$\frac{\partial f_{\alpha,i}^{n+1}}{\partial P_{i\pm1}^{n+1}} = \frac{\partial F_{\alpha,i}^{n+1}}{\partial P_{i\pm1}^{n+1}} - \frac{\partial A_{\alpha,i}^{n+1}}{\partial P_{i\pm1}^{n+1}} + \frac{\partial W_{\alpha,i}^{n+1}}{\partial P_{i\pm1}^{n+1}} \tag{C.45}$$

$$\frac{\partial f_{\alpha,i}^{n+1}}{\partial S_{w,i\pm1}^{n+1}} = \frac{\partial F_{\alpha,i}^{n+1}}{\partial S_{w,i\pm1}^{n+1}} - \frac{\partial A_{\alpha,i}^{n+1}}{\partial S_{w,i\pm1}^{n+1}} + \frac{\partial W_{\alpha,i}^{n+1}}{\partial S_{w,i\pm1}^{n+1}} \tag{C.46}$$

$$\frac{\partial f_{\alpha,i}^{n+1}}{\partial S_{g,i\pm1}^{n+1}} = \frac{\partial F_{\alpha,i}^{n+1}}{\partial S_{g,i\pm1}^{n+1}} - \frac{\partial A_{\alpha,i}^{n+1}}{\partial S_{g,i\pm1}^{n+1}} + \frac{\partial W_{\alpha,i}^{n+1}}{\partial S_{g,i\pm1}^{n+1}} \tag{C.47}$$

$$\frac{\partial f_{\alpha,i}^{n+1}}{\partial R_{s,i\pm1}^{n+1}} = \frac{\partial F_{\alpha,i}^{n+1}}{\partial R_{s,i\pm1}^{n+1}} - \frac{\partial A_{\alpha,i}^{n+1}}{\partial R_{s,i\pm1}^{n+1}} + \frac{\partial W_{\alpha,i}^{n+1}}{\partial R_{s,i\pm1}^{n+1}} \tag{C.48}$$

Notice that the derivatives of the non-flux term in **Eqs. (C.45) – (C.48)** equal zero.

$$\frac{\partial A_{\alpha,i}^{n+1}}{\partial P_{i\pm1}^{n+1}} = 0, \quad \frac{\partial W_{\alpha,i}^{n+1}}{\partial P_{i\pm1}^{n+1}} = 0, \quad \frac{\partial A_{\alpha,i}^{n+1}}{\partial S_{w,i\pm1}^{n+1}} = 0, \quad \frac{\partial W_{\alpha,i}^{n+1}}{\partial S_{w,i\pm1}^{n+1}} = 0,$$
$$\frac{\partial A_{\alpha,i}^{n+1}}{\partial S_{g,i\pm1}^{n+1}} = 0, \quad \frac{\partial W_{\alpha,i}^{n+1}}{\partial S_{g,i\pm1}^{n+1}} = 0, \quad \frac{\partial A_{\alpha,i}^{n+1}}{\partial R_{s,i\pm1}^{n+1}} = 0, \quad \frac{\partial W_{\alpha,i}^{n+1}}{\partial R_{s,i\pm1}^{n+1}} = 0 \tag{C.49}$$

The derivatives of the flux term in **Eqs. (C.45) – (C.48)** are

$$\frac{\partial F_{\alpha,i}^{n+1}}{\partial P_{i\pm1}^{n+1}} = T_{\alpha,i\pm1/2}^{n+1} + \frac{\partial T_{\alpha,i\pm1/2}^{n+1}}{\partial P_{i\pm1}^{n+1}} \left(P_{i\pm1}^{n+1} - P_i^{n+1}\right) \tag{C.50}$$

$$\frac{\partial F_{\alpha,i}^{n+1}}{\partial S_{w,i\pm1}^{n+1}} = \frac{\partial T_{\alpha,i\pm1/2}^{n+1}}{\partial S_{w,i\pm1}^{n+1}} \left(P_{i\pm1}^{n+1} - P_i^{n+1}\right) \tag{C.51}$$

$$\frac{\partial F_{\alpha,i}^{n+1}}{\partial S_{g,i\pm1}^{n+1}} = \frac{\partial T_{\alpha,i\pm1/2}^{n+1}}{\partial S_{g,i\pm1}^{n+1}} \left(P_{i\pm1}^{n+1} - P_i^{n+1}\right) \tag{C.52}$$

$$\frac{\partial F_{\alpha,i}^{n+1}}{\partial R_{s,i\pm1}^{n+1}} = \frac{\partial T_{\alpha,i\pm1/2}^{n+1}}{\partial R_{s,i\pm1}^{n+1}} \left(P_{i\pm1}^{n+1} - P_i^{n+1}\right) \tag{C.53}$$

The derivatives of the phase transmissibility in **Eqs. (C.50)** – **(C.53)** are

$$\frac{\partial T_{\alpha,i\pm1/2}^{n+1}}{\partial P_{i\pm1}^{n+1}} = \frac{w_{i\pm1/2}}{\Delta\tau_{i\pm1/2}} \left(\frac{c_t}{\lambda_t}\right)_{\text{init},i\pm1/2} \frac{\partial \lambda_{\alpha,up}^{n+1}}{\partial P_{i\pm1}^{n+1}} \tag{C.54}$$

$$\frac{\partial T_{\alpha,i\pm1/2}^{n+1}}{\partial S_{w,i\pm1}^{n+1}} = \frac{w_{i\pm1/2}}{\Delta\tau_{i\pm1/2}} \left(\frac{c_t}{\lambda_t}\right)_{\text{init},i\pm1/2} \frac{\partial \lambda_{\alpha,up}^{n+1}}{\partial S_{w,i\pm1}^{n+1}} \tag{C.55}$$

$$\frac{\partial T_{\alpha,i\pm1/2}^{n+1}}{\partial S_{g,i\pm1}^{n+1}} = \frac{w_{i\pm1/2}}{\Delta\tau_{i\pm1/2}} \left(\frac{c_t}{\lambda_t}\right)_{\text{init},i\pm1/2} \frac{\partial \lambda_{\alpha,up}^{n+1}}{\partial S_{g,i\pm1}^{n+1}} \tag{C.56}$$

$$\frac{\partial T_{\alpha,i\pm1/2}^{n+1}}{\partial R_{s,i\pm1}^{n+1}} = \frac{w_{i\pm1/2}}{\Delta\tau_{i\pm1/2}} \left(\frac{c_t}{\lambda_t}\right)_{\text{init},i\pm1/2} \frac{\partial \lambda_{\alpha,up}^{n+1}}{\partial R_{s,i\pm1}^{n+1}} \tag{C.57}$$

If the upstream grid is the grid of i, the derivatives of the phase mobility in **Eqs. (C.54)** - **(C.57)** are zero.

$$\frac{\partial \lambda_{\alpha,i}^{n+1}}{\partial P_{i\pm1}^{n+1}} = 0, \quad \frac{\partial \lambda_{\alpha,i}^{n+1}}{\partial S_{w,i\pm1}^{n+1}} = 0, \quad \frac{\partial \lambda_{\alpha,i}^{n+1}}{\partial S_{g,i\pm1}^{n+1}} = 0, \quad \frac{\partial \lambda_{\alpha,i}^{n+1}}{\partial R_{s,i\pm1}^{n+1}} = 0 \tag{C.58}$$

If the upstream grid is the neighbor grid, the derivatives of the phase mobility in **Eqs. (C.54) - (C.57)** are calculated using **Eqs. (C.17)** – **(C.28)**.

Therefore, the diagonal blocks of the Jacobian are constructed by using **Eqs. (C.8) - (B.44)** as well as the off-diagonal blocks are constructed with **Eqs. (C.50) - (C.57)**.

C.2 Implicit BHP Calculation

If the bottom-hole pressure is specified, we can explicitly calculate the production rate using the well equation (**Eq. (2.65)**). If the production rate is specified, we implicitly solve the bottom-hole pressure during the Newton iteration. In such case, the primary variable consists of a $(3M+1)\times 1$ vactor.

$$\mathbf{y}^{n+1} = \left[P_1, S_{w,1}, S_{g,1}, \dots, P_M, S_{M,1}, S_{M,1}, P_{wf}\right]^T \tag{C.59}$$

In addition to the finite difference equations, the well governing equation, that is the well residual equation (R_w) is imposed on the residual.

$$\mathbf{R}^{n+1} = \left[f_{w,1}, f_{o,1}, f_{g,1}, \dots, f_{w,M}, f_{o,M}, f_{g,M}, R_w\right]^T \tag{C.60}$$

The residual consists of a $(3M+1)\times 1$ vactor. The well residual term R_w is defined by summating **Eq. (3.65)** for all the existing phases.

$$R_w^{n+1} = w_i \left(\frac{c_t}{\lambda_t}\right)_{\text{init},1} \sum_{\alpha=w,o,g} \lambda_{\alpha,1}^{n+1} \left(\frac{P_1^{n+1} - P_{wf}^{n+1}}{\tau_1 - \tau_{\text{well}}}\right) - \sum_{\alpha=w,o,g} q_{s\alpha}^{n+1} \tag{C.61}$$

The Jacobian consists of a $(3M+1)\times(3M+1)$ matrix as shown in **Fig. C.3**.

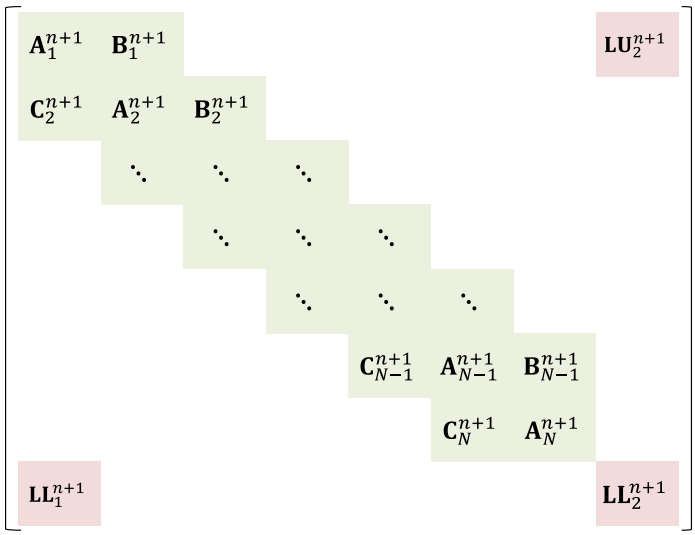

Fig. C.3 – Jacobian of the multiphase single-porosity model with well residual terms

The additional elements $\mathbf{LL}_1, \mathbf{LL}_2$, and $\mathbf{LU}_2$in **Fig. C.3** is comprised of a vector and scalar value. The row vector $\mathbf{LL}_1$ (1×3 vector) is given by

$$\mathbf{LL}_1^{n+1} = \begin{bmatrix} \frac{\partial R_w^{n+1}}{\partial P_1^{n+1}} & \frac{\partial R_w^{n+1}}{\partial S_{w,1}^{n+1}} & \frac{\partial R_w^{n+1}}{\partial S_{g,1}^{n+1}} \end{bmatrix} \tag{C.62}$$

If the primary variable is $R_{s,1}^{n+1}$ instead of $S_{g,1}^{n+1}$, the row vector $\mathbf{LL}_1^{n+1}$ is

$$\mathbf{LL}_1^{n+1} = \begin{bmatrix} \frac{\partial R_w^{n+1}}{\partial P_1^{n+1}} & \frac{\partial R_w^{n+1}}{\partial S_{w,1}^{n+1}} & \frac{\partial R_w^{n+1}}{\partial R_{s,1}^{n+1}} \end{bmatrix} \tag{C.63}$$

The scalar vale $\mathbf{LL}_2$ is given by

$$\mathbf{LL}_2^{n+1} = \frac{\partial R_w^{n+1}}{\partial P_{wf}^{n+1}} \tag{C.64}$$

The column vector $\mathbf{LU}_2$ (3×1 vector) is given by

$$\mathbf{LU}_2^{n+1} = \begin{bmatrix} \frac{\partial f_w^{n+1}}{\partial P_{wf}^{n+1}} & \frac{\partial f_o^{n+1}}{\partial P_{wf}^{n+1}} & \frac{\partial f_g^{n+1}}{\partial P_{wf}^{n+1}} \end{bmatrix}^T \tag{C.65}$$

Notice that the production rate is specified, thus this is a fixed value. The $\mathbf{LL}_1^{n+1}$ elements in **Eqs. (C.62)** and **(C.63)** are calculated as follows.

$$\frac{\partial R_w^{n+1}}{\partial P_1^{n+1}} = w_i \left(\frac{c_t}{\lambda_t}\right)_{\text{init},1} \left[\sum_\alpha \frac{\partial \lambda_{\alpha,1}^{n+1}}{\partial P_1^{n+1}} \left(\frac{P_1^{n+1} - P_{wf}^{n+1}}{\tau_1 - \tau_{\text{well}}}\right) + \sum_\alpha \lambda_{\alpha,1}^{n+1} \left(\frac{1}{\tau_1 - \tau_{\text{well}}}\right)\right] \quad \text{(C.66)}$$

$$\frac{\partial R_w^{n+1}}{\partial S_{w,1}^{n+1}} = w_i \left(\frac{c_t}{\lambda_t}\right)_{\text{init},1} \sum_\alpha \frac{\partial \lambda_{\alpha,1}^{n+1}}{\partial S_{w,1}^{n+1}} \left(\frac{P_1^{n+1} - P_{wf}^{n+1}}{\tau_1 - \tau_{\text{well}}}\right) \quad \text{(C.67)}$$

$$\frac{\partial R_w^{n+1}}{\partial S_{g,1}^{n+1}} = w_i \left(\frac{c_t}{\lambda_t}\right)_{\text{init},1} \sum_\alpha \frac{\partial \lambda_{\alpha,1}^{n+1}}{\partial S_{g,1}^{n+1}} \left(\frac{P_1^{n+1} - P_{wf}^{n+1}}{\tau_1 - \tau_{\text{well}}}\right) \quad \text{(C.68)}$$

$$\frac{\partial R_w^{n+1}}{\partial R_{s,1}^{n+1}} = w_i \left(\frac{c_t}{\lambda_t}\right)_{\text{init},1} \sum_\alpha \frac{\partial \lambda_{\alpha,1}^{n+1}}{\partial R_{s,1}^{n+1}} \left(\frac{P_1^{n+1} - P_{wf}^{n+1}}{\tau_1 - \tau_{\text{well}}}\right) \quad \text{(C.69)}$$

In **Eqs. (C.66) - (C.69)**, the derivatives of the phase mobility are calculated using **Eqs. (C.17)** – **(C.28)**.

The $\mathbf{LL}_2$ element in **Eq. (C.64)** is obtained by

$$\frac{\partial R_w^{n+1}}{\partial P_{wf}^{n+1}} = -w_i \left(\frac{c_t}{\lambda_t}\right)_{\text{init},1} \sum_\alpha \lambda_{\alpha,1}^{n+1} \left(\frac{1}{\tau_1 - \tau_{\text{well}}}\right) \quad \text{(C.70)}$$

The LU_2^{n+1} elements in **Eq. (C.65)** are calculated by

$$\frac{\partial f_w^{n+1}}{\partial P_{wf}^{n+1}} = w_i \left(\frac{c_t}{\lambda_t}\right)_{\text{init},1} \lambda_{w,1}^{n+1} \left(\frac{1}{\tau_1 - \tau_{\text{well}}}\right) \quad \text{(C.71)}$$

$$\frac{\partial f_o^{n+1}}{\partial P_{wf}^{n+1}} = w_i \left(\frac{c_t}{\lambda_t}\right)_{\text{init},1} \lambda_{o,1}^{n+1} \left(\frac{1}{\tau_1 - \tau_{\text{well}}}\right) \quad \text{(C.72)}$$

$$\frac{\partial f_g^{n+1}}{\partial P_{wf}^{n+1}} = w_i \left(\frac{c_t}{\lambda_t}\right)_{\text{init},1} \lambda_{g,1}^{n+1} \left(\frac{1}{\tau_1 - \tau_{\text{well}}}\right) \quad \text{(C.73)}$$

C.3 Derivatives in Dual-Porosity Model

In the blackoil dual-porosity model, we solve the three phase finite difference equations for the fracture grid as well as for the matrix grid.

The finite difference equations in the fracture grid i is expressed by

$$f_{wf,i}^{n+1} = F_{wf,i}^{n+1} - A_{wf,i}^{n+1} + A_{wf,i}^{n} + W_{wf,i}^{n+1} - v_i \Delta\tau_i F_{FM,w,i}^{n+1} = 0 \tag{C.74}$$

$$f_{of,i}^{n+1} = F_{of,i}^{n+1} - A_{of,i}^{n+1} + A_{of,i}^{n} + W_{of,i}^{n+1} - v_i \Delta\tau_i F_{FM,o,i}^{n+1} = 0 \tag{C.75}$$

$$f_{gf,i}^{n+1} = F_{gf,i}^{n+1} - A_{gf,i}^{n+1} + A_{gf,i}^{n} + W_{gf,i}^{n+1} - v_i \Delta\tau_i F_{FM,g,i}^{n+1} = 0 \tag{C.76}$$

where $v_i \Delta\tau_i$ represents the 'bulk' volume of the grid block i.

In the dual-porosity model, the matrix grid has no flux to the neighbor grid. The finite difference equations in the matrix grid i are defined by the accumulation and fracture-matrix transfer term.

$$f_{wm,i}^{n+1} = -A_{wm,i}^{n+1} + A_{wm,i}^{n} + F_{FM,w,i}^{n+1} = 0 \tag{C.77}$$

$$f_{om,i}^{n+1} = -A_{om,i}^{n+1} + A_{om,i}^{n} + F_{FM,o,i}^{n+1} = 0 \tag{C.78}$$

$$f_{gm,i}^{n+1} = -A_{gm,i}^{n+1} + A_{gm,i}^{n} + F_{FM,g,i}^{n+1} = 0 \tag{C.79}$$

where $F_{FM,\alpha,i}^{n+1}$ is the fracture-matrix transfer term of phase α (o, w, g).

$$F_{FM,\alpha,i}^{n+1} = \sigma k_m \lambda_{\alpha,up}^{n+1} \left(P_{f,i}^{n+1} - P_{m,i}^{n+1}\right) \tag{C.80}$$

Notice that the shape factor σ and the matrix permeability k_m are the uniform parameter throughout all the grid blocks.

The primary variable is the fracture pressure and the matrix pressure ($6M \times 1$ vector).

$$\mathbf{y}^{n+1} = \left[\mathbf{y}_{f,1}^{n+1}, \dots, \mathbf{y}_{f,M}^{n+1}, \mathbf{y}_{m,1}^{n+1}, \dots, \mathbf{y}_{m,M}^{n+1}\right]^T \tag{C.81}$$

where $\mathbf{y}_f^{n+1}$ and $\mathbf{y}_m^{n+1}$ are the vector comprised of the pressure, water saturation, and gas saturation or solution gas oil ratio for each grid.

$$\mathbf{y}_{f,i}^{n+1} = \left[P_{f,i}^{n+1}, S_{wf}^{n+1}, S_{gf}^{n+1}\right] \tag{C.82}$$

$$\mathbf{y}_{m,i}^{n+1} = \left[P_{m,i}^{n+1}, S_{wm}^{n+1}, S_{gm}^{n+1}\right] \tag{C.83}$$

The residual term is comprised of the finite difference equations of the fracture grids (**Eqs. (C.74)** – **(C.76)**) and of the matrix grids (**Eqs. (C.77)** – **(C.79)**) ($6M \times 1$ vector).

$$\mathbf{R}^{n+1} = \left[\mathbf{R}_{f,1}^{n+1}, \dots, \mathbf{R}_{f,M}^{n+1}, \mathbf{R}_{m,1}^{n+1}, \dots, \mathbf{R}_{m,M}^{n+1}\right]^T \tag{C.84}$$

where $\mathbf{R}_f^{n+1}$ and $\boldsymbol{R}_m^{n+1}$ are the vector comprised of the three finite difference equations for each grid.

$$\mathbf{R}_{f,i}^{n+1} = \left[f_{wf,i}^{n+1}, f_{of,i}^{n+1}, f_{gf,i}^{n+1}\right] \tag{C.85}$$

$$\mathbf{R}_{m,i}^{n+1} = \left[f_{wm,i}^{n+1}, f_{om,i}^{n+1}, f_{gm,i}^{n+1}\right] \tag{C.86}$$

The Jacobian ($6M \times 6M$ matrix) is obtained by differentiating **Eq. (C.84)** by **Eq. (C.81)**. The matrix form is shown in **Fig. C.4**. The elements $A - C$ in **Fig.C.4** is the block-tridiagonal entries. The elements D and E represents the fracture-matrix connectivity, which is locally diagonal in the Jacobian. The element F is the diagonal term in the Jacobian.

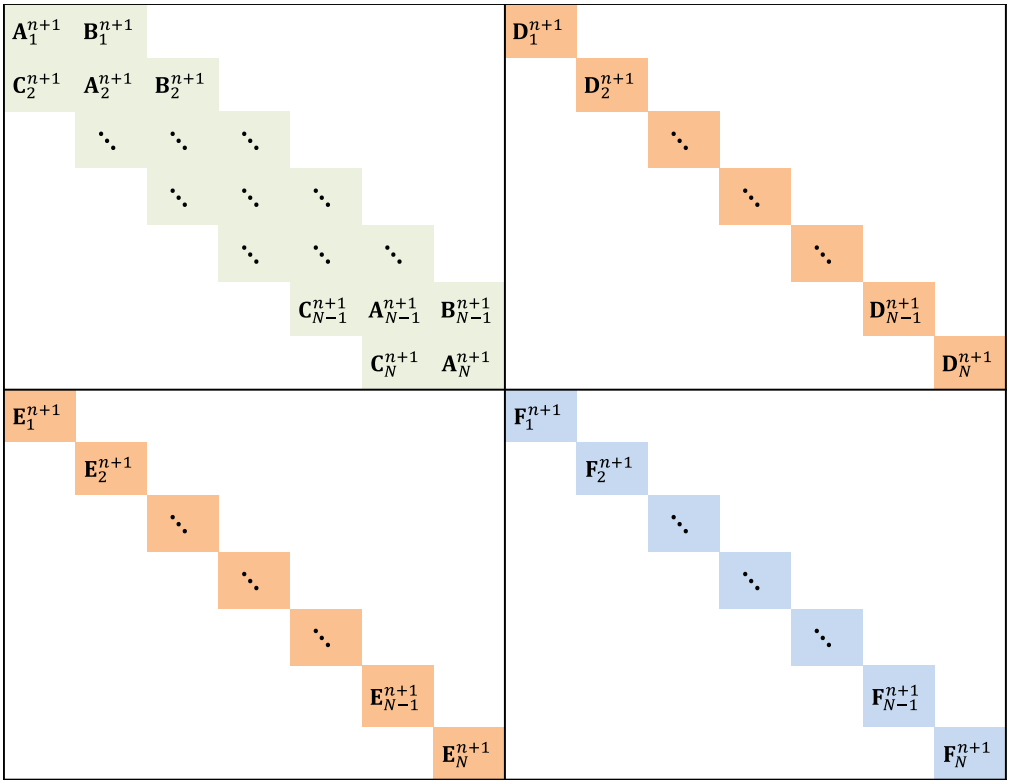

Fig. C.4 – Jacobian of the multiphase dual-porosity model

The Jacobian elements $A - F$ in **Fig. C.4** are classified to four types of the derivatives.

(1) The derivative of fracture eq. (R_f) with respect to fracture variable (y_f)

$$\mathbf{A}, \mathbf{B}, \mathbf{C} = \frac{\partial \mathbf{R_f}}{\partial \mathbf{y_f}} = \begin{bmatrix} \frac{\partial f_{wf}}{\partial P_f} & \frac{\partial f_{wf}}{\partial S_{wf}} & \frac{\partial f_{wf}}{\partial S_{gf}} \\ \frac{\partial f_{of}}{\partial P_f} & \frac{\partial f_{of}}{\partial S_{wf}} & \frac{\partial f_{of}}{\partial S_{gf}} \\ \frac{\partial f_{gf}}{\partial P_f} & \frac{\partial f_{gf}}{\partial S_{wf}} & \frac{\partial f_{gf}}{\partial S_{gf}} \end{bmatrix} \text{ or } \begin{bmatrix} \frac{\partial f_{wf}}{\partial P_f} & \frac{\partial f_{wf}}{\partial S_{wf}} & \frac{\partial f_{wf}}{\partial R_{sf}} \\ \frac{\partial f_{of}}{\partial P_f} & \frac{\partial f_{of}}{\partial S_{wf}} & \frac{\partial f_{of}}{\partial R_{sf}} \\ \frac{\partial f_{gf}}{\partial P_f} & \frac{\partial f_{gf}}{\partial S_{wf}} & \frac{\partial f_{gf}}{\partial R_{sf}} \end{bmatrix} \tag{C.87}$$

(2) The derivative of fracture phase eq. (R_f) with respect to matrix pressure (y_m)

$$\mathbf{D} = \frac{\partial \mathbf{R_f}}{\partial \mathbf{y_m}} = \begin{bmatrix} \frac{\partial f_{wf}}{\partial P_m} & \frac{\partial f_{wf}}{\partial S_{wm}} & \frac{\partial f_{wf}}{\partial S_{gm}} \\ \frac{\partial f_{of}}{\partial P_m} & \frac{\partial f_{of}}{\partial S_{wm}} & \frac{\partial f_{of}}{\partial S_{gm}} \\ \frac{\partial f_{gf}}{\partial P_m} & \frac{\partial f_{gf}}{\partial S_{wm}} & \frac{\partial f_{gf}}{\partial S_{gm}} \end{bmatrix} \text{ or } \begin{bmatrix} \frac{\partial f_{wf}}{\partial P_m} & \frac{\partial f_{wf}}{\partial S_{wm}} & \frac{\partial f_{wf}}{\partial R_{sm}} \\ \frac{\partial f_{of}}{\partial P_m} & \frac{\partial f_{of}}{\partial S_{wm}} & \frac{\partial f_{of}}{\partial R_{sm}} \\ \frac{\partial f_{gf}}{\partial P_m} & \frac{\partial f_{gf}}{\partial S_{wm}} & \frac{\partial f_{gf}}{\partial R_{sm}} \end{bmatrix} \tag{C.88}$$

(3) The derivative of matrix phase eq. (R_m) with respect to fracture pressure (y_f)

$$\mathbf{E} = \frac{\partial \mathbf{R_m}}{\partial \mathbf{y_f}} = \begin{bmatrix} \frac{\partial f_{wm}}{\partial P_f} & \frac{\partial f_{wm}}{\partial S_{wf}} & \frac{\partial f_{wm}}{\partial S_{gf}} \\ \frac{\partial f_{om}}{\partial P_f} & \frac{\partial f_{om}}{\partial S_{wf}} & \frac{\partial f_{om}}{\partial S_{gf}} \\ \frac{\partial f_{gm}}{\partial P_f} & \frac{\partial f_{gm}}{\partial S_{wf}} & \frac{\partial f_{gm}}{\partial S_{gf}} \end{bmatrix} \text{ or } \begin{bmatrix} \frac{\partial f_{wm}}{\partial P_f} & \frac{\partial f_{wm}}{\partial S_{wf}} & \frac{\partial f_{wm}}{\partial R_{sf}} \\ \frac{\partial f_{om}}{\partial P_f} & \frac{\partial f_{om}}{\partial S_{wf}} & \frac{\partial f_{om}}{\partial R_{sf}} \\ \frac{\partial f_{gm}}{\partial P_f} & \frac{\partial f_{gm}}{\partial S_{wf}} & \frac{\partial f_{gm}}{\partial R_{sf}} \end{bmatrix} \tag{C.89}$$

(4) The derivative of matrix phase eq. (R_m) with respect to matrix pressure (y_m)

$$\mathbf{F} = \frac{\partial \mathbf{R_m}}{\partial \mathbf{y_m}} = \begin{bmatrix} \frac{\partial f_{wm}}{\partial P_m} & \frac{\partial f_{wm}}{\partial S_{wm}} & \frac{\partial f_{wm}}{\partial S_{gm}} \\ \frac{\partial f_{om}}{\partial P_m} & \frac{\partial f_{om}}{\partial S_{wm}} & \frac{\partial f_{om}}{\partial S_{gm}} \\ \frac{\partial f_{gm}}{\partial P_m} & \frac{\partial f_{gm}}{\partial S_{wm}} & \frac{\partial f_{gm}}{\partial S_{gm}} \end{bmatrix} \text{ or } \begin{bmatrix} \frac{\partial f_{wm}}{\partial P_m} & \frac{\partial f_{wm}}{\partial S_{wm}} & \frac{\partial f_{wm}}{\partial R_{sm}} \\ \frac{\partial f_{om}}{\partial P_m} & \frac{\partial f_{om}}{\partial S_{wm}} & \frac{\partial f_{om}}{\partial R_{sm}} \\ \frac{\partial f_{gm}}{\partial P_m} & \frac{\partial f_{gm}}{\partial S_{wm}} & \frac{\partial f_{gm}}{\partial R_{sm}} \end{bmatrix} \tag{C.90}$$

The diagonal element A (**Eq. (C.87)**) is

$$\frac{\partial f_{\alpha f,i}^{n+1}}{\partial P_{f,i}^{n+1}} = \frac{\partial F_{\alpha f,i}^{n+1}}{\partial P_{f,i}^{n+1}} - \frac{\partial A_{\alpha f,i}^{n+1}}{\partial P_{f,i}^{n+1}} + \frac{\partial W_{\alpha f,i}^{n+1}}{\partial P_{f,i}^{n+1}} - v_i \Delta\tau_i \frac{\partial F_{FM,\alpha,i}^{n+1}}{\partial P_{f,i}^{n+1}} \tag{C.91}$$

$$\frac{\partial f_{\alpha f,i}^{n+1}}{\partial S_{wf,i}^{n+1}} = \frac{\partial F_{\alpha f,i}^{n+1}}{\partial S_{wf,i}^{n+1}} - \frac{\partial A_{\alpha f,i}^{n+1}}{\partial S_{wf,i}^{n+1}} + \frac{\partial W_{\alpha f,i}^{n+1}}{\partial S_{wf,i}^{n+1}} - v_i \Delta\tau_i \frac{\partial F_{FM,\alpha,i}^{n+1}}{\partial S_{wf,i}^{n+1}} \tag{C.92}$$

$$\frac{\partial f_{\alpha f,i}^{n+1}}{\partial S_{gf,i}^{n+1}} = \frac{\partial F_{\alpha f,i}^{n+1}}{\partial S_{gf,i}^{n+1}} - \frac{\partial A_{\alpha f,i}^{n+1}}{\partial S_{gf,i}^{n+1}} + \frac{\partial W_{\alpha f,i}^{n+1}}{\partial S_{gf,i}^{n+1}} - v_i \Delta\tau_i \frac{\partial F_{FM,\alpha,i}^{n+1}}{\partial S_{gf,i}^{n+1}} \tag{C.93}$$

$$\frac{\partial f_{\alpha f,i}^{n+1}}{\partial R_{sf,i}^{n+1}} = \frac{\partial F_{\alpha f,i}^{n+1}}{\partial R_{sf,i}^{n+1}} - \frac{\partial A_{\alpha f,i}^{n+1}}{\partial R_{sf,i}^{n+1}} + \frac{\partial W_{\alpha f,i}^{n+1}}{\partial R_{sf,i}^{n+1}} - v_i \Delta\tau_i \frac{\partial F_{FM,\alpha,i}^{n+1}}{\partial R_{sf,i}^{n+1}} \tag{C.94}$$

The first derivatives of the right hand side in **Eqs. (C.91)** – **(C.94)** are obtained by **Eqs. (C.8)** – **(C.11)**. The second derivatives are calculated by **Eqs. (C.29)** – **(C.40)**. The third terms are given by **Eqs. (C.41)** – **(C.44)**. The fourth derivatives are

$$\frac{\partial F_{FM,\alpha,i}^{n+1}}{\partial P_{f,i}^{n+1}} = \sigma k_m \left[\lambda_{\alpha,up}^{n+1} + \frac{\partial \lambda_{\alpha,up}^{n+1}}{\partial P_{f,i}^{n+1}} \left(P_{f,i}^{n+1} - P_{m,i}^{n+1} \right) \right] \tag{C.95}$$

$$\frac{\partial F_{FM,\alpha,i}^{n+1}}{\partial S_{wf,i}^{n+1}} = \sigma k_m \frac{\partial \lambda_{\alpha,up}^{n+1}}{\partial S_{wf,i}^{n+1}} \left(P_{f,i}^{n+1} - P_{m,i}^{n+1} \right) \tag{C.96}$$

$$\frac{\partial F_{FM,\alpha,i}^{n+1}}{\partial S_{gf,i}^{n+1}} = \sigma k_m \frac{\partial \lambda_{\alpha,up}^{n+1}}{\partial S_{gf,i}^{n+1}} \left(P_{f,i}^{n+1} - P_{m,i}^{n+1} \right) \tag{C.97}$$

$$\frac{\partial F_{FM,\alpha,i}^{n+1}}{\partial R_{sf,i}^{n+1}} = \sigma k_m \frac{\partial \lambda_{\alpha,up}^{n+1}}{\partial R_{sf,i}^{n+1}} \left(P_{f,i}^{n+1} - P_{m,i}^{n+1} \right) \tag{C.98}$$

In **Eqs. (C.95)** – **(C.96)**, the derivatives of the phase mobility are determined by the up-winding scheme (**Eqs. (C.16) – (C.28)**).

The off-diagonal elements B and C (**Eq. (C.87)**) are

$$\frac{\partial f_{\alpha f,i}^{n+1}}{\partial P_{f,i\pm1}^{n+1}} = \frac{\partial F_{\alpha f,i}^{n+1}}{\partial P_{f,i\pm1}^{n+1}} \tag{C.99}$$

$$\frac{\partial f_{\alpha f,i}^{n+1}}{\partial S_{wf,i\pm1}^{n+1}} = \frac{\partial F_{\alpha f,i}^{n+1}}{\partial S_{wf,i\pm1}^{n+1}} \tag{C.100}$$

$$\frac{\partial f_{\alpha f,i}^{n+1}}{\partial S_{gf,i\pm1}^{n+1}} = \frac{\partial F_{\alpha f,i}^{n+1}}{\partial S_{gf,i\pm1}^{n+1}} \tag{C.101}$$

$$\frac{\partial f_{\alpha f,i}^{n+1}}{\partial R_{sf,i\pm1}^{n+1}} = \frac{\partial F_{\alpha f,i}^{n+1}}{\partial R_{sf,i\pm1}^{n+1}} \tag{C.102}$$

where these derivatives are given by **Eqs. (C.50)** – **(C.53)**.

The local diagonal element D (**Eq. (C.88)**) is

$$\frac{\partial f_{\alpha f,i}^{n+1}}{\partial P_{m,i}^{n+1}} = -v_i \Delta\tau_i \frac{\partial F_{FM,\alpha,i}^{n+1}}{\partial P_{m,i}^{n+1}} \tag{C.103}$$

$$\frac{\partial f_{\alpha f,i}^{n+1}}{\partial S_{wm,i}^{n+1}} = -v_i \Delta\tau_i \frac{\partial F_{FM,\alpha,i}^{n+1}}{\partial S_{wm,i}^{n+1}} \tag{C.104}$$

$$\frac{\partial f_{\alpha f,i}^{n+1}}{\partial S_{gm,i}^{n+1}} = -v_i \Delta\tau_i \frac{\partial F_{FM,\alpha,i}^{n+1}}{\partial S_{gm,i}^{n+1}} \tag{C.105}$$

$$\frac{\partial f_{\alpha f,i}^{n+1}}{\partial R_{sm,i}^{n+1}} = -v_i \Delta\tau_i \frac{\partial F_{FM,\alpha,i}^{n+1}}{\partial R_{sm,i}^{n+1}} \tag{C.106}$$

In **Eqs. (C.103)** – **(C.106)**, the derivative of the transfer function with respect to the matrix variables is

$$\frac{\partial F_{FM,\alpha,i}^{n+1}}{\partial P_{m,i}^{n+1}} = \sigma k_m \left[-\lambda_{\alpha,up}^{n+1} + \frac{\partial \lambda_{\alpha,up}^{n+1}}{\partial P_{m,i}^{n+1}} \left(\frac{1}{B\mu} \right)_{up}^{n+1} \left(P_{f,i}^{n+1} - P_{m,i}^{n+1} \right) \right] \tag{C.107}$$

$$\frac{\partial F_{FM,\alpha,i}^{n+1}}{\partial S_{wm,i}^{n+1}} = \sigma k_m \frac{\partial \lambda_{\alpha,up}^{n+1}}{\partial S_{wm,i}^{n+1}} \left(\frac{1}{B\mu} \right)_{up}^{n+1} \left(P_{f,i}^{n+1} - P_{m,i}^{n+1} \right) \tag{C.108}$$

$$\frac{\partial F_{FM,\alpha,i}^{n+1}}{\partial S_{gm,i}^{n+1}} = \sigma k_m \frac{\partial \lambda_{\alpha,up}^{n+1}}{\partial S_{gm,i}^{n+1}} \left(\frac{1}{B\mu} \right)_{up}^{n+1} \left(P_{f,i}^{n+1} - P_{m,i}^{n+1} \right) \tag{C.109}$$

$$\frac{\partial F_{FM,\alpha,i}^{n+1}}{\partial R_{sm,i}^{n+1}} = \sigma k_m \frac{\partial \lambda_{\alpha,up}^{n+1}}{\partial R_{sm,i}^{n+1}} \left(\frac{1}{B\mu} \right)_{up}^{n+1} \left(P_{f,i}^{n+1} - P_{m,i}^{n+1} \right) \tag{C.110}$$

The local diagonal element E (**Eq. (C.89)**) is

$$\frac{\partial f_{\alpha m,i}^{n+1}}{\partial P_{f,i}^{n+1}} = \frac{\partial F_{FM,\alpha,i}^{n+1}}{\partial P_{f,i}^{n+1}} \tag{C.111}$$

$$\frac{\partial f_{\alpha m,i}^{n+1}}{\partial S_{wf,i}^{n+1}} = \frac{\partial F_{FM,\alpha,i}^{n+1}}{\partial S_{wf,i}^{n+1}} \tag{C.112}$$

$$\frac{\partial f_{\alpha m,i}^{n+1}}{\partial S_{gf,i}^{n+1}} = \frac{\partial F_{FM,\alpha,i}^{n+1}}{\partial S_{gf,i}^{n+1}} \tag{C.113}$$

$$\frac{\partial f_{\alpha m,i}^{n+1}}{\partial R_{sf,i}^{n+1}} = \frac{\partial F_{FM,\alpha,i}^{n+1}}{\partial R_{sf,i}^{n+1}} \tag{C.114}$$

where these derivatives are given by **Eqs. (C.95)** – **(C.96)**.

The diagonal element F (**Eq. (C.90)**) is

$$\frac{\partial f_{\alpha m,i}^{n+1}}{\partial P_{m,i}^{n+1}} = -\frac{\partial A_{\alpha m,i}^{n+1}}{\partial P_{m,i}^{n+1}} + \frac{\partial F_{FM,\alpha,i}^{n+1}}{\partial P_{m,i}^{n+1}} \tag{C.115}$$

$$\frac{\partial f_{\alpha m,i}^{n+1}}{\partial S_{wm,i}^{n+1}} = -\frac{\partial A_{\alpha m,i}^{n+1}}{\partial S_{wm,i}^{n+1}} + \frac{\partial F_{FM,\alpha,i}^{n+1}}{\partial S_{wm,i}^{n+1}} \tag{C.116}$$

$$\frac{\partial f_{\alpha m,i}^{n+1}}{\partial S_{gm,i}^{n+1}} = -\frac{\partial A_{\alpha m,i}^{n+1}}{\partial S_{gm,i}^{n+1}} + \frac{\partial F_{FM,\alpha,i}^{n+1}}{\partial S_{gm,i}^{n+1}} \tag{C.117}$$

$$\frac{\partial f_{\alpha m,i}^{n+1}}{\partial R_{sm,i}^{n+1}} = -\frac{\partial A_{\alpha m,i}^{n+1}}{\partial R_{sm,i}^{n+1}} + \frac{\partial F_{FM,\alpha,i}^{n+1}}{\partial R_{sm,i}^{n+1}} \tag{C.118}$$

In **Eqs. (C.115)** – **(C.118)**, the first derivatives in the right hand side are

$$\frac{\partial A_{wm,i}^{n+1}}{\partial P_{m,i}^{n+1}} = \frac{1}{\Delta t^{n+1}}\left(\frac{\partial \phi_{m,i}^{n+1}}{\partial P_{m,i}^{n+1}}\frac{S_{w,i}^{n+1}}{B_{w,i}^{n+1}} - \phi_{m,i}^{n+1}\frac{S_{w,i}^{n+1}}{B_{w,i}^{n+1\,2}}\frac{\partial B_{w,i}^{n+1}}{\partial P_{m,i}^{n+1}}\right) \tag{C.119}$$

$$\frac{\partial A_{wm,i}^{n+1}}{\partial S_{wm,i}^{n+1}} = \frac{1}{\Delta t^{n+1}}\left(\phi_{m,i}^{n+1}\frac{1}{B_{w,i}^{n+1}}\right) \tag{C.120}$$

$$\frac{\partial A_{wm,i}^{n+1}}{\partial S_{gm,i}^{n+1}} = 0 \tag{C.121}$$

$$\frac{\partial A_{wm,i}^{n+1}}{\partial R_{sm,i}^{n+1}} = 0 \tag{C.122}$$

$$\frac{\partial A_{om,i}^{n+1}}{\partial P_{m,i}^{n+1}} = \frac{1}{\Delta t^{n+1}}\left[\frac{\partial \phi_{m,i}^{n+1}}{\partial P_{m,i}^{n+1}}\left(\frac{S_{o,i}^{n+1}}{B_{o,i}^{n+1}} + R_{v,i}^{n+1}\frac{S_{g,i}^{n+1}}{B_{g,i}^{n+1}}\right)\right.$$

$$- \phi_{m,i}^{n+1}\left(\frac{S_{o,i}^{n+1}}{B_{o,i}^{n+1\,2}}\frac{\partial B_{o,i}^{n+1}}{\partial P_{m,i}^{n+1}} - \frac{\partial R_{v,i}^{n+1}}{\partial P_i^{n+1}}\frac{S_{g,i}^{n+1}}{B_{g,i}^{n+1}}\right. \tag{C.123}$$

$$\left.\left. + R_{v,i}^{n+1}\frac{S_{g,i}^{n+1}}{B_{g,i}^{n+1\,2}}\frac{\partial B_{g,i}^{n+1}}{\partial P_{m,i}^{n+1}}\right)\right]$$

$$\frac{\partial A_{om,i}^{n+1}}{\partial S_{wm,i}^{n+1}} = -\frac{1}{\Delta t^{n+1}}\left(\phi_{m,i}^{n+1}\frac{1}{B_{o,i}^{n+1}}\right) \tag{C.124}$$

$$\frac{\partial A_{om,i}^{n+1}}{\partial S_{gm,i}^{n+1}} = -\frac{1}{\Delta t^{n+1}}\left(\phi_{m,i}^{n+1}\frac{1}{B_{o,i}^{n+1}}\right) \tag{C.125}$$

$$\frac{\partial A_{om,i}^{n+1}}{\partial R_{sm,i}^{n+1}} = 0 \tag{C.126}$$

$$\frac{\partial A_{gm,i}^{n+1}}{\partial P_{m,i}^{n+1}} = \frac{1}{\Delta t^{n+1}}\left[\frac{\partial \phi_{m,i}^{n+1}}{\partial P_{m,i}^{n+1}}\left(\frac{S_{g,i}^{n+1}}{B_{g,i}^{n+1}} + R_{s,i}^{n+1}\frac{S_{o,i}^{n+1}}{B_{o,i}^{n+1}}\right)\right.$$

$$- \phi_{m,i}^{n+1}\left(\frac{S_{g,i}^{n+1}}{B_{g,i}^{n+1\,2}}\frac{\partial B_{g,i}^{n+1}}{\partial P_{m,i}^{n+1}} - \frac{\partial R_{s,i}^{n+1}}{\partial P_i^{n+1}}\frac{S_{o,i}^{n+1}}{B_{o,i}^{n+1}}\right. \tag{C.127}$$

$$\left.\left. + R_{s,i}^{n+1}\frac{S_{o,i}^{n+1}}{B_{o,i}^{n+1\,2}}\frac{\partial B_{o,i}^{n+1}}{\partial P_{m,i}^{n+1}}\right)\right]$$

$$\frac{\partial A_{gm,i}^{n+1}}{\partial S_{wm,i}^{n+1}} = -\frac{1}{\Delta t^{n+1}}\left[\phi_{m,i}^{n+1}\left(R_{s,i}^{n+1}\frac{1}{B_{o,i}^{n+1}}\right)\right] \tag{C.128}$$

$$\frac{\partial A_{gm,i}^{n+1}}{\partial S_{gm,i}^{n+1}} = \frac{1}{\Delta t^{n+1}}\left[\phi_{m,i}^{n+1}\left(\frac{1}{B_{g,i}^{n+1}} - R_{s,i}^{n+1}\frac{1}{B_{o,i}^{n+1}}\right)\right] \tag{C.129}$$

$$\frac{\partial A_{gm,i}^{n+1}}{\partial R_{sm,i}^{n+1}} = \frac{1}{\Delta t^{n+1}}\left[\phi_{m,i}^{n+1}\left(\frac{S_{o,i}^{n+1}}{B_{o,i}^{n+1}}\right)\right] \tag{C.130}$$

where the derivative of the matrix porosity $\phi_{m,i}^{n+1}$ with respect to the matrix pressure $P_{m,i}^{n+1}$ is given by **Eq. (B.38)**. In **Eqs. (C.115)** – **(C.118)**, the second derivatives in the right hand side are obtained by **Eqs. (C.107) – (C.110)**.

If the production rate is specified, we impose the well residual term in the residual vector to implicitly solve the bottom-hole pressure. The matrix form of the Jacobian is shown in **Fig. C.5**. The well residual term is calculated using **Eqs. (C.61)** – **(C.73)**.

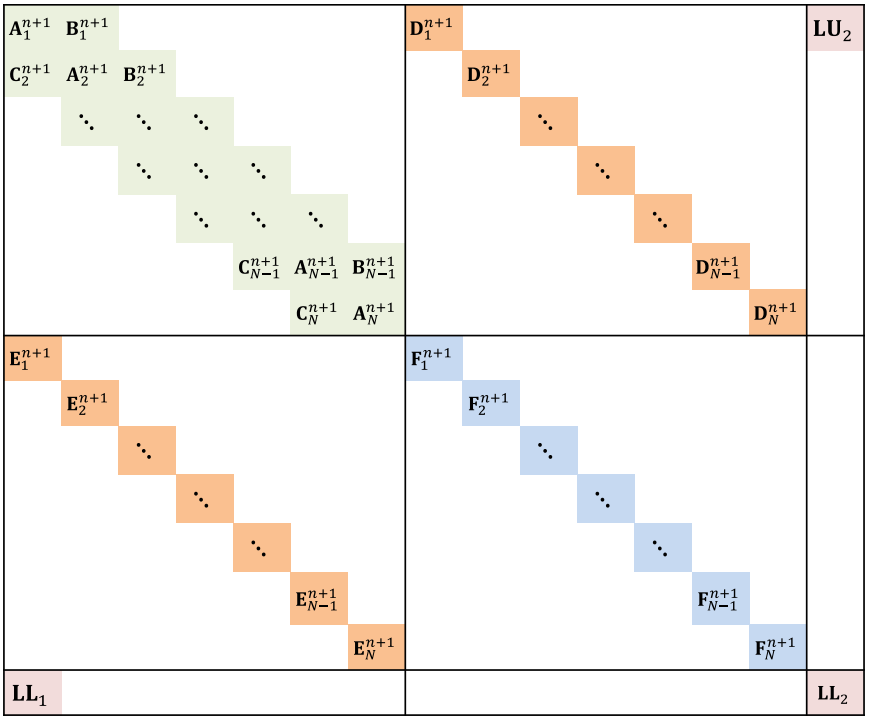

Fig. C.5 – Jacobian of the multiphase dual-porosity model with well residual terms

APPENDIX D

VLE EQUILIBRIUM CALCUALTION

D.1 Standard Flash Procedure

In this study, three-parameter Peng-Robinson EOS is used for a vapor-liquid flash calculation. The procedure is discussed next.

(1) Make an initial guess of the K-values using the Wilson empirical equation.

$$K_i = \frac{y_i}{x_i} = \frac{1}{P_{ri}} \exp\left[5.37(1+\omega_i)\left(1-\frac{1}{T_{ri}}\right)\right] \tag{D.1}$$

where ω_i is the acentric factor of component i, and T_{ri} and P_{ri} are the reduced pressure and temperature of component i, respectively.

(2) Compute the liquid and vapor mole fraction, L and V, based on the Rachford-Rice procedure. The nonlinear equation is solved by Newton-Raphson iteration. The objective function (residual) is given by

$$F(V) = \sum_{i=1}^{N_c} \frac{(1-K_i)z_i}{1-V(1-K_i)} \tag{D.2}$$

The gradient is given by

$$F'(V) = \frac{dF}{dV} = \sum_{i=1}^{N_c} \frac{(1-K_i)^2 z_i}{[1-V(1-K_i)]^2} \tag{D.3}$$

The vapor mole fraction is updated by

$$V^{l+1} = V^l - \frac{F(V)}{F'(V)} \tag{D.4}$$

where l denotes the Newton iteration level.

The convergence criterion is given by

$$\left|\frac{V^{l+1}}{V^{l}} - 1\right| < 1 \times 10^{-5} \tag{D.5}$$

For the first iteration, an initial guess of the liquid guess is given by 0.1.

(3) Compute the component mole fraction for vapor and liquid phase, x_i and y_i.

- If $L = 1$, then $x_i = z_i$ (single-phase liquid).
- If $V = 1$, then $y_i = z_i$ (single-phase vapor).
- If $0 < L < 1$, then $x_i = \frac{z_i}{1-V(1-K_i)}$ and $y_i = K_i x_i$ (two-phase).

(4) Compute the EOS parameters using the mixing rule.

$$(a\alpha)_m = \sum_{i=1}^{N_c}\sum_{j=1}^{N_c} X_i X_j \left(1 - \theta_{ij}\right)\sqrt{(a\alpha)_i (a\alpha)_j} \tag{D.6}$$

$$b_m = \sum_{i=1}^{N_c} X_i b_i \tag{D.7}$$

where X_i is the phase mole fraction ($X_i = y_i$ for vapor phase, and $X_i = x_i$ for liquid phase), θ_{ij} is the binary interaction coefficient (BIC), and a and b are the component EOS parameters.

$$a_i = \Omega_A \frac{R^2 {T_{ci}}^2}{P_{ci}} \tag{D.8}$$

$$b_i = \Omega_B \frac{R T_{ci}}{P_{ci}} \tag{D.9}$$

where Ω_A and Ω_B are constants. If $\omega_i \leq 0.49$, α_i is calculated by the quadratic equation in terms of ω_i.

$$\alpha_i = \left(1 + (0.3746 + 1.5423\omega_i - 0.2699\omega_i^2)\left(1 - {T_{ri}}^{0.5}\right)\right)^2 \quad \text{(D.10)}$$

If $\omega_i > 0.49$, α_i is given by the cubic equation in terms of ω_i.

$$\alpha_i = \left[1 + (0.3796 + 1.485\omega_i - 0.1644\omega_i^2 + 0.01667\omega_i^3)\left(1 - T_{ri}^{0.5}\right)\right]^2 \quad \text{(D.11)}$$

(5) Solve the Peng-Robinson EOS (cubic equation) for the phase z-factor, z_L and z_V, with the Cardano method.

$$z^3 + (B-1)z^2 + (A - 3B^2 - 2B)z + (B^3 + B^2 - AB) = 0 \quad \text{(D.12)}$$

where A and B are obtained from the mixing rule.

$$A = (a\alpha)_m \frac{P}{R^2T^2} \quad \text{(D.13)}$$

$$B = b_m \frac{P}{RT} \quad \text{(D.14)}$$

(6) Compute the component fugacity of each component in each phase, f_i^L and f_i^V.

$$f_i^L = x_i P \phi_i^L \quad \text{(D.15)}$$

$$f_i^V = y_i P \phi_i^V \quad \text{(D.16)}$$

where c_i is the volume shift parameter (a 'third' EOS parameter) of component i, and ϕ_i^L and ϕ_i^V are the fugacity coefficient of liquid and vapor phase, respectively. Using the Peng-Robinson EOS, the fugacity coefficient of phase α is written as

$$\phi_i^\alpha = \exp\left[\frac{b_i}{b_m}(z_\alpha - 1) - \ln(z_\alpha - B) - \frac{A}{2\sqrt{2}B}\left(\frac{a_{mi}}{(a\alpha)_m} - \frac{b_i}{b_m}\right)\ln\frac{z_\alpha + \left(1+\sqrt{2}\right)B}{z_\alpha + \left(1-\sqrt{2}\right)B}\right] \quad \text{(D.17)}$$

where α is the phase ($\alpha = L, V$) and a_{mi} is defined by

$$a_{mi} = \frac{\partial (a\alpha)_m}{\partial X_i} = 2\sum_{j=1}^{N_c} X_j (1 - \theta_{ij}) \sqrt{(a\alpha)_i (a\alpha)_j} \tag{D.18}$$

(7) Check to see if the equilibrium condition (fugacity equality) has been achieved.

$$\left[\sum_{i=1}^{N_c} \left(\frac{f_i^V}{f_i^L} - 1\right)\right]^2 < 1 \times 10^{-12} \tag{D.19}$$

- If the criterion is achieved, the iterative flash is terminated. Go to step (9).
- If the criterion is not achieved, the iterative flash is continued. Go to step (8).

(8) Update the K-values. The K-values are updated based on the Successive Substitution Method (SSM).

$$K_i^{new} = \frac{\phi_i^L}{\phi_i^V} = \frac{f_i^L}{f_i^V}\frac{y_i}{x_i} = \frac{f_i^L}{f_i^V} K_i^{old} \tag{D.20}$$

Once the K-values are updated, step (2) through step (7) is repeated until the convergence criterion in step (7) is satisfied.

(9) Calculate phase properties

- The phase molar volume with the volume shift (ft^3/mole)

$$V_o = \frac{z_L RT}{P} - \sum_{i=1}^{N_c} x_i c_i \tag{D.21}$$

$$V_g = \frac{z_V RT}{P} - \sum_{i=1}^{N_c} y_i c_i \tag{D.22}$$

- The phase molar density (moles/ ft^3)

$$\xi_o = \frac{1}{V_o}, \qquad \xi_g = \frac{1}{V_g} \tag{D.23}$$

- The phase mass density (lb/ ft^3)

$$\rho_o = \frac{M_{w,i}}{V_o}, \qquad \rho_g = \frac{M_{w,i}}{V_g} \tag{D.24}$$

- The phase volume fractions (hydrocarbon phase saturation without water)

$$f_o = \frac{\frac{L}{\xi_o}}{\frac{L}{\xi_o} + \frac{V}{\xi_g}}, \qquad f_g = \frac{\frac{V}{\xi_g}}{\frac{L}{\xi_o} + \frac{V}{\xi_g}} \tag{D.25}$$

- The phase mass fractions

$$MF_o = \frac{f_o \rho_o}{f_o \rho_o + f_g \rho_g}, \qquad MF_g = \frac{f_g \rho_g}{f_o \rho_o + f_g \rho_g} \tag{D.26}$$

D.2 Negative Flash Procedure for Saturation Point Calculation

At the dew-point, we obtain the following objective function.

$$F(P) = \sum_{i=1}^{N_c} \frac{z_i}{K_i} - 1 = 0 \tag{D.27}$$

The gradient is given by

$$F'(P) = \frac{\partial f}{\partial P} = -\sum_{i=1}^{N_c} \frac{z_i}{{K_i}^2} \frac{\partial K_i}{\partial P} \tag{D.28}$$

At the bubble-point, we obtain the following objective function.

$$F(P) = \sum_{i=1}^{N_c} z_i K_i - 1 = 0 \tag{D.29}$$

The gradient is given by

$$F'(P) = \frac{\partial f}{\partial P} = \sum_{i=1}^{N_c} z_i \frac{\partial K_i}{\partial P} \tag{D.30}$$

For each condition, the saturation pressure is iteratively calculated by using Newton-Raphson iteration.

$$P^{l+1} = P^{l} - \frac{F(P^{l})}{F'(P^{l})} \tag{D.31}$$

where l denotes the Newton iteration level.

APPENDIX E

CONSTRUCTION OF JACOBIAN FOR COMPOSITIONAL FLOWS

E.1 Derivatives of Primary Equations

In the compositional model, there are $2N_c + 1$ primary equations – a water equation, $2N_c$ hydrocarbon component equations, and $2N_c$ fugacity equality in each grid.

$$R_{w,i}^{n+1} = F_{w,i}^{n+1} - A_{w,i}^{n+1} + A_{w,i}^{n} + W_{w,i}^{n+1} = 0 \tag{E.1}$$

$$R_{j,i}^{n+1} = F_{j,i}^{n+1} - A_{j,i}^{n+1} + A_{j,i}^{n} + W_{j,i}^{n+1} = 0 \tag{E.2}$$

$$F_{j,i}^{n+1} = {f_{j,i}^{V}}^{n+1} - {f_{j,i}^{L}}^{n+1} = 0 \tag{E.3}$$

where the superscript $n + 1$ denotes the time-step level, j is the hydrocarbon component ($j = 1, \dots, N_c$), i denotes the grid number, and f^V and f^L represent the fugacity of vapor and liquid phase, respectively. The number of primary equations and the corresponding variables are determined by identifying the number of phase in the grid as summarized in **Table 3.1**. The grid-wise phase identification will be conducted by checking the phase saturation in each grid for each Newton iteration step. For example, if every grid is saturated with oil, gas, and water, the number of primary variables is $(2N_c + 1)M \times 1$.

The residual vector $\mathbf{R}^{n+1}$ and primary variables are expressed as follows.

$$\mathbf{R}^{n+1} = [\mathbf{R}_1^{n+1}, \mathbf{R}_2^{n+1}, \dots, \mathbf{R}_3^{n+1}]^T \tag{E.4}$$

$$\mathbf{u}^{n+1} = [\mathbf{u}_1^{n+1}, \mathbf{u}_2^{n+1}, \dots, \mathbf{u}_3^{n+1}]^T \tag{E.5}$$

The Jacobian forms a block-tridiagonal band as shown in **Fig. E.1**. The size of the entries varies depending on the number of phase saturated in the corresponding grid.

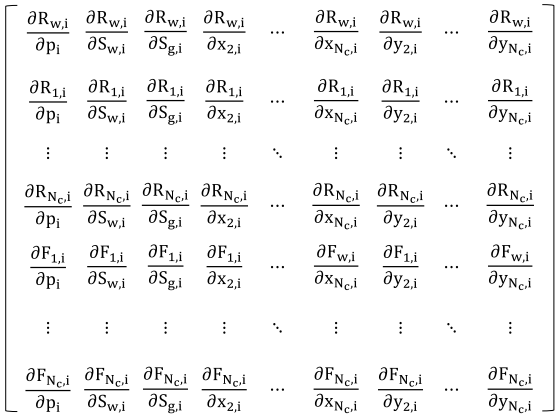

(a) Three-phase Oil, Gas, and Water

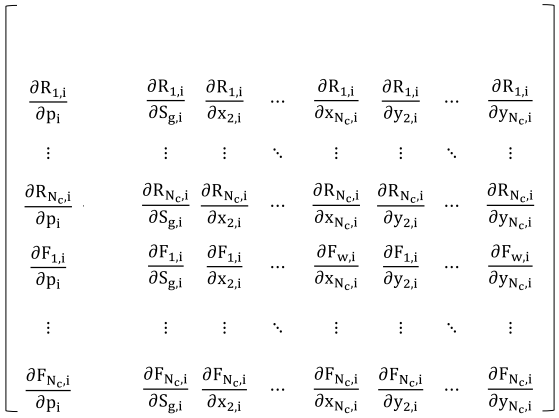

(b) Two-phase Oil and Gas

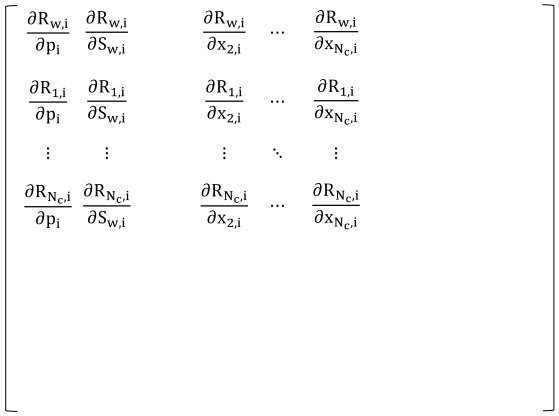

(c) Two-phase Oil and Water

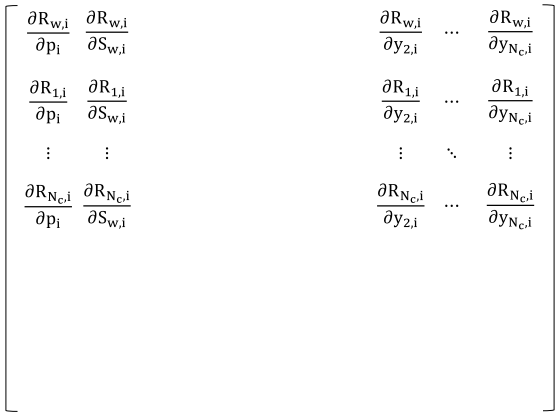

(d) Two-phase Gas and Water

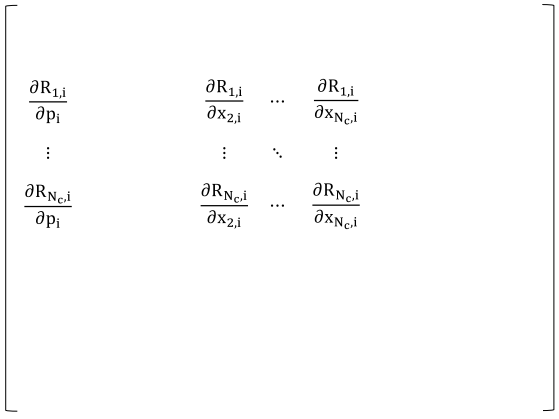

(e) Single-phase Oil

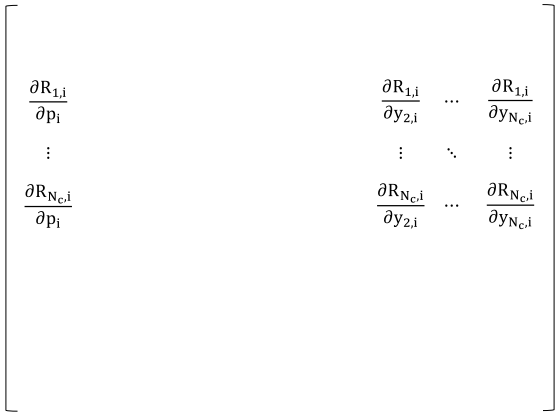

(f) Single-phase Gas

Fig. E.1 – Block diagonal elements in the Jacobian

The block-diagonal elements are calculated by differentiating the primary equations (**Eqs. (E.1)** – **(E.3)**) of the grid i by the primary variables (**Eq. (E.5)**) of the grid i. The details are as follows.

The derivatives of the water equation with respect to the primary variables is obtained by

$$\frac{\partial R_{w,i}^{n+1}}{\partial P_i^{n+1}} = \frac{\partial F_{w,i}^{n+1}}{\partial P_i^{n+1}} - \frac{\partial A_{w,i}^{n+1}}{\partial P_i^{n+1}} + \frac{\partial W_{w,i}^{n+1}}{\partial P_i^{n+1}} \tag{E.6}$$

$$\frac{\partial R_{w,i}^{n+1}}{\partial S_{w,i}^{n+1}} = \frac{\partial F_{w,i}^{n+1}}{\partial S_{w,i}^{n+1}} - \frac{\partial A_{w,i}^{n+1}}{\partial S_{w,i}^{n+1}} + \frac{\partial W_{w,i}^{n+1}}{\partial S_{w,i}^{n+1}} \tag{E.7}$$

$$\frac{\partial R_{w,i}^{n+1}}{\partial S_{g,i}^{n+1}} = 0 \tag{E.8}$$

$$\frac{\partial R_{w,i}^{n+1}}{\partial x_{k,i}^{n+1}} = 0 \tag{E.9}$$

$$\frac{\partial R_{w,i}^{n+1}}{\partial y_{k,i}^{n+1}} = 0 \tag{E.10}$$

In **Eqs. (E.6)** and **(E.7)**, the derivative of the water flux term is calculated by

$$\frac{\partial F_{w,i}^{n+1}}{\partial P_i^{n+1}} = \frac{\partial T_{w,i-1/2}^{n+1}}{\partial P_i^{n+1}}(P_{i-1}^{n+1} - P_i^{n+1}) + \frac{\partial T_{w,i+1/2}^{n+1}}{\partial P_i^{n+1}}(P_{i+1}^{n+1} - P_i^{n+1}) - \left(T_{\alpha,i-1/2}^{n+1} + T_{\alpha,i+1/2}^{n+1}\right) \tag{E.11}$$

$$\frac{\partial F_{w,i}^{n+1}}{\partial S_{w,i}^{n+1}} = \frac{\partial T_{w,i-1/2}^{n+1}}{\partial S_{w,i}^{n+1}}(P_{i-1}^{n+1} - P_i^{n+1}) + \frac{\partial T_{w,i+1/2}^{n+1}}{\partial S_{w,i}^{n+1}}(P_{i+1}^{n+1} - P_i^{n+1}) \tag{E.12}$$

The derivative of the transmissibility is

$$\frac{\partial T_{\alpha,i\pm1/2}^{n+1}}{\partial P_i^{n+1}} = \frac{w_{i\pm1/2}}{\Delta\tau_{i\pm1/2}}\left(\frac{c_t}{\lambda_t}\right)_{\text{init},i\pm1/2}\frac{\partial \lambda_{w,up}^{n+1}}{\partial P_i^{n+1}} \tag{E.13}$$

$$\frac{\partial T_{\alpha,i\pm1/2}^{n+1}}{\partial S_{w,i}^{n+1}} = \frac{w_{i\pm1/2}}{\Delta\tau_{i\pm1/2}}\left(\frac{c_t}{\lambda_t}\right)_{\text{init},i\pm1/2}\frac{\partial \lambda_{w,up}^{n+1}}{\partial S_{w,i}^{n+1}} \tag{E.14}$$

The phase mobility is determined based on the up-winding scheme. If the upstream grid is the neighbor grid, the derivative of the water mobility equals zero.

$$\frac{\partial \lambda_{w,i\pm1}^{n+1}}{\partial P_i^{n+1}} = 0, \quad \frac{\partial \lambda_{w,i\pm1}^{n+1}}{\partial S_{w,i}^{n+1}} = 0 \tag{E.15}$$

If the upstream is the grid i, the derivative of the water mobility is

$$\frac{\partial \lambda_{w,i}^{n+1}}{\partial P_i^{n+1}} = \frac{k_{rw,i}^{n+1}}{\mu_{w,i}^{n+1}}\frac{\partial \rho_{w,i}^{n+1}}{\partial P_i^{n+1}} - \rho_{w,i}^{n+1}\frac{k_{rw,i}^{n+1}}{{\mu_{w,i}^{n+1}}^2}\frac{\partial \mu_{w,i}^{n+1}}{\partial P_i^{n+1}} \tag{E.16}$$

$$\frac{\partial \lambda_{w,i}^{n+1}}{\partial S_{w,i}^{n+1}} = \frac{\rho_{w,i}^{n+1}}{\mu_{w,i}^{n+1}}\frac{\partial k_{rw,i}^{n+1}}{\partial S_{w,i}^{n+1}} \tag{E.17}$$

Notice that, in the compositional simulation, the water mobility is defined by the mass basis, while the blackoil simulation is formulated by volumetric flow using the formation volume factor. Thus, the water mobility term in **Eqs. (E.16)** and **(E.17)** contains the mass density $\rho_{w,i}^{n+1}$ instead of the formation volume factor $B_{w,i}^{n+1}$.

In **Eqs. (E.6)** and **(E.7)**, the derivative of the water accumulation term is

$$\frac{\partial A_{w,i}^{n+1}}{\partial P_i^{n+1}} = \frac{w_i\Delta\tau_i}{\Delta t^{n+1}}\left(\frac{\partial M_{\phi,i}^{n+1}}{\partial P_i^{n+1}}\rho_{w,i}^{n+1}S_{w,i}^{n+1} - M_{\phi,i}^{n+1}\frac{\partial \rho_{w,i}^{n+1}}{\partial P_i^{n+1}}S_{w,i}^{n+1}\right) \tag{E.18}$$

$$\frac{\partial A_{w,i}^{n+1}}{\partial S_{w,i}^{n+1}} = \frac{w_i\Delta\tau_i}{\Delta t^{n+1}}\left(M_{\phi,i}^{n+1}\rho_{w,i}^{n+1}\right) \tag{E.19}$$

In **Eqs. (E.6)** and **(E.7)**, the derivative of the well term is

$$\frac{\partial W_{w,i}^{n+1}}{\partial P_i^{n+1}} = w_1(\mu c_t)_{\text{init},1}\left[\lambda_{w,1}^{n+1}\left(\frac{1}{\tau_1 - \tau_{\text{well}}}\right) + \frac{\partial \lambda_{w,1}^{n+1}}{\partial P_1^{n+1}}\left(\frac{P_1^{n+1} - P_{wf}^{n+1}}{\tau_1 - \tau_{\text{well}}}\right)\right] \tag{E.20}$$

$$\frac{\partial W_{w,i}^{n+1}}{\partial S_{w,i}^{n+1}} = w_1(\mu c_t)_{\text{init},1} \frac{\partial \lambda_{w,1}^{n+1}}{\partial S_{w,1}^{n+1}} \left(\frac{P_1^{n+1} - P_{wf}^{n+1}}{\tau_1 - \tau_{\text{well}}} \right) \tag{E.21}$$

where the derivative of the water mobility is defined by **Eqs. (E.16)** and **(E.17)**.

The derivative of the jth component equations ($j = 1, \dots, N_c$) (**Eq. (E.2)**) with respect to the primary variables is obtained by

$$\frac{\partial R_{j,i}^{n+1}}{\partial P_i^{n+1}} = \frac{\partial F_{j,i}^{n+1}}{\partial P_i^{n+1}} - \frac{\partial A_{j,i}^{n+1}}{\partial P_i^{n+1}} + \frac{\partial W_{j,i}^{n+1}}{\partial P_i^{n+1}} \tag{E.22}$$

$$\frac{\partial R_{j,i}^{n+1}}{\partial S_{w,i}^{n+1}} = \frac{\partial F_{j,i}^{n+1}}{\partial S_{w,i}^{n+1}} - \frac{\partial A_{j,i}^{n+1}}{\partial S_{w,i}^{n+1}} + \frac{\partial W_{j,i}^{n+1}}{\partial S_{w,i}^{n+1}} \tag{E.23}$$

$$\frac{\partial R_{j,i}^{n+1}}{\partial S_{g,i}^{n+1}} = \frac{\partial F_{j,i}^{n+1}}{\partial S_{g,i}^{n+1}} - \frac{\partial A_{j,i}^{n+1}}{\partial S_{g,i}^{n+1}} + \frac{\partial W_{j,i}^{n+1}}{\partial S_{g,i}^{n+1}} \tag{E.24}$$

$$\frac{\partial R_{j,i}^{n+1}}{\partial x_{k,i}^{n+1}} = \frac{\partial F_{j,i}^{n+1}}{\partial x_{k,i}^{n+1}} - \frac{\partial A_{j,i}^{n+1}}{\partial x_{k,i}^{n+1}} + \frac{\partial W_{j,i}^{n+1}}{\partial x_{k,i}^{n+1}} \tag{E.25}$$

$$\frac{\partial R_{j,i}^{n+1}}{\partial y_{k,i}^{n+1}} = \frac{\partial F_{j,i}^{n+1}}{\partial y_{k,i}^{n+1}} - \frac{\partial A_{j,i}^{n+1}}{\partial y_{k,i}^{n+1}} + \frac{\partial W_{j,i}^{n+1}}{\partial y_{k,i}^{n+1}} \tag{E.26}$$

Note that the subscript k is the component number ($k = 2, \dots, N_c$). The phase mole fractions, x_1 and y_1 are the dependent (secondary) variable, and the other phase mole fractions are the independent (primary) variables.

$$x_1 = 1 - \sum_{k=2}^{N_c} x_k \tag{E.27}$$

$$y_1 = 1 - \sum_{k=2}^{N_c} y_k \tag{E.28}$$

In **Eqs. (E.22)** – **(E.26)**, the derivative of the jth component flux term is

$$\frac{\partial F_{j,i}^{n+1}}{\partial P_i^{n+1}} = \frac{\partial T_{j,i-1/2}^{n+1}}{\partial P_i^{n+1}}\left(P_{i-1}^{n+1} - P_i^{n+1}\right) + \frac{\partial T_{j,i+1/2}^{n+1}}{\partial P_i^{n+1}}\left(P_{i+1}^{n+1} - P_i^{n+1}\right) - \left(T_{\alpha,i-1/2}^{n+1} + T_{\alpha,i+1/2}^{n+1}\right) \tag{E.29}$$

$$\frac{\partial F_{j,i}^{n+1}}{\partial S_{w,i}^{n+1}} = \frac{\partial T_{j,i-1/2}^{n+1}}{\partial S_{w,i}^{n+1}}\left(P_{i-1}^{n+1} - P_i^{n+1}\right) + \frac{\partial T_{j,i+1/2}^{n+1}}{\partial S_{w,i}^{n+1}}\left(P_{i+1}^{n+1} - P_i^{n+1}\right) \tag{E.30}$$

$$\frac{\partial F_{j,i}^{n+1}}{\partial S_{g,i}^{n+1}} = \frac{\partial T_{j,i-1/2}^{n+1}}{\partial S_{g,i}^{n+1}}\left(P_{i-1}^{n+1} - P_i^{n+1}\right) + \frac{\partial T_{j,i+1/2}^{n+1}}{\partial S_{g,i}^{n+1}}\left(P_{i+1}^{n+1} - P_i^{n+1}\right) \tag{E.31}$$

$$\frac{\partial F_{j,i}^{n+1}}{\partial x_{k,i}^{n+1}} = \frac{\partial T_{j,i-1/2}^{n+1}}{\partial x_{k,i}^{n+1}}\left(P_{i-1}^{n+1} - P_i^{n+1}\right) + \frac{\partial T_{j,i+1/2}^{n+1}}{\partial x_{k,i}^{n+1}}\left(P_{i+1}^{n+1} - P_i^{n+1}\right) \tag{E.32}$$

$$\frac{\partial F_{j,i}^{n+1}}{\partial y_{k,i}^{n+1}} = \frac{\partial T_{j,i-1/2}^{n+1}}{\partial y_{k,i}^{n+1}}\left(P_{i-1}^{n+1} - P_i^{n+1}\right) + \frac{\partial T_{j,i+1/2}^{n+1}}{\partial y_{k,i}^{n+1}}\left(P_{i+1}^{n+1} - P_i^{n+1}\right) \tag{E.33}$$

In **Eqs. (E.29)** – **(E.33)**, the derivative of the *j*th component transmissibility is

$$\frac{\partial T_{j,i\pm1/2}^{n+1}}{\partial P_i^{n+1}} = \frac{w_{i\pm1/2}}{\Delta\tau_{i\pm1/2}}\left(\frac{c_t}{\lambda_t}\right)_{\text{init},i\pm1/2}\frac{\partial \lambda_{j,up}^{n+1}}{\partial P_i^{n+1}} \tag{E.34}$$

$$\frac{\partial T_{j,i\pm1/2}^{n+1}}{\partial S_{w,i}^{n+1}} = \frac{w_{i\pm1/2}}{\Delta\tau_{i\pm1/2}}\left(\frac{c_t}{\lambda_t}\right)_{\text{init},i\pm1/2}\frac{\partial \lambda_{j,up}^{n+1}}{\partial S_{w,i}^{n+1}} \tag{E.35}$$

$$\frac{\partial T_{j,i\pm1/2}^{n+1}}{\partial S_{g,i}^{n+1}} = \frac{w_{i\pm1/2}}{\Delta\tau_{i\pm1/2}}\left(\frac{c_t}{\lambda_t}\right)_{\text{init},i\pm1/2}\frac{\partial \lambda_{j,up}^{n+1}}{\partial S_{g,i}^{n+1}} \tag{E.36}$$

$$\frac{\partial T_{j,i\pm1/2}^{n+1}}{\partial x_{k,i}^{n+1}} = \frac{w_{i\pm1/2}}{\Delta\tau_{i\pm1/2}}\left(\frac{c_t}{\lambda_t}\right)_{\text{init},i\pm1/2}\frac{\partial \lambda_{j,up}^{n+1}}{\partial x_{k,i}^{n+1}} \tag{E.37}$$

$$\frac{\partial T_{j,i\pm1/2}^{n+1}}{\partial y_{k,i}^{n+1}} = \frac{w_{i\pm1/2}}{\Delta\tau_{i\pm1/2}}\left(\frac{c_t}{\lambda_t}\right)_{\text{init},i\pm1/2}\frac{\partial \lambda_{j,up}^{n+1}}{\partial y_{k,i}^{n+1}} \tag{E.38}$$

In **Eqs. (E.34)** – **(E.38)**, the derivative of the component mobility is determined by the up-winding scheme. If the upstream grid is the neighbor grid, the derivatives are zero.

$$\frac{\partial \lambda_{j,i\pm1}^{n+1}}{\partial P_i^{n+1}} = 0, \quad \frac{\partial \lambda_{j,i\pm1}^{n+1}}{\partial S_{w,i}^{n+1}} = 0, \quad \frac{\partial \lambda_{j,i\pm1}^{n+1}}{\partial S_{g,i}^{n+1}} = 0, \quad \frac{\partial \lambda_{j,i\pm1}^{n+1}}{\partial x_{k,i}^{n+1}} = 0, \quad \frac{\partial \lambda_{j,i\pm1}^{n+1}}{\partial y_{k,i}^{n+1}} = 0 \tag{E.39}$$

If the upstream grid is the grid i, the derivatives are

$$\frac{\partial \lambda_{j,i}^{n+1}}{\partial P_i^{n+1}} = x_{j,i}^{n+1}\xi_{o,i}^{n+1}\frac{k_{ro,i}^{n+1}}{\mu_{o,i}^{n+1}} + y_{j,i}^{n+1}\xi_{g,i}^{n+1}\frac{k_{rg,i}^{n+1}}{\mu_{g,i}^{n+1}} \tag{E.40}$$

$$\frac{\partial \lambda_{j,i}^{n+1}}{\partial S_{w,i}^{n+1}} = x_{j,i}^{n+1}\xi_{o,i}^{n+1}\frac{1}{\mu_{o,i}^{n+1}}\frac{\partial k_{ro,i}^{n+1}}{\partial S_{w,i}^{n+1}} + y_{j,i}^{n+1}\xi_{g,i}^{n+1}\frac{1}{\mu_{g,i}^{n+1}}\frac{\partial k_{rg,i}^{n+1}}{\partial S_{w,i}^{n+1}} \tag{E.41}$$

$$\frac{\partial \lambda_{j,i}^{n+1}}{\partial S_{g,i}^{n+1}} = x_{j,i}^{n+1}\xi_{o,i}^{n+1}\frac{1}{\mu_{o,i}^{n+1}}\frac{\partial k_{ro,i}^{n+1}}{\partial S_{g,i}^{n+1}} + y_{j,i}^{n+1}\xi_{g,i}^{n+1}\frac{1}{\mu_{g,i}^{n+1}}\frac{\partial k_{rg,i}^{n+1}}{\partial S_{g,i}^{n+1}} \tag{E.42}$$

$$\frac{\partial \lambda_{j,i}^{n+1}}{\partial x_{k,i}^{n+1}} = \frac{\partial x_{j,i}^{n+1}}{\partial x_{k,i}^{n+1}}\xi_{o,i}^{n+1}\frac{k_{ro,i}^{n+1}}{\mu_{o,i}^{n+1}} + x_{j,i}^{n+1}\frac{\partial \xi_{o,i}^{n+1}}{\partial x_{k,i}^{n+1}}\frac{k_{ro,i}^{n+1}}{\mu_{o,i}^{n+1}} - x_{j,i}^{n+1}\xi_{o,i}^{n+1}\frac{k_{ro,i}^{n+1}}{\mu_{o,i}^{n+1^2}}\frac{\partial \mu_{o,i}^{n+1}}{\partial x_{k,i}^{n+1}} \tag{E.43}$$

$$\frac{\partial \lambda_{j,i}^{n+1}}{\partial y_{k,i}^{n+1}} = \frac{\partial y_{j,i}^{n+1}}{\partial y_{k,i}^{n+1}}\xi_{g,i}^{n+1}\frac{k_{rg,i}^{n+1}}{\mu_{g,i}^{n+1}} + y_{j,i}^{n+1}\frac{\partial \xi_{g,i}^{n+1}}{\partial y_{k,i}^{n+1}}\frac{k_{rg,i}^{n+1}}{\mu_{g,i}^{n+1}} - y_{j,i}^{n+1}\xi_{g,i}^{n+1}\frac{k_{rg,i}^{n+1}}{\mu_{g,i}^{n+1^2}}\frac{\partial \mu_{g,i}^{n+1}}{\partial y_{k,i}^{n+1}} \tag{E.44}$$

Notice that the component fraction x_1 and y_1 are the dependent variables of the other mole fractions and are computed based on **Eqs. (E.27)** and **(E.28)**.

If $j = 1$, the derivatives of the jth phase mole fraction in **Eqs. (E.43)** and **(E.44)** are

$$\frac{\partial x_{j,i}^{n+1}}{\partial x_{k,i}^{n+1}} = \frac{\partial}{\partial x_{k,i}^{n+1}}\sum_{p=2}^{N_c}\left(1 - x_{p,i}^{n+1}\right) = -\frac{\partial x_{k,i}^{n+1}}{\partial x_{k,i}^{n+1}} = -1 \tag{E.45}$$

$$\frac{\partial y_{j,i}^{n+1}}{\partial y_{k,i}^{n+1}} = \frac{\partial}{\partial y_{k,i}^{n+1}}\sum_{p=2}^{N_c}\left(1 - y_{p,i}^{n+1}\right) = -\frac{\partial y_{k,i}^{n+1}}{\partial y_{k,i}^{n+1}} = -1 \tag{E.46}$$

If $j \neq 1 \; and \; j = k$, then

$$\frac{\partial x_{j,i}^{n+1}}{\partial x_{k,i}^{n+1}} = 1 \tag{E.47}$$

$$\frac{\partial y_{j,i}^{n+1}}{\partial y_{k,i}^{n+1}} = 1 \tag{E.48}$$

If $j \neq 1$ and $j \neq k$, then

$$\frac{\partial x_{j,i}^{n+1}}{\partial x_{k,i}^{n+1}} = 0 \tag{E.49}$$

$$\frac{\partial y_{j,i}^{n+1}}{\partial y_{k,i}^{n+1}} = 0 \tag{E.50}$$

In **Eqs. (E.22)** – **(E.26)**, the derivative of the jth component accumulation term is

$$\frac{\partial A_{j,i}^{n+1}}{\partial P_i^{n+1}} = \frac{w_i \Delta\tau_i}{\Delta t^{n+1}} \left[\frac{\partial M_{\phi,i}^{n+1}}{\partial P_i^{n+1}} \left(x_{j,i}^{n+1} \xi_{o,i}^{n+1} S_{o,i}^{n+1} + y_{j,i}^{n+1} \xi_{g,i}^{n+1} S_{g,i}^{n+1} \right) - M_{\phi,i}^{n+1} \left(x_{j,i}^{n+1} \frac{\partial \xi_{o,i}^{n+1}}{\partial P_i^{n+1}} S_{o,i}^{n+1} + y_{j,i}^{n+1} \frac{\partial \xi_{g,i}^{n+1}}{\partial P_i^{n+1}} S_{g,i}^{n+1} \right) \right] \tag{E.51}$$

$$\frac{\partial A_{j,i}^{n+1}}{\partial S_{w,i}^{n+1}} = \frac{w_i \Delta\tau_i}{\Delta t^{n+1}} M_{\phi,i}^{n+1} \left(-x_{j,i}^{n+1} \xi_{o,i}^{n+1} \right) \tag{E.52}$$

$$\frac{\partial A_{j,i}^{n+1}}{\partial S_{g,i}^{n+1}} = \frac{w_i \Delta\tau_i}{\Delta t^{n+1}} M_{\phi,i}^{n+1} \left(-x_{j,i}^{n+1} \xi_{o,i}^{n+1} + y_{j,i}^{n+1} \xi_{g,i}^{n+1} \right) \tag{E.53}$$

$$\frac{\partial A_{j,i}^{n+1}}{\partial x_{k,i}^{n+1}} = \frac{w_i \Delta\tau_i}{\Delta t^{n+1}} M_{\phi,i}^{n+1} \left(\frac{\partial x_{j,i}^{n+1}}{\partial x_{k,i}^{n+1}} \xi_{o,i}^{n+1} S_{o,i}^{n+1} - x_{j,i}^{n+1} \frac{\partial \xi_{o,i}^{n+1}}{\partial x_{k,i}^{n+1}} S_{o,i}^{n+1} \right) \tag{E.54}$$

$$\frac{\partial A_{j,i}^{n+1}}{\partial y_{k,i}^{n+1}} = \frac{w_i \Delta\tau_i}{\Delta t^{n+1}} M_{\phi,i}^{n+1} \left(\frac{\partial y_{j,i}^{n+1}}{\partial y_{k,i}^{n+1}} \xi_{g,i}^{n+1} S_{g,i}^{n+1} - y_{j,i}^{n+1} \frac{\partial \xi_{g,i}^{n+1}}{\partial y_{k,i}^{n+1}} S_{g,i}^{n+1} \right) \tag{E.55}$$

In **Eqs. (E.22)** – **(E.26)**, the derivative of the jth component well term is

$$\frac{\partial W_{j,i}^{n+1}}{\partial P_i^{n+1}} = w_1 (\mu c_t)_{\text{init},1} \left[\lambda_{j,1}^{n+1} \left(\frac{1}{\tau_1 - \tau_{\text{well}}} \right) + \frac{\partial \lambda_{j,1}^{n+1}}{\partial P_1^{n+1}} \left(\frac{P_1^{n+1} - P_{wf}^{n+1}}{\tau_1 - \tau_{\text{well}}} \right) \right] \tag{E.56}$$

$$\frac{\partial W_{j,i}^{n+1}}{\partial S_{w,i}^{n+1}} = w_1 \left(\frac{c_t}{\lambda_t} \right)_{\text{init},1} \frac{\partial \lambda_{j,1}^{n+1}}{\partial S_{w,1}^{n+1}} \left(\frac{P_1^{n+1} - P_{wf}^{n+1}}{\tau_1 - \tau_{\text{well}}} \right) \tag{E.57}$$

$$\frac{\partial W_{j,i}^{n+1}}{\partial S_{g,i}^{n+1}} = w_1 \left(\frac{c_t}{\lambda_t}\right)_{\text{init},1} \frac{\partial \lambda_{j,1}^{n+1}}{\partial S_{g,i}^{n+1}} \left(\frac{P_1^{n+1} - P_{wf}^{n+1}}{\tau_1 - \tau_{\text{well}}}\right) \tag{E.58}$$

$$\frac{\partial W_{j,i}^{n+1}}{\partial x_{k,i}^{n+1}} = w_1 \left(\frac{c_t}{\lambda_t}\right)_{\text{init},1} \frac{\partial \lambda_{j,1}^{n+1}}{\partial x_{k,i}^{n+1}} \left(\frac{P_1^{n+1} - P_{wf}^{n+1}}{\tau_1 - \tau_{\text{well}}}\right) \tag{E.59}$$

$$\frac{\partial W_{j,i}^{n+1}}{\partial y_{k,i}^{n+1}} = w_1 \left(\frac{c_t}{\lambda_t}\right)_{\text{init},1} \frac{\partial \lambda_{j,1}^{n+1}}{\partial y_{k,i}^{n+1}} \left(\frac{P_1^{n+1} - P_{wf}^{n+1}}{\tau_1 - \tau_{\text{well}}}\right) \tag{E.60}$$

In **Eqs. (E.56)** – **(E.60)**, the derivatives of the *j*th component mobility are obtained using **Eqs. (E.40)** – **(E.44)**.

The derivative of the fugacity equality (**Eq. (E.3)**) with respect to the primary variables is obtained by

$$\frac{\partial F_{j,i}^{n+1}}{\partial P_i^{n+1}} = \frac{\partial f_{j,i}^{V\,n+1}}{\partial P_i^{n+1}} - \frac{\partial f_{j,i}^{L\,n+1}}{\partial P_i^{n+1}} \tag{E.61}$$

$$\frac{\partial F_{j,i}^{n+1}}{\partial S_{w,i}^{n+1}} = 0 \tag{E.62}$$

$$\frac{\partial F_{j,i}^{n+1}}{\partial S_{g,i}^{n+1}} = 0 \tag{E.63}$$

$$\frac{\partial F_{j,i}^{n+1}}{\partial x_{k,i}^{n+1}} = -\frac{\partial f_{j,i}^{L\,n+1}}{\partial x_{k,i}^{n+1}} \tag{E.64}$$

$$\frac{\partial F_{j,i}^{n+1}}{\partial y_{k,i}^{n+1}} = \frac{\partial f_{j,i}^{V\,n+1}}{\partial y_{k,i}^{n+1}} \tag{E.65}$$

In this study, the phase fugacity is calculated using the three-parameter Peng-Robinson Equation of State (3-PR-EOS). The fugacity is the function of the pressure, temperature, and phase composition, thus non-zero values are entered in **Eqs. (E.61)**, **(E.64)**, and **(E.65)**. The calculation procedure are described in **APPENDIX E.3**.

On the other hand, the off-diagonal elements are calculated by differentiating the primary equations (**Eqs. (E.1)** – **(E.3)**) of the grid i by the primary variables (**Eq. (E.5)**) of the neighbor grids. The details are as follows.

The derivatives of the water flow equation with respect to the primary variables of the neighbor grids is obtained by

$$\frac{\partial R_{w,i}^{n+1}}{\partial P_{i\pm1}^{n+1}} = \frac{\partial F_{w,i}^{n+1}}{\partial P_{i\pm1}^{n+1}} \tag{E.66}$$

$$\frac{\partial R_{w,i}^{n+1}}{\partial S_{w,i\pm1}^{n+1}} = \frac{\partial F_{w,i}^{n+1}}{\partial S_{w,i\pm1}^{n+1}} \tag{E.67}$$

$$\frac{\partial R_{w,i}^{n+1}}{\partial S_{g,i\pm1}^{n+1}} = 0 \tag{E.68}$$

$$\frac{\partial R_{w,i}^{n+1}}{\partial x_{k,i\pm1}^{n+1}} = 0 \tag{E.69}$$

$$\frac{\partial R_{w,i}^{n+1}}{\partial y_{k,i\pm1}^{n+1}} = 0 \tag{E.70}$$

In **Eqs. (E.66)** and **(E.67)**, the derivative of the water flux term is

$$\frac{\partial F_{w,i}^{n+1}}{\partial P_{i\pm1}^{n+1}} = T_{w,i\pm1/2}^{n+1} + \frac{\partial T_{w,i\pm1/2}^{n+1}}{\partial P_{i\pm1}^{n+1}}\left(P_{i\pm1}^{n+1} - P_i^{n+1}\right) \tag{E.71}$$

$$\frac{\partial F_{w,i}^{n+1}}{\partial S_{w,i\pm1}^{n+1}} = \frac{\partial T_{w,i\pm1/2}^{n+1}}{\partial S_{w,i\pm1}^{n+1}}\left(P_{i\pm1}^{n+1} - P_i^{n+1}\right) \tag{E.72}$$

In **Eqs. (E.71)** – **(E.72)**, the derivative of the water transmissibility is

$$\frac{\partial T_{w,i\pm1/2}^{n+1}}{\partial P_{i\pm1}^{n+1}} = \frac{w_{i\pm1/2}}{\Delta\tau_{i\pm1/2}}\left(\frac{c_t}{\lambda_t}\right)_{\text{init},i\pm1/2}\frac{\partial \lambda_{w,up}^{n+1}}{\partial P_{i\pm1}^{n+1}} \tag{E.73}$$

$$\frac{\partial T_{w,i\pm1/2}^{n+1}}{\partial S_{w,i\pm1}^{n+1}} = \frac{w_{i\pm1/2}}{\Delta\tau_{i\pm1/2}}\left(\frac{c_t}{\lambda_t}\right)_{\text{init},i\pm1/2}\frac{\partial \lambda_{w,up}^{n+1}}{\partial S_{w,i\pm1}^{n+1}} \tag{E.74}$$

If the upstream grid is the grid i, the derivative of the water mobility equals zero. If the upstream grid is the neighbor grid, the water mobility is calculated using **Eqs. (E.16)** and **(E.17)**.

The derivative of the jth component flow equations ($j = 1, \dots, N_c$) (**Eq. (E.2)**) with respect to the primary variables is

$$\frac{\partial R_{j,i}^{n+1}}{\partial P_{i\pm1}^{n+1}} = \frac{\partial F_{j,i}^{n+1}}{\partial P_{i\pm1}^{n+1}} \tag{E.75}$$

$$\frac{\partial R_{j,i}^{n+1}}{\partial S_{w,i\pm1}^{n+1}} = \frac{\partial F_{j,i}^{n+1}}{\partial S_{w,i\pm1}^{n+1}} \tag{E.76}$$

$$\frac{\partial R_{j,i}^{n+1}}{\partial S_{g,i\pm1}^{n+1}} = \frac{\partial F_{j,i}^{n+1}}{\partial S_{g,i\pm1}^{n+1}} \tag{E.77}$$

$$\frac{\partial R_{j,i}^{n+1}}{\partial x_{k,i\pm1}^{n+1}} = \frac{\partial F_{j,i}^{n+1}}{\partial x_{k,i\pm1}^{n+1}} \tag{E.78}$$

$$\frac{\partial R_{j,i}^{n+1}}{\partial y_{k,i\pm1}^{n+1}} = \frac{\partial F_{j,i}^{n+1}}{\partial y_{k,i\pm1}^{n+1}} \tag{E.79}$$

In **Eqs. (E.75)** and **(E.79)**, the derivatives of the jth component flux term are

$$\frac{\partial F_{j,i}^{n+1}}{\partial P_{i\pm1}^{n+1}} = \frac{\partial T_{j,i\pm1/2}^{n+1}}{\partial P_{i\pm1}^{n+1}}\left(P_{i\pm1}^{n+1} - P_i^{n+1}\right) \tag{E.80}$$

$$\frac{\partial F_{j,i}^{n+1}}{\partial S_{w,i\pm1}^{n+1}} = \frac{\partial T_{j,i\pm1/2}^{n+1}}{\partial S_{w,i\pm1}^{n+1}}\left(P_{i\pm1}^{n+1} - P_i^{n+1}\right) \tag{E.81}$$

$$\frac{\partial F_{j,i}^{n+1}}{\partial S_{g,i\pm1}^{n+1}} = \frac{\partial T_{j,i\pm1/2}^{n+1}}{\partial S_{g,i\pm1}^{n+1}}\left(P_{i\pm1}^{n+1} - P_i^{n+1}\right) \tag{E.82}$$

$$\frac{\partial F_{j,i}^{n+1}}{\partial x_{k,i\pm1}^{n+1}} = \frac{\partial T_{j,i\pm1/2}^{n+1}}{\partial x_{k,i\pm1}^{n+1}} \left(P_{i\pm1}^{n+1} - P_i^{n+1}\right) \tag{E.83}$$

$$\frac{\partial F_{j,i}^{n+1}}{\partial y_{k,i\pm1}^{n+1}} = \frac{\partial T_{j,i\pm1/2}^{n+1}}{\partial y_{k,i\pm1}^{n+1}} \left(P_{i\pm1}^{n+1} - P_i^{n+1}\right) \tag{E.84}$$

In **Eqs. (E.80)** and **(E.84)**, the derivative of the jth component transmissibility term is

$$\frac{\partial T_{j,i\pm1/2}^{n+1}}{\partial P_{i\pm1}^{n+1}} = \frac{w_{i\pm1/2}}{\Delta\tau_{i\pm1/2}} \left(\frac{c_t}{\lambda_t}\right)_{\text{init},i\pm1/2} \frac{\partial \lambda_{j,up}^{n+1}}{\partial P_{i\pm1}^{n+1}} \tag{E.85}$$

$$\frac{\partial T_{j,i\pm1/2}^{n+1}}{\partial S_{w,i\pm1}^{n+1}} = \frac{w_{i\pm1/2}}{\Delta\tau_{i\pm1/2}} \left(\frac{c_t}{\lambda_t}\right)_{\text{init},i\pm1/2} \frac{\partial \lambda_{j,up}^{n+1}}{\partial S_{w,i\pm1}^{n+1}} \tag{E.86}$$

$$\frac{\partial T_{j,i\pm1/2}^{n+1}}{\partial S_{g,i\pm1}^{n+1}} = \frac{w_{i\pm1/2}}{\Delta\tau_{i\pm1/2}} \left(\frac{c_t}{\lambda_t}\right)_{\text{init},i\pm1/2} \frac{\partial \lambda_{j,up}^{n+1}}{\partial S_{g,i\pm1}^{n+1}} \tag{E.87}$$

$$\frac{\partial T_{j,i\pm1/2}^{n+1}}{\partial x_{k,i\pm1}^{n+1}} = \frac{w_{i\pm1/2}}{\Delta\tau_{i\pm1/2}} \left(\frac{c_t}{\lambda_t}\right)_{\text{init},i\pm1/2} \frac{\partial \lambda_{j,up}^{n+1}}{\partial x_{k,i\pm1}^{n+1}} \tag{E.88}$$

$$\frac{\partial T_{j,i\pm1/2}^{n+1}}{\partial y_{k,i\pm1}^{n+1}} = \frac{w_{i\pm1/2}}{\Delta\tau_{i\pm1/2}} \left(\frac{c_t}{\lambda_t}\right)_{\text{init},i\pm1/2} \frac{\partial \lambda_{j,up}^{n+1}}{\partial y_{k,i\pm1}^{n+1}} \tag{E.89}$$

In **Eqs. (E.85)** – **(E.89)**, the derivative of the component mobility is determined by the up-winding scheme. If the upstream grid is the grid i, the derivatives are zero. If the upstream grid is the grid i, the derivatives are calculated using **Eqs. (E.40)** – **(E.44)**.

The derivative of the fugacity equality (**Eq. (E.3)**) is

$$\frac{\partial F_{j,i}^{n+1}}{\partial P_{i\pm1}^{n+1}} = 0 \tag{E.90}$$

$$\frac{\partial F_{j,i}^{n+1}}{\partial S_{w,i\pm1}^{n+1}} = 0 \tag{E.91}$$

$$\frac{\partial F_{j,i}^{n+1}}{\partial S_{g,i\pm1}^{n+1}} = 0 \tag{E.92}$$

$$\frac{\partial F_{j,i}^{n+1}}{\partial x_{k,i\pm1}^{n+1}} = 0 \tag{E.93}$$

$$\frac{\partial F_{j,i}^{n+1}}{\partial y_{k,i\pm1}^{n+1}} = 0 \tag{E.94}$$

The thermodynamic condition of the grid i has no relation to the pressure, temperature, and fluid compositions of the neighbor grids. Thus, all the derivatives in **Eqs. (E.90) - (E.94)**) are zero.

E.2 Derivative of Three-Parameter PR-EOS

In this study, we use the three-parameter Peng-Robinson cubic EOS. The derivative of the z-factor is obtained by differentiating the Peng-Robinson EOS by pressure and phase component, respectively.

$$\frac{\partial z}{\partial P} = -\frac{\frac{\partial B}{\partial P}z^2 + \left[\frac{\partial A}{\partial P} - 2(1+3B)\frac{\partial B}{\partial P}\right]z - \left[\frac{\partial A}{\partial P}B + (A - 2B - 3B^2)\frac{\partial B}{\partial P}\right]}{3z^2 + 2(B-1)z + (A - 3B^2 - 2B)} \tag{E.95}$$

$$\frac{\partial z}{\partial \mathbf{x}} = -\frac{\frac{\partial B}{\partial \mathbf{x}}z^2 + \left[\frac{\partial A}{\partial \mathbf{x}} - 2(1+3B)\frac{\partial B}{\partial \mathbf{x}}\right]z - \left[\frac{\partial A}{\partial \mathbf{x}}B + (A - 2B - 3B^2)\frac{\partial B}{\partial \mathbf{x}}\right]}{3z^2 + 2(B-1)z + (A - 3B^2 - 2B)} \tag{E.96}$$

where $\mathbf{x}$ denotes the phase mole fractions ($\mathbf{x} = \{y_i\}$ in the vapor phase, and $\mathbf{x} = \{x_i\}$ in the liquid phase). Notice that $i = 2, \ldots, N_c$.

The derivatives of the EOS parameters are calculated as follows.

$$\frac{\partial A}{\partial P} = \frac{(a\alpha)_m}{R^2T^2} \tag{E.97}$$

$$\frac{\partial B}{\partial P} = \frac{b_m}{RT} \tag{E.98}$$

$$\frac{\partial A}{\partial X_k} = \frac{\partial (a\alpha)_m}{\partial X_k}\frac{P}{R^2T^2} \tag{E.99}$$

$$\frac{\partial B}{\partial X_k} = \frac{\partial b_m}{\partial X_k}\frac{P}{RT} \tag{E.100}$$

where X_k is the kth mole fraction of vapor or liquid. The derivative of $(a\alpha)_m$ and b_m with respect to the kth phase mole fraction ($k = 2, \dots, N_c$) is

$$\frac{\partial (a\alpha)_m}{\partial X_k} = 2\sum_{j=1}^{N_c} X_j \left[\left(1-\theta_{kj}\right)\sqrt{(a\alpha)_k (a\alpha)_j} - \left(1-\theta_{1j}\right)\sqrt{(a\alpha)_1 (a\alpha)_j}\right] \tag{E.101}$$

$$\frac{\partial b_m}{\partial X_k} = b_k - b_1 \tag{E.102}$$

Hence, the derivatives of the phase properties ($\alpha = L, V$) are obtained as follows.

$$\frac{\partial V_\alpha}{\partial P} = -\frac{z_\alpha RT}{P^2} + \frac{\partial z_\alpha}{\partial P}\frac{RT}{P} \tag{E.103}$$

$$\frac{\partial V_\alpha}{\partial X_k} = \frac{\partial z_\alpha}{\partial X_k}\frac{RT}{P} - (c_k - c_1) \tag{E.104}$$

$$\frac{\partial \xi_\alpha}{\partial P} = -\frac{1}{V_\alpha^2}\frac{\partial V_\alpha}{\partial P} \tag{E.105}$$

$$\frac{\partial \xi_\alpha}{\partial X_k} = -\frac{1}{V_\alpha^2}\frac{\partial V_\alpha}{\partial X_k} \tag{E.106}$$

The capillary pressure calculation is based on the Young-Laplace equation (**Eq. (3.57)**). The derivative of the capillary pressure is

$$\frac{\partial P_{cgo}}{\partial P} = \frac{2}{r}\frac{\partial \sigma}{\partial P} \tag{E.107}$$

$$\frac{\partial P_{cgo}}{\partial x_k} = \frac{2}{r}\frac{\partial \sigma}{\partial x_k} \tag{E.108}$$

$$\frac{\partial P_{cgo}}{\partial y_k} = \frac{2}{r}\frac{\partial \sigma}{\partial y_k} \tag{E.109}$$

where the derivatives of the surface tension are

$$\frac{\partial \sigma}{\partial P} = 4\left[\sum_{j=1}^{N_c} \varphi_j\left(\xi_o x_j - \xi_g y_j\right)\right]^3 \times \sum_{j=1}^{N_c} \varphi_j \left(\frac{\partial \xi_o}{\partial P} x_j - \frac{\partial \xi_g}{\partial P} y_j\right) \tag{E.110}$$

$$\frac{\partial \sigma}{\partial x_k} = 4\left[\sum_{j=1}^{N_c} \varphi_j\left(\xi_o x_j - \xi_g y_j\right)\right]^3 \times \sum_{j=1}^{N_c} \varphi_j \left(\frac{\partial \xi_o}{\partial x_k} x_j + \xi_o \frac{\partial x_j}{\partial x_k}\right) \tag{E.111}$$

$$\frac{\partial \sigma}{\partial y_k} = 4\left[\sum_{j=1}^{N_c} \varphi_j\left(\xi_o x_j - \xi_g y_j\right)\right]^3 \times \sum_{j=1}^{N_c} \varphi_j \left(-\frac{\partial \xi_g}{\partial y_k} y_j - \xi_g \frac{\partial y_j}{\partial y_k}\right) \tag{E.112}$$

In **Eqs. (E.110)** – **(E.112)**, the derivative of the jth mole fraction with respect to the kth mole fraction is calculated by **Eqs. (E.45)** – **(E.50)**.

E.3 Derivative of Fugacity

The derivative of the jth component fugacity is written by using fugacity coefficient ϕ_j.

$$\frac{\partial f_j}{\partial P} = X_j \phi_j + X_j P \frac{\partial \phi_j}{\partial P} \tag{E.113}$$

$$\frac{\partial f_j}{\partial X_k} = P \phi_j \delta_{jk} + X_j P \frac{\partial \phi_j}{\partial X_k} \tag{E.114}$$

where X_k is the kth mole fraction of the vapor or liquid, and δ_{jk} is the Kronecker delta function ($\delta_{jk} = 1$ if $j = k$, and $\delta_{jk} = 0$ otherwise). The derivative of the fugacity is

$$\frac{\partial \phi_j}{\partial P} = \phi_j \left[\frac{b_j}{b_m}\frac{\partial z}{\partial P} - \frac{\frac{\partial z}{\partial P} - \frac{\partial B}{\partial P}}{z - B} \right.$$

$$- \frac{1}{2\sqrt{2}} \left(\frac{a_{mj}}{(a\alpha)_m} \right.$$

$$\left. - \frac{b_j}{b_m} \right) \left\{ \left(\frac{1}{B}\frac{\partial A}{\partial P} - \frac{A}{B^2}\frac{\partial B}{\partial P} \right) \ln \frac{z_L + \left(1+\sqrt{2}\right)B}{z_L + \left(1-\sqrt{2}\right)B} \right.$$

$$\left. \left. + \frac{A}{B} \left(\frac{\frac{\partial z}{\partial P} + \left(1+\sqrt{2}\right)\frac{\partial B}{\partial P}}{z + \left(1+\sqrt{2}\right)B} - \frac{\frac{\partial z}{\partial P} + \left(1-\sqrt{2}\right)\frac{\partial B}{\partial P}}{z + \left(1-\sqrt{2}\right)B} \right) \right\} \right] \quad \text{(E.115)}$$

$$\frac{\partial \phi_j}{\partial X_k} = \phi_j \left[\left(\frac{b_j}{b_m}\frac{\partial z}{\partial X_k} - \frac{b_j}{b_m^2}(z-1)\frac{\partial b_m}{\partial X_k} \right) - \frac{\frac{\partial z}{\partial X_k} - \frac{\partial B}{\partial X_k}}{z - B} \right.$$

$$- \frac{1}{2\sqrt{2}} \left(\frac{a_{mj}}{(a\alpha)_m} \right.$$

$$\left. - \frac{b_j}{b_m} \right) \left\{ \left(\frac{1}{B}\frac{\partial A}{\partial X_k} - \frac{A}{B^2}\frac{\partial B}{\partial X_k} \right) \ln \frac{z_L + \left(1+\sqrt{2}\right)B}{z_L + \left(1-\sqrt{2}\right)B} \right.$$

$$\left. + \frac{A}{B} \left(\frac{\frac{\partial z}{\partial X_k} + \left(1+\sqrt{2}\right)\frac{\partial B}{\partial X_k}}{z + \left(1+\sqrt{2}\right)B} - \frac{\frac{\partial z}{\partial X_k} + \left(1-\sqrt{2}\right)\frac{\partial B}{\partial X_k}}{z + \left(1-\sqrt{2}\right)B} \right) \right\} \quad \text{(E.116)}$$

$$- \frac{A}{2\sqrt{2}B} \ln \frac{z_L + \left(1+\sqrt{2}\right)B}{z_L + \left(1-\sqrt{2}\right)B} \left(\frac{1}{(a\alpha)_m}\frac{\partial a_{mj}}{\partial X_k} - \frac{a_{mj}}{(a\alpha)_m^2}\frac{\partial (a\alpha)_m}{\partial X_k} \right.$$

$$\left. + \frac{b_j}{b_m^2}\frac{\partial b_m}{\partial X_k} \right) \Bigg]$$

where the derivative of a_{mi} with respect to x_k is calculated by

$$\frac{\partial a_{mj}}{\partial X_k} = \frac{\partial^2 (a\alpha)_m}{\partial X_j \partial X_k} = 2\left[\left(1-\theta_{jk}\right)\sqrt{(a\alpha)_j (a\alpha)_k} - \left(1-\theta_{j1}\right)\sqrt{(a\alpha)_j (a\alpha)_1}\right] \quad \text{(E.117)}$$

E.4 Implicit BHP Calculation

If the bottom-hole pressure is specified, we can explicitly calculate the production rate using the well equation. If the production rate is specified, we implicitly solve the bottom-hole pressure during the Newton iteration. The implicit BHP calculation is performed by adding the additional equation (R_{ss}^{n+1}) and unknown (P_{wf}^{n+1}) on the residual vector ($\mathbf{R}^{n+1}$) and primary variable vector ($\mathbf{u}^{n+1}$), respectively.

$$\mathbf{R}^{n+1} = [\mathbf{R}_1^{n+1}, \mathbf{R}_2^{n+1}, \dots, \mathbf{R}_3^{n+1}, R_{ss}^{n+1}]^T \quad \text{(E.118)}$$

$$\mathbf{u}^{n+1} = \left[\mathbf{u}_1^{n+1}, \mathbf{u}_2^{n+1}, \dots, \mathbf{u}_3^{n+1}, P_{wf}^{n+1}\right]^T \quad \text{(E.119)}$$

The well residual term R_{ss} is obtained by summating the well equations of water (**Eq. (3.65)**) and hydrocarbon components (**Eq. (3.88)**).

$$R_{ss}^{n+1} = w_i \left(\frac{c_t}{\lambda_t}\right)_{\text{init},1} \left(\lambda_{w,1}^{n+1} + \sum_{j=1}^{N_c} \lambda_{j,1}^{n+1}\right)\left(\frac{P_1^{n+1} - P_{wf}^{n+1}}{\tau_1 - \tau_{\text{well}}}\right) - \sum_{\alpha=w,o,g} \tilde{q}_{w\alpha}^{n+1} \quad \text{(E.120)}$$

The derivatives of the well residual term are placed on the last row and column as shown in **Fig. C.3**.

The elements $\mathbf{LL}_1, \mathbf{LL}_2$, and $\mathbf{LU}_2$in **Fig. C.3** is comprised of a vector and scalar value. The row vector $\mathbf{LL}_1$ is given by

$$\mathbf{LL}_1 = \left[\frac{\partial R_{ss}}{\partial P_1} \quad \frac{\partial R_{ss}}{\partial S_{w,1}} \quad \frac{\partial R_{ss}}{\partial S_{g,1}} \quad \frac{\partial R_{ss}}{\partial x_{2,1}} \quad \cdots \quad \frac{\partial R_{ss}}{\partial x_{N_c,1}} \quad \frac{\partial R_{ss}}{\partial y_{2,1}} \quad \cdots \quad \frac{\partial R_{ss}}{\partial y_{N_c,1}}\right] \quad \text{(E.121)}$$

The dimension of the vector depends on the number of phases saturated in the grid 1. The scalar vale $\mathbf{LL}_2$ is given by

$$\mathbf{LL}_2^{n+1} = \frac{\partial R_{ss}}{\partial P_{wf}} \tag{E.122}$$

The column vector $\mathbf{LU}_2$ is given by

$$\mathbf{LU}_2^{n+1} = \left[\frac{\partial R_w}{\partial P_{wf}} \quad \frac{\partial R_1}{\partial P_{wf}} \quad \cdots \quad \frac{\partial R_{N_c}}{\partial P_{wf}} \quad \frac{\partial F_1}{\partial P_{wf}} \quad \cdots \quad \frac{\partial F_{N_c}}{\partial P_{wf}}\right]^T \tag{E.123}$$

The dimension of the vector depends on the number of phases saturated in the grid 1. Notice that the production rate is specified, thus this is a fixed value. The $\mathbf{LL}_1^{n+1}$ elements in **Eqs. (E.121)** are calculated as follows.

$$\frac{\partial R_{ss}^{n+1}}{\partial P_1^{n+1}} = w_i \left(\frac{c_t}{\lambda_t}\right)_{\text{init},1} \left[\left(\frac{\partial \lambda_{w,1}^{n+1}}{\partial P_1^{n+1}} + \sum_{j=1}^{N_c} \frac{\partial \lambda_{j,1}^{n+1}}{\partial P_1^{n+1}}\right)\left(\frac{P_1^{n+1} - P_{wf}^{n+1}}{\tau_1 - \tau_{\text{well}}}\right) + \left(\lambda_{w,1}^{n+1} + \sum_{j=1}^{N_c} \lambda_{j,1}^{n+1}\right)\left(\frac{1}{\tau_1 - \tau_{\text{well}}}\right)\right] \tag{E.124}$$

$$\frac{\partial R_{ss}^{n+1}}{\partial S_{w,1}^{n+1}} = w_i \left(\frac{c_t}{\lambda_t}\right)_{\text{init},1} \left(\frac{\partial \lambda_{w,1}^{n+1}}{\partial S_{w,1}^{n+1}} + \sum_{j=1}^{N_c} \frac{\partial \lambda_{j,1}^{n+1}}{\partial S_{w,1}^{n+1}}\right)\left(\frac{P_1^{n+1} - P_{wf}^{n+1}}{\tau_1 - \tau_{\text{well}}}\right) \tag{E.125}$$

$$\frac{\partial R_{ss}^{n+1}}{\partial S_{g,1}^{n+1}} = w_i \left(\frac{c_t}{\lambda_t}\right)_{\text{init},1} \left(\frac{\partial \lambda_{w,1}^{n+1}}{\partial S_{g,1}^{n+1}} + \sum_{j=1}^{N_c} \frac{\partial \lambda_{j,1}^{n+1}}{\partial S_{g,1}^{n+1}}\right)\left(\frac{P_1^{n+1} - P_{wf}^{n+1}}{\tau_1 - \tau_{\text{well}}}\right) \tag{E.126}$$

$$\frac{\partial R_{ss}^{n+1}}{\partial x_{k,1}^{n+1}} = w_i \left(\frac{c_t}{\lambda_t}\right)_{\text{init},1} \left(\frac{\partial \lambda_{w,1}^{n+1}}{\partial x_{k,1}^{n+1}} + \sum_{j=1}^{N_c} \frac{\partial \lambda_{j,1}^{n+1}}{\partial x_{k,1}^{n+1}}\right)\left(\frac{P_1^{n+1} - P_{wf}^{n+1}}{\tau_1 - \tau_{\text{well}}}\right) \tag{E.127}$$

$$\frac{\partial R_{ss}^{n+1}}{\partial y_{k,1}^{n+1}} = w_i \left(\frac{c_t}{\lambda_t}\right)_{\text{init},1} \left(\frac{\partial \lambda_{w,1}^{n+1}}{\partial y_{k,1}^{n+1}} + \sum_{j=1}^{N_c} \frac{\partial \lambda_{j,1}^{n+1}}{\partial y_{k,1}^{n+1}}\right)\left(\frac{P_1^{n+1} - P_{wf}^{n+1}}{\tau_1 - \tau_{\text{well}}}\right) \tag{E.128}$$

In **Eqs. (E.124)** - **(E.128)**, the derivatives of the phase mobility are calculated using **Eqs. (E.39)** – **(E.44)**.

The $\mathbf{LL}_2$ element in **Eq. (E.122)** is obtained by

$$\frac{\partial R_{ss}^{n+1}}{\partial P_{wf}^{n+1}} = -w_i \left(\frac{c_t}{\lambda_t}\right)_{\text{init},1} \left(\lambda_{w,1}^{n+1} + \sum_{j=1}^{N_c} \lambda_{j,1}^{n+1} \right) \left(\frac{1}{\tau_1 - \tau_{\text{well}}}\right) \tag{E.129}$$

The $\mathbf{LU}_2^{n+1}$ elements in **Eq. (E.121)** are calculated by

$$\frac{\partial R_{w}^{n+1}}{\partial P_{wf}^{n+1}} = w_i \left(\frac{c_t}{\lambda_t}\right)_{\text{init},1} \lambda_{w,1}^{n+1} \left(\frac{1}{\tau_1 - \tau_{\text{well}}}\right) \tag{E.130}$$

$$\frac{\partial R_{j}^{n+1}}{\partial P_{wf}^{n+1}} = w_i \left(\frac{c_t}{\lambda_t}\right)_{\text{init},1} \lambda_{j,1}^{n+1} \left(\frac{1}{\tau_1 - \tau_{\text{well}}}\right) \tag{E.131}$$

$$\frac{\partial F_{j}^{n+1}}{\partial P_{wf}^{n+1}} = 0 \tag{E.132}$$

APPENDIX F

GRADIENT CALCULATION BASED ON ADJOINT METHOD

F.1 Methodology

In history matching or optimization problems, we are interested in knowing the sensitivity of the model responses (i.e. bottom-hole pressure, production rate) to the model parameters (i.e. permeability, porosity). The sensitivity is obtained by applying a chain rule as follows.

$$\frac{\delta p_{wf}(\mathbf{d})}{\delta k(\mathbf{x})} = \frac{\partial p_{wf}(\mathbf{d})}{\partial V_p(\mathbf{i})}\frac{\partial V_p(\mathbf{i})}{\partial \tau(\mathbf{i})}\frac{\delta \tau(\mathbf{i})}{\delta \tau(\mathbf{x})}\frac{\delta \tau(\mathbf{x})}{\delta k(\mathbf{x})} \tag{F.1}$$

$$\frac{\delta p_{wf}(\mathbf{d})}{\delta \phi(\mathbf{x})} = \frac{\partial p_{wf}(\mathbf{d})}{\partial V_p(\mathbf{i})}\frac{\partial V_p(\mathbf{i})}{\partial \tau(\mathbf{i})}\frac{\delta \tau(\mathbf{i})}{\delta \tau(\mathbf{x})}\frac{\delta \tau(\mathbf{x})}{\delta \phi(\mathbf{x})} \tag{F.2}$$

where **d** represents the data point with D observations ($D \times 1$ vector), **x** denotes the grid in the Cartesian space with a vector of the size N ($N \times 1$ vector), and **i** denotes the grid in τ-space with a vector of the size M ($M \times 1$ vector). Similarly, the sensitivity of the production rate with respect to the model parameters is given by

$$\frac{\delta Q(\mathbf{d})}{\delta k(\mathbf{x})} = \frac{\partial Q(\mathbf{d})}{\partial V_p(\mathbf{i})}\frac{\partial V_p(\mathbf{i})}{\partial \tau(\mathbf{i})}\frac{\delta \tau(\mathbf{i})}{\delta \tau(\mathbf{x})}\frac{\delta \tau(\mathbf{x})}{\delta k(\mathbf{x})} \tag{F.3}$$

$$\frac{\delta Q(\mathbf{d})}{\delta \phi(\mathbf{x})} = \frac{\partial Q(\mathbf{d})}{\partial V_p(\mathbf{i})}\frac{\partial V_p(\mathbf{i})}{\partial \tau(\mathbf{i})}\frac{\delta \tau(\mathbf{i})}{\delta \tau(\mathbf{x})}\frac{\delta \tau(\mathbf{x})}{\delta \phi(\mathbf{x})} \tag{F.4}$$

Applying the chain rule, we divide the sensitivity into the four sub-sensitivities. In **Eq. (F.1)** – **(F.4)**, the first sub-sensitivities, $\partial p_{wf}(\mathbf{d})/\partial V_p(\mathbf{i})$ and $\partial Q(\mathbf{d})/\partial V_p(\mathbf{i})$ are the $D \times M$ sensitivity matrix distributed in the data points and in the τ-space, and are obtained by

using '*Adjoint method*'. The second term $\partial V_p(\mathbf{i})/\partial\tau(\mathbf{i})$ is the $M \times M$ diagonal matrix whose diagonal elements correspond to the w-function that is the derivative of the drainage volume with respect to the diffusive time of flight. The third term $\delta\tau(\mathbf{i})/\delta\tau(\mathbf{x})$ is the map-back matrix that returns 1 if $x \in i$ and returns 0 if $x \notin i$ (i.e. if the Cartesian grid x exists in the τ-contour i, the corresponding matrix element returns 1). The last sub-sensitivities, $\delta\tau(\mathbf{x})/\delta k(\mathbf{x})$ and $\delta\tau(\mathbf{x})/\delta\phi(\mathbf{x})$ are the $N \times N$ diagonal sensitivity matrix whose diagonal term is obtained by the calculation of '*Travel Time Sensitivity*'. Vasco and Datta-Gupta (1999) proposed an analytical calculation of the tracer travel time sensitivity for the convective time of flight on the basis of the streamline tracing. The analogy can be applied for the diffusive time of flight based on the Fast Marching Method.

F.2 Calculation of Travel Time Sensitivity based on the Fast Marching Method

The diffusive time of flight at the Cartesian grid n is defined by the integral form in terms of a slowness f, which starts from the sink or source point and travels along the pressure front propagation.

$$\tau(n) = \int_1^n f(\mathbf{s})dr \approx \sum_{x=1}^{n} f(x)\Delta r(x) \tag{F.5}$$

where the function f is the inverse of the square root of the diffusivity, **s** is the pressure propagation trajectory, and Δr is the grid length in the direction of the propagation. For the convective time of flight, the integral is calculated along the streamline trajectory. For the diffusive time of flight, the integral is strictly given by the 'ray' equation in seismology, while we approximate this trajectory using the Fast Marching Method. In

the calculation of the Fast Marching Method, f is calculated at the cell center of each Cartesian grid. Hence, $\tau(\mathbf{x})$ is approximated by summing up the product of f (slowness) and Δr (distance) of the finite number of discretized grids where the pressure propagation passes through. The function f is defined as follows.

$$f(\mathbf{x}) = \frac{1}{\sqrt{\alpha(\mathbf{x})}} = \sqrt{\frac{\phi(\mathbf{x})\mu c_t}{k(\mathbf{x})}} \tag{F.6}$$

Because $f(\mathbf{x})$ is a composite quantity involving reservoir properties at the Cartesian grid x, its first-order variation will be given by

$$\delta f(\mathbf{x}) = \frac{\partial f(\mathbf{x})}{\partial k(\mathbf{x})}\delta k(\mathbf{x}) + \frac{\partial f(\mathbf{x})}{\partial \phi(\mathbf{x})}\delta\phi(\mathbf{x}) \tag{F.7}$$

The partial derivative of $f(\mathbf{x})$ with respect to the model parameters is calculated by

$$\frac{\partial f(\mathbf{x})}{\partial k(\mathbf{x})} = \frac{\partial}{\partial k(\mathbf{x})}\left(\sqrt{\frac{\phi(\mathbf{x})\mu c_t}{k(\mathbf{x})}}\right) = -\frac{1}{2}\sqrt{\frac{\phi(\mathbf{x})\mu c_t}{k(\mathbf{x})^3}} = -\frac{1}{2}\frac{f(\mathbf{x})}{k(\mathbf{x})} \tag{F.8}$$

$$\frac{\partial f(\mathbf{x})}{\partial \phi(\mathbf{x})} = \frac{\partial}{\partial \phi(\mathbf{x})}\left(\sqrt{\frac{\phi(\mathbf{x})\mu c_t}{k(\mathbf{x})}}\right) = \frac{1}{2}\sqrt{\frac{\mu c_t}{\phi(\mathbf{x})k(\mathbf{x})}} = \frac{1}{2}\frac{f(\mathbf{x})}{\phi(\mathbf{x})} \tag{F.9}$$

Hence, the small variation in $\tau(n)$ is obtained by summing up the small variation in δf along the pressure propagation trajectory.

$$\delta\tau(n) = \sum_{x=1}^{n}\delta f(x)\Delta r(x) = \sum_{x=1}^{n}\frac{1}{2}\left[-\frac{f(x)}{k(x)}\delta k(x) + \frac{f(x)}{\phi(x)}\delta\phi(x)\right]\Delta r(x) \tag{F.10}$$

On the basis of **Eq. (F.10)**, the partial derivative of $\tau(\mathbf{x})$ with respect to the model parameters can be calculated by

$$\frac{\delta\tau(\mathbf{x})}{\delta k(\mathbf{x})} = -\frac{1}{2}\frac{f(\mathbf{x})}{k(\mathbf{x})}\Delta r(\mathbf{x}) \tag{F.11}$$

$$\frac{\delta\tau(\mathbf{x})}{\delta \phi(\mathbf{x})} = \frac{1}{2}\frac{f(\mathbf{x})}{\phi(\mathbf{x})}\Delta r(\mathbf{x}) \tag{F.12}$$

Notice that Δr is approximated by the length of grid **x** on the direction of the pressure propagation (i.e. if the propagation direction is x-direction, then Δr is approximated by Δx). The product of $f(\mathbf{x})$ and $\Delta r(\mathbf{x})$ is corresponding to $\Delta\tau(\mathbf{x})$.

$$f(\mathbf{x})\Delta r(\mathbf{x}) = \frac{\Delta r(\mathbf{x})}{\sqrt{\alpha(\mathbf{x})}} = \Delta\tau(\mathbf{x}) \tag{F.13}$$

Using **Eqs. (F.11)** - **(F.13)**, we finally obtain the travel time sensitivity for the diffusive time of flight as follows.

$$\frac{\delta\tau(\mathbf{x})}{\delta k(\mathbf{x})} = -\frac{1}{2}\frac{\Delta\tau(\mathbf{x})}{k(\mathbf{x})} \tag{F.14}$$

$$\frac{\delta\tau(\mathbf{x})}{\delta \phi(\mathbf{x})} = \frac{1}{2}\frac{\Delta\tau(\mathbf{x})}{\phi(\mathbf{x})} \tag{F.15}$$

The sensitivity form is similar to the streamline travel time sensitivity, while the constant factor $1/2$ is added in the equations.

F.3 Calculation of 1-D Sensitivity Based on Adjoint Method

In **Eqs. (F.1)** - **(F.4)**, the first sub-sensitivities, $\partial p_{wf}(\mathbf{d})/\partial V_p(\mathbf{i})$ and $\partial Q(\mathbf{d})/\partial V_p(\mathbf{i})$ are obtained by using the Adjoint method. The Adjoint method is traditionally applied in the numerical reservoir simulation and is regarded as one of the most efficient approach to compute sensitivity (Chen et al. 1971, Wu et al. 1999, Li et al. 2003). The method is commonly called the Method of Lagrange Multiplier in mathematics. Suppose the model response vector β consist of $D \times 1$ vectors (i.e. observed bottom-hole pressures).

$$\beta = [\beta_1, \beta_2, \dots, \beta_L, \dots, \beta_D\ ]^T \tag{F.16}$$

where the component β_L represents the scalar value of the model response at time L. In the reservoir simulation along τ-coordinate, we integrate all the heterogeneities (i.e. porosity, permeability) into the drainage volumes. Hence, the heterogeneous model parameter is identical to the drainage volume at each 1-D grids.

For each data points, the Lagragian is formulated by imposing a Lagrange multiplier λ.

$$J_L = \beta_L + \sum_{l=0}^{L} [(f^{l+1})^T \lambda^{l+1}] \tag{F.17}$$

where J_L represents the Lagragian at time L (scalar), β denotes the model responses at time L (scalar), f^{l+1} represents the residual form of the finite difference equation along τ-coordinate at the simulation step $l+1$ ($M \times 1$ vector in single-phase case), and λ^{l+1} is the Lagrange multiplier at the simulation step $l+1$ ($M \times 1$ vector in single-phase case). We may think of L as the number of time steps to compute the model response β_L from the reservoir simulation.

In single-phase model, the finite difference equation ($M \times 1$ vector) is formulated by **Eq. (2.47)**. The residual form is simply expressed as

$$f^{l+1} = F^{l+1} - A^{l+1} + A^l + W^{l+1} = 0 \tag{F.18}$$

where F^{l+1} is the flux term, A^{l+1} is the accumulation term, A^l is the accumulation term at previous time-step, and W^{l+1} is the sink/source term that is imposed on the inner boundary. At the last iteration of each simulation time step, f (the residuals) must be sufficiently close to zero ($f \approx 0$). Hence, we can take any arbitrary number for λ^{l+1}.

The dimension of the Lagrange multiplier corresponds to the dimension of the finite difference equations ($M \times 1$ vector in single-phase case, $2M \times 1$ vector in two-phase case, and $3M \times 1$ vector in three-phase case). Each component is assigned to each 1-D τ grids for each time-step.

$$\lambda^{l+1} = \left[\lambda_1^{l+1}, \lambda_2^{l+1}, \ldots, \lambda_M^{l+1}\right]^T \tag{F.19}$$

Differentiating **Eq. (F.17)** with respect to the primary variables and drainage volumes, y and V_p, and rearranging the equation, a total differential of the Lagrangian is obtained by

$$\begin{aligned} dJ_L = d\beta_L + B_T + \sum_{l=1}^{L} \left\{ (\lambda^l)^T \left[\nabla_{y^l} (f^l)^T\right]^T + (\lambda^{l+1})^T \left[\nabla_{y^l} (f^{l+1})^T\right]^T \right\} dy^l \\ + \sum_{l=1}^{L} \left\{ (\lambda^l)^T \left[\nabla_{V_p} (f^l)^T\right]^T dV_p \right\} \end{aligned} \tag{F.20}$$

where B_T is the boundary terms.

$$\begin{aligned} B_T = (\lambda^{L+1})^T \left\{ \left[\nabla_{y^{L+1}} (f^{L+1})^T\right]^T dy^{L+1} + \left[\nabla_{V_p} (f^{L+1})^T\right]^T dV_p \right\} \\ + (\lambda^1)^T \left[\nabla_{y^0} (f^1)^T\right]^T dy^0 \end{aligned} \tag{F.21}$$

The initial reservoir condition is fixed, thus $dy^0 = 0$ (i.e. $dP^0 = 0$). Let λ^{L+1} be zero ($\lambda^{L+1} = 0$). These facts follows that $B_T = 0$. Hence, **Eq. (F.20)** is rewritten as

$$\begin{aligned} dJ_L = \sum_{l=1}^{L} \left\{ (\lambda^l)^T \left[\nabla_{y^l} (f^l)^T\right]^T + (\lambda^{l+1})^T \left[\nabla_{y^l} (f^{l+1})^T\right]^T + \left[\nabla_{y^l} \beta_L\right]^T \right\} dy^l \\ + \left\{ \left[\nabla_{V_p} \beta_L\right]^T + (\lambda^l)^T \left[\nabla_{y^l} (f^l)^T\right]^T \right\} dV_p \end{aligned} \tag{F.22}$$

where y^l is the vector of the primary variables in the DTOF-based reservoir simulation. In single-phase model, y^l corresponds to the grid pressures ($M \times 1$ vectors).

$$y^l = \left[P_1^l, P_2^l, \dots, P_M^l\right]^T \tag{F.23}$$

To obtain the adjoint system, we take a Lagrange multiplier so that the terms multiplying dy^l in **Eq. (E.22)** equals to zero.

$$\left[\nabla_{y^l}(f^l)^T\right]\lambda^l = -\left[\nabla_{y^l}(f^{l+1})^T\right]\lambda^{l+1} - \nabla_{y^l}\beta_L \tag{F.24}$$

In this equation, the Lagrange multiplier λ can be solved backward in time. In **Eq. (F.24)**, the matrix $\left[\nabla_{y^l}(f^l)^T\right]$ is identical to the transpose of the Jacobian that is constructed in the reservoir simulation. The matrix $\left[\nabla_{y^l}(f^{l+1})^T\right]$ is a diagonal matrix, which is only related to the derivative of the accumulation terms. Hence, the calculation can be simplified using the expression of **Eq. (F.18)** as follows.

$$\left[\nabla_{y^l}(f^{l+1})^T\right] = \left[\nabla_{y^l}(A^l)^T\right] \tag{F.25}$$

Considering **Eqs. (F.20)** and **(F.22)**, the remaining term is

$$dJ_L = \left\{\left[\nabla_{V_p}\beta_L\right]^T + (\lambda^l)^T\left[\nabla_{y^l}(f^l)^T\right]^T\right\}dV_p \tag{F.26}$$

The sensitivity of the Lagrangian with respect to the drainage volume is obtained by

$$\nabla_{V_p}J_L = \nabla_{V_p}\beta_L + \sum_{l=1}^{L}\left[\nabla_{V_p}(f^l)^T\right](\lambda^l) \tag{F.27}$$

where the gradient $\nabla_{V_p}(f^l)^T$ corresponds to the derivative of the finite difference equation with respect to the primary variables, which needs to be constructed inside the reservoir simulator for each time-step. The gradient $\nabla_{V_p}\beta$ is the explicit sensitivity vector of the model response (i.e. bottom-hole pressure, production rate) with respect to the drainage volume, which can be calculated by differentiating the well term. The drainage

volumes of the grids of $i \neq 1$ are not explicitly appeared in the expression of β, thus we set $\nabla_{V_p}\beta = 0$. Using **Eqs. (F.24)** and **(F.27)**, we obtain the sensitivity coefficient for each time-step.

F.4 Gradient Calculation inside Reservoir Simulator

In the Adjoint-based sensitivity calculation, we first solve **Eq. (F.24)** to obtain λ and, then compute the final sensitivity matrix using **Eq. (F.27)**. In order to solve these equations, several matrices and vectors have to be constructed at the last Newton iteration of each time-step. At the last Newton iteration, it must be satisfied that the residuals of the finite difference equations are sufficiently small ($f \approx 0$).

In the rest of the development, we present the calculation of the gradients for a single-phase reservoir simulation. The matrix $\left[\nabla_{y^l}(f^{l+1})^T\right]$ in **Eq. (F.24)** is simply the derivative of the accumulation term with respect to the primary variables as described in **Eq. (F.25)**. The notations of the equation follows **Eq. (2.47)**.

$$\frac{\partial A_i^l}{\partial P_i^l} = \frac{w_i \Delta\tau_i}{\Delta t^l}\left[-\frac{\partial M_{\phi,i}^l}{\partial P_i^l}\frac{1}{B_i^l} + \frac{M_{\phi,i}^l}{B_i^{l\,2}}\frac{\partial B_i^l}{\partial P_i^l}\right] \tag{F.28}$$

The vector $\nabla_{y^l}\beta_L$ in **Eq. (F.22)** is the derivative of the well term with respect to the primary variables. A non-zero value is entered in the first elements in the vector). When the well rate is specified, the model response β corresponds to the bottom-hole pressure. When the bottom-hole pressure is specified, β corresponds to the well production rate. Using a definition of the well term (**Eq. (2.50)**), the non-zero element in $\nabla_{y^l}\beta_L$ is calculated by

$$\frac{\partial P_{wf}^{l}}{\partial P_1^{l}} = 1 - \frac{Q^{l}(\tau_1 - \tau_{\text{well}})}{w_1(\mu c_t)_{\text{init},1}} \frac{\partial (B\mu)_1^{l}}{\partial P_1^{l}} \tag{F.29}$$

$$\frac{\partial q_s^{l}}{\partial P_1^{l}} = w_1(\mu c_t)_{\text{init},1} \left[\left(\frac{1}{B\mu}\right)_1^{l} \left(\frac{1}{\tau_1 - \tau_{\text{well}}}\right) + \frac{\partial}{\partial P_1^{l}} \left(\frac{1}{B\mu}\right)_1^{l} \left(\frac{P_1^{l} - P_{wf}^{l}}{\tau_1 - \tau_{\text{well}}}\right) \right] \tag{F.30}$$

where P_1 is the pressure at the first grid $i = 1$. Notice that all the elements in the vector $\nabla_{y^n}\beta$ equals zero for $i \neq 1$. The derivatives of the mobility in **Eqs. (F.29)** and **(F.30)** are calculated by

$$\frac{\partial (B\mu)_1^{l}}{\partial P_1^{l}} = B_1^{l} \frac{\partial \mu_1^{l}}{\partial P_1^{l}} + \mu_1^{l} \frac{\partial B_1^{l}}{\partial P_1^{l}} \tag{F.31}$$

$$\frac{\partial}{\partial P_1^{l}} \left(\frac{1}{B\mu}\right)_1^{l} = -\frac{1}{B_1^{l} {\mu_1^{l}}^2} \frac{\partial \mu_1^{l}}{\partial P_1^{l}} - \frac{1}{{B_1^{l}}^2 \mu_1^{l}} \frac{\partial B_1^{l}}{\partial P_1^{l}} \tag{F.32}$$

The vector $\nabla_{V_p}\beta$ in **Eq. (F.27)** is the derivative of the well term with respect to the drainage volumes.

$$\frac{\partial p_{wf}^{l}}{\partial V_{p,1}} = \frac{q_s^{l}(\tau_1 - \tau_{\text{well}})(B\mu)_1^{l}}{(\mu c_t)_{\text{init},1}} \frac{\partial}{\partial V_{p,1}} \left(\frac{1}{w_1}\right) \tag{F.33}$$

$$\frac{\partial q_s^{l}}{\partial V_{p,1}} = \frac{\partial w_1}{\partial V_{p,1}} (\mu c_t)_{\text{init},1} \left(\frac{1}{B\mu}\right)_1^{l} \left(\frac{P_1^{l} - P_{wf}^{l}}{\tau_1 - \tau_{\text{well}}}\right) \tag{F.34}$$

Notice that all the elements in the vector $\nabla_{V_p}\beta$ equals zero for $i \neq 1$. In **Eqs. (F.33)** and **(F.34)**, the derivatives of the w-function at grid $i = 1$ are calculated by

$$\frac{\partial w_1}{\partial V_{p,1}} = \frac{\partial}{\partial V_{p,1}} \left(\frac{\partial V_{p,1}}{\partial \tau_1}\right) = \frac{1}{\Delta\tau_1} \tag{F.35}$$

$$\frac{\partial}{\partial V_{p,1}} \left(\frac{1}{w_1}\right) = -\frac{1}{{w_1}^2} \frac{\partial w_1}{\partial V_{p,1}} = -\frac{1}{{w_1}^2 \Delta\tau_1} \tag{F.36}$$

The matrix $\nabla_{V_p}(f^l)^T$ in **Eq. (F.25)** is the derivative of the finite difference equation with respect to the drainage volumes. The diagonal element is obtained by taking the derivative of **Eq. (2.47)**.

$$\frac{\partial f_i^l}{\partial V_{p,i}} = \frac{\partial T_{i-1/2}^l}{\partial V_{p,i}} P_{i-1}^l - \left(\frac{\partial T_{i-1/2}^l}{\partial V_{p,i}} + \frac{\partial T_{i+1/2}^l}{\partial V_{p,i}}\right) P_i^l + \frac{\partial T_{i+1/2}^l}{\partial V_{p,i}} P_{i+1}^l - \frac{\partial w_i}{\partial V_{p,i}} \frac{\Delta\tau_i}{\Delta t^l} \left[\left(\frac{M_\phi}{B}\right)_i^l - \left(\frac{M_\phi}{B}\right)_i^{l-1}\right] + \frac{\partial q_s^l}{\partial V_{p,i}} \tag{F.37}$$

where the derivatives of the transmissibility is calculated by

$$\frac{\partial T_{i-1/2}^l}{\partial V_{p,i}} = \frac{1}{\Delta\tau_{i-1/2}} \frac{\partial w_{i-1/2}}{\partial V_{p,i}} (\mu c_t)_{\text{init},i-1/2} \left(\frac{1}{B\mu}\right)_{up}^l \tag{F.38}$$

$$\frac{\partial T_{i+1/2}^l}{\partial V_{p,i}} = \frac{1}{\Delta\tau_{i+1/2}} \frac{\partial w_{i+1/2}}{\partial V_{p,i}} (\mu c_t)_{\text{init},i+1/2} \left(\frac{1}{B\mu}\right)_{up}^l \tag{F.39}$$

On the basis of the finite difference calculations (**Eqs. (2.40)** – **(2.42)**), the derivatives of the w-function in **Eqs. (E.38)** – **(E.39)** are obtained by

$$\frac{\partial w_{i-1/2}}{\partial V_{p,i}} = \frac{\partial}{\partial V_{p,i}} \left(\frac{V_{p,i} - V_{p,i-1}}{\tau_i - \tau_{i-1}}\right) = \frac{1}{\tau_i - \tau_{i-1}} \tag{F.40}$$

$$\frac{\partial w_{i+1/2}}{\partial V_{p,i}} = \frac{\partial}{\partial V_{p,i}} \left(\frac{V_{p,i+1} - V_{p,i}}{\tau_{i+1} - \tau_i}\right) = -\frac{1}{\tau_{i+1} - \tau_i} \tag{F.41}$$

The off-diagonal elements of the matrix $\nabla_{V_p}(f^l)^T$ are obtained as follows.

$$\frac{\partial f_i^l}{\partial V_{p,i-1}} = \frac{\partial T_{i-1/2}^l}{\partial V_{p,i-1}} \left(P_{i-1}^l - P_i^l\right) \tag{F.42}$$

$$\frac{\partial f_i^l}{\partial V_{p,i+1}} = \frac{\partial T_{i+1/2}^l}{\partial V_{p,i+1}} \left(P_{i+1}^l - P_i^l\right) \tag{F.43}$$

where the derivatives of the transmissibility are calculated by

$$\frac{\partial T_{i-1/2}^{l}}{\partial V_{p,i-1}} = \frac{1}{\Delta\tau_{i-1/2}} \frac{\partial w_{i-1/2}}{\partial V_{p,i-1}} (\mu c_t)_{\text{init},i-1/2} \left(\frac{1}{B\mu}\right)_{up}^{l} \tag{F.44}$$

$$\frac{\partial T_{i+1/2}^{l}}{\partial V_{p,i+1}} = \frac{1}{\Delta\tau_{i+1/2}} \frac{\partial w_{i+1/2}}{\partial V_{p,i+1}} (\mu c_t)_{\text{init},i+1/2} \left(\frac{1}{B\mu}\right)_{up}^{l} \tag{F.45}$$

The derivatives of the w-function in **Eqs. (F.44)** – **(F.45)** are obtained by

$$\frac{\partial w_{i-1/2}}{\partial V_{p,i-1}} = \frac{\partial}{\partial V_{p,i-1}} \left(\frac{V_{p,i} - V_{p,i-1}}{\tau_i - \tau_{i-1}}\right) = -\frac{1}{\tau_i - \tau_{i-1}} \tag{F.46}$$

$$\frac{\partial w_{i+1/2}}{\partial V_{p,i+1}} = \frac{\partial}{\partial V_{p,i+1}} \left(\frac{V_{p,i+1} - V_{p,i}}{\tau_{i+1} - \tau_i}\right) = \frac{1}{\tau_{i+1} - \tau_i} \tag{F.47}$$